UNIVERSITY OF STRATHCLYDE

Department of Biomedical Engineering

REAL-TIME, HIGH-THROUGHPUT ASSESSMENT OF NANOPARTICLE INTERACTIONS WITH SINGLE-CELLS USING MICROFLUIDICS: APPLICATIONS IN VACCINE DEVELOPMENT

Carlota F. A. de Albuquerque Rodrigues da Cunha-Matos

A thesis presented in partial fulfilment of the requirements for the degree of

Doctor of Engineering

2017

Declaration of Authorship

This thesis is the result of the author's original research. It has been composed by the author and has not been previously submitted for examination which has led to the award of a degree.

The copyright of this thesis belongs to the author under the terms of the United Kingdom Copyright Acts as qualified by University of Strathclyde Regulation 3.50. Due acknowledgement must always be made of the use of any material contained in, or derived from, this thesis.

Signed:
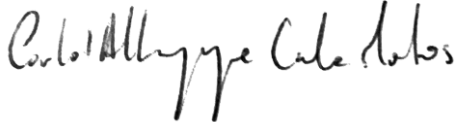
Date: 19th May 2017

Abstract

Nanomaterials are increasingly being developed for applications in biotechnology, including the delivery of therapeutic drugs and vaccine antigens. However, there is a lack of screening systems that can rapidly assess nanoparticle uptake and their consequential effects on cells. Established analytical *in vitro* approaches are often carried out on single time points, rely on time-consuming bulk measurements and are based primarily on populations of immortalised cell lines. As such, these procedures provide averaged results, do not guarantee precise control over the delivery of nanoparticles to cells and cannot easily generate information about the dynamic nature of nanoparticle-cell interactions and/or nanoparticle-mediated compound delivery. The present work addresses these issues by combining microfluidics, nanotechnology and imaging techniques into a high-throughput microfluidic platform to monitor nanoparticle uptake and intracellular processing in real-time and at the single-cell level. For this, a microfluidic device and protocols for cell trapping and live-cell monitoring were developed. In parallel, specific formulations of gold nanorods were produced, tested and optimised for intracellular multimodal imaging. Subsequently, controlled nanorod delivery to cells trapped in the microfluidic array was achieved across a range of concentrations, with intracellular nanorod signal detected using both fluorescence microscopy and surface-enhanced Raman scattering spectroscopy. Furthermore, on-chip measurement of specific cellular responses to nanorod delivery was also demonstrated. As a proof-of-concept application, the potential of the developed platform for understanding nanovaccine delivery and processing was investigated. Controlled delivery of ovalbumin-conjugated gold nanorods to primary dendritic cells was demonstrated, followed by real-time monitoring of nanoparticle uptake and antigen processing across a range of concentrations over several hours on hundreds of single-cells. This system represents a novel application of single-cell microfluidics for nanomaterial screening, providing a general platform for studying the dynamics of cell-nanomaterial interactions and representing a cost-saving and time-effective screening tool for many nanomaterial formulations and cell types.

Acknowledgements

Firstly, I would like to thank the University of Strathclyde, the Biomedical Engineering Department and the Centre for Doctoral Training in Medical Devices for the opportunity to be part of this programme, particularly Professor Patricia Connolly and Dr. Richard Black for putting their trust in me and making this research work possible.

I cannot be grateful enough to my three supervisors, Dr. Alastair Wark, Dr. Owain Millington and Dr. Michele Zagnoni, for their invaluable support, enthusiasm and mentoring over these years. With them, working in three separate departments with very diverse laboratory facilities and skill requirements became an exciting challenge, where I had the opportunity to truly experience hands-on interdisciplinary research. Their collaboration has been a great example for me – and I also immensely value how each of their doors was never closed.

I need to also thank Dr. Arjan Buis and Sarah Day for taking me onboard a new project with the necessary flexibility that allowed for the (sane!) completion of this thesis.

Big thanks also to the people working alongside me during these research years, especially Alison for smoothing my way into nanoparticle chemistry, Jenny and Kerrie for all their help with managing the cell cultures and their ever cheerful presence, and Graham, Barbara, Kay and the rest of the Zagnoni Lab for joyfully sharing the microfluidics road with me. Also to everyone else at the Centre for Microsystems and Photonics, remembering the old Royal College days – a group where I felt at home since the very beginning and where most of the research in this thesis was done.

A special note to the University of Strathclyde, through the above mentioned academic staff as well as Professor Bernard Conway and Professor Helen Grant, for outstanding kindness when it came to maternity leave arrangements and subsequent flexibility requirements.

Whole-hearted thanks to my family, especially my parents, for supporting me in this crazy idea of moving countries to do research, and for always being there for me. A special mention to my Mum for her enthusiasm in proof-reading this work!

Most of all I thank my husband Luís, for changing his own life to join me in this adventure, and for making this journey possible by supporting me every micrometre of the way. To him and Maria do Carmo, my heartfelt thanks for making all the normal days very happy days.

Contents

List of Figures

List of Tables

Abbreviations

AFBSA   Alexa Fluor 647-conjugated bovine serum albumin

APC   allophocyanin

BSA   bovine serum albumin

cRPMI   complete Roswell Park Memorial Institute culture medium

CTAB   hexadecyltrimethylammonium bromide

DC   dendritic cell

DAPI   4',6-diamidino-2-phenylindole

DCI   1,1'-diethyl-2,2'-cyanine iodide

DQOVA   DQ™ Ovalbumin

DTDCI   3,3'-diethylthiadicarbocyanine iodide

DTTCI   3,3'-diethyl-thiatricarbocyanine iodide

ELISA   enzyme-linked immunosorbent assay

FACS   fluorescence-activated cell sorting

FCS   foetal calf serum

FITC   fluorescein isothiocyanate

HBSS   Hanks' balanced salt solution

HRP   horseradish peroxidase

IFN   interferon

IL   interleukin

LED   light-emitting diode

MFI   mean fluorescence intensity

MGITC   malachite green isothiocyanate

NIR   near-infrared

NIR-797   near-infrared-797

NR   nanorod

OD   optical density (absorbance)

OVA   ovalbumin

PAA   poly(acrylic acid, sodium salt)

PAH   poly(allylamine hydrochloride)

PDDAC   poly(diallyldimethylammonium chloride)

PDMS   polydimethylsiloxane

PSS   poly-(sodium 4-styrenesulfonate)

PE   phycoerythrin

PFA   paraformaldehyde

PI   propidium iodide

ROI   region of interest

s.d.   standard deviation

s.e.m.   standard error of the mean

SEM   scanning electron microscopy

SERS   surface-enhanced Raman scattering

SERRS   surface-enhanced resonance Raman scattering

TMB   tetramethylbenzidine

UST   universal SERRS tag

UV   ultraviolet

Thesis Overview

This introductory section will outline the context and motivation behind the work presented in subsequent chapters, as well as the main aims of the research, followed by a short description of the general structure of the thesis, project contributions and publications. The underlying background concepts as well as more in-depth analysis of the literature will be presented in Chapter 1.

Motivation

Nanomedicine is a rapidly emerging and promising field for diagnostic, therapeutic and prophylactic applications.[1-3] Central to the successful development of these various nanomedicines (e.g. polymeric, lipidic, and inorganic) is the ability to systematically explore how particle properties and environmental factors influence parameters such as cellular uptake, intracellular processing and cell toxicity.[1,4] Specifically, gold nanoparticles have unique versatile optical properties and surface chemistry, which together with their relative biocompatibility have made these particles increasingly interesting candidates for imaging, drug or vaccine delivery and therapeutic (e.g. photothermal) applications.[2,4] So far, numerous *in vitro* studies have been reported for gold nanoparticles showing that factors such as shape,[5,6] surface coating,[7-11] charge[12] and hydrophobicity[13] of the particles, as well as environmental factors such as temperature[14] and pH,[15] can influence these interactions. However, currently available data is typically obtained from end-point measurements rather than from dynamic monitoring and studies are generally limited to a narrow range of parameters (e.g. a specific nanomaterial formulation or cell type), making it difficult to achieve global conclusions.[4,16,17] Therefore, there is an urgent need to develop low-cost technological tools that enable assessment of the interactions of nanoparticles with cells to be achieved in real-time, with high-throughput and high-resolution.[1,2] This project sets out

to address this need. Figure A shows a Venn diagram illustrating the main research fields involved, as well as aspects within each field which are key to this project.
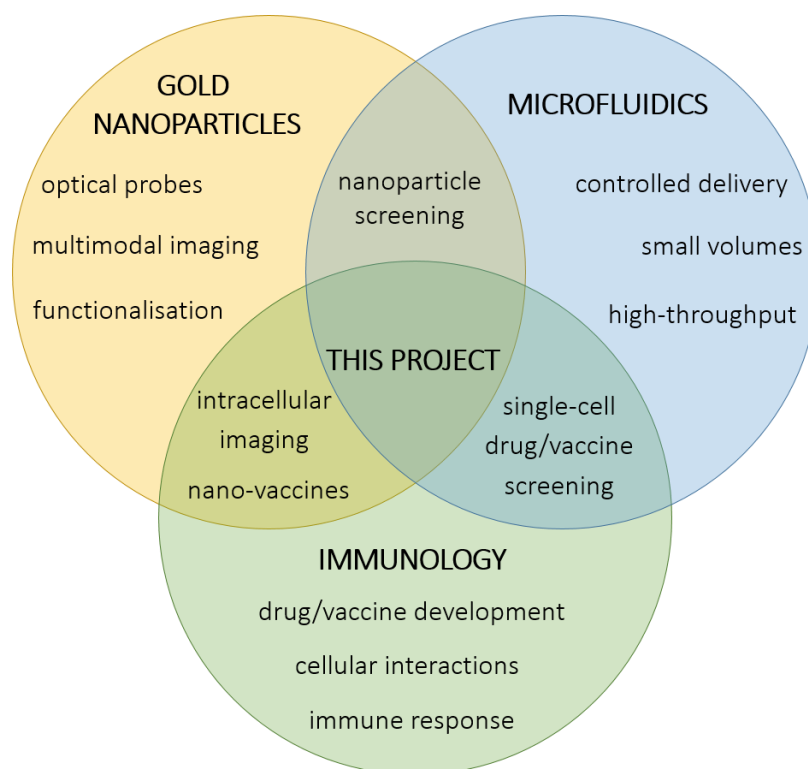
Figure A. Venn diagram depicting the context of the interdisciplinary project described in this thesis.

Microfluidic technologies offer interesting opportunities to nanoparticle research, due to inherent advantages such as minimising sample volumes and maximising control over the manipulation of particles suspended in laminar flows.[18,19] Specifically, lab-on-a-chip approaches have been explored for applications ranging from on-chip synthesis of nanoparticles[20,21] to the development of new nanoparticle-based applications and assessment of cell-nanoparticle interactions.[17,22-24] On one side, organ,[25] tumour[26,27] and body-on-a-chip[28] examples have shown the importance of producing physiologically relevant microenvironments when testing nanomaterials with respect to static flow well-plate systems, by providing complex information on models of the living tissue. On the other hand, single-cell microfluidic approaches[29-31] provide experimental statistical data acquired within a single device with a throughput comparable to that of standard flow cytometry, while being amenable to real-time cell imaging for long periods of time. This way, microfluidic techniques can facilitate nanoparticle tracking with intracellular resolution, therefore providing

information on the effect of nanomaterials at the single-cell level[17,23,24] and insight into the heterogeneity of responses to nanomaterials.[32,33]

One application that would benefit greatly from such an approach is the development and screening of nano-vaccines.[3,34,35] Dendritic cells are a privileged target for vaccine delivery due to their role in the initiation of the immune response through antigen internalization, processing and presentation to lymphocytes.[36-38] Thus, assessment of nano-vaccine uptake and antigen delivery to dendritic cells would provide information about the fundamental pathways involved in those interactions and allow for investigations to improve targeting and delivery efficiencies.[38-40] Gold nanoparticles have great potential as vaccine carriers due to their biocompatibility and potent adjuvant ability[9,35] and successful targeting to dendritic cells may allow for increased activation at lower antigen dose, potentially reducing side-effects, increasing stability and lowering vaccine production costs.[35,38,41] Additionally, anisotropic particles such as gold nanorods have extremely versatile optical properties, which can be tuned for specific applications, originating highly specific and stable substrates for intracellular multimodal imaging with sensitivities at the single nanoparticle level.[42,43] To date, microfluidics has shown great promise for providing tools to investigate immunological functions,[44] from cell migration[45,46] to lymphocyte function,[47,48] cell pairing[49] and adjuvant screening.[50] However, despite the increasing interest in nanomaterial development for immune-based applications and lab-on-a-chip technologies for nanomaterial screening,[17,22-24,51-53] the successful development of *in vitro* models that can be used as a robust, high-throughput predictive screening tool for nanomaterial toxicity and particle-cell interaction studies before *in vivo* experiments is still to be achieved.[17,23]

Aims and Novelty

Consequently, the aims of this work were to develop a system comprising:

1) A **microfluidic platform,** featuring:
   a) Trapping of cells into a biocompatible environment where cells could be cultured and individually monitored;
   b) Controlled delivery of a range of nanoparticle concentrations to cells;
   c) Real-time monitoring of cell-nanoparticle uptake and interactions;
   d) Parallel investigation of single-cell responses with high-throughput;
   e) Compatibility with multimodal imaging techniques.

2) A model **nanoparticle system**, comprising:

   a) Anisotropic shape (nanorods) with tunable optical properties;

   b) Highly specific multimodal imaging capabilities e.g. fluorescence, SERRS and dark-field;

   c) Versatile surface chemistry, biocompatible and amenable to bioconjugation;

   d) Applicability as a nano-vaccine model.

To achieve a biologically-relevant proof-of-concept for the integrated platform, primary **dendritic cells** were used throughout this work, given that these cells represent a relevant model for *in vivo* interaction of nanomaterials, as foreign objects, with the immune system and, consequently, for testing of nanoparticle-mediated antigen delivery and processing.

This novel combination of single-cell microfluidics with customised nanorods and imaging techniques provided unique information regarding the dynamics of nanoparticle/single-cell interactions. To validate the platform for nano-vaccine screening applications, nanoparticle-mediated antigen delivery was monitored simultaneously on hundreds of single-cells using the integrated platform.

Thesis outline

The thesis starts by presenting the background concepts required to develop the project and a review of the current state-of-the-art, to provide context and justify the motivation for the research (Chapter 1). Relevant aspects from the three main fields of research as set out in the Venn diagram above are critically explored. Subsequently, a practical description of the materials and methods used in all the experimental procedures underlying the research is presented (Chapter 2). Reporting and discussion of results is then divided into four separate chapters. Firstly, the development, preparation and characterisation of customised gold nanorods for a range of cellular imaging applications composes Chapter 3. Chapter 4 then sets out to describe the design considerations gathered to achieve a microfluidic platform for cell trapping and nanoparticle gradient generation. The integration of microfluidics with nanorods for cell trapping and multimodal imaging is then presented in Chapter 5, with Chapter 6 showing the application of the integrated platform for real-time assessment of nanoparticle-mediated antigen delivery and processing. Finally, a general discussion of results together with conclusions and envisioned future developments is presented in Chapter 7.

Project contributions

All the research presented in this work, including experimental and data analysis, was performed by the author unless otherwise stated. Briefly, the author independently developed and tested different nanorod formulations and microfluidic device designs (Chapters 3-4), while also optimising the experimental protocol to achieve a robust cell trapping and imaging platform, with fluorescence imaging and SERRS mapping of live cells and nanorods within the microfluidic device and associated data analysis (Chapters 5-6). Initial training was provided in nanoparticle synthesis, characterisation and SERRS mapping techniques by Dr. Alastair Wark and Dr. Alison McLintock; in microfluidic device design, prototyping and testing by Dr. Michele Zagnoni, Dr. Graham Robertson and Bárbara Schlicht; and in dendritic cell preparation, culture and associated analysis and microscopy procedures by Dr. Owain Millington and Dr. Jenny Crowe. The UST formulation presented in Chapter 3 was developed by Dr. Alison McLintock. All nanorod SEM was performed by Dr. Alastair Wark. Dr. Michele Zagnoni performed the 3D simulations of concentration gradients within the microfluidic device as presented in Chapter 4.

Publications

The research achievements described in this thesis have been published in the following peer-reviewed journal articles:

- "Universal Surface-Enhanced Raman Tags: Individual Nanorods for Measurements from the Visible to the Infrared (514–1064 nm)", A. McLintock, C. A. Cunha-Matos, M. Zagnoni, O. R. Millington, and A. W. Wark, ACS Nano, 8, 8600-8609, 2014.
- "Real-Time Assessment of Nanoparticle-Mediated Antigen Delivery and Cell Response", C. A. Cunha-Matos, O. R. Millington, A. W. Wark and M. Zagnoni, Lab on a Chip, 16, 3374-3381, 2016.

And conference proceedings:

- "A Microfluidics Tool for High-throughput, Real-time Multimodal Imaging of Nanoparticle-cell Interactions", C. A. Cunha-Matos, O. R. Millington, A. W. Wark and M. Zagnoni, Oral presentation at the Microfluidics'14 Conference in Limerick, Ireland, December 2014.

- "Real-time multimodal imaging of nanoparticle-cell interactions in high-throughput microfluidics", C. A. Cunha-Matos, O. R. Millington, A. W. Wark and M. Zagnoni, Poster presentation (by Dr. M. Zagnoni) at the MicroTAS Conference in San Antonio, Texas, October 2014.
- "Real-time assessment of nanoparticle-cell interactions and multimodal imaging in high-throughput microfluidics", C. A. Cunha-Matos, O. R. Millington, A. W. Wark and M. Zagnoni, Poster presentation at the Global Engage Microfluidics Congress in London, UK, October 2015.
- "Time-Lapse Measurement of Single-Cell Response to Nanomaterial: A Microfluidic Approach", C. A. Cunha-Matos, O. R. Millington, A. W. Wark and M. Zagnoni, Poster presentation at the MicroTAS Conference in Dublin, Ireland, October 2016.

Chapter 1

Background

This chapter presents a review of the current state-of-the-art for the areas outlined in the Thesis Overview, to provide a foundation and motivation for the subsequently presented work. Considering the multidisciplinary and fast-developing aspects of this research, focus will be given to techniques and applications which are directly related to the work carried out in this studentship.

1.1 Dendritic cells and their role in the immune system

Dendritic cells are a type of phagocytic immune cell, also known as antigen-presenting cells. Their principal role is to present antigen to T cells to generate an adaptive immune response. Thus, dendritic cells represent the crucial connection between the innate immune system and the adaptive immune system.[36] This section will briefly outline some of the general aspects of dendritic cell biology that make these cells privileged targets for nanovaccine development.[38]

1.1.1 Generation of an adaptive immune response

Immature dendritic cells continuously sample antigen from the environment, and non-pathogenic antigen is routinely presented to T cells to maintain self-tolerance. Following sensing of pathogenic material, exposure to endogenous "danger" signals (such as proinflammatory cytokines or complement activation) or stimulation by adjuvants, dendritic cells become activated and begin their maturation process. This includes important functional and phenotypic changes, such as the upregulation of Major Histocompatibility

Complex (MHC) and costimulatory molecules. Additionally, activated dendritic cells express CCR7, a chemokine receptor that allows them to migrate from peripheral tissue into the draining lymphoid organs. When fully matured, these cells have the ability to present antigen peptides to naïve T cells and activate them to initiate an adaptive, or antigen-specific, immune response.

A general overview of antigen internalisation, processing and presentation pathways is presented in Figure 1.1. Dendritic cells take up particulate matter from the surrounding environment by phagocytosis (for particles >1 μm) or receptor-mediated endocytosis, from caveolæ (~60 nm) or clathrin-coated pits (~120 nm). Importantly, these cells also non-specifically engulf large quantities of extracellular matter by a process called macropinocytosis. Following uptake through any of these pathways, processing of exogenous antigens generally occurs in endocytic vesicles, where proteases digest the antigen. Subsequently, MHC class II molecules, which originate in the endoplasmic reticulum, are targeted to these endocytic compartments. There, they bind to antigen peptides, and these peptide–MHC complexes are transported in exocytic vesicles to the cell surface, where antigen presentation occurs. Endogenous antigen found in the cytosol is most generally processed through the proteasome and presented by MHC class I molecules instead.[36,54,55]
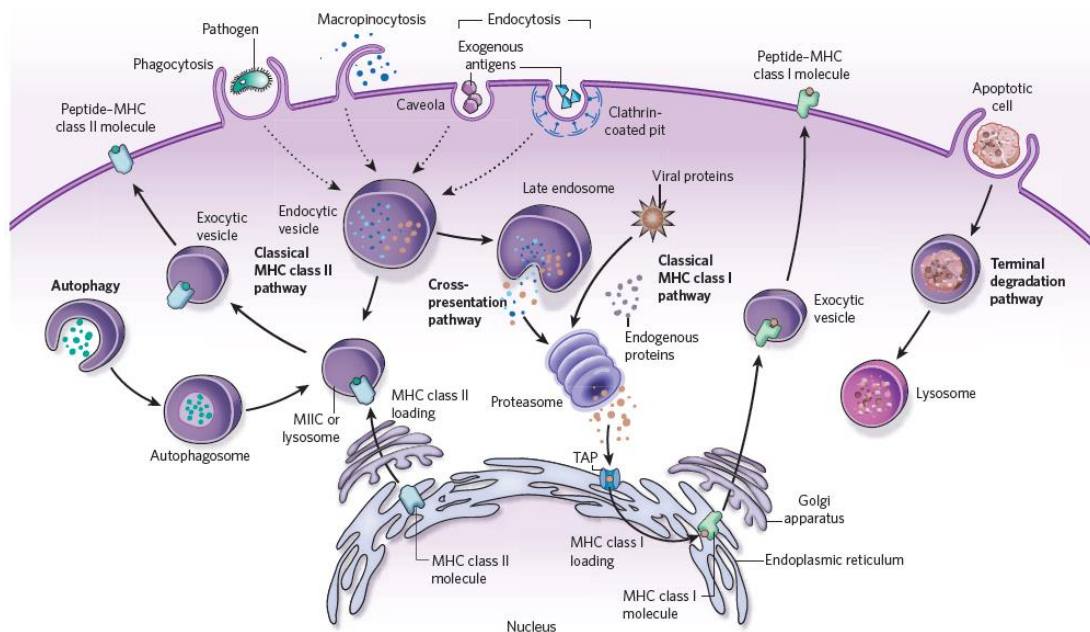
Figure 1.1 Antigen processing and presentation by dendritic cells. Schematic representing a simplified view of the various antigen internalisation, processing and presentation pathways within a dendritic cell. Reproduced from Hubbell et al, 2009.[55]

Naïve T cells are fully activated only when the antigen-presenting cell simultaneously presents a specific antigen to the T cell antigen receptor along with costimulatory molecules, forming the so-called immunological synapse. Following this stimulus, T cells will proliferate and differentiate into effector T cells, which can then specifically act on cells displaying antigen on the surface without the need for further costimulation. Different antigen presentation routes target different subsets of T lymphocytes. Generally, CD8$^+$ T cells will interact with MHC-I molecules and differentiate into cytotoxic CD8$^+$ T cells, while CD4$^+$ T cells will interact with MHC-II molecules and differentiate into a range of effector T cell subsets with different functions. Examples of these subsets, specialised for responding to different types of pathogens, are T$_H$1 cells, which produce cytokines that activate macrophages in bacterial infections (such as interferon-γ), and T$_H$2 cells, which produce cytokines to promote barrier immunity (such as IL-5). Importantly, the type of response generated depends on the biochemical and cellular context. Effector T cells are also responsible for inducing antigen-specific antibody production by B cells, which is the basis of acquired immunity. This leads to immunological memory for that specific antigen, allowing for a more efficient response to be generated in subsequent exposures to the same antigen – a feature which forms the base for vaccination.[36,54]

1.1.2 Dendritic cells as targets for vaccine delivery

Vaccination, or immunisation, is the intentional stimulation of an immune response against specific antigens to prevent disease. Generally, it is achieved through inoculation of inactive forms of the antigen, which induce an adaptive immune response that becomes protective against the active form of the same antigen on subsequent exposures. It has been one of the greatest developments in public health, leading to the complete eradication of some epidemic diseases in specific regions. However, current vaccine delivery techniques present limitations, namely the requirement for multiple injections and the induction of side-effects due to use of large doses, while there is still a complete lack of vaccines for many chronic diseases.[35,38]

One of the approaches that can be taken to more specifically deliver antigen, minimising dose requirements and side-effects, is targeting the delivery of antigen to specific cells. Dendritic cells appear as the obvious candidates, due to their role in the initiation of antigen-specific T cell response, as detailed in the previous section. However, successful targeting and activation of dendritic cells is an ongoing challenge, as it requires delivery of antigen to areas

rich in these cells (such as lymph nodes), as well as subsequent antigen uptake, processing and presentation. Additionally, the great heterogeneity between dendritic cell subsets has also raised questions as to which subset should be targeted, as well as to the relationship between different subsets *in vivo* and whether it is enough to target a single one.[40] Another question is whether to target dendritic cells at the injection site, relying on their migration to the lymph nodes, or to directly target those residing in the lymph nodes, which could potentially increase vaccine efficacy further.[56]

Currently, most vaccines used are composed of purified antigen molecules, rather than the whole pathogen, being less prone to side-effects. However, these "subunit vaccines" are not very immunogenic by themselves, and thus vaccine formulations also need to include substances that enhance the stimulation of the immune response, called adjuvants.[34,35] Toll-like receptor activation, inflammatory cytokines or complement activation are examples of ways through which these danger signals can be produced.[56] Overall, the current challenge is in fine-tuning vaccine formulations into robust combinations of antigen, adjuvant and targeting molecules, resulting in a more controlled dosage of antigen and potentially a tailored lymphocyte response.[38,40] For this purpose, new multidisciplinary approaches are being explored, such as the development of nanoparticle-based vaccines.[35,38] This subject will be further explored in section 1.4.3, with a focus on gold nanorods as vaccine carriers.

1.1.3 New technologies to investigate the immune system

The complexity of the immune system, in aspects ranging from the role of each cell type in different situations to cell-cell communication and intracellular pathways, is a very active area of research, with many of the underlying processes still being poorly understood. Traditionally, animal models have been used to investigate these functions in health and disease and have led to many great developments in fundamental and applied immunology. However, these models often present limitations when translating to human immunity and disease, and it is increasingly important that animal use is reduced as much as possible.[44,57] Additionally, the complexity of the behaviour of individual cell types or specific signalling mechanisms, often impossible to isolate *in vivo*, calls for the development of new tools to isolate and assess specific cell functions or responses *in vitro*.[44,58,59] The development of microfluidic technologies for this purpose will be explored in section 1.7.1 below. As a different approach, the use of gold nanoparticles for investigating intracellular phenomena or tracking vaccine delivery will be described in section 1.4.

1.2 Gold nanorods as versatile imaging and sensing tools

Gold nanoparticles, especially anisotropic gold nanoparticles such as gold nanorods, are increasingly being used for analytical and bioanalytical applications. The optical properties of these nanoparticles have opened the way for new possibilities for imaging and sensing. This section presents an outline of the nanorod features and associated techniques which are relevant to the present work.

1.2.1 Plasmonic characteristics of gold nanorods

The localised surface plasmon resonances (LSPRs) of noble metal nanoparticles are coherent oscillations of conduction band electrons across the particle which couple with electromagnetic radiation, with field being highest at the metal surface. The anisotropy of gold nanorods allows for these particles to have two distinct LSPR extinction bands (longitudinal and transverse), which relate to electron motion along the rod length and width (Figure 1.2 a). The longitudinal resonance is especially sensitive to nanorod aspect ratio and can be tuned from the visible to the near-infrared (NIR) simply by adjusting the synthesis procedure (Figure 1.2 b-g).[2,60]
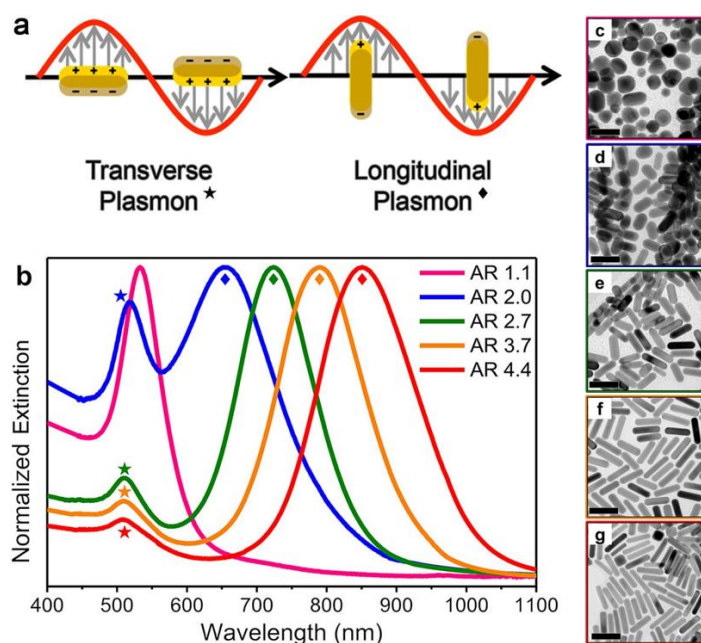
Figure 1.2 Plasmonic properties of gold nanorods. (a) Diagram representing the conduction band electron oscillation (grey arrows) upon transverse and longitudinal localized surface plasmon resonances of gold nanorods. (b) Visible/NIR extinction spectra of gold nanorods with different aspect ratios (ARs). Symbols indicate the (★) transverse and (◆) longitudinal extinction peaks. (c-f) Transmission electron microscopy (TEM) images of gold nanorods of AR (c) 1.1, (d) 2.0, (e) 2.7, (f) 3.7, and (g) 4.4. Scale bars are 50 nm. Adapted from Burrows et al, 2016.[61]

Nanoparticle LSPR depends on the material properties of the nanoparticle surface, the particle shape and the dielectric constant of the surrounding medium, as well as the aggregation state of the particles.[60,62] Additionally, the anisotropic nature of gold nanorods makes them more sensitive to changes in the local refractive index near to the nanoparticle surface than spherical nanoparticles.[63] This way, changes in particle LSPR, measured as peak shifts in UV-visible spectroscopy, can be used for chemical sensing. Specifically, adsorption of molecules (such as proteins) to the particle surface or chemically specific changes in local dielectric constant or nanoparticle aggregation state can be detected using this method.[64] However, although LSPR shifts can be useful as a generic indication of change in surface chemistry, the technique presents great limitations in terms of multiplexing capabilities and specific molecule identification.[4,65]

1.2.2   Gold nanorod preparation

The most widespread, scalable and tunable method currently used for gold nanorod synthesis is the seed-mediated growth method. In this method, a solution of spherical "seed" particles is first prepared through the reduction of gold salts in surfactant by a strong reducing agent (sodium borohydride). This reaction takes place in water, in air and at room temperature, and yields <5 nm particles. Subsequently, a growth solution containing gold salt, a structure-directing surfactant (cetyltrimethylammonium bromide, CTAB) a weak reducing agent (ascorbic acid) and trace silver nitrate is prepared in a separate flask. Upon addition of the seeds, the growth reaction takes place on the seed surface, producing larger, rod-shaped nanoparticles.[43,66,67] This reaction can be scaled to large volumes in order to minimise the potential for inter-batch variability for subsequent applications.[68] This surfactant-directed synthesis procedure results in a stabilising CTAB bilayer around the surface of the nanorods, which is believed to result from electrostatic interactions between the ammonium headgroup on CTAB and the anionic metal surface.[43,61] The presence of a bilayer leads to the nanorods being soluble and relatively stable in aqueous media, while the approximately 3 nm of hydrophobic region can be used to sequester hydrophobic organic molecules,[69,70] such as dyes, very near the metal surface – providing favourable conditions for Raman signal enhancement (see below).

In addition to being amenable to molecule sequestering, the CTAB bilayer around the surface of synthesised gold nanorods provides a stable platform for further surface modifications, depending on the intended application of the particles. One popular option, given the

positive charge of the outer CTAB surface of the nanorods, is the sequential electrostatic self-assembly of oppositely-charged polyelectrolytes onto the surface, also known as layer-by-layer (LbL) coating.[61,71] This simple coating procedure relies on a balance between the ionic strength of the salt solution used for dissolving the polyelectrolytes and the polymer molecular weights. Also, successful self-assembly of each polymer layer onto the nanorod surface can be monitored using UV-visible spectroscopy and zeta potential measurements. Importantly, this method can be used to control the final surface charge of the gold nanorods based on the choice of polyelectrolyte layers applied, providing great flexibility for biological imaging and sensing applications[72], as well as for subsequent adsorption of proteins.[73] Another important feature of polyelectrolyte-coated gold nanorods is their increased biocompatibility, due to the enclosure of the cytotoxic surfactant bilayer and consequent prevention of CTAB desorption from the surface.[7] The biomedical applications of these nanoparticles will be further discussed below.

1.2.3   The Raman effect and Surface-Enhanced Raman Scattering

The measurement of the interaction of light with matter, be it absorption or scattering, provides important information on the characteristics of the irradiated material, being the base of all spectroscopy techniques. In terms of scattering, elastic (Rayleigh) scattering is the dominant scattering process, where there are negligible energy differences between the incident and scattered photons. However, a more specific way of probing a molecule lies on the measurement of Raman, or inelastic, scattering events. These events occur when the energy from an incident photon is different to that of the scattered photon by an amount of energy equivalent to one vibrational unit, due to the induction of nuclear motion during the scattering process.[74] These scattering events are schematised in Figure 1.3.

There are two types of Raman scattering: Stokes, where the energy of the scattered photon is lower than that of the incident photon, and anti-Stokes, where the emitted photon is of a higher energy than the incident photon. Generally, Stokes scattering is more prevalent than anti-Stokes, at room temperature conditions, and thus that is what is most commonly measured in Raman spectroscopy. Overall, Raman scattering is a weak process, occurring approximately in one in a million scattered photons. In any case, due to its ability to provide complex information about molecular structure and the local environment, Raman spectroscopy is a powerful technique for biological imaging and sensing applications, with much better specificity than electronic spectroscopy techniques (e.g. fluorescence).[75,76]
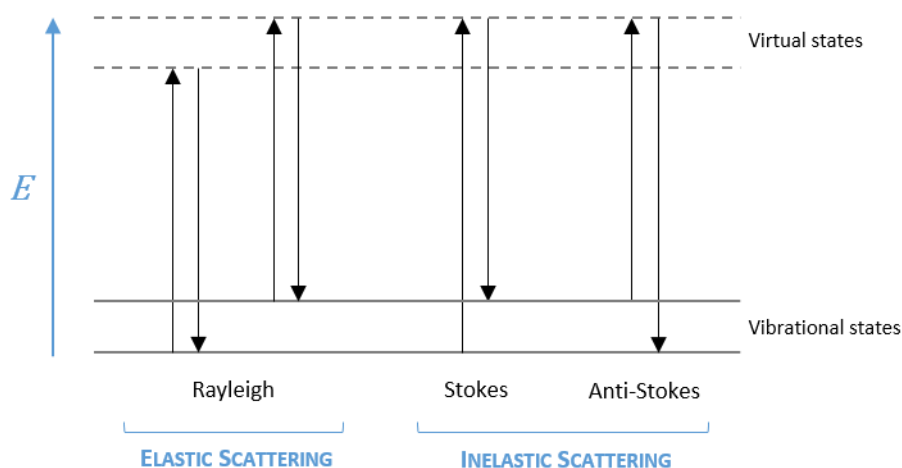
Figure 1.3 Diagram of Rayleigh and Raman (Stokes and Anti-Stokes) scattering processes. Adapted from Smith and Dent, 2005.[74]

When Raman scattering takes place on molecules which are in close proximity to nanoscale metal surfaces, the corresponding Raman-active vibrations are enhanced by many orders of magnitude (typically around 10^{10}, depending on the substrate). This phenomenon is termed Surface-enhanced Raman scattering (SERS). The fundamental requirements for SERS are that the substrate supports a surface plasmon resonance (generally, gold and silver nanostructures) and that the analyte of interest is within nanometres of the surface.[76,77] Generally, SERS-based assays can either be label-free assays or Raman reporter assays. In the former, molecule adsorption on the nanoparticle surface is detected by the molecule's own Raman signal enhancement, making this a molecularly specific technique. However, this method is prone to interference from other molecular species surrounding the surface of the nanoparticles. In reporter-based assays, molecules with high Raman scattering cross-section, called Raman reporter dyes, are adsorbed onto the metallic surface of the nanoparticles, and their specific SERS spectrum can then be used as a highly specific readout for tracking and accumulation of these particles, without interference from neighbouring species.[2,78,79] Because of the high specificity of Raman spectra, even molecularly similar labels are unlikely to present spectral overlap. This fingerprinting aspect means that multiplex detection can be achieved by using a range of different labels.[76,80] Additionally, when the excitation wavelength used to excite the plasmon (and create SERS) overlaps with the reporter dye resonance, increased enhancements of the signal can be achieved from the combination of the molecular resonance of the dye with SERS from the metallic surface. In these cases, the phenomenon is termed surface-enhanced resonance Raman scattering, SERRS.[76,78]

1.2.4 Gold nanoparticles for SERS

The great enhancement obtained with SERS has allowed this technique to be used in complex samples, such as biological environments.[81,82] Importantly, it allows for short collection times to be used, opening the way for mapping of intracellular events at more realistic timescales than non-enhanced Raman spectroscopy.[76,77] In addition, SERS probes do not photobleach, can be excited at a number of different wavelengths and present much better multiplexing capabilities than, for example, fluorescence imaging.[82] Table 1 presents a general overview of the properties of such SERS tags (combinations of metal nanoparticles with organic Raman reporter dyes) compared to those of quantum dots and traditional fluorescence dyes.

Table 1. Comparison of SERS tags, quantum dots and fluorescence dyes (adapted from Wang et al, 2012[79])

	SERS tags	quantum dots	conventional dyes
physical principle	Raman scattering	fluorescence emission	fluorescence emission
core composition	Au/Ag nanoparticles	cadmium nanocrystals	organic compounds
approximate size	10-100 nm	2-10 nm	< 2 nm
bandwidth	< 2 nm	~30-50 nm	> 50 nm
structural information	fingerprint	non-fingerprint	non-fingerprint
multiplexing capacity	~10-100	~3-10	~1-3
photostability	no photobleaching	decay (strong excit. power)	decay (weak excit. power)

The most widely used SERS substrates for bioimaging and biosensing applications are metal nanoparticles, and a number of different approaches have been taken to maximise signal enhancement. One approach is the controlled aggregation of particles, leading to the formation of "SERS hot spots" between particles. Examples of individually-wrapped assemblies of spherical particles[83], rod-shaped particles [68] and combinations of both shapes[84] have been reported for this purpose. However, variability in cluster size, relative nanoparticle orientation within clusters and location of dye molecules leads to variable LSPR profiles within these aggregates, making uniformly bright clusters hard to achieve.[69] Additionally, the overall aggregate size might complicate their *in vivo* application.[69,85] Therefore, the use of bright, monodispersed single-particle suspensions has become a promising route for biomedical applications of SERS.[42,69] This can be achieved via the sequestering of Raman active dyes into the CTAB bilayer of gold nanorods, as mentioned above, with very high signal enhancement obtained due to the proximity of the dyes to the gold surface of the nanorods. Specific tuning of the nanorod LSPR excitation (from visible to NIR wavelengths), together with coupling between the nanorod and the dye resonances, allows for optimisation of the

SERRS behaviour of these particles.[69] Additionally, multi-dye combinations can also be explored for this purpose, creating single particles able to emit bright signals across a wide range of wavelengths simultaneously.[42]

1.2.5 Gold nanoparticles for multimodal imaging

Due to their versatile plasmonic properties, gold nanoparticles can be specifically detected using light scattering, SERS, fluorescence and other techniques, such as two-photon luminescence and photothermal/photoacoustic imaging, making them potential multimodal imaging tools.[2,72,79] In addition, gold nanorods are amenable to single-nanoparticle tracking applications using various techniques. For example, correlated SEM and SERRS imaging of single gold nanorods containing a combination of Raman reporter dyes has been demonstrated, showing the multimodal imaging and strong SERRS signal capacities of these particles (Figure 1.4).
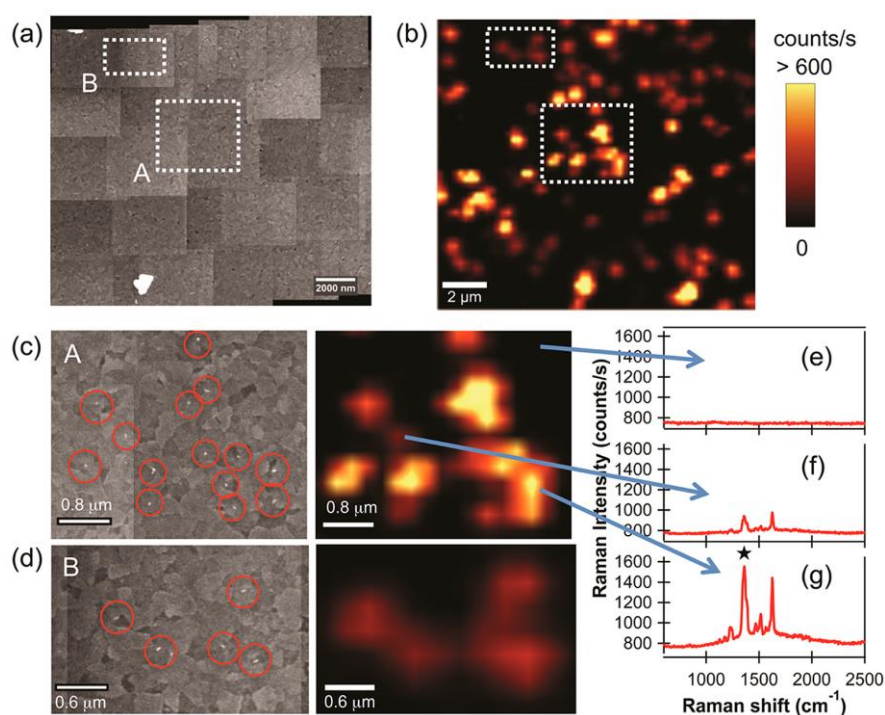
Figure 1.4 Correlated SEM and SERRS imaging of single gold nanorods on an ITO-coated glass slide. (a) Stitched high resolution SEM images of a large area (~14 μm x 13 μm) and (b) corresponding confocal Raman map. (c) Zoomed in views of area A and (e-g) representative raw SERRS spectra from different surface regions. Analysis of the peak at 1360 cm^{-1} (★) following background subtraction was used to generate the Raman map with the brightest areas corresponding to peak intensities >600-1700max counts/s. (d) Magnified view of area B with encircled isolated nanorods. Raman data was obtained at 532 nm excitation, 0.6 mW laser power, 1 s integration time and at 0.25 μm spatial steps. Rep. from McLintock et al, 2014.[42]

1.3 Cellular interactions with nanomaterials

When using nanomaterials for biomedical applications, it is important to assess their interactions with cells, considering cellular uptake, induced toxicity and cellular functional responses to the nanomaterial. This section will provide an overview of available data considering the different factors that can affect these interactions. It is important to note however, that most of these studies are performed on a specific cell type and nanomaterial formulation, using a specific type of readout assay to reach conclusions, and hence generalisations are difficult to obtain.[4,16,86]

1.3.1 Uptake mechanisms

In order for nanomaterials to be delivered to the intracellular environment and subcellular targets, it is important to understand the mechanisms through which particles can penetrate the cell membrane. As seen above, extracellular materials can enter the intracellular environment through different mechanisms (Figure 1.1). Of these, receptor-mediated endocytosis is generally accepted as the primary route of entry for nanoparticles (Figure 1.5).[87] This is not a rule, however, and will vary not only with nanoparticle characteristics, such as size, shape and surface chemistry, but also for different cell types. For instance, some uptake mechanisms can be a very important route of entry in some cells and not as important in others, while only some cells are capable of specific mechanisms such as phagocytosis. In addition, it is possible to functionalise the nanoparticles with biomolecules that will influence their mode of uptake,[88] and it has been reported that nanoparticles can also directly penetrate the cell membrane.[89] Thus, it is vital that uptake pathways are characterised for each specific application, as these will have a direct effect on the intracellular fate of the nanoparticles and consequently on their effect on the cell.[87,90,91] Additionally, environmental factors such as temperature,[14] pH[15] and substrate stiffness[92] have also been found to influence, and possibly be used to control, the initial interaction of nanoparticles with cells.

Marchesano et al[89] studied the traffic of gold nanospheres through a whole organism, by imaging a simple water invertebrate which was exposed to these particles. Their results showed that nanoparticle uptake was a rapid process, with efficiencies depending on the surface coating. Results also importantly showed that, under the experimental conditions used, the nanoparticles were cleared of the system at less than 48 h after exposure, through a combination of different exocytosis mechanisms.
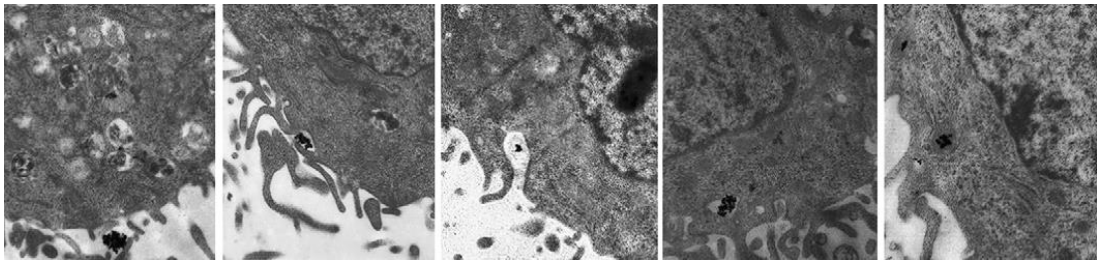
Figure 1.5 Nanoparticle uptake by cells. Sequence of TEM images showing the different stages of gold nanorod uptake via endocytosis by cells of a human breast adenocarcinoma cell line (MCF-7). Reproduced from Qiu et al, 2010.[93]

1.3.2 Effect of particle shape and size

Gold nanoparticles can have numerous different shapes, which have different effects in their interaction with cells. Chithrani et al.[5,94] reported differences between uptake of a range of sizes of spherical and rod-shaped gold nanoparticles for the same cell type, making claims that the spherical particles were more efficiently taken up than the rods. However, these studies were performed on HeLa cells, an immortalised cancer cell line which is unlikely to reflect *in vivo* uptake and processing characteristics. Importantly, some multi-parametric studies have suggested that the aspect ratio of gold nanorods does not have a determinant effect on their cytotoxicity, when compared to surface chemistry.[11,93]

Another study involving more physiologically relevant primary macrophages[6] investigated the mechanisms of uptake of silica nanoparticles of different shapes. The study reported interesting data on the preferred mechanism for each shape of particle, with spheres being predominantly taken up by endocytosis and elongated structures primarily by macropinocytosis or phagocytosis. Additionally, that same report showed that different cell types presented very different uptake profiles under the same exposure conditions, reiterating the fact that each cell population will potentially show different levels of nanomaterial-induced effects. Bartczak et al[95] studied the effect of different shapes of gold nanoparticles (spheres, rods, hollow spheres and gold/silica nanocrystals) with the same surface coating on primary endothelial cells. Viability studies indicated that none of the particles used were toxic, but differences in uptake were detected for the different particle morphologies. In a separate study, different levels of aggregation were induced to spherical nanoparticles and their uptake compared with monodisperse samples. It was observed that different cell lines responded differently to the aggregated samples, again underlining the

need for specific cell types and nanomaterial formulations to be assessed for each application.[85]

1.3.3 Effect of surface chemistry

The outer surface of nanomaterials, which is the surface that first interacts with the biological environment, is crucial in determining nanoparticle uptake, biological fate within the cell and consequent cytotoxicity.[7,10] Concerning gold nanorods, it is generally known that the outer CTAB bilayer has cytotoxic effects on cells, with the mechanisms of cell death having been studied by some groups for specific cell types.[8,11] Comparison of uncoated nanorods (with CTAB as the outer layer) with polyelectrolyte-wrapped rods has shown that the latter have much better biocompatibility in all reported cases.[7,11,93,96] An example from one of these studies is shown in Figure 1.6.
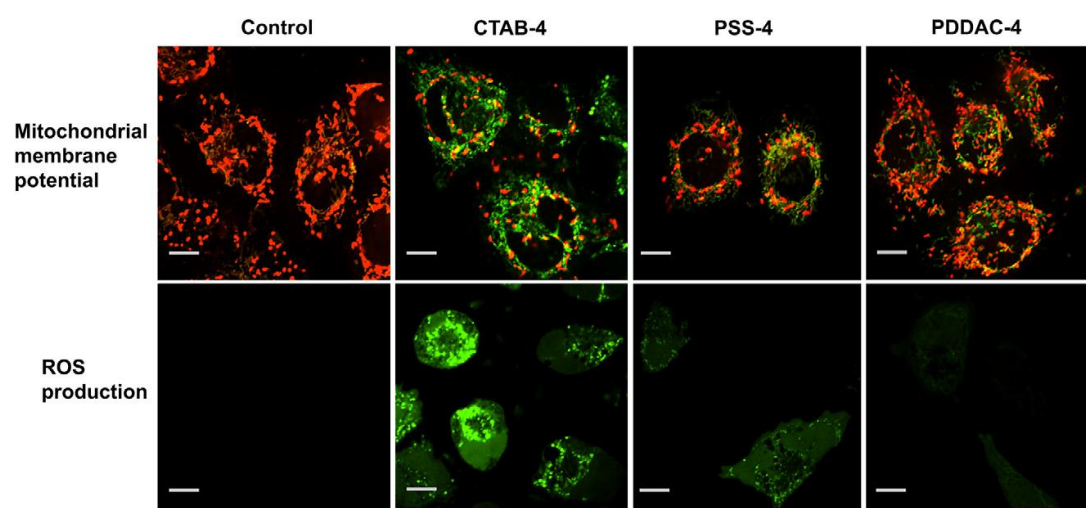
Figure 1.6 Mitochondrial damage of cells caused by gold nanorods of different coatings. In the mitochondrial membrane potential assay, red fluorescence represents aggregated JC-1 dye, indicating the maintenance of mitochondrial membrane potential, suggesting the integrity of the mitochondrial membrane. In intracellular reactive oxygen species (ROS) assay, ROS level is shown as green fluorescence, which indicates the oxidative stress that is a consequence of mitochondrial damage. Scale bar is 10 µm. Reproduced from Qiu et al, 2010.[93]

There have been some suggestions in the literature that positively charged particles (such as CTAB or PSS-PDDAC coated) present higher uptake rates in cell lines, with consequently higher cytotoxic potential.[12] However, as will be noted below, the formation of a protein corona around the surface of the nanoparticles following exposure to serum proteins does not support these simple charge-based predictions of uptake and toxicity.[7]

As a different surface modification approach, the exchange of the outer CTAB layer for a layer of poly(ethylene glycol) (PEG) has also been extensively investigated and found to reduce non-specific uptake of nanorods, as well as cytotoxicity, when compared to CTAB-coated particles.[97,98]

1.3.4   Protein corona

It is known that nanoparticles, and biomaterials in general, when exposed to biological media immediately interact with the molecules of the media. Importantly, proteins (such as serum proteins) will dynamically adsorb onto the nanoparticle surface, forming the so-called "protein corona". The composition of the protein corona is of great importance as that is what will interact, in the first instance, with the cells, thus having potential effects in the uptake, toxicity, intracellular processing and immunogenicity of the nanoparticles.[4,99]

It has been reported that the composition of this protein layer depends not only on the material composing the nanoparticles but also, importantly, on particle size and surface properties.[99] The study reported by Tenzer et al[100] for polystyrene and silica nanoparticles suggested protein adsorption following contact with biological media to be a very quick process. The corona was rapidly assembled and displayed a very complex and dynamic nature, with a universe of around 300 proteins having been identified. Additionally, the corona was found to change significantly in terms of amount and conformation of bound protein, while no important changes in composition were detected.[100] Such a wide range of proteins, with great variability in biological function, underline the importance of the corona for the subsequent interaction of nanoparticles with cells.[99]

In a separate study,[101] serum protein adsorption to gold nanoparticles of different sizes and with different densities of PEG on the surface was investigated, as well as their subsequent uptake by macrophages. It was found that higher densities of PEG resulted in lower protein adsorption, while also leading to differences in corona composition, and that the efficiency and mechanism of uptake was consequently affected. Exposure of gold nanorods with CTAB and a range of different polyelectrolyte coatings to serum-containing culture medium has shown that it not only affects the overall nanorod zeta potential (Figure 1.7) but also the uptake of nanorods, leading to an increase in uptake especially for particles with PSS and PSS-PDDAC-PSS wrappings.[7,96]
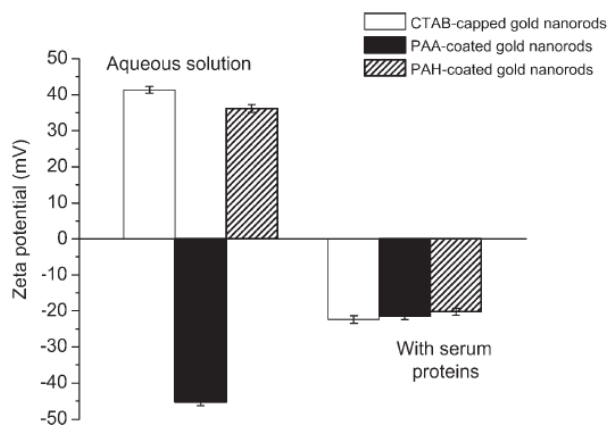
Figure 1.7 Exposure to serum proteins affects nanorod surface charge. Zeta potential measurements of gold nanorods coated with CTAB,PAA and PAH before and after 30 minutes of exposure to culture medium containing 10% bovine serum albumin. All samples were measured in water. Reproduced from Alkilany et al, 2009.[7]

Generally, the formation of a protein corona is seen as a somewhat unwanted effect, as it is not within the control of the initial nanomaterial design phase. For instance, it has been reported[102] that PEG-modified silica nanoparticles which were functionalised with transferrin for transferrin-mediated uptake lost their targeting ability as a consequence of the adsorption of serum proteins. On the other hand, Kah et al[103] suggested that the protein corona can be used for enhancing nanoparticle functionality. In their study, a serum-protein corona was used for loading a drug onto the surface of gold nanorods, while also stabilising the colloid. Subsequently, drug molecules could be controllably released by exciting the nanorods at their longitudinal plasmon resonance. However, that study used CTAB-coated nanorods, so it is uncertain what would happen following drug delivery as the risk of CTAB desorption from the surface could lead to unwanted toxic effects.

1.3.5 New techniques for assessing nanoparticle-cell interactions and toxicity

Most of the data available in the literature, of which some examples were presented in this section, is generally based on end-point averages of cell population response or on very small numbers of cells, and thus presents limitations in terms of simultaneously understanding the population heterogeneity and the intracellular dynamics of these interactions. Additionally, as nanomaterials are increasingly being incorporated into medical and consumer products, there is a growing call for a deeper understanding of their toxic effects in the short- and long-term.[104-107]

A multi-parametric study[108] of a range of cell types exposed to gold nanospheres coated with poly(methacrylic acid) (PMA) assessed cell viability, morphology and function for different exposure concentrations, with results indicating the low cytotoxicity of these particles. However, the authors pointed out that the "safe" concentration value obtained from these multiple measurements was approximately 10 times lower than that obtained from traditional cytotoxicity assays, indicating the limitations of those techniques to fully assess the effect of nanomaterials on cells.[108]

Manshian et al[109] used confocal fluorescence imaging and high-content analysis to obtain quantitative information from single-cell imaging. They reported that exposure to different concentrations of particles elicited different cellular responses, which were not directly related to the initial exposure concentration but to the intracellular levels of nanomaterial after exposure. Cytotoxicity was detected only in some cases, with great heterogeneity being detected for each cell sample. This emphasises the importance of single-cell approaches, as averaging population data means that the occurrence of high cytotoxicity for some subsets of the population is overseen. In another not-dynamic, single-cell approach, Rosman et al[110] combined dark-field with TEM to quantify gold nanoparticle uptake while still acquiring information on intracellular localisation. These techniques, despite their higher resolution and new levels of information, do not provide information on the dynamics of the interaction between nanoparticles and cells.

Overall, from this section it becomes clear that assessment of the interaction of nanoparticles with cells should be performed for specific nanoparticle composition, size, shape, surface coating and functionalisation, with the relevant cell type for each application. This highlights the need for new, low-cost technological tools that allow for robust, high-throughput screening of nanoparticles at the population and single-cell level.[17,23,51] Microfluidics-based technologies have shown promise for this application, of which some examples will be outlined in section 1.7.2.

1.4 Biomedical applications of gold nanoparticles

As seen above, the development of nanomaterials for biomedical applications, despite great promise, has so far been held back by the complexity of their interactions with cells and biological media.[1,111] For gold nanorods, their tunability to preferentially absorb light at specific visible or near-infrared wavelengths, together with their plasmonic features and

22

versatile surface chemistry, have made these particles increasingly interesting for biomedical applications. Specifically, the near-infrared region of the spectrum (~700-1200 nm) is considered the best to achieve imaging and therapy without damaging neighbouring tissue, due to low absorbance by aqueous tissue at these wavelengths. This way, applications such as *in vivo* tracking, photothermal therapy and drug delivery see new possibilities with these rod-shaped gold nanoparticles.[4,112,113] This section will explore some of these applications, with a focus on intracellular imaging and drug delivery.

1.4.1 High-resolution intracellular imaging and sensing

Gold nanoparticles with incorporated reporter dyes have been used as intracellular probes, with the dye allowing for SERS tracking of the nanoparticles while, simultaneously, more subtle changes in SERS signal provided sensitive information on the molecular environment surrounding the nanoparticles, giving insight into the biochemical composition of the cell.[81] The use of gold nanoparticles with different reporter dyes targeted to different subcellular regions has also been demonstrated, for example, by Kang et al.[114] In that study, nanospheres with an intra-nanogap, where the reporter dyes were introduced, made the most of the "hotspot" effect for SERS enhancement. Those nanoparticles were then targeted to the cytoplasm, mitochondria or nucleus and live-cell imaging of single-cells was obtained, showing successful colocalisation of the SERS signal and the targeted regions.[114]

Multimodal imaging of these particles can provide access to complementary levels of information about many aspects of cell function, nanoparticle processing and nanoparticle-mediated molecule delivery.[115] In one multimodal imaging approach, Ando et al[116,117] also reported dynamic SERS imaging and sensing within living cells. A single, unlabelled gold nanosphere was imaged intracellularly using dark-field and SERS, providing spatial and biochemical information on the uptake and transport pathways (Figure 1.8). That work is an example of the confirmed ability of these particles to serve as highly-specific intracellular probes, down to the single-nanoparticle level, even in complex environments such as within cells or tissue.[118]
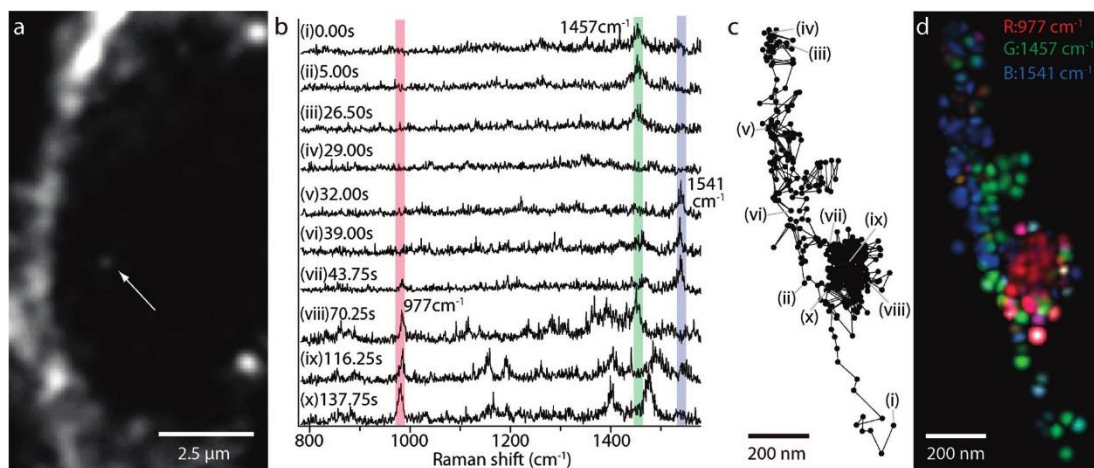
Figure 1.8 SERS analysis of intracellular pathways using an endocytosed gold nanoparticle. (a) Dark-field image of a J774A.1 macrophage, where the white arrow indicates a gold nanoparticle within the cell. (b) SERS spectra obtained from the nanoparticle indicated in (a). Characteristic Raman peaks were observed at 977 cm^{-1} (phosphate), 1457 cm^{-1} (CH$_2$ and CH$_3$), and 1541 cm^{-1} (Amide II).These three Raman peaks are overlaid with bars in red, green and blue. c) Trajectory of the nanoparticle from panel (a) obtained from the dark-field images. (d) RGB colour map of the molecular distribution displayed on the nanoparticle trajectory, as per colours in (b). Spatial resolution of these measurements was ~65 nm, from particle diameter ~50 nm and measurement accuracy ~15 nm. Reproduced from Ando et al, 2011.[116]

The electromagnetic field enhancement obtained with gold nanoparticles, which is the base of their SERS behaviour, is also very important for two-photon excitation. Thus, for excitation wavelengths overlapping with the nanoparticle plasmon resonance, two-photon luminescence signals are greatly enhanced, especially for anisotropic particles.[119] This property has allowed researchers to obtain images of single gold nanorods *in vivo*[120] and, more recently, to track intracellular gold nanorods in 3D.[121] Additionally, it has been suggested that the two-photon luminescence properties of gold nanorods can also be used to monitor fast dynamic events, such as neuron action potentials, which are of great biological importance.[122]

Other techniques have also been explored for intracellular tracking of nanorods. Liquid scanning transmission electron microscopy (STEM),[123,124] performed within microfluidic chambers, also showed promising results for intracellular tracking of gold nanoparticles within live cells. The use of X-rays in a nano-computed tomography configuration was also reported for high resolution 3D imaging of gold nanorods within cells, but not on live cells, which lacks the (very relevant) dynamics aspect of these interactions.[125]

Overall, it is clear that gold nanoparticles, in particular gold nanorods, have great potential to serve as intracellular probes with integrated sensing and multimodal imaging capabilities.

However, most studies demonstrating these high-resolution features have extremely low throughput, being in many cases limited to single-cell imaging, due to limitations in instrumentation such as confocal Raman spectrometers to perform rapid scanning of larger surfaces. This also has limitations in terms of assessing cell dynamics – for instance, one of the studies mentioned[114] reported a mapping time of 125 seconds for a single-cell. Conversely, the single-nanoparticle tracking approach presents better time resolution, but is always limited to a single-nanoparticle and hence cannot be translated to higher throughput applications for now. In any case, the demonstration of non-invasive imaging of gold nanoparticles *in vivo* also shows the potential for other biomedical applications such as tumour detection, guided surgery, or tracked drug delivery.[126,127]

1.4.2   Drug delivery

For the many reasons outlined above, it becomes evident that gold nanoparticles have great potential as drug carriers.[128,129] Specifically, three features can make these particles privileged carriers for therapeutic applications: i) flexible surface chemistry, allowing for control of internalisation and processing pathways and for targeting to specific subcellular locations; ii) versatile optical properties, allowing for live tracking of delivery of drug molecules; and iii) both, enabling triggering of drug molecule release from the nanoparticle surface using different methods.

Control of the release of drug molecules from the surface of carrier molecules is important to minimise the occurrence of side-effects and simultaneously increase the efficacy of the drug dose given. The most reported methods for gold nanoparticles include redox-triggered release, pH-sensitive release and photothermal triggers.[128] Redox-based systems are generally glutathione-dependent, where drug molecules are loaded onto the surface of gold nanoparticles using a chemical bond that is disrupted in the presence of the high concentrations of glutathione occurring within the cell.[130-132] For pH-responsive systems, the nanocarriers are designed based on the concept that intracellular processing begins within vesicles where the microenvironment is highly acidic. Control is achieved by attaching drug molecules to the nanoparticles by means of a pH-sensitive bond, which is then disrupted when the pH changes within those vesicles.[133,134] One example is the combination of this method with aptamer functionalisation, for targeted tumour chemotherapy, as reported by Zhao et al.[134]

The fact that SERS provides a structural fingerprint of a molecule means that SERS spectra of drug molecules attached to the surface of gold nanoparticles can be used as a tool to directly assess the kinetics of drug release within a cell.[4] This has been demonstrated for glutathione-triggered release: Ock et al reported label-free SERS monitoring of this process *in vitro*[131,132] and *in vivo*,[131] while Zong et al used labelled SERS tags for the same purpose.[130] A combination of SERS and fluorescence was used by Kang et al to successfully monitor pH-dependent delivery of doxorubicin from gold nanoparticles *in vitro*.[133]

The fact that gold nanorods can be tailored to preferentially absorb specific wavelengths of light can also be used for improving drug delivery. The increase in temperature that occurs when a specific aspect ratio of nanorods is excited with the corresponding plasmon wavelength can lead to highly controlled release of drug molecules from the rod surface. Additionally, this phenomenon is the base for photothermal therapy, opening way for novel cancer therapies based on a combination of photothermal and chemotherapy. This combination has been tested *in vitro* and *in vivo* by various groups,[135,136] with results showing that treatment was more effective when both the drug and the photothermal effect were used. Drug release monitoring from gold nanorods in those studies was achieved using either SERS[135] or NIR fluorescence.[136]

Overall, the literature indicates the great versatility and potential of gold nanorods for drug delivery applications. In the next section, the development of nanovaccines will be addressed as a more specific field of interest to the current project.

1.4.3   Nanovaccines

When applying biomaterials to vaccine delivery, it is important to consider the interactions between nanovaccines and immune cells, which depend on many factors such as carrier composition, size, shape, surface chemistry, and others (see also section 1.3).[35,55,137] One important factor is the immunogenicity of the carrier material, or whether it will induce the generation of an immune response to itself, in addition to the antigen, which would be unfavourable. So far, studies assessing this issue have reported that the nanomaterials used as carriers generally act as bystanders in the vaccine delivery process, not being antigenic themselves.[35,137] It is also important to consider other variables such as the route of administration and the surface coating of the particles. For instance, biomimetic particles,[138-140] as well as targeted delivery via specific receptors such as toll-like receptors expressed on dendritic cells,[41] have been found to enhance nanoparticle adjuvanticity. One *in vivo* study[141]

also assessed the effect of surface hydrophobicity of gold nanospheres, with results indicating that hydrophobicity had a nearly linear correlation with the generation of an immune response. Nanoparticle size has also been reported as an important feature in the successful generation of an immune response for various types of nanoparticles.[142-146] Additionally, numerous studies have found that nanoparticles can act as powerful adjuvants themselves, eliminating the need for addition of adjuvant molecules to the particle surface and thus reducing the complexity of nanovaccine formulations.[9,35,147] Another important feature of nanovaccines that can provide better insight on the underlying immune system pathways is their *in vivo* traceability using non-invasive imaging techniques,[148] a point for which gold nanoparticles have demonstrated potential, as seen in the previous section.

Focusing on gold nanorods, Xu et al[9] investigated the *in vivo* adjuvant activity of gold nanorods with different surface chemistries. CTAB-only and polyelectrolyte-wrapped (PSS-PDDAC and PSS-PEI) gold nanorods were used for HIV gene delivery in mice. Results demonstrated that gold nanorods coated with polyelectrolytes were not cytotoxic and were very successful in inducing an immune response, while CTAB-capped nanorods attached to the same molecule were not, and even inhibited dendritic cell function. From the data obtained it was suggested that gold nanorods played two roles in the generation of an antigen-specific immune response: the role of vaccine carriers and the role of adjuvants. Specifically, polyelectrolyte-wrapped gold nanorods were found to not only promote dendritic cell maturation but also enhance T cell activation and proliferation, demonstrating the great potential of these particles for vaccine delivery.[9]

Together, these aspects indicate that nanoparticle-based vaccines are a promising route to achieve more efficient immunisation. Nevertheless, the fact that so many parameters are implied in nanovaccine performance again underlines the need for better high-throughput assessment tools (see section 1.7.2).

1.5 Microfluidics for biomedical applications

Microfluidics is the manipulation of nano-litre to femto-litre volumes of liquid within well-defined structures and environments in the micrometre-size range. Due to its scale, this technology allows for the minimisation of sample volume requirements whilst maximising the control over fluid flow and the flow of any suspended particles.[149,150] Overall, this leads to increased efficiency of all the steps involved in one analysis process – from sample

preparation and manipulation to the required chemical reactions and biological or biochemical readouts. Additionally, microfluidic structures have great potential to integrate multi-step analytical processes into the same device and for parallelisation, which can lead to increased data throughput being obtained from very small sample volumes, as well as detection of rare events. These features, together with the fact that the microfluidic structures are at a similar scale to that of biological materials such as cells (Figure 1.9), have opened many possibilities for the biomedical use of these devices. Examples include high-throughput immunoassays, capillary electrophoresis, cell sorting, and cell trapping, monitoring and analysis down to the single-cell level – with applications ranging from laboratory-based drug screening to point-of-care diagnostics.[19,32,151-153] This section will outline some of the technical aspects of microfluidics that are relevant to the current project, namely to applications in single-cell analysis, immunology research and nanoparticle screening, which will be explored in subsequent sections.
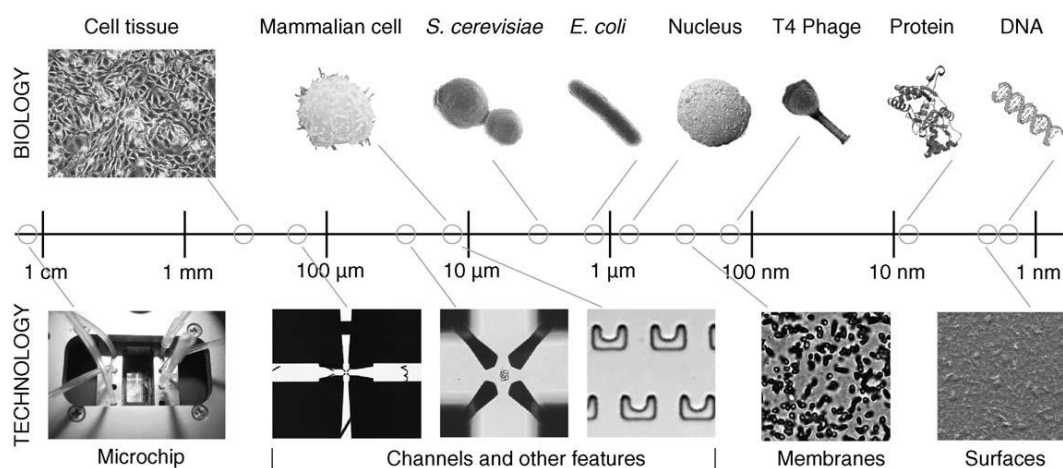
Figure 1.9 Comparison of sizes between biological entities and microfluidic structures. Reproduced from Schmid et al, 2010.[154]

1.5.1   Laminar flow in microfluidics

The dimensions of microfluidic structures lead to new relationships among viscous forces, surface tension forces and inertial forces. While in the macroscale world inertial forces generally have a dominant role, in microfluidics their effect becomes mostly negligible, with viscous and surface tension forces prevailing. In order to fully characterise and predict the behaviour of fluid flow at the microscale, dimensionless quantities are normally defined.[149,150] The Reynolds number is one such dimensionless parameter which provides a measure of the ratio between viscous and inertial forces for a given flow condition, indicating

the characteristics of the flow (laminar/turbulent). The Reynolds number can be calculated by:

$$Re = \rho \frac{\text{v}L}{\mu}$$ [1]

Where:

- μ and ρ are the dynamic viscosity and density of the liquid;
- v is the average velocity of the fluid and $\text{v} = Q/A$, with Q being the volumetric flow and A the cross-sectional area of the chamber;
- L is a characteristic dimension, defined in the case of rectangular cross-section channels as $L = 4A/P$, with P being the wetted perimeter of the chamber.

Generally, given the dimensions of microfluidic devices, the Reynolds number in these devices is very small (<<1), indicating that flow will typically be laminar. This gives an unprecedented level of fluid flow control, but also brings challenges in terms of achieving effective mixing, as will be shown next.

1.5.2   Convection and diffusion in microfluidics

Mixing of solutes in a liquid occurs due to a combination of diffusion and convection processes. Convection is the name given to mass transfer that occurs due to fluid motion. The low Reynolds number of microfluidic flows means that, in most cases, convection occurs only in the direction of flow, having negligible effect in mixing of fluids flowing side by side. Under those conditions, mixing (or mass transfer perpendicular to the direction of flow) occurs only by diffusion. Molecules suspended in a solution are continuously in random movement, or Brownian motion. This motion leads to the molecules to migrate from an area of high concentration to an area of low concentration and, ultimately, be uniformly distributed across the available volume, when an equilibrium is reached (Fick's law of diffusion). In general, diffusion is a slow process as it depends only on the temperature of the molecules in suspension, but being a statistical process it is also predictable – for a given solute, solvent and chamber dimensions. The fact that microfluidic chambers have very precise dimensions containing very small volumes means that diffusion processes can happen much faster in these environments than in the macroscale world. This, with the high levels of fluid flow control that can be obtained within these systems, enables fine tuning of the level of fluid mixing required – from virtually no mixing to controlled gradient formation. In the latter case, complex channel structures allow for some level of mixing to occur

between two adjacent streams of fluid, yielding predictable concentration gradients across a microfluidic chamber.[18,150]

In this context, it is relevant to introduce the Péclet number (Pe), another dimensionless quantity which can be used to assess the relative importance of convection and diffusion in a given flow situation, for a given molecule. The Péclet number can be calculated from:

$$Pe = \frac{\text{v}L}{D} \qquad [2]$$

Where v is the velocity of the fluid, L is a characteristic dimension and D is the diffusion coefficient. The relative importance of convection and diffusion as given by the Péclet number is schematised in Figure 1.10.
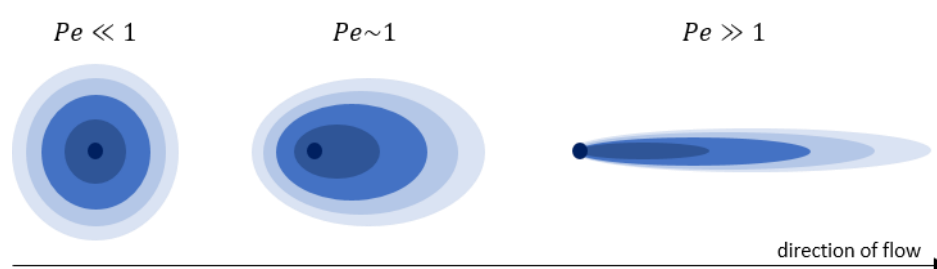
Figure 1.10 Flow conditions influence mixing processes. Schematic representation of the relative importance of diffusion and convection and the corresponding Péclet number ranges for a generic concentration gradient in a liquid. The intensity of the blue colour represents the concentration of a substance. For low Péclet numbers, diffusion is the most important mass transfer process, while for very high Péclet numbers convection becomes the main process and there is virtually no diffusion.

These properties can be explored, for example, to create precise concentration gradients based only on the diffusion of molecules perpendicularly to the direction of the flow.[18,155] One such example is shown in Figure 1.11. This level of flow control has opened new possibilities for chemical and biological analysis using microfluidic devices. For example, cells can be exposed to different doses of the same compound and their response monitored in real-time.[155]
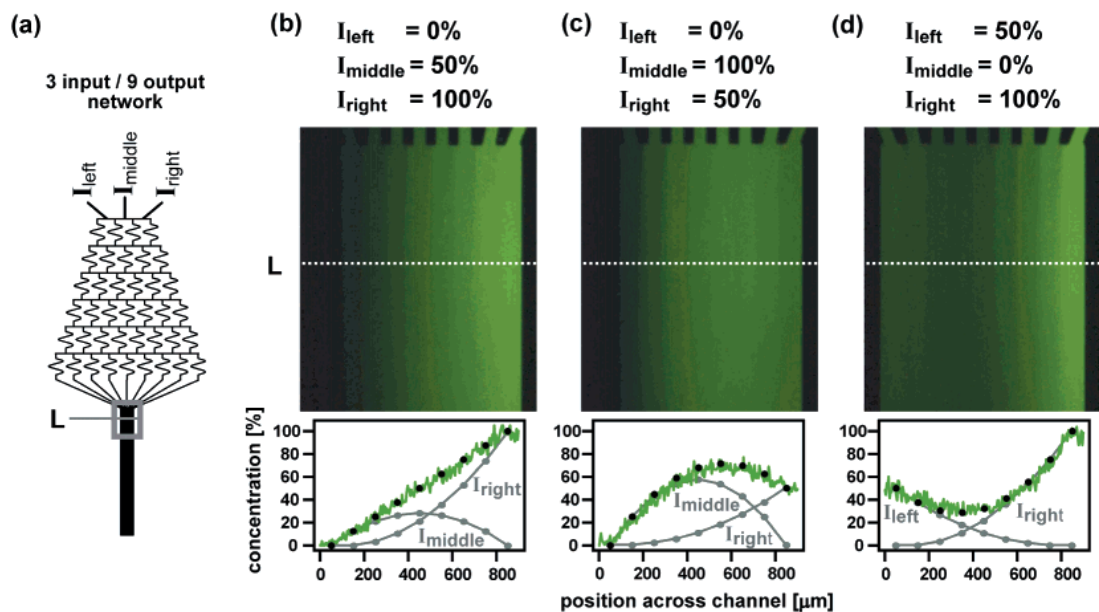
Figure 1.11 Controlled gradient generation in a microfluidic device. (a) Schematic of the microfluidic network used, with 3 inlets and 9 outlets. (b-d) Fluorescence images showing (b) linear and (c, d) parabolic gradients of fluorescein in solution. The concentration of the solutions introduced into each inlet is indicated above the micrographs. The plots below the micrographs show the corresponding fluorescence intensity profile (green line) across the broad channel. Reproduced from Dertinger et al, 2001.[18]

1.6 Cellular analysis in microfluidic devices

Traditional *in vitro* approaches for cell culture and analysis present limitations. Firstly, static cell culture conditions fail to provide a physiologically relevant environment for cells, which may have an effect in cellular behaviour and consequently in the measurements obtained from those cultures.[53,156] In addition, most measurements obtained are bulk, end-point measurements, providing information on the averaged response of the cell population at fixed time points and lacking vital information on the dynamics and heterogeneity of single-cells.[31] As mentioned above, microfluidics and lab-on-a-chip technologies allow for precise control of fluidic conditions, surface chemistries, device geometries, cell culture conditions and exposure to stimuli. These technologies allow for high-throughput, multi-parameter analysis of tissue and single-cell dynamics to be implemented with minimal sample volumes.[31,32,44]

1.6.1 On-chip cell culture and organ-on-chip models

The characteristics of microfluidic flows described above, together with the relative ease of fabrication of polymeric microfluidic devices and biocompatibility of the polymers used

means that these devices can be used to create highly controlled environments for cell culture and analysis.[153,157] Importantly, scaling down the experiments allows for small sample volumes to be used, while the implementation of perfusion into microfluidic cell culture systems gives additional flexibility to refresh culture media and perfuse specific stimuli, such as drugs or nanomaterials, as well as staining or fixing agents.[158]

One important aspect to consider when manipulating cell suspensions within microfluidic systems is the shear stress to which cells are exposed. Shear stress is the mechanical stress caused on a surface adjacent to fluid flow across that surface, which depends on the flow rate and the viscosity of the fluid. It is known that some degree of constant, low magnitude shear stress is favourable for cell development and differentiation, as it resembles physiological conditions.[159,160] Specifically, the physiological shear stress on cells due to interstitial flow is in the order of 0.1 dyn/cm^2, while shear stress exerted on the vascular endothelium reaches 10-15 dyn/cm^2.[156,160] However, it is also known that excessive shear stress is harmful to the cells, influencing cell function, shape, and viability.[156] Thus, the high level of control of flow conditions achieved within microfluidic devices allows for the specification of shear stress conditions on cells within these microenvironments.

One of the first reports of a cell culture array for live cell monitoring on-chip was presented by Hung et al in 2005.[161] In that work, HeLa cells were trapped into an array of microchambers, with medium perfusion maintained perpendicular to the cell loading direction. Cell growth was monitored and confluent samples were passaged on-chip. Additionally, a gradient of dyes was generated across the columns of microchambers, showing the potential for the response of cells to different concentrations of drugs to be monitored in real-time. In that study, the microchambers contained numerous cells each, which means the single-cell aspect was not addressed, but the in-flow cell culture conditions and live assessment of response presented great improvements to the traditional techniques, demonstrating the potential of microfluidic devices for these applications.[161]

The optimisation of microfluidics for biological applications, in parallel with the increased understanding of cellular behaviour and the development of biomaterials of specific properties as scaffolds for cell culture has led to the development of complex 3D cell culture models of tissue and organs on-chip.[156] These models, where one or more cell types are cultured in very controlled microenvironments, provide physiologically-relevant information on tissue- and organ-level functions, from cell-cell interactions and cell-matrix interactions

to more complex drug or particle trafficking pathways. This functionality can be improved by the combination of biochemical stimuli with mechanical stimuli – for example, to simulate breathing[162] or the peristaltic movements of the gut.[163] Successful development of these techniques can have an impact in reducing the use of animals in research, while providing a better understanding of the *in vivo* behaviour of specific cell types from human sources.[164] In any case, it is often hard to isolate all the variables that are having an effect on cell function in such complex environments, and thus for some applications it is important to obtain information on the behaviour of different cell types separately, and different cells individually, in order to isolate specific cell responses to stimuli.[31]

1.6.2   Single-cell analysis

As mentioned above, one of the great limitations of conventional cell-based assays (e.g. flow cytometry) is that measurements are performed by considering the average response of a population of cells. This inevitably leads to assumptions that the measured response is representative of a typical cell under that set of conditions. However, with the large heterogeneity of cellular responses, due to different stages of maturation, differentiation or gene expression within the same population, these averaged results may not be representative of any cell in a given sample.[31]   Consequently, failure to assess the true response of individual cells may lead to, for example, failure to correctly assess nanoparticle toxicity.[109] Conversely, existing single-cell approaches such as microscopy, patch-clamping or the use of patterned substrates have limitations in data throughput and, in many cases, require complex fabrication capabilities or analysis equipment.[31]

Due to its privileged characteristics of flow control, small volumes and flexibility of design and prototyping, microfluidics has allowed for the development of many new approaches to single-cell analysis. Generally, trapping cells into microfluidic arrays facilitates the way of looking at numerous parameters with single-cell resolution, while simultaneously being amenable to generate high-throughput data at a level comparable to that of flow cytometry. For example, analysis of population heterogeneity, morphological studies, gene and protein expression studies, drug delivery testing and intracellular imaging can all be achieved at the single-cell level and in real-time. Additionally, if the device and experimental setup allow for cell culture, it becomes possible to monitor those individual cells over long periods of time.[29-31,165] Table 2 presents an overview of some of the microfluidic tools for single-cell trapping together with their main distinctive features. It is important to note that advantages (✓) and

disadvantages (✖) of each technique are noted here specifically from the point of view of this project, according to the aims described in the Thesis Overview.

Table 2. Examples of microfluidic tools for single-cell trapping[31,154]

microwell arrays[48,166]

cell trapping by sedimentation into microwells

- ✓ simple, cheap, high-throughput, amenable to automation
- ✓ medium perfusion (potential occurrence of dead volume)
- ✓ long-term single-cell imaging
- ✓ may allow for dispensing drug/nanoparticle gradients
- ✖ potential sedimentation of nanoparticles in wells
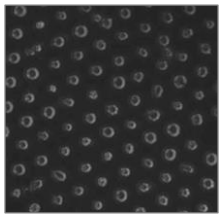
micropatterned arrays[167,168]

cell trapping by adherence to micropatterned surfaces

- ✓ high-throughput, amenable to automation
- ✓ medium and drug perfusion, may allow for concentration gradients
- ✓ long-term single-cell imaging
- ✖ potential cell perturbation from direct exposure to medium flow
- ✖ complex fabrication methods

flow chamber[169]

single-cell trapping into flow chamber for monitoring of proliferation

- ✓ simple, cheap
- ✓ medium perfusion
- ✖ potential cell perturbation from direct exposure to medium flow
- ✖ limited single-cell monitoring
- ✖ does not allow drug gradients within single flow chamber
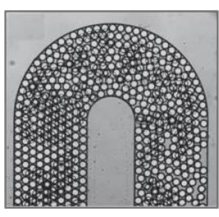
droplet microfluidics[170]

trapping of cells within water-in-oil droplets

- ✓ simple, cheap, high-throughput, amenable to automation
- ✓ sample storage and recovery
- ✓ single-cell imaging
- ✖ cell isolation
- ✖ technical challenges in medium replacement for long-term analysis
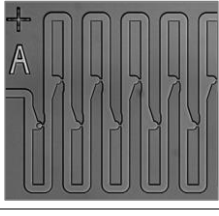
in-channel traps[171-175]

hydrodynamic trapping of cells in pockets along channels
cells act as valves to redirect fluid flow

- ✓ simple, cheap, high-throughput, amenable to automation
- ✓ long-term single-cell imaging
- ✖ does not allow drug gradients
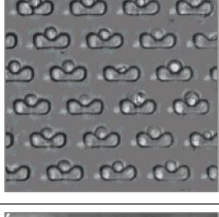
microtrap arrays[30,155,165,176]

hydrodynamic cell trapping by physical obstacles

- ✓ simple, cheap, high-throughput, amenable to automation
- ✓ medium and drug perfusion, allows for gradients across cell array
- ✓ long-term single-cell imaging
- ✖ size-specificity may limit general observations for each cell type
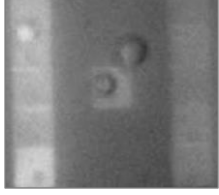
optoelectronic tweezers[177]

cells are trapped using laser beams

- ✓ levitated single-cell, high precision
- ✖ low throughput
- ✖ complex experimental setup
- ✖ effects on cell and device temperature

Besides the presented whole-cell analysis methods, which generally probe the biological state of live cells, there are also numerous reports of microfluidic platforms for single-cell biochemical analysis, or analysis of cell content from arrays of single-cells.[31,154,178] These techniques explore the miniaturisation features of microfluidic devices to, for example, controllably rupture cell membranes and analyse or quantify specific proteins or DNA from within the cells.[152,179] Additionally, real-time assessment of protein secretion by live single-cells has been reported by Kortmann et al,[180] albeit with a complex experimental setup and very low throughput. In that study, a single yeast cell was trapped within an optical trap and kept in flow, with confocal microscopy imaging of downstream fluid providing a quantitative assessment of GFP-labelled protein secretion.[180] In a different approach, Wu et al[181] presented an integrated platform where cells could be loaded into different channels, exposed to separate stimuli in each channel and then on-chip flow cytometry and fluorescence microscopy provided information on cell response. Overall, this is a very broad research area with many interesting possibilities in terms of automation for cell analysis. However, this thesis will focus on microfluidic devices that enable live, whole single-cell analysis. Specifically, hydrodynamic trapping of cells using microtrap arrays will be explored in more detail in the next section.

1.6.3 Microtrap arrays for single-cell trapping and monitoring

As seen in Table 2, arrays of dam-like obstacles can be used to trap cells into well-defined positions, with the trapping structures sometimes being referred to as "microsieves", "C-traps" or simply "microtraps". This hydrodynamic trapping mechanism was first adapted by Di Carlo et al[29,176] into an array format for high-throughput single-cell testing. In that work, devices were fabricated such that there was a gap between the trap structures and the glass surface, allowing for fluid to flow over the traps as well as through the intervals between traps. With such a design, when cells got trapped into individual trapping structures, flow through that gap was diverted, thus "blocking" the trap with one single-cell and causing other cells to flow to subsequent traps (Figure 1.12).
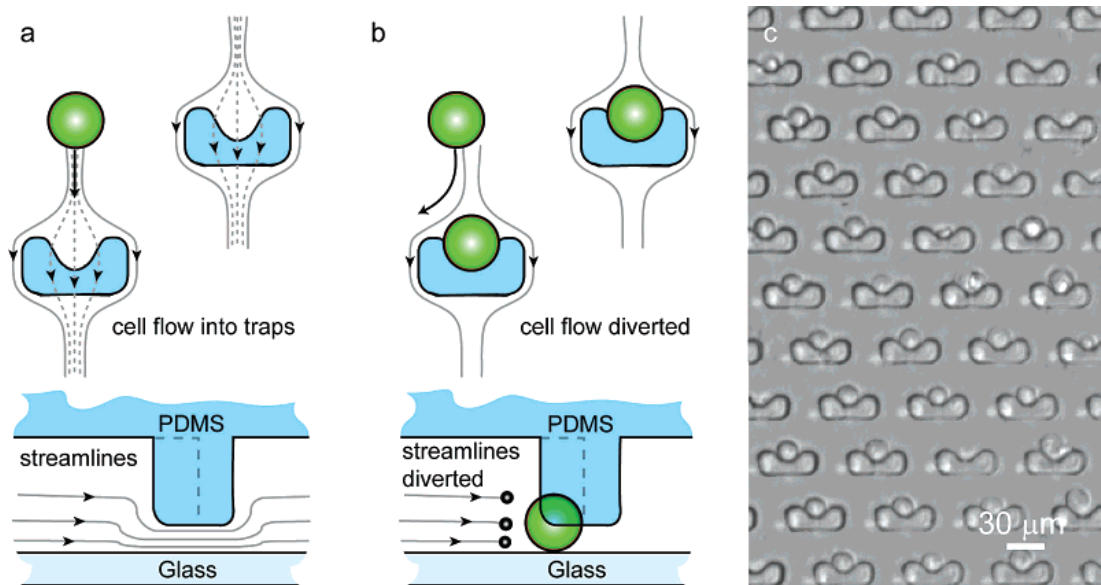
Figure 1.12 High-density single-cell isolation. (a,b) Schematic depicting the mechanism of cell trapping using an array of flow-through suspended obstacles (not to scale). Two-layer (40 and 2 μm) cup-shaped PDMS trapping sites allow a fraction of fluid streamlines to enter the traps. After a cell is trapped and partially occludes the 2 μm open region, the fraction of streamlines through the barred trap decreases, leading to the self-sealing quality of the traps and a high quantity of single-cell isolates. (c) Phase contrast image of an array of single trapped cells. Reproduced from Di Carlo et al, 2006.[176]

The work shown in Figure 1.12 demonstrated successful cell trapping for adherent and non-adherent cell lines, and fluorescence microscopy was used to assess enzyme kinetics as proof-of-concept of the cell analysis platform.[176] Additionally, computer modelling showed that despite the array being under constant medium flow, shear stress within the trap region was very low, mitigating the risk of shear-induced damage to the trapped cells.[29]

A later version of this passive hydrodynamic trapping device was reported by Faley et al,[182] based on a sieve-like structure reported earlier,[183] where the gaps that allowed fluid flow were introduced into the trap design itself (Figure 1.13 a). This eliminated the need for two-layer fabrication, which greatly simplified the manufacturing process. That design was also shown to perform well in terms of creating low-shear stress pockets within the traps, as reported by Wlodkowic et al (Figure 1.13 b). [30]
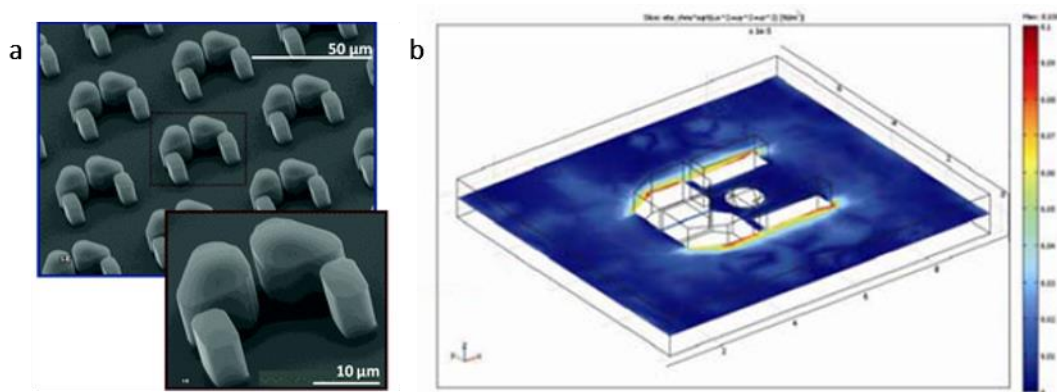
Figure 1.13 Sieve-like structures for cell trapping. (a) Scanning electron microscope images of PDMS cell traps. Reproduced from Faley et al, 2009.[182] (b) 3D simulation results of the shear stress exerted on a trapped cell in the highest velocity region of the array. Reproduced from Wlodkowic et al, 2009.[30]

The same group reported applications in drug screening for chronic myeloid leukaemia: real-time analysis of cell morphology, division, viability and response to drugs was performed on trapped patient-derived stem cells,[182] while another report[184] demonstrated live assessment of intracellular protein trafficking. For those studies, readouts used were based on fluorescence microscopy and obtained for only a few traps at a time. Subsequently, fluorescence-based assessment of drug-induced cytotoxicity was demonstrated in leukaemia cell lines with higher throughput, using the same design (Figure 1.14), with results similar to those obtained using flow cytometry.[30]

The possibility of using different measurement tools on these arrays was demonstrated in a study where cells were incubated with labelled gold nanoparticles before loading into the trapping array, with subsequent SERS mapping of intracellular nanoparticles being obtained on-chip.[185] In that study, time-lapse analysis was performed for small numbers of cells, but the dynamics of nanoparticle internalisation and processing could not be assessed due to those events having taken place off-chip. In any case, the fact that SERS mapping was successfully performed on-chip indicated that multimodal imaging using these microfluidic devices would also be possible.
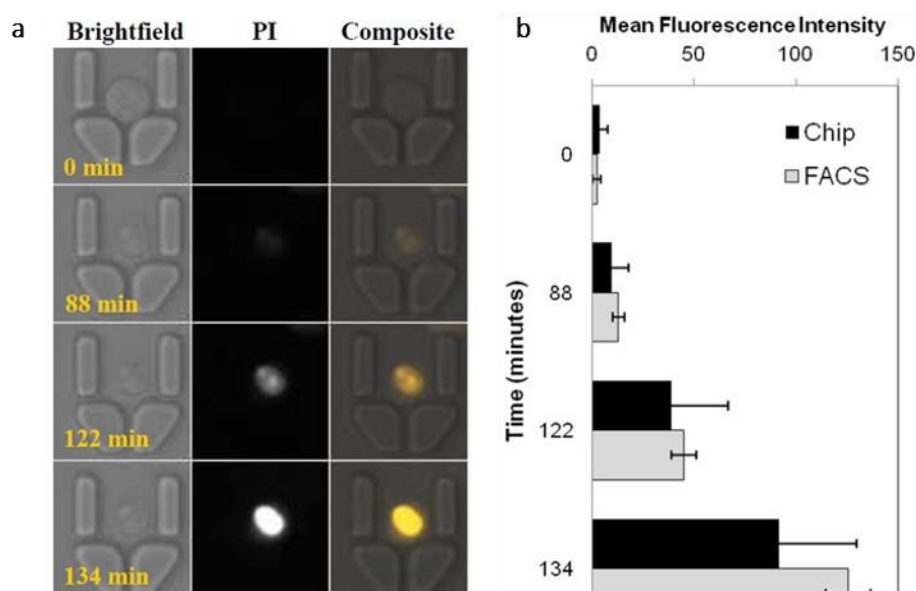
Figure 1.14 Dynamic analysis of drug-induced cytotoxicity in a microfluidic array. Cells from a human leukaemia cell line (HL60) were trapped into the array and perfused with a cytotoxic drug in the presence of propidium iodide (PI). Time-lapse images were collected every minute for 250 cells. (a) Typical images of an HL60 cell after perfusion with drug, with time points indicated at the lower left corner. The gradual increase in plasma membrane permeability to PI indicates cell death. (b) Comparison between mean fluorescence intensity distributions achieved by on-chip imaging and flow cytometry (FACS) for the same time points. Rep. from Wlodkowic et al, 2009.[30]

Another useful feature of this microarray chamber is the possibility for gradient generation, such that cells in different regions of the array are exposed to different concentrations of drugs simultaneously. This was shown for yeast cells in a similar trapping design by Fernandes et al, where a gradient generating channel network was used.[155] This feature has great potential for high-throughput drug screening. For instance, at the point-of-care, trapping patient tumour cells and screening a range of concentrations of chemotherapy drugs would allow for personalised assessment of the most appropriate dose for each patient. This is just a glimpse of the potential of microfluidics for, beyond biological analysis, providing robust and novel drug discovery tools.[186]

1.7 Biomedical applications of microfluidics

In previous sections, the breadth and importance of some biomedical applications of microfluidic devices has been touched upon. Here, two main fields will be explored in more detail, which are of great relevance to the current project – the use of microfluidics for immunology and for nanomaterial development.

1.7.1 Immunology research

The creation of precise microenvironments for co-culture of different cell types into organ-on-chip models, on one hand, and single-cell monitoring platforms, on the other hand, have opened new possibilities for investigating the more complex dynamics of the immune response.[44,58,164]

Immune cell migration is crucial for many aspects of the immune system function and response to threats, and the dimensions of microfluidic devices allow for a privileged look at cellular movement.[45,46,187-190] For example, Mahmood et al[45] investigated natural killer cell migration by adapting a typical chemotaxis assay into a microfluidic chamber. The chamber was coated with fibronectin, cells were seeded and subsequently exposed to gradients of soluble factors from immature and mature dendritic cells by using the laminar flow conditions of the chamber. Cell motility was analysed at the single-cell level, with the assay having potential for investigating immune cell migration under a range of very controlled biochemical and environmental conditions. Similar work has also been reported for neutrophils.[191] In another report, Gopalakrishnan et al[46] proposed a new type of chemotactic assay, where two chambers were separated by a network of bifurcated channels. This device allowed for analysis of cellular decision-making of primary dendritic cells and a range of immune cell lines when migrating towards the infected chamber under no flow. Mitra et al[189] proposed a novel two-layer design where dendritic cells that underwent chemotaxis would then be led to interact with T cells in a separate chamber. That way, the study achieved an integrated assessment of dendritic cell migration and subsequent interaction with T cells. However, it is worth pointing out that a cell line was used, which has been shown to be of less physiological relevance than primary dendritic cells.[192] In another different use of microfluidics, Ricart et al[190] seeded primary dendritic cells onto micropost arrays downstream of a gradient generator. Micropost deflection was analysed to obtain information on dendritic cell traction forces when exposed to chemotactic gradients. Overall, these reports demonstrate that microfluidics can be used to gain insight into the migratory behaviour of immune cells, towards a better understanding of the underlying physiological processes.

Another crucial aspect of immune system function is cell-cell communication, which has also been investigated through various microfluidics approaches. Using hydrodynamic traps similar to those described in Figure 1.13, Faley et al[47] trapped mature dendritic cells into one device and naïve T cells into another device, with the output of the first device connected to

an input of the second. That way, molecules secreted by dendritic cells could flow into the T cell chamber and the consequent T cell activation detected in real-time using calcium imaging. By testing dendritic cells in different stages of maturation, the signalling processes that take place before the formation of the immunological synapse could be interrogated, even if at a population level. In a closer look at individual lymphocyte function, Zaretsky et al[48] trapped naïve CD4^{+} T cells into microwell arrays, exposed them to antigen and analysed their proliferation and activation over 3-4 days. Cell pairing was assessed in another hydrodynamic trapping approach by Dura et al,[49] where fluorescently-labelled T cells and B cells were sequentially trapped into pairing traps (Figure 1.15). Using just capillary forces to fill the device and pipetting into either side to change the direction of the flow, this clever design allowed for cell pairing events to be controlled and for individual cell pairs to be tracked over time. Fluorescence microscopy was then used to assess expression of a range of markers, and the breadth of data obtained from the array demonstrated the ability of the platform for investigating immune cell pairing events in high-throughput and under well-defined environmental and biochemical conditions.
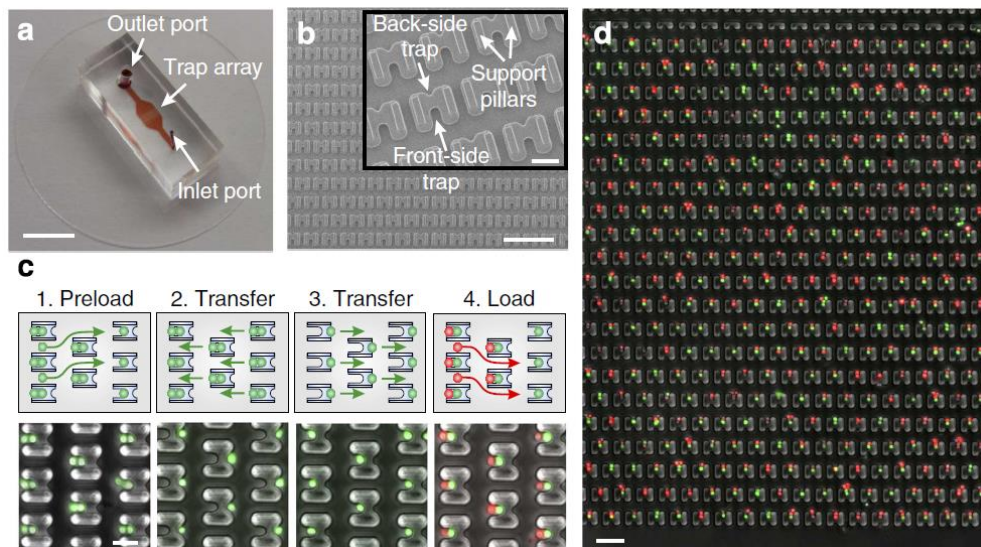
Figure 1.15 Immune cell pairing in a microfluidic device. (a) Microfluidic cell pairing device with channels and trap array shown in red. (b) SEM image of the microtrap array showing the back-side single-cell traps, front-side two-cell traps and support pillars. (c) Four-step cell-loading and pairing protocol. The first cell population (green) is preloaded into the front-side traps by directly pipetting 1–5 µl of cell solutions into the inlet reservoir (1). The direction of the flow is then reversed to move the cells into the back-side single-cell traps (2) and again to transfer the cells into the larger front-side two-cell traps two rows below (3). Finally, the second cell population (red) is loaded and paired with the first cell type (4). (d) Overlaid phase contrast and fluorescence image showing primary mouse lymphocytes stained with membrane dyes paired in the traps. Scale bar: (a) 5 µm, (b) 100 µm, 20 µm (inset), (c) 20 µm, (d) 50 µm. Rep. from Dura et al, 2015.[49]

Microfluidic tools for immunology also include platforms for high-throughput screening of vaccine adjuvants, as performed by Garcia-Cordero et al,[50] and other nucleic acid or protein-based measurements.[59,193] Overall, the advent of microfluidic technologies has led to new opportunities to answer some of the fundamental questions underlying immune system function, while having tangible applications in areas such as vaccine development and cancer immunotherapy.

1.7.2   Nanomaterial screening

Due to the increasing interest in nanoparticle development for biomedical applications, it is essential to achieve a better understanding of the interactions of nanomaterials with cells. As seen in section 1.3 above, these interactions depend on many factors and will be different for each specific nanomaterial design and cell type. Hence, the development of *in vitro* models for robust, high-throughput screening of the dynamic interaction of nanoparticles with cells would not only shorten the path to their clinical application but also provide important information on the biological processes determining nanoparticle fate, leading to better nanoparticle design.[17,23,51]

Lab-on-a-chip technologies appear again as promising candidates for this application, due to the high levels of control achieved in microfluidic conditions and the versatility of designs and imaging techniques that can be used. One of the important features of microfluidic environments is that nanoparticle delivery to cells can be performed under flow conditions, rather than in static (zero flow) conditions. Besides being more physiologically relevant, as *in vivo* cells are exposed to some level of shear stress from interstitial flow,[53,156] it also avoids the heterogeneous distribution of nanoparticles which happens when nanoparticles sediment to the bottom of static cell culture wells (Figure 1.16).[22]

Despite the inherent promise of microfluidics as a powerful tool for nanomaterial screening, there are still very few reports of this application available in the literature. Some groups have used microfluidic flow chambers under nanoparticle gradients[22] or microwells with specific cell densities[52] for assessing quantum dot cytotoxicity, looking at fluorescence information from groups of cells. Farokhzad et al[194] patterned cells onto a glass slide and then used a simple microfluidic chamber to test their interaction with nanoparticles under a range of flow conditions. In one single-cell approach, Qiao et al[24] studied the genotoxicity of nanomaterials. For this, cells were exposed to a range of nanoparticles of different compositions at a range of concentrations and subsequently embedded into hydrogel beads

and patterned onto a substrate in an array format. Subsequently, fluorescence imaging could be obtained from the cells on various markers. However, despite its potential for automation, the platform is of complex fabrication and provides only end-point measurements on individual cells, lacking the dynamic aspect of their interaction with nanomaterials. Thus, even if it tries to perform a comprehensive assessment of different exposure conditions, that approach does not seem to fulfil the requirements of a robust tool for nanomaterial testing.
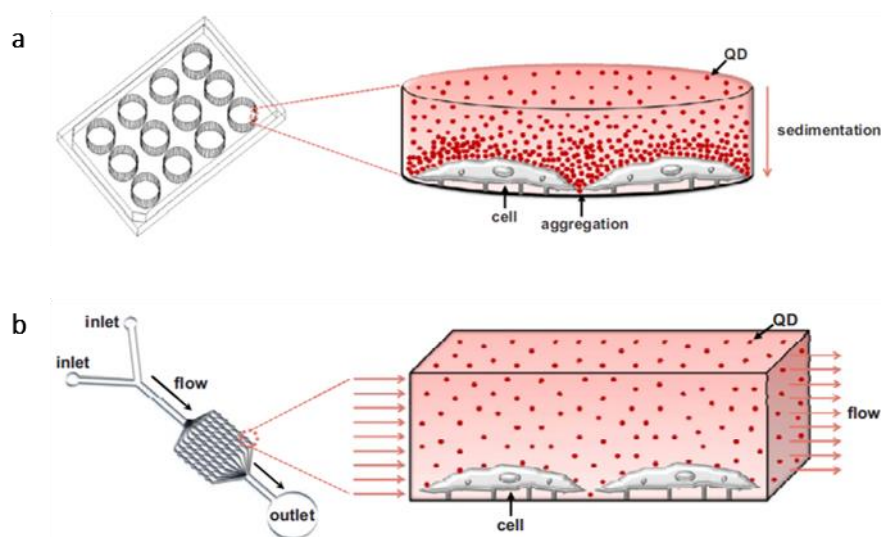
Figure 1.16 Static and in-flow exposure to nanoparticles. (a) Schematic representation of static exposure conditions in a conventional well-plate system. Nanoparticle sedimentation in these conditions can lead to heterogeneous distribution of nanoparticles to cells. (b) Schematic representation of in-flow exposure conditions in a microfluidic compartment, showing homogeneous distribution of nanoparticles. Reproduced from Mahto et al, 2010.[22]

A few more complex models of nanoparticle interactions with tissue have also been reported. For example, two separate groups[26,195] have used spheroids on chip to assess nanoparticle penetration into tumours, while another group[27] reported a more complex tumour microenvironment on-chip for the same purpose. In the latter study, by Kwak et al,[27] nanoparticle transport between tumour "compartments" was evaluated for a comprehensive range of physical characteristics of the device, towards the best device design for the experiment. Additionally, even more complex organ[25] and body-on-a-chip[28] models have been used to investigate nanoparticle trafficking phenomena. However, while these models demonstrate the importance of producing physiologically relevant microenvironments for some aspects of nanomaterial testing, there is currently no platform for screening nanomaterials at the single-cell level. This simplified assessment using a single

cell type is essential to isolate the variables involved in the interaction of cells with nanomaterials and to assess cell heterogeneity within each population.

1.8   Thesis context

Overall, the analysis of the literature presented in this chapter led to the following important points:

- Gold nanorods have exceptional optical capabilities for intracellular imaging, permitting multiplexing and sensing with SERRS as well as dark-field and fluorescence-based measurements. In addition, these are highly versatile nanoparticles in terms of surface functionalisation for drug delivery applications.

- Despite the promise of nanomaterials for clinical applications and of lab-on-a-chip platforms for cellular analysis, there is currently no report of a robust, high-throughput nanomaterial screening platform that provides dynamic information at the single-cell level.

- Currently available vaccines present some limitations, and nanomaterials are appearing as a powerful tool for increased vaccine efficiency with lower side-effects.

Thus, having identified a necessity for a tool that can screen nanoparticle-cell interactions dynamically, at the single-cell level, in high-throughput and ideally using multimodal imaging, and recognising the potential of microfluidic technologies for this purpose, this thesis sets out to describe the development of an integrated platform that includes:

- A microfluidic device capable of trapping and maintaining hundreds of single-cells, providing a platform for time-lapse, fluorescence-based analysis of live cells simultaneously with their exposure to specifically defined stimuli, in high-throughput and with multimodal imaging capabilities;

- A nanovaccine model, based on biocompatible, stable and imageable polymer-wrapped gold nanorods, which is capable of delivering antigen to primary dendritic cells and successfully generating an immune response.

- Application-based proof-of-concept of the developed platform with real-time assessment of nanoparticle-mediated antigen delivery and processing by primary dendritic cells being achieved in high-throughput with single-cell resolution over several hours.

Chapter 2

Materials and Methods

This chapter presents the general methods for gold nanoparticle preparation and characterisation, microfluidic device fabrication, cell preparation and cell analysis used for the development and optimisation of an integrated microfluidic platform for cell imaging and controlled nanoparticle delivery.

2.1 Gold nanorod preparation and characterization

2.1.1 Synthesis

Synthesis of gold nanorods (NRs) was performed using an adapted, scaled-up version[68,69] of the seed-mediated growth method using cetyltriethylammonium bromide (CTAB).[66,67] Unless otherwise stated, all chemicals were purchased from Sigma-Aldrich [UK] and used as received. All solutions for the nanorod synthesis were prepared using ultrapure water. All glassware was previously cleaned with aqua regia for at least 2 hours and thoroughly rinsed with deionised water.

Seed solution preparation: under vigorous stirring, a CTAB solution (5 ml, 0.2 M) was mixed with $HAuCl_4$ (5 ml, 0.5 mM), to which freshly-prepared $NaBH_4$ (0.6 ml, 0.01 M) was added. This produced a light brown solution which was kept at 25-30°C and used within 30 min.

Growth solution preparation (targeting a longitudinal plasmon resonance of 780 nm): $HAuCl_4$ (200 ml, 1.0 mM) was added to CTAB (200 ml, 0.2 M), as well as $AgNO_3$ (10 ml, 4 mM), and the solution gently mixed by inversion. Ascorbic acid (2.8 ml, 0.08 M) was then added and the solution mixed again, changing from orange to colourless. Freshly prepared seed solution

(0.25 ml) was added to the growth solution, which was gently mixed again and kept in a water bath at 37°C for 48h. Concentrations of AgNO₃ and seed solution were varied to adjust the longitudinal plasmon resonance of the nanorods (Table 3). The nanorod solution was washed by centrifuging at 7500 rpm (7798 g) for 1 hour and resuspended in 1 mM CTAB. This was repeated a further 2 times and the rods resuspended in approximately half the initial volume to achieve a higher stock concentration.

Table 3. Control of nanorod longitudinal plasmon resonance

AgNO₃ concentration (mM)	Seed volume (μl)	Longitudinal λ_{max} (nm)	Used in chapter
0.94	500	666	3
1.18	480	712	3
1.30	450	738	3
4.03	250	765	5
4.32	250	802	6

2.1.2   Preparation of nanorod-dye conjugates

2.1.2.1   Single dye conjugates

A range of Raman reporter dyes were tested to assess their suitability for multimodal intracellular imaging. 1 mM solutions of near-infrared-797 (NIR-797), malachite green isothyocyanate (MGITC) [Life Technologies, UK], 3,3'-diethylthiadicarbocyanine iodide (DTDCI), 3,3'-diethyl-thiatricarbocyanine iodide (DTTCI) and 1,1'-diethyl-2,2'-cyanine iodide (DCI) were prepared in methanol and diluted to 100 μM in deionised water. 0.7 ml of each dye was then added to separate 6 ml samples of freshly synthesised gold nanorods (optical density ~1), to achieve bulk dye concentrations of 10 μM.

2.1.2.2   Multiple dye conjugates

Using the same stock concentrations and nanorod suspension, a combination of NIR-797, MGITC and DCI (0.9 ml each) was premixed and added to a 6 ml nanorod sample, achieving a 10 μM bulk concentration for each dye. Samples were mixed and left to stabilise overnight at 37°C. Polyelectrolyte wrapping was then performed (section 2.1.3).

2.1.2.3   Scaled-up DTDCI conjugation

3,3'-diethylthiadicarbocyanine iodide (DTDCI) incorporation into the CTAB layer of the gold nanorods was achieved by adding 10 ml of 100 μM DTDCI solution (diluted in deionised water

from 10 mM stock in methanol) to 90 ml of rod stock solution, mixing gently and leaving overnight.[42] Polyelectrolyte wrapping was then performed (section 2.1.3).

2.1.2.4 Universal SERRS Tags (USTs)

Gold nanorods with incorporated DCI, DTDCI and IR-1048 dyes and PSS-PDDAC coating (section 2.1.3) were produced in parallel to this project. These Universal SERRS Tags (USTs, named due to their ability to produce enhanced Raman signals at a large range of wavelengths) were prepared as follows: 1 M dye stock solutions were prepared in methanol and further diluted in ultrapure water immediately prior to use. 4 ml of DCI and IR1048 were premixed prior to addition to 40 ml of NR solution. 4 ml of DTDCI were introduced 1 h later. Following the addition of DTDCI, the samples were allowed to equilibrate for a further 14 h. These nanorods were tested under various imaging methods and used for cell mapping with confocal SERRS, confocal fluorescence and dark-field imaging to assess their suitability for multimodal intracellular imaging (section 2.3.6).

2.1.3 Polyelectrolyte wrapping

Polyelectrolyte coating of gold nanorods was based on established layer-by-layer (LbL) procedures.[71] For the present study, poly-(sodium 4-styrenesulfonate) (PSS, MW≈70,000) and polydiallyldimethylammonium chloride (PDDAC, MW≤ 100,000) were used. Aliquots of polyelectrolyte solutions (10 mg/ml in 5 mM NaCl, 0.25 ml per 1 ml of nanorod solution) were added dropwise to the nanorod solution under vigorous stirring and left stirring for a further 10 minutes. The coated nanorod sample was centrifuged at 7500 rpm (7798 g) for 1 hour (7000 and 6500 rpm for second and third layer coatings) and resuspended in deionised water. The final sample was centrifuged a further two times to wash out any remaining dye from the bulk solution.

2.1.4 Nanorod characterisation

2.1.4.1 Absorbance

Depending on the wavelength range required, gold nanorod extinction measurements were obtained using either a UV-Visible spectrophotometer (Cary 300 Bio Varian with Win UV Scan software, 400-900nm) or a UV-NIR spectrophotometer (Thermo Spectronic Unicam UV300 with Vision 32 software, 400-1100 nm). Before spectral acquisition, the lamp was left on for

a few minutes to allow for warm-up and equilibration. Samples were analysed using disposable plastic micro-cuvettes [VWR, UK].

2.1.4.2   Concentration estimation

Extinction coefficients for each nanorod sample were estimated based on a previously reported study,[196] as follows:

$$\varepsilon = (0.0123 \times \lambda_{max} - 5.0192) \times 10^9 \text{ M}^{-1}\text{cm}^{-1}$$

As examples, for nanorods used in chapters 5 and 6 as per section 2.1.1, extinction coefficients obtained were 4.3903×10^9 and 4.9069×10^9 M^{-1}cm^{-1}, respectively. Stock nanorod concentrations, c, were then calculated using the optical density of the sample measured at the corresponding longitudinal λ_{max} as per the Beer-Lambert Law, where l is the path length (1 cm for all cases):

$$OD = c \times \varepsilon \times l$$

This allowed for estimations of the nanorod concentrations to be obtained in a comparable way for different nanorod samples prior to their addition to cells. Thus, throughout this work, whenever NR or NR conjugate concentrations are stated these will always refer to the concentration of particles in solution, estimated according to this section.

2.1.4.3   Solution-based SERRS

Bulk Raman spectra for the nanorod samples containing DTDCI were obtained at 633 nm using a Renishaw InVia Raman inverted microscope system with an incident laser power of ~1 mW focused through a transparent bottom micro-titre plate with a 300 µl aliquot in individual wells. A 10 s signal collection time for spectra acquisition was used. Cyclohexane was used to optimise the signal collection as well as to provide an intensity reference for data normalisation.

For Universal SERRS Tags and all the other dye coatings tested, bulk Raman spectra for all samples were obtained at 633 nm and 785 nm using a Renishaw InVia Raman inverted microscope system and at 532 nm using a Renishaw Probe system.

2.1.4.4   SEM

Silicon wafer substrates [Ted Pella Inc, UK] were plasma-cleaned and coated with of 10 mg/ml PDDAC in 5mM NaCl for 20 minutes. Slides were then gently rinsed with deionised water and dried with nitrogen gas. Nanorod monolayer immobilisation was performed by applying a

drop of nanorod suspension to the glass surface for varying periods of time, typically between 30 and 300 seconds, after which the slides were again rinsed with deionised water and dried with nitrogen gas. Thus, particle monolayers were formed without drying-induced aggregation. SEM images were obtained using an FEI Sirion 20 ultra-high resolution Schottky field emission scanning electron microscope with FEI software.

2.1.4.5   DLS and z-potential

Dynamic Light Scattering (DLS) and zeta potential measurements [Nano-ZS Zetasizer, Malvern] were obtained routinely to assess polyelectrolyte coating efficiency and colloid stability.

2.1.5   Assessment of gold nanorod stability in culture medium.

Nanorods with encapsulated DTDCI and coated with a) PSS-PDDAC and b) PSS-PDDAC-PSS polyelectrolyte layers as above were tested for stability in complete Roswell Park Memorial Institute culture medium (cRPMI, composition in section 2.2.2). Samples were prepared at similar concentrations (approximate optical density of 1). These were then centrifuged at 7500 rpm (3773 g) for 30 minutes using an Eppendorf Minispin centrifuge, resuspended in complete RPMI, mixed and left at room temperature for one hour, after which a UV-Visible spectrum was acquired. At this point, solutions were transferred to new tubes (leaving behind any potential larger aggregates that had formed during centrifugation) and centrifuged again, resuspended in water and measured for UV-Visible absorption.

2.1.6   Nanorod bioconjugation

2.1.6.1   Bovine serum albumin

Bovine serum albumin (BSA, MW ~66,000) solution was prepared at 5% (w/w) and added to the coated nanorod solution to achieve 0.1% bulk BSA concentration (20 µl per ml of nanorod stock). The mixture was shaken vigorously and left to incubate at room temperature for 30 min, after which it was centrifuged twice at 7500 rpm (3773 g) for 30 min and resuspended in deionised water.

AlexaFluor647-labelled BSA (AFBSA) [Life Technologies, UK] was prepared (200 µl, 0.1 mM) and kept in a foil-wrapped tube to prevent photobleaching. This solution was then added to the nanorod samples (optical density of ~1) at 0.3 or 2 µM bulk concentration, mixed and left to incubate at room temperature for 30 min, after which it was centrifuged three times at

7500 rpm (3773 g) for 30 min and resuspended in deionised water. Fluorescence spectroscopy measurements [Cary Eclipse, Varian] were obtained to evaluate whether the BSA-dye conjugate had adhered to the nanorod surface. The instrument was switched on and allowed a few minutes to warm up prior to use, and the emission and excitation slits were set to 5 nm. A new disposable cuvette was used for each measurement and an excitation wavelength of 650 nm was used.

2.1.6.2   Ovalbumin

Ovalbumin (OVA, MW ~45,000) is widely used as a model antigen. DQ™ Ovalbumin is an ovalbumin conjugate containing a quenched BODIPY fluorescence dye which becomes fluorescent upon cleavage by intracellular proteases, and is thus a good indicator of the initial antigen processing by dendritic cells.[197] Conjugation of nanorods with encapsulated DTDCI and coated with PSS-PDDAC-PSS to DQ™ Ovalbumin (DQOVA) [Life Technologies, UK] or Ovalbumin (OVA) [Sigma-Aldrich, UK] was achieved by mixing together an aliquot of the protein (reconstituted in water) to an aliquot of the gold nanorod solution, achieving bulk concentrations of 10 µM and 0.2 nM respectively (50000:1 ratio), and incubating at 4°C overnight. Samples were then washed by centrifuging at 6000 rpm (2415 g) for 30 minutes and resuspended in deionised water three times, before checking the UV-Vis spectrum and concentrating the samples accordingly for addition to the cells.
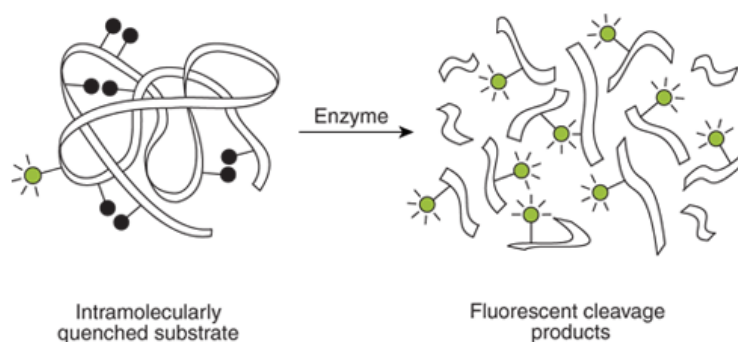
Figure 2.1 Principle of DQOVA use for detection of intracellular processing. Proteases catalyse the hydrolysis of the heavily labelled self-quenched BODIPY dye, yielding brightly fluorescent reaction products. Reproduced from The Molecular Probes Handbook.[197]

2.2 Cell culture

2.2.1 Animals

BALB/c, C57BL/6 and Ly5.1 congenic mice were bred and maintained under specific pathogen-free conditions in the Biological Procedures Unit at the University of Strathclyde. OT-II mice, a transgenic strain of C57BL/6 which express a T cell receptor specific for ovalbumin in CD4+ T cells,[198] were originally purchased from Charles River Labs and maintained as an in-bred colony in the BPU. These mice have a four times higher ratio of CD4 to CD8 peripheral T cells when compared to non-transgenic C57BL/6 mice.[198] All experiments were performed under the guidelines of the UK Home Office Animals (Scientific Procedures) Act 1986.

2.2.2 Dendritic cells

Primary, bone marrow-derived dendritic cells (DCs) were generated from bone marrow of 6-10 week old mice as previously described.[199] Briefly, the tibiae and femurs were collected and the epiphyses were removed from the bones. Bone marrow was then flushed out using a 25G needle and disaggregated to form a single cell suspension, which was resuspended in complete RPMI (RPMI 1640 with 10% FCS, 100 U/ml penicillin, 100 µg/ml streptomycin [all Life Technologies, UK] and 2mM L-glutamine [Sigma-Aldrich, UK]) supplemented with 10% medium derived from x63 cells expressing GMCSF (granulocyte-macrophage colony-stimulating factor), to induce the generation of DCs. This suspension was seeded into petri dishes (10 ml/dish) and incubated for 7 days at 37°C, 5% CO_2. On day 3 of culture, an additional 10 ml of fresh cRPMI with 10% GMCSF was added to each dish and on day 5 of culture half of the volume was replaced with fresh medium. Differentiated DCs were harvested on day 7 of culture by collecting the medium and rinsing the culture plate with cold sterile Hank's balanced salt solution (HBSS) [Life Technologies, UK] with gentle scraping to lift the adherent cells. Cells were washed, counted using a haemocytometer and resuspended in cRPMI to obtain a 5×10^5 cells/ml concentration that was replated into appropriate containers and allowed to settle for at least 2 hours before use. Cells were routinely checked for specific surface phenotype (CD11c) and activation (CD40) markers using flow cytometry, with typically 75-95% of the cells being CD11c positive in the samples used.

2.2.3 OVA-specific T cells

Lymph nodes were recovered from donor OT-II mice into a small amount of cRPMI. Cells were obtained by gently disrupting the tissue through a cell strainer [BD Biosciences, UK] using the plunger of a 1 ml syringe, after which they were counted and resuspended in cRPMI to the appropriate concentration.

2.3 Off-chip cell analysis

Standard techniques such as flow cytometry and microscopy of cell samples cultured in static conditions were used either as a pre-screening tool for conditions to use on-chip or as comparative studies to validate the effects of nanorod uptake by cells measured using the microfluidic system.

2.3.1 Dendritic cell-nanoparticle interactions

Freshly prepared dendritic cells (section 2.2.2) were generally replated into 24-well Costar® plates [Corning, USA] (0.5 ml/well) and incubated with the appropriate nanoparticle concentrations of the specific nanoparticle formulation being assessed. For viability studies, camptothecin treatment [Sigma-Aldrich, UK] (5 µM final concentration) or permeabilisation buffer (HBSS + 0.05% Tween-20) were used as positive controls for apoptosis and necrosis, respectively.

2.3.2 T cell activation and proliferation analysis

Ly5.1 congenic mouse-derived dendritic cells were replated into 24-well plates (0.5 ml/well) at 5×10^5 cells/ml. After being allowed to settle into the wells for at least 2 h at 37 °C and 5% CO_2, cells were inoculated with different concentrations of soluble OVA, NR or NR-OVA conjugates, in triplicates. Ovalbumin-specific OT-II T cells (section 2.2.3) were counted using a haemocytometer and added to the DC plate at a ratio of 5:1 in a volume of 0.5 ml. The cell mixture was incubated at 37°C and 5% CO_2 for a total of 72 h.

2.3.3 General flow cytometry procedure

For flow cytometry, cells were harvested at specific times and collected into flow cytometry tubes [BD Bioscience, UK] for staining with the appropriate fluorophore-conjugated molecules. Table 4 shows details of the stains used throughout this work.

Table 4. Stains used for flow cytometry

Binding molecule	Fluorophore	Supplier	Detects
Annexin-V	FITC	eBioscience, UK	Apoptosis (phosphatidylserine)
Propidium Iodide		eBioscience, UK	Disrupted cell membrane
Anti-CD11c	PE	BD Biosciences, UK	Dendritic cells
Anti-CD40	APC	BD Biosciences, UK	Dendritic cell activation
Anti-CD4	FITC	BD Biosciences, UK	CD4+ T cells
Anti-CD69	PE	BD Biosciences, UK	T cell activation
Anti-Ki67	PerCP-Cy5.5	BD Biosciences, UK	Cell proliferation
DQ Ovalbumin	BODIPY	Life Technologies, UK	Intracellular OVA cleavage

The appropriate incubation and washing steps were performed as per manufacturer instructions for each stain. For Ki67 staining, cells were permeabilised and fixed with Cytofix/Cytoperm buffer [BD Biosciences, UK] prior to staining and subsequently kept in Perm/Wash buffer [BD Biosciences, UK] for the staining steps. At the end of all staining procedures, cells were resuspended in 200 or 300 µl FACSFlow™ and analysed using a BD FACSCanto™ with BD FACSDiva™ software. Data was analysed using FlowJo [FlowJo LLC, USA] analysis software. Figure 2.2 shows an example of the gating procedure typically used for dendritic cell samples.
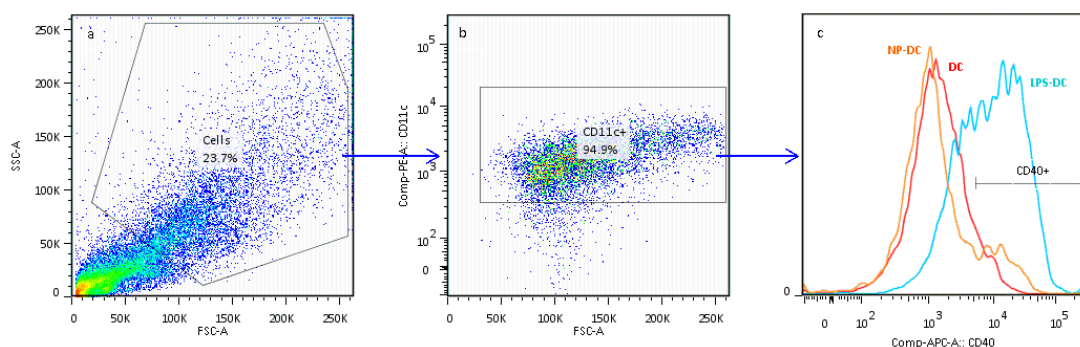
Figure 2.2 Flow cytometry data analysis of bone-marrow derived dendritic cells. (a) Gating for cells according to forward and side scatter data, to exclude small non-cell like objects. (b) Gating for CD11c positive cells (dendritic cells) based on fluorescence intensity above samples stained with isotype controls. (c) Comparative analysis of activation marker CD40 expression (based on fluorescence intensity of APC-conjugated anti-CD40) between unstimulated dendritic cells (DC; red line), nanoparticle-pulsed dendritic cells (NP-DC; orange line) and lipopolyssacharide-stimulated dendritic cells (LPS-DC; turquoise line) and corresponding gate definition.

2.3.4   Quantification of IFNγ and IL-5 by ELISA

For the T cell experiments, supernatants were collected at 72 h for an enzyme-linked immunosorbent assay (ELISA). All antibodies were obtained from BD Bioscience, UK. Flat-

bottomed 96-well plates were coated with 50 µl of 0.5 µg/ml Anti-IL-5 or 2 µg/ml Anti-IFNγ (in pH 9 PBS) overnight at 4°C. Plates were washed three times in wash buffer (0.05% Tween 20 in pH 7.4 PBS) after each incubation step. Plates were blocked for 1 h at 37°C using 10% FCS in pH 7.4 PBS. Samples were then added to appropriate wells (undiluted, 30 µl/well) as well as serial dilutions of the standards (recombinant IL-5 and recombinant IFNγ) and the plates incubated for 2 h at 37°C. Plates were washed again and incubated for 1 h at 37°C with 50 µl biotin-conjugated Anti-IL-5/Anti-IFNγ at 0.5 µg/ml 10% FCS in PBS. HRP-conjugated streptavidin was then added at 1/2000 in FCS/PBS and incubated for 45 min at 37°C. Development was achieved using TMB substrate [KPL, US] and the catalysis of HRP was stopped when the colour change was sufficient for detection by adding 10% H_2SO_4. The absorbance was measured at 450 nm using a spectrophotometer.

2.3.5 General confocal microscopy procedure

DCs were replated at $5x10^5$ cells/ml into 8-well glass slides [Lab-Tek II Chamber Slide, Nunc] (0.5 ml/well) and inoculated with the appropriate concentrations of nanoparticles. These samples were left to incubate for specific times according to the experiment. For some tests, samples were then stained for 10 minutes at 37°C with Cholera Toxin Subunit B (Recombinant) Alexa Fluor 488 Conjugate [Life Technologies, UK] to reveal lipid rafts and cell membranes prior to fixation with 4% paraformaldehyde [Sigma-Aldrich, UK] for at least 20 min at 4°C. Cells were then gently washed with HBSS [Life Technologies, UK] and a coverslip mounted onto the slide using VectaShield mounting medium with DAPI [Vector Laboratories, UK]. These samples were imaged using a Leica SP5 confocal microscope and images analysed using Volocity software [Perkin Elmer] to assess whether the nanoparticles were located within the cell, using the stained membrane lipids to identify the cell boundaries.

2.3.6 Intracellular mapping of Universal SERRS Tags

USTs (section 2.1.2.4) were tested under various imaging methods and used for cell mapping with confocal Raman, confocal fluorescence and dark-field microscopy to assess their suitability for multimodal intracellular imaging.[42] DCs at $5x10^4$ cells/ml were replated onto 35 mm Grid-50 µ-dishes [Ibidi, Germany] (0.5 ml/dish) and incubated overnight at 37 °C and 5% CO_2. USTs were then added to one of the cell dishes at an approximate final concentration of 100 pM in the cell suspension and the dishes incubated for 4 h. Cells were subsequently fixed and washed as above and samples left to air-dry. Confocal Raman imaging was carried

out using a WITec Alpha300 R instrument with 532, 633, and 785 nm excitation lasers (laser power 0.54 mW, 0.66 and 0.73 mW respectively). All maps were acquired using a 100X objective (Olympus MPlan, NA = 0.9), using a 0.5 s integration time and at 0.4 μm spatial steps. WITec Project 2.10 software was used for data processing, where the Raman maps were created from max/min intensity analysis in peak regions at 1360 cm^{-1} for 532 nm and at 1245 cm^{-1} for both 633 and 785 nm . Next, for confocal fluorescence mapping, coverslips were mounted onto the cell samples using VectaShield mounting medium with DAPI. Samples were then fluorescence mapped (with excitations at 405 and 633 nm wavelengths), with z-stacks obtained for each analysed cell at 0.5 μm steps and two-frame average acquisition. Finally, dark-field imaging in transmission was performed using a Nikon Eclipse LV100 microscope equipped with an oil dark-field condenser, a 100X (NA = 0.9) objective and a Nikon D50 camera.

2.4 Microfluidic device preparation

Microfluidic devices were designed based on a previously described design[30] and fabricated in polydimethylsiloxane (PDMS) using standard soft lithography procedures.[153] This section describes these procedures and the specific parameters and materials used. An overview of the fabrication procedure is presented in Figure 2.3.
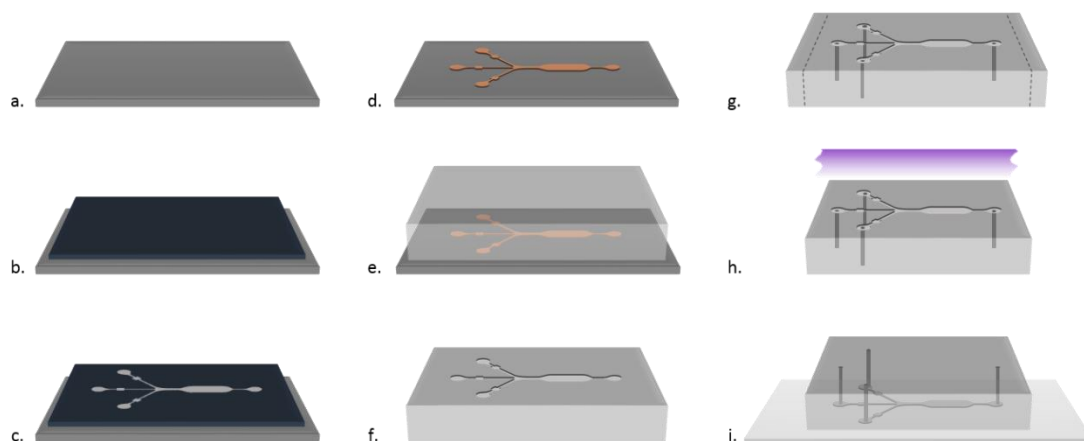
Figure 2.3 Schematic of the microfluidic device prototyping procedure.A silicon wafer was cleaned and dehydrated (a) and photoresist spun onto the surface and soft-baked (b). Specific areas of the negative photoresist were then exposed to UV light via a chrome-on-glass mask (c), developed and hard-baked forming a master for the devices (d). Liquid PDMS could then be cast onto the wafer (e) and baked to form the PDMS microstructures (f). The PDMS device could then be trimmed and holes punched as required (g), cleaned and exposed to oxygen plasma (h) for bonding to a glass coverslip, forming the closed microfluidic device (i).

2.4.1 Microfabrication of patterned silicon wafers

Silicon wafers [University Wafer, USA] for photolithography were cleaned sequentially with 3-minute sonications in acetone, methanol and isopropanol. They were then dried with nitrogen gas, dehydrated on a hotplate at 180°C for at least 1 hour and cooled down to room temperature. A wafer was then placed on a spinner and SU-8 3035 negative photoresist [Chestech, UK] poured over its centre and spun at 4000 rpm to obtain a resist layer with 25 μm thickness. Soft-baking was achieved by placing the wafer on a hotplate at 95°C and gradually increasing the temperature to 105°C over 20 minutes, followed by gentle cooling to room temperature. The wafer was then exposed to collimated UV light through a chrome-on-glass mask [JD Photo-Tools, UK] for 25 seconds. Post-exposure baking was done on the hotplate, with temperatures gradually increasing from 75 to 90°C for 4 minutes and slowly cooling back to room temperature. Exposed areas of the resist were developed by immersing the wafer in Microposit EC solvent [Chestech, UK] for 6 minutes under constant agitation. The wafer was then rinsed with isopropanol and dried with nitrogen gas, hard-baked for one hour in an oven at gradually increasing temperature (80 to 200°C) and cooled down inside the oven. Finalised patterned wafers were visually inspected using an upright microscope and feature height measured using a stylus profilometer. Silanisation of the wafer was carried out by vapour deposition of 1H,1H,2H,2H-perfluorooctyl-trichlorosilane [Sigma-Aldrich, UK] for 1 hour, to render the surface hydrophobic and amenable to soft lithography prototyping. Wafers patterned in this way were used as master moulds to create the microfluidic devices and could be reused numerous times, with new fabrication being required only when there were changes in the design.

2.4.2 Polymeric microfluidic devices

Devices were produced by casting poly(dimethylsiloxane) (PDMS) [Sylgard 184 Silicone Elastomer, Dow Corning, USA] in a ratio of 10:1 w/w elastomer base/curing agent onto the wafers to achieve 5 mm thickness. PDMS was then degassed and cured at 80°C for 2 hours. The mould was then removed from the silicon master, trimmed to size with a scalpel and fluidic inlets and outlets punched manually using a flattened-tip G22 needle. Fabrication quality assessment was achieved through PDMS microtrap visualisation using a Hitachi S-3000N Environmental Scanning Electron Microscope (SEM).

PDMS devices were cleaned by two 3-minute sonications in methanol, followed by drying with nitrogen gas and dehydrating in the oven at 80°C for 15 minutes. Alternatively,

microfluidic feature cleaning was performed by firmly pressing Scotch® tape[200] [3M, UK] onto the surface and gently peeling off at least two times, leaving a third piece tape on the surface until bonding. In general, the latter method was preferred as it was more time efficient and reduced the chances of PDMS absorbing solvents which could be detrimental to its biocompatibility. Additionally, the fact that the tape was kept on the surface until just before bonding the device to a glass substrate provided protection of the microfluidic features against contaminants. Glass microscope slides [Fisher Scientific, UK] or coverslips [22 x 50 mm, VWR, UK] were washed via sequential 3-minute sonications in acetone, methanol and isopropanol and dried with nitrogen gas. The two surfaces (PDMS and glass) were then exposed to oxygen-plasma treatment (0.26 mbar, 40% power, 12 s) and irreversibly bonded together, with two PDMS devices typically bonded onto one coverslip so that two experiments could be carried out simultaneously. Metal connectors were made by cutting and filing 25G hypodermic needles [Fisher Scientific, UK] which were then inserted manually into the device inlets and outlets and connected to tubing.

2.4.3   Fluorescence imaging in the microfluidic device

The following sections describe experiments where real-time bright-field and fluorescence imaging was performed within the microfluidic chamber. To achieve this, a set of fluorophores was used, which are shown in Table 5 together with the corresponding filter characteristics.

Table 5. Fluorescence microscopy parameters

Stain (Fluorophore)	Supplier	Excitation filter / LED	Emission filter
DAPI	Vector Labs, UK	365 nm	> 420 nm
Sytox Blue	Life Technologies, UK	426-450 nm	467-499 nm
Annexin-V (FITC)	eBioscience, UK	450-490 / 488 nm	515-565 nm
Fluorescein	Sigma Aldrich, UK	450-490 / 488 nm	515-565 nm
DQOVA (BODIPY)	Life Technologies, UK	450-490 / 488 nm	515-565 nm
Propidium Iodide	eBioscience, UK	540-560 nm	575-640 nm
Nanorods (DTDCI)	BD Biosciences, UK	608-648 / 625 nm	> 654 nm
AFBSA (Alexa Fluor 647)	BD Biosciences, UK	608-648 / 625 nm	> 654 nm

2.5   Gradient generation in the microfluidic chamber

2.5.1   Fluorescein

Fluorescein gradients were used for calibration experiments and validation of the numerical models used to simulate microfluidic flows, used then to estimate flow rates for nanorod gradient generation. For this, a solution of 100 µM fluorescein [Sigma Aldrich, UK] in ultrapure water was injected into the device through one side inlet while water only was injected through the other side inlet. Different flow rates were tested (0.01, 0.03, 0.05, 0.1, 0.2, 0.3, 0.5 and 1 µl/min) and each gradient profile allowed to stabilise for 5 minutes before imaging. Additionally, time-lapse imaging of the gradient was acquired at 1 frame/s for 120 s for the 0.1 µl/min condition, to assess the occurrence of pulsatile flow. Fluorescence images were obtained using a Zeiss Axiovert A1 inverted microscope and an Andor LucaR EMCCD camera with Andor Solis software, at 485-515 nm excitation with 1 s exposure time (5X objective).

2.5.2   NR conjugates

Initial gradient testing of NR with incorporated DTDCI and PSS-PDDAC-PSS coating was done by flowing a suspension of ~1 nM NR in cRPMI through one side inlet while flowing cRPMI only through the inlet on the opposite side, with both sides flowing at 0.5 µl/min. Images were taken every 10 minutes for 30 minutes during NR delivery into the trapping chamber. Fluorescence imaging was acquired using a Zeiss Axiovert A1 inverted microscope and an Andor LucaR EMCCD camera with Andor Solis software, at 620-648 nm excitation with 500 ms exposure time (10X objective).

2.5.3   Fluorescent BSA

In order to establish the appropriate delivery conditions for a gradient of soluble DQOVA, an equivalent gradient of AlexaFluor647-conjugated BSA (AFBSA) in cRPMI was tested. For this, cRPMI was delivered into the trapping chamber for 30 minutes before flowing through one side inlet only while a 100 nM solution of AFBSA in cRPMI was delivered through the opposite inlet. This led to the formation of a gradient of fluorescent protein within the microfluidic chamber. Subsequently, different flow rates were applied on both inlets (0.1, 0.2, 0.3 and 0.5 µl/min) and the gradient profile allowed to stabilise for 15 minutes each time before imaging. Wide-field phase contrast and fluorescence imaging was performed using an

automated Zeiss Axiovert Observer inverted microscope with Colibri 2 LED illumination, AxioCam MR R3 camera and Zen 2 Pro acquisition software. A 625 nm LED at 50% intensity was used for AFBSA excitation, with the emission being acquired at >650 nm with 1 s exposure time. Fluorescence intensity profiles were extracted from the images using Zen 2 Pro software.

2.6 Cell trapping and monitoring in the microfluidic device

This section outlines the methods used for validating the microfluidic array for integrated cell trapping and nanoparticle delivery, with live monitoring of nanoparticle uptake, viability assessment and multimodal imaging of the cells exposed to different nanoparticle concentrations.

2.6.1 General experimental set-up

Syringe pumps [Aladdin 220, World Precision Instrument, UK] with typically 1 or 5 ml plastic syringes [Fisher Scientific, UK] were connected to the device inlets via 60 cm-long pieces of microbore polytetrafluoroethylene (PTFE) tubing with small Tygon tubing inserts at the extremities [both Cole Parmer, UK]. To guarantee biocompatible conditions over long periods of time, the devices were inserted in a Tokai Hit INUB-WELS-F1 microscope stage incubator [Tokai, Japan] and kept at 37°C, 5% CO_2 and high humidity conditions for the duration of the experiments. Devices were primed manually from the outlet with 70% isopropanol and deionised water prior to cell injection. Real-time bright-field and fluorescence imaging was acquired using a Zeiss Axiovert A1 inverted microscope and an Andor LucaR EMCCD camera with Andor Solis software, or a Zeiss Axiovert Observer inverted automated microscope with Colibri LED illumination system, AxioCam MR R3 camera and Zen 2 Pro acquisition software.

2.6.2 Bead trapping

Initial bead trapping experiments were performed using a suspension of 20 μm diameter polystyrene beads [Park Scientific Limited, UK] in water at 2.84×10^6 beads/ml with 1% Tween-80 [Sigma Aldrich, UK].

2.6.3 Cell trapping

Dendritic cells were harvested from culture plates, centrifuged and concentrated to 1.5-5×10^6 cells/ml in complete RPMI. Cells were then reversely pumped[201] into the PTFE tubing

of a cRPMI-filled syringe using a syringe pump (typically 5 µl at 2.5 µl/min plus 25 µl at 5 µl/min), and subsequently loaded into the device at 1-1.5 µl/min. For three-inlet devices, cells were always loaded through the middle inlet to ensure a uniform coverage of the trapping array. After allowing for cell trapping for at least 2 h to allow for settling of the cells into the traps, unless otherwise stated, culture medium was continuously perfused through the array of cells for the duration of the experiment at 0.5-1.5 µl/min.

2.6.4 Viability assessment

For viability studies, a HBSS-filled syringe was loaded with a solution of 1 µM Sytox-Blue [Life Technologies, UK] and Annexin-V FITC [eBioscience, UK] at the concentration recommended by the manufacturer in Annexin buffer [eBioscience, UK] by withdrawing into the PTFE tubing (typically 15 µl at 0.15 ml/h plus 5 µl HBSS at 0.15 ml/h). The dye solution was perfused through the cell array when required at 1-1.5 µl/min, followed by washing with HBSS.

2.6.5 Real-time gold nanorod uptake and toxicity assessment

Cell injection and trapping was performed as described above in two devices simultaneously. After loading cells into the device, a suspension of 440 pM (approximate optical density of 2) DTDCI-containing, PSS-PDDAC-PSS-coated NR in complete RPMI was delivered into the trap arrays at 0.3 µl/min through one inlet whilst another was used to dispense medium alone at the same flow rate, forming a concentration gradient of nanoparticles across the arrays of trapped cells. This flow condition was maintained for 2 h. Cells in one device were then stained for viability as described above whilst cells trapped in the second device were incubated for a further 18 hours (37°C and 5% CO_2) with medium perfused at 0.5 µl/min across the whole array before staining. Bright-field and fluorescence images were obtained on a Zeiss Axiovert A1 inverted microscope and recorded with an Andor LucaR EMCCD camera. At the end of the experiment, trapped cells were fixed by perfusing a solution of 4% paraformaldehyde through the array, followed by VectaShield mounting medium (with DAPI) [Vector Labs, UK], diluted to 50% in dH_2O. Subsequently, the tubing connected to the device inlets was carefully cut approximately 4 cm away from the connectors and the outlet tubing was removed, in order to keep some differential pressure within the trapping array to prevent cells from coming out of traps. Confocal SERRS maps of the fixed cells were obtained using a Renishaw InVia Raman upright microscope at 633 nm excitation, 8.6 mW laser power,

5 s integration time, and confocal fluorescence maps were acquired using a Leica SP5 confocal microscope, using 633 nm for the nanorod-DTDCI conjugate excitation.

Analysis of imaging data was performed using a combination of different software tools: Andor Solis [Andor Technologies, UK] was used for bright-field and fluorescence image acquisition. Images were normalised to grey values for each fluorescence channel and exported. GiMP 2.0 was subsequently used to create a view of the whole width of the trap array by stitching together the bright-field images of separate fields of view. Volocity [Perkin Elmer, UK] was used to quantify the fluorescence intensity values, to identify DAPI-bright objects, to assess cell viability and to measure the temporal increase of nanoparticle fluorescence within the device. WiRE [Renishaw, UK] was used to perform background correction of the SERS spectra and removal of cosmic rays and to obtain graphic maps of DTDCI-specific SERS intensity (1560 - 1620 cm^{-1}) across the mapped cells.

2.6.6 Real-time monitoring of antigen processing in the microfluidic device

Microfluidic devices were prepared and dendritic cells loaded into the trapping array as previously described. Following cell trapping, a suspension of 10 µg/ml (approximately 222 nM) DQOVA in cRPMI was delivered into the trap arrays at 0.5 µl/min through a side inlet, whilst the contralateral inlet was used to dispense medium at the same flow rate. This flow condition was maintained for 2h, after which culture medium was continuously perfused across the entire array of cells at 0.5 µl/min for the remaining duration of the experiment. Time-lapse phase-contrast and fluorescence imaging (12 frames/h, 20X objective - 0.323 µm/pixel, 24 tiles) covering over a third of the trapping array was performed using an automated Zeiss Axiovert Observer inverted microscope with Colibri 2 LED illumination, AxioCam MR R3 camera and Zen 2 Pro acquisition software. A 488 nm LED at 50% intensity was used for DQOVA (BODIPY) excitation, with the emission being acquired at 500-550 nm with 100 ms exposure time.

Microscopy data was analysed using Zen 2 Pro image processing software. Tiled areas were stitched and fused using the "stitching" function and rotated if necessary. The "mean ROI" tool was then used to define regions of interest (ROIs) around the inside of each trap, providing mean fluorescence intensity (MFI) data for each trap over the course of the experiment. Traps that were empty at t = 4 h were excluded from the analysis. Background correction was done using a circular ROI situated outside the traps in the region where no antigen was delivered. For analysis of population response depending on antigen dose

delivered, ROI data was grouped into three regions of the array containing approximately the same number of traps.

2.6.7   Real-time assessment of nanoparticle-mediated antigen delivery

Microfluidic devices were prepared and dendritic cells loaded into the trapping array as previously described (section 2.4). After trapping, a suspension of 400 pM (approximate optical density of 2) NR-DQOVA conjugates in cRPMI was delivered into the trap array at 0.5 µl/min through one side inlet, whilst the contralateral inlet was used to dispense medium at the same flow rate, forming an adjustable gradient of NR concentrations across the trap array chamber. This flow condition was maintained for 2 h, after which culture medium was continuously perfused through the array of cells for the remaining duration of the experiment at 0.5 µl/min. Time-lapse phase-contrast and fluorescence imaging (12 frames/h, 20X objective - 0.323 µm/pixel, 32 tiles) covering over a third of the trapping array was performed using an automated Zeiss Axiovert Observer inverted microscope with Colibri 2 LED illumination, AxioCam MR R3 camera and Zen 2 Pro acquisition software. DQOVA fluorescence was obtained using a 488 nm LED (50% intensity) for excitation and acquiring emission at 500-550 nm with 100 ms exposure time. NR fluorescence was obtained using a 625 nm LED (50% intensity) for excitation and acquiring emission from 635 nm (long pass filter) with 1 s exposure time.

Microscopy data was analysed using Zen 2 Pro image processing software. Tiled areas were stitched and fused using the "stitching" function and rotated if necessary. The "mean ROI" tool was then used to define circular ROIs around each trapped cell, which were corrected for position if the cells moved over time so that single-cell data could be obtained over the course of the experiment. Cells adhering to the outside of the traps and cells that could not be tracked for the duration of the experiment were not considered. The mean fluorescence intensity (MFI) for each ROI was then extracted and analysed. Background correction was done using a circular ROI situated outside the traps in the null concentration region and a 5th-degree polynomial curve was used to fit the data. For analysis of population response depending on nanoparticle dose delivered, ROI data was grouped into three regions of the array containing approximately the same number of traps: a null NR concentration region, a medium NR concentration region, corresponding to the NR concentration gradient, and a high NR concentration region.

Chapter 3

Gold Nanorods for Enhanced Cellular Imaging and Biomolecule Delivery

The unique optical properties of gold nanoparticles, together with a versatile surface chemistry and relative biocompatibility, make these particles very interesting candidates for imaging, delivery and therapeutic applications.[2,4] This chapter presents the design, development and characterisation of gold nanorod (NR) conjugates to achieve highly specific optical properties for cell imaging. Specifically, fine tuning of gold nanorod optical properties and of dye and polymer coatings are described, achieving imaging tags that could also be bioconjugated to proteins for delivery. Additionally, the development of multi-dye complexes for intracellular multimodal imaging is presented.[42]

3.1 Nanorod synthesis

Anisotropic particles such as gold nanorods have two distinct localised surface plasmon resonance (LSPR) extinction bands (longitudinal and transverse) relating to electron motion along the rod length and width, respectively. The relative peak maxima positions are thus directly related to the nanorod aspect ratio. Nanorod optical properties can be tuned simply by adjusting the synthesis procedure to get different rod sizes, which gives unique versatility to the nanorods for imaging applications. The excitation of surface plasmons and enhancement of local electromagnetic fields makes gold nanorods highly specific substrates for multimodal imaging, from surface-enhanced Raman scattering (SERS) spectroscopy to

fluorescence and dark-field microscopy.[2,43,72,202] In this section, the preparation of NR-dye conjugates will be described, as well as their characterisation using a range of techniques.

3.1.1 Colloid synthesis and plasmon tunability

Nanorods were synthesised using the seed-mediated growth method,[66,67] which has typically been described for small reaction volumes (around 10 ml). In this work, in order to minimise the variability in aspect ratio and consequently in optical properties of NRs associated with different synthesis batches, a scaled-up version[68] of this method was used. This way, reaction volumes of approximately 500 ml (see section 2.1.1) yielded approximately 200 ml of NRs with an optical density of around 1. Control of the optical properties was achieved by varying the rod aspect ratio, through fine tuning of the concentration of silver nitrate in the growth solution and the volume of seed solution added. Specifically, it is known that the NR length will decrease with either increased volumes of seed solution[66] or reduced concentrations of silver nitrate,[67] and generally a combination of these parameters was used to achieve the desired longitudinal λ_{max} for these studies. Figure 3.1 shows extinction spectra of four different samples synthesised during this project using this scaled-up method which are representative of the tunability of the optical properties of gold nanorods.
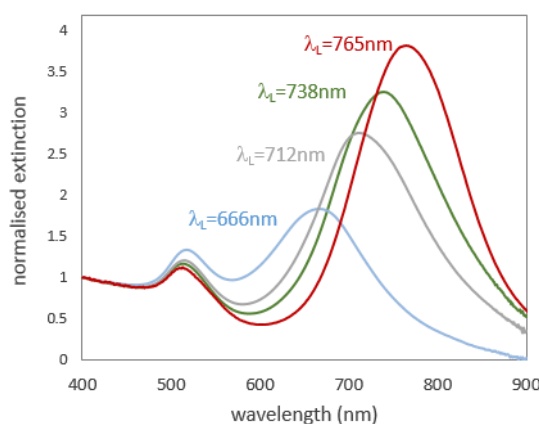
Figure 3.1 Gold nanorod optical properties were tuned by adjusting the synthesis procedure. UV-visible spectra of nanorod samples of different aspect ratios synthesised using the scaled up method (as per section 2.1.1). Spectra were normalised at 400 nm for clarity.

The surfactant hexadecyltrimethylammonium bromide (CTAB) is used in the synthesis as it maintains colloidal stability and promotes the growth of rod-shaped particles.[66,67] However, the surfactant molecules tend to desorb from the surface when bulk CTAB concentrations

are low, which can result in NR aggregation and, additionally, high cytotoxicity, due to the inherent toxicity of the surfactant.[7] Thus, in order to maintain stability during the colloid cleaning steps, NRs were washed at least twice and kept in 1 mM CTAB at ~30°C for up to several weeks before further functionalization.

3.1.2 SEM analysis of gold nanorods

It was important to ensure that the nanoparticles produced were stable in solution and not forming aggregates, as uncontrolled formation of aggregates would lead to changes in the optical properties[68] and potentially the cellular interactions of these particles.[85] Scanning electron microscopy (SEM) of gold nanorod monolayers was thus performed to monitor particle aggregation, in combination with UV-visible spectroscopy analysis, while also providing a measure of particle size. Importantly, the procedure used for preparing the SEM substrates for imaging was such that the occurrence of drying-induced aggregation was minimised. Representative SEM images are shown in Figure 3.2.
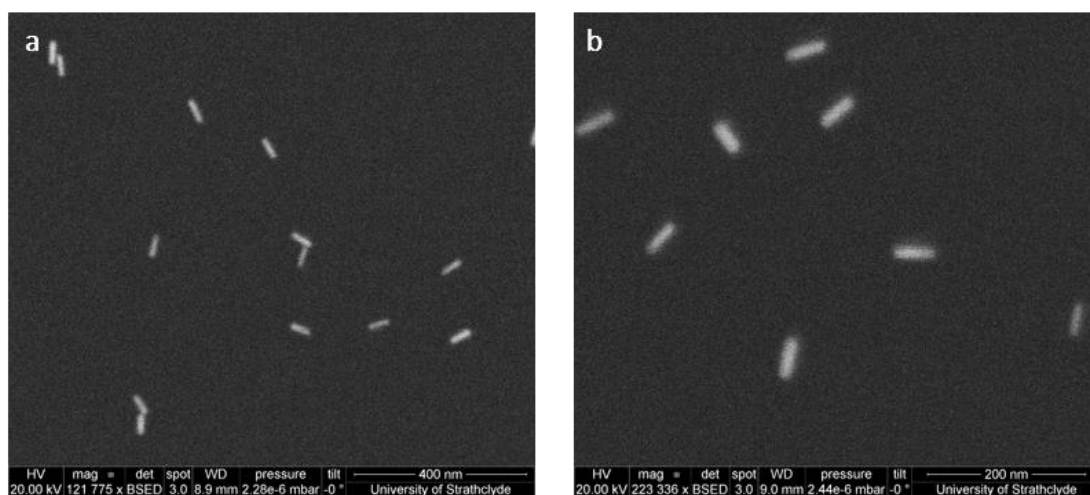
Figure 3.2 Gold nanorod monodispersity and absence of aggregation was verified by Scanning Electron Microscopy. SEM images of NRs with λ_{max}=765 nm coated onto a silicon substrate, showing similar size and shape of the particles as well as a clear separation between individual rods.

Size measurements could then be obtained from the SEM images. For NR with longitudinal λ_{max}=765 nm (Figure 3.2), 44 particles were measured, yielding an average length of 48±6 nm, width of 15±3 nm, and aspect ratio of approximately 3.3.

3.2 General nanorod design

The ideal nanoparticle probe for intracellular imaging and vaccine delivery is highly specific, easy to detect, stable in solution, able to be functionalised with various biomolecules and not toxic to the cells.[80] With this in mind, gold nanorods were synthesised and procedures developed such that different Raman reporter dyes, polyelectrolyte coatings and bioconjugation configurations could be achieved for specific applications. Figure 3.3 shows a schematic representation of the procedures used when producing the gold nanorods for this work. Specifically, incorporation of reporter dyes and polyelectrolyte coating were performed, and these procedures are described in more detail below.
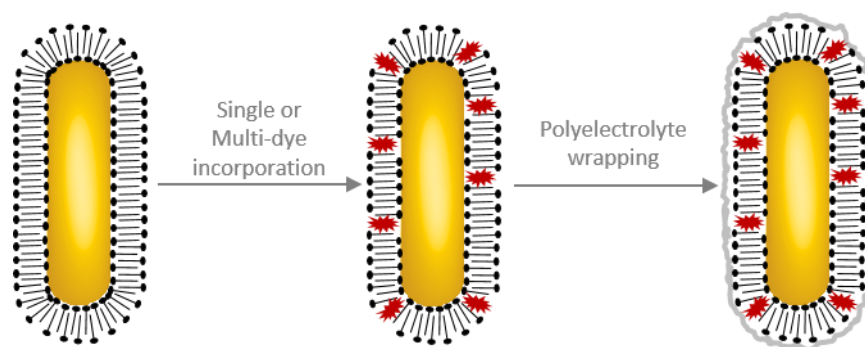
Figure 3.3 Gold nanorod coatings could be tailored for specific applications. Schematic diagram illustrating the general gold nanorod design. Following synthesis, NRs are surrounded by a bilayer of CTAB molecules. Dye molecules are sequestered into the surfactant bilayer and at least one polyelectrolyte layer is self-assembled around the rod to stabilise the dye-nanorod conjugate.

3.2.1 Raman reporter dye incorporation

Following NR synthesis, Raman reporter dyes were added to the NRs in order to obtain highly specific imaging tags.[42,69] In general, Raman reporter molecules have a characteristic spectral signature and, ideally, high Raman scattering cross-section, low photobleaching and functional groups that will adsorb onto the gold surface.[80] It has been shown that certain dyes will be readily sequestered into the CTAB bilayer surrounding the gold core of the nanorods.[69,70] Importantly, the surfactant bilayer will provide control of the orientation of the dye molecules on the rod surface, making this a reliable and reproducible procedure.[69] Subsequent polyelectrolyte wrapping results in a highly stable rod-dye combination, preventing aggregation and CTAB and dye desorption from the gold surface.

Throughout this work, the most commonly used dye was 3,3'-diethylthiadicarbocyanine iodide (DTDCI - Figure 3.4), a hydrophobic dye which, for that reason, has a high affinity for the CTAB bilayer surrounding the gold nanorods in an aqueous environment. This dye can be successfully sequestered into the CTAB bilayer to form NR-dye conjugates with good optical properties, as demonstrated by McLintock et al.[69] Testing was also performed with a range of different dyes, in order to determine the most appropriate NR-dye design for cellular applications, and this will be discussed later in this chapter.
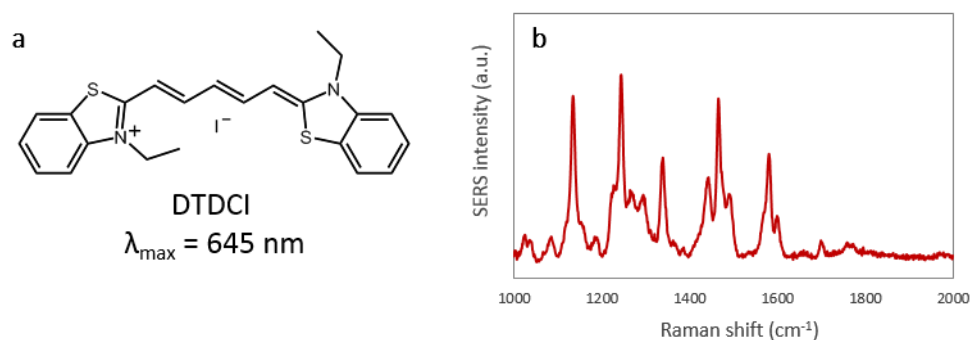
Figure 3.4 DTDCI is a hydrophobic dye that is readily incorporated into the gold nanorod CTAB bilayer. (a) Chemical structure of 3,3'-diethylthiadicarbocyanine iodide (DTDCI). (b) Representative SERRS spectrum (background corrected) of a colloidal solution of the polymer wrapped NR-DTDCI conjugate obtained at 633 nm excitation.

3.2.2 Polyelectrolyte wrapping

Polyelectrolyte coating was performed by the electrostatic deposition of oppositely-charged polymers, or layer-by-layer coating, according to established procedures.[71] The surfactant bilayer around the gold nanorods is positively charged and thus facilitates the adsorption of negatively charged poly-(sodium 4-styrenesulfonate) (PSS) as a first layer. The positively charged polydiallyldimethylammonium chloride (PDDAC) was used as a second layer and a third layer of PSS was used when required. Successful layer deposition was confirmed by UV-visible spectral analysis, showing a red-shift of the longitudinal λ_{max} for each added layer. This shift indicates the successful self-assembly of an extra layer and consequent change in the dielectric environment of the rods (Figure 3.5 a). Additionally, the measured zeta potential alternating between negative and positive values for consecutive wrapping steps also indicated successful deposition of each polymer layer (Figure 3.5 b). Coating the NRs with self-assembled polymer layers promotes stability in buffer and cellular environments, preventing aggregation of the particles and CTAB desorption from the surface[7] and ensuring successful long-term encapsulation of Raman reporter molecules within the CTAB layer.[69]
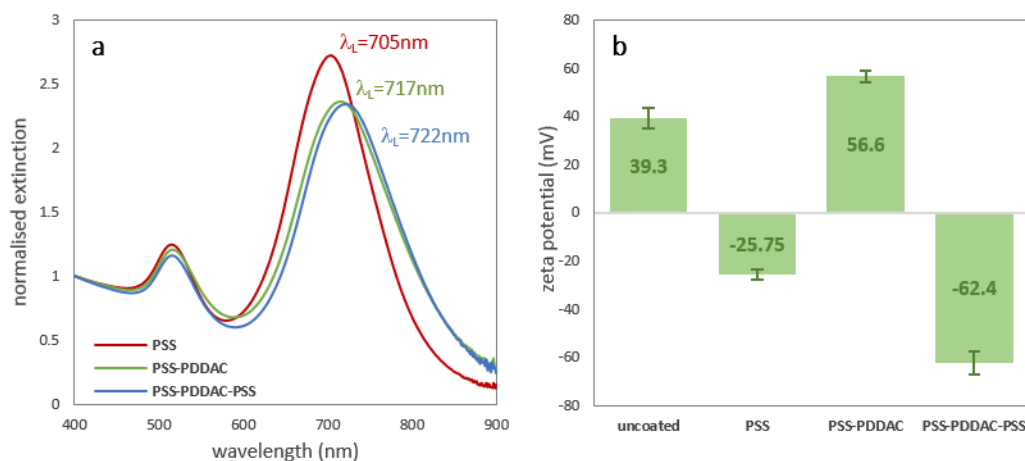
Figure 3.5 Gold nanorods were polymer-wrapped using layer-by-layer coating. (a) UV-visible spectra of coated NR samples (in water), showing that the longitudinal peak red-shifts for each coated layer. Spectra were normalised at 400 nm. Stock NR longitudinal λ_{max} was 708 nm (in CTAB). There was a blue-shift of the peak after the first polymer coating, which is due to the difference in refractive index between CTAB and water. (b) Example of zeta potential values obtained for each coated layer, showing the alternating surface charge of the particles and the increasing stability with each layer coating. Values shown are the mean ± s.d. for two separate NR batches coated at different times.

Other polymers were also used for coating the NRs in the same way, in order to investigate their performance for cell imaging and biomolecule delivery applications. Namely, poly(acrylic acid) (PAA) and poly(allylamine hydrochloride) (PAH), in combinations such as PAA-PAH or PSS-PAH, were explored. However, colloid stability in water and after bioconjugation was found to be better with either the PSS-PDDAC or PSS-PDDAC-PSS configurations as above. Those other options were thus abandoned, as a deep study of optimal layer-by-layer coatings for biological applications would move away from the main aims of this project.

3.2.3 Colloid stability in serum-containing culture medium

It is known that when exposed to serum-containing medium, nanoparticles become coated with a layer of serum proteins, called the protein corona,[7] and that this can not only affect colloid stability but also the subsequent interaction of nanoparticles with cells.[99,100] To assess the suitability of the developed gold nanorods for use in cellular environments, colloid stability in serum-containing culture medium (cRPMI, see chapter 2) was assessed for NRs with different polyelectrolyte coatings. Representative UV-visible analysis is shown in Figure 3.6. Comparison of the extinction data in Figure 3.6 (a) and Figure 3.6 (b) demonstrates that

for NRs with a PSS-PDDAC coating (positively charged outer layer) partial aggregation of the colloid occurred when a concentrated aliquot of rods was added to culture medium. This is indicated by the broadening and a significant red-shift of the localised SPR peak verified after a one-hour incubation with medium (orange trace in Figure 3.6 a). Additionally, further centrifugation led to complete aggregation of the colloid, and thus no further spectra could be acquired in that case. On the other hand, for a PSS-PDDAC-PSS coating (negatively charged outer layer), only a small shift was observed in the longitudinal λ_{max} (orange trace in Figure 3.6 b), associated with the adsorption of serum proteins onto the outer PSS surface, and the colloid also remained stable on further centrifugation and resuspension in water (green trace). Thus, all of the work that will be described in Chapters 5 and 6 was performed using the three-layer PSS-PDDAC-PSS configuration, which ensured colloidal stability in both the cell culture and microfluidic environments.
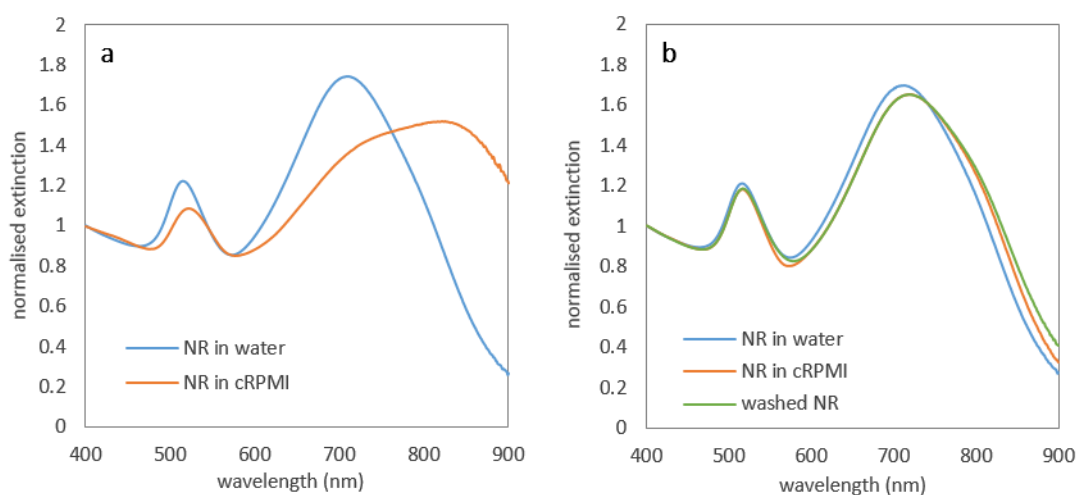
Figure 3.6 Stability of gold nanorods in serum-containing medium. UV-visible measurements obtained for NRs with (a) PSS-PDDAC and (b) PSS-PDDAC-PSS polyelectrolyte coating when exposed to serum-containing medium (cRPMI) for 1h compared with the same NR sample in water only. In (b) additional spectra are shown following the centrifugation and water resuspension of the colloid after exposure to medium. All spectra were normalised at 400 nm.

3.2.4 Gold nanorod bioconjugation

One essential aim of this project was to achieve the delivery of biomolecules from the surface of the developed polymer-wrapped nanorods, towards a robust combination of an optical probe with a molecule carrier for cellular applications.[4,9,112] In this section, the conjugation of NRs to bovine serum albumin is investigated, in order to assess whether simple electrostatic attachment would be enough to achieve good surface coverage and stability in biological media. For this test, BSA labelled with Alexa Fluor 647, a fluorescent dye (here termed

AFBSA), was attached to NRs of different coatings and the conjugation efficiency was assessed by bulk fluorimetry or flow cytometry of cells exposed to different NR-AFBSA conjugates. Initially, a 100 µM stock solution of AFBSA in water was prepared. A NR suspension with longitudinal λ_{max}=664 nm, PSS-PDDAC wrapping, ~0.3 nM in water was used. For coating, an aliquot of the AFBSA stock solution was added to the colloid to achieve 0.3 µM AFBSA bulk concentration (molecular ratio 1000 AFBSA : 1 NR) and incubated for 30 minutes at room temperature. After incubation, three washing steps were performed as detailed in section 2.1.6. Figure 3.7 (a) shows the bulk fluorimetry data obtained from various steps of this procedure – specifically, NR suspension with added AFBSA before washing (*0W*), the supernatant from the first NR wash (*sup W1*), the NR suspension after three washes (*3W*) and a solution of 0.3 µM AFBSA only.
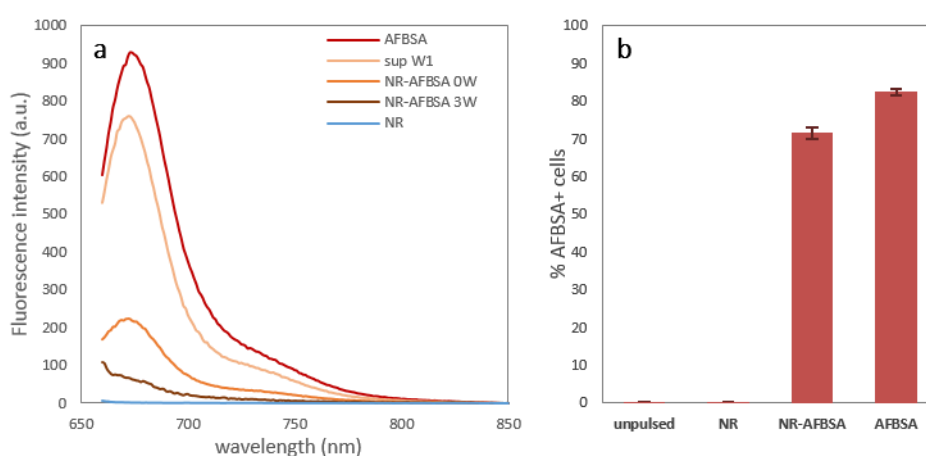
Figure 3.7 Gold nanorods were successfully conjugated to fluorescently-labelled BSA. (a) Bulk fluorimetry data obtained at 650 nm excitation for a solution of AFBSA, unconjugated NR, conjugated NR before (0W) and after (3W) washing and the supernatant from the first wash of the NR conjugates (sup W1). (b) Flow cytometry data obtained from cells exposed to unconjugated and AFBSA-conjugated NR, showing that the NR conjugates were taken up by the cells and were brightly fluorescent. Data shows mean ± s.d. of triplicate samples.

The purpose of this experiment was to prove that AFBSA molecules were successfully conjugated to the NRs by simple electrostatic interaction. For this, it is important to observe a few points from Figure 3.7 (a). Firstly, the concentration of AFBSA was the same (0.3 µM) in the AFBSA stock and the NR-AFBSA suspension before washing (*0W*). However, it was observed that the measured fluorescence intensity of the NR-AFBSA sample was much lower than the dye-only control. This has to do with a limitation in using solution-based fluorimetry for gold nanoparticles, as the presence of rods in the colloidal solution affects bulk efficient excitation and collection of fluorescent photons from the dye molecules, leading to random

signal loss. In any case, residual fluorescence could still be measured from the coated NR sample after three washes, indicating successful conjugation to AFBSA. Additionally, comparison of the dye-only sample (*AFBSA*) with the supernatant from the first wash of the NR-AFBSA solution (*sup W1*) showed that the maximum fluorescence magnitude of the supernatant was 18% lower than the dye control, indicating that some of the AFBSA molecules could have attached to the NRs. This was reiterated by the fact that the optical density of the supernatant from the first wash (measured by UV-visible spectroscopy) was 33% lower than that of the dye-only control.

Subsequently, NR (λ_{max}=722 nm, PSS-PDDAC wrapping, ~0.25 nM) were conjugated to 2 µM AFBSA and washed three times, as above, before being added to dendritic cell samples at 200 pM NR-AFBSA concentration. Cells were incubated overnight, harvested and analysed using flow cytometry, showing (Figure 3.7 b) that cells exposed to the bioconjugated NR samples were clearly displaying AFBSA fluorescence at a level comparable to that obtained with 0.3 µM soluble AFBSA. Together, the results shown in Figure 3.7 not only indicate that the NRs were efficiently coated with the albumin-dye conjugate, but also that all samples were stable enough to endure a number of repeat washes without NR aggregation. This provided confidence for later work that simple electrostatic attachment was suitable for protein bioconjugation and could be used for nanorod-based biomolecule delivery to cells, which was one of the aims of this project.

3.3 Nanorod-dye conjugates for multimodal imaging

In order to determine the most appropriate dyes for specific applications and to confirm the versatility of the developed nanoparticle design, different NR-dye combinations were explored. Assessment of the optical properties and suitability of polymer-wrapped NR-dye conjugates for multimodal imaging was then performed using SERS and fluorescence, with the results presented in this section.

3.3.1 NR-dye combinations

A range of dyes with different absorption maxima was compared. Specifically, 1,1'-diethyl-2,2'-cyanine iodide (DCI, λ_{max}=524 nm), malachite green isothyocyanate (MGITC, λ_{max}=630 nm), 3,3'-diethylthiadicarbocyanine iodide (DTDCI, λ_{max}=655 nm), 3,3'-diethyl-thiatricarbocyanine iodide (DTTCI, λ_{max}=765 nm) and near-infrared-797 (NIR-797, λ_{max}=795

nm). Absorbance spectra for all the dyes are shown in Figure 3.8 (a). Dyes were added to aliquots of the same NR stock in 1 mM CTAB at a bulk concentration of 10 µM, mixed and left to equilibrate overnight (section 2.1.2). The dye concentration used has been previously shown to provide good dye incorporation within the CTAB bilayer on the NR surface (as schematised in Figure 3.3).[69] NR-dye conjugates were then wrapped with two polyelectrolyte layers (PSS-PDDAC) and centrifuged and resuspended in water three times so that any excess dye would be removed from the solution. Dye stocks and dye-conjugated NR samples were analysed using UV-visible spectroscopy and the results obtained are shown in Figure 3.8.
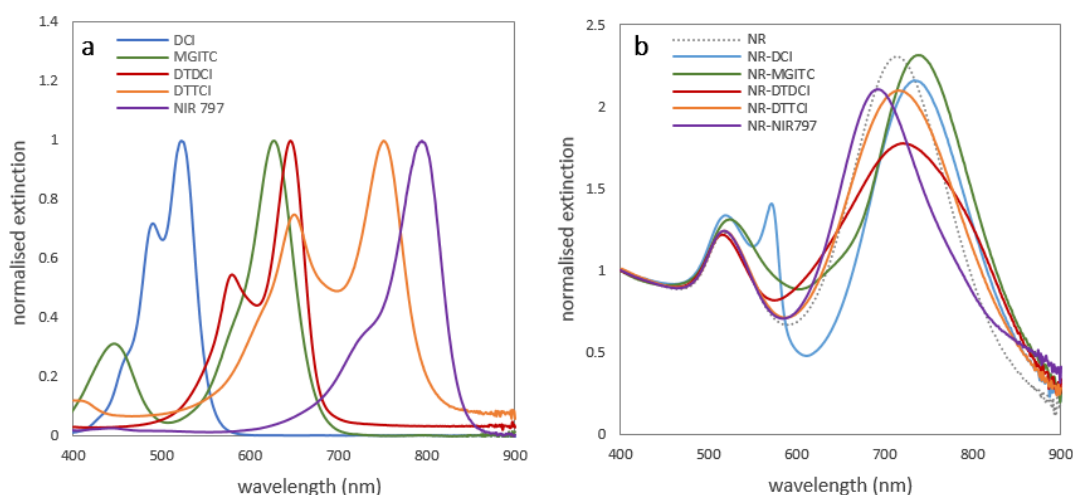
Figure 3.8 Nanorods were successfully conjugated to a range of reporter dyes. (a) UV-visible spectra of the dye stock solutions, normalised to a maximum OD of 1. (b) UV-visible spectra of PSS-PDDAC-wrapped NR-dye conjugates. All samples were prepared using ~0.27 nM of NR with longitudinal λ_{max} = 712 nm. Dyes were added at 10 µM bulk concentrations and samples were washed twice in distilled water following 2-layer polymer wrapping to remove any excess dye from the solutions. Spectra were normalised at 400 nm.

Importantly, it was observed that all NR samples with incorporated dyes were stable, not having formed aggregates even following repeated centrifugation and washing steps. From the data it could also be observed that all the dye-conjugated samples demonstrated a shift in the longitudinal plasmon peak. Table 6 summarises these observations for the different rod/dye combinations, from the data shown in Figure 3.8 (b) for NR with initial longitudinal λ_{max} = 712 nm. Data shown indicates that the magnitude and direction – red-shift (+) or blue-shift (-) – depends on the absorbance spectrum of the dye used.[203]

Table 6. Effect of dye incorporation in the NR longitudinal λ_{max}.	
Dye	Plasmon shift (nm)
DCI	21
DTDCI	9
MGITC	28
DTTCI	4
NIR 797	-21

Additionally, different levels of dampening (reduction in peak height) of the longitudinal plasmon peak were also observed, with the largest amount of dampening being observed for the dyes with the greatest overlap between the dye resonance and the NR LSPR (here, DTTCI and DTDCI). These changes in the extinction spectra of the NR relate to changes in the refractive index close to the NR surface when coated with different dyes, which in turn depend on factors such as the dye fractional surface coverage of the nanorod, the relative rod/dye resonances and the excitation wavelength.[69,203] It is important to note that despite the dyes having been added to the NRs at equal concentrations, some degree of variability in fractional surface is expected. This is due to different dyes having different affinities towards the CTAB bilayer, depending on functional groups, hydrophobicity and environmental factors such as temperature and pH. In any case, the fact that the effects (shift/dampening) observed were present in the NR stock following repeated washing steps to remove excess dye from the bulk solution indicated that those features could be associated with the successful incorporation of the dyes into the CTAB bilayer surrounding the NRs.[69,70]

3.3.2   SERS spectroscopy of NR-dye combinations

In order to assess and compare the performance of the different dyes for SERS under consistent coating and testing conditions, bulk SERS spectra were obtained at 532, 633 and 785 nm for each NR-dye combination. Figure 3.9 shows an overview of the SERS intensities obtained for NRs with each of the dyes incorporated and PSS-PDDAC coating.
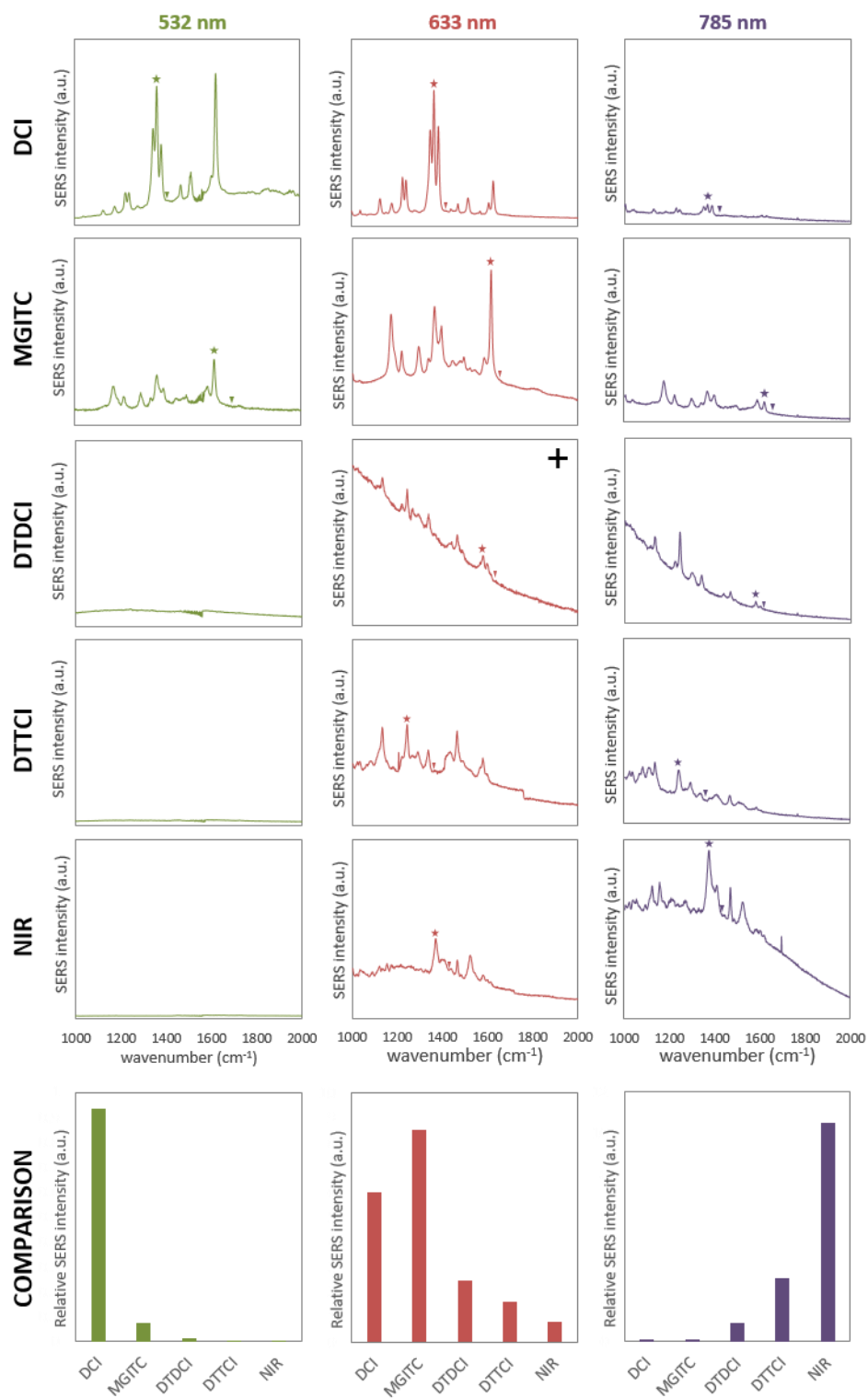
Figure 3.9 Comparison of SERS signals for the developed NR-single dye complexes. Bulk spectra were obtained at 532, 633 and 785 nm excitation as indicated. Graphs show raw spectra obtained for each NR-dye combination in a single screening experiment. For the comparison plots, peak intensities were obtained by min/max analysis for the peaks marked with ★ (min marked with ▼) and normalised to the corresponding cyclohexane control peak at ~1270 cm⁻¹, acquired under identical conditions for each setting. The peaks used were chosen based on their visibility across the three wavelengths. The symbol ✛ denotes the SERRS spectrum for DTDCI at 633 nm showing fluorescence background, as described in the text.

Results obtained (Figure 3.9) showed that some single dyes, such as MGITC or DCI, displayed good signal at more than one excitation wavelength in the visible region, which means that either of these dyes combined with a near-infrared dye could potentially lead to signals across a wide excitation range, as the three-dye combinations which will be described later in this chapter. In any case, good signal was obtained for each of the NR-dye combinations when excited at a wavelength closest to their absorbance maximum. Importantly, when the excitation wavelength overlaps with the dye resonance, the signal is even more enhanced and the phenomenon is termed surface-enhanced resonance Raman Scattering, or SERRS.[78] This effect could be maximised if the longitudinal plasmon resonance of the rods was also in the same spectral region. In this case, the NRs used had a λ_{max} of 712 nm, which was between the 633 and 785 excitation wavelengths, but fine tuning of the rod resonance would be something to consider for future nanotag designs with optimal SERS ability. Here, the goal of comparing directly the performance of different dyes for the same batch of NRs, under the same coating and measurement conditions, was achieved.

3.3.3   Fluorescence of NR-dye combinations

Fluorescence measurements were obtained to assess the ability of the single-dye nanorod configurations to provide fluorescence and SERS signals simultaneously without the need for additional labels. However, solution-based fluorimetry methods are of limited use for this purpose, as described in section 3.2.4. For this reason, more sensitive measurements were required, and hence confocal fluorescence imaging of cell samples incubated for 2 h with each of the different NR-dye combinations was performed (Figure 3.10). Data obtained showed that despite all of the NR-dye complexes having been taken up by the cells, none of the dyes showed excitable fluorescence at any of the wavelengths used, except for DTDCI, which fluoresced when excited at 633 nm. This means that for this dye, despite the close proximity of the dye molecules to the quenching metallic surface (which is favourable for SERS enhancement), there is still sufficient luminescence at 633 nm excitation to enable detection in a fluorescence microscope. This can be observed in the raw SERS spectrum for NR-DTDCI conjugates, which shows very high background when excited at 633 nm (denoted ✚ in Figure 3.9). Hence, NR-DTDCI conjugates were considered a favourable configuration for testing nanoparticle delivery within the microfluidic system, allowing for fluorescence microscopy to be used to monitor nanoparticle uptake without requiring additional fluorescent probes, while being amenable to integration with SERS for multimodal imaging.
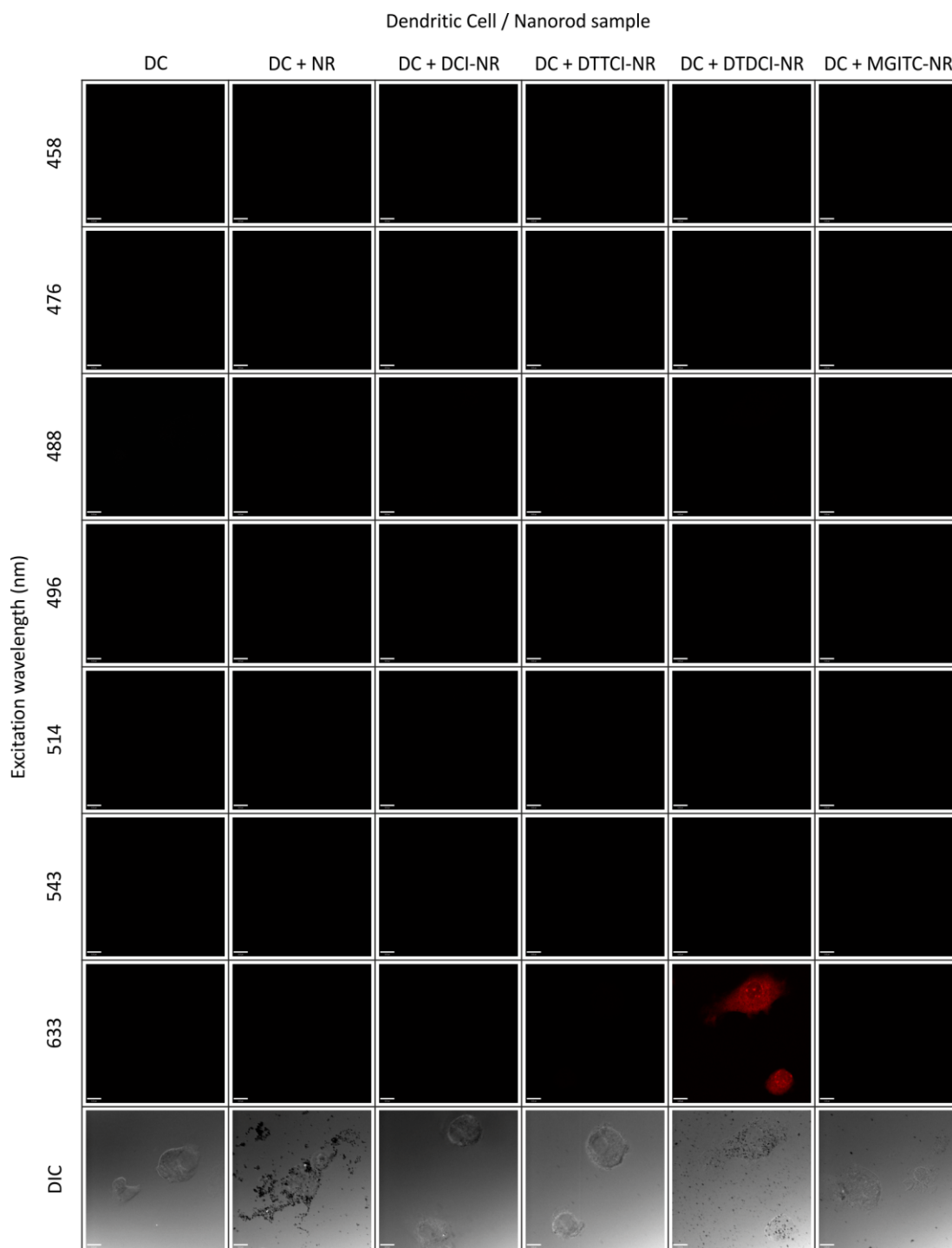
Figure 3.10 Confocal fluorescence images were obtained for dendritic cells exposed to different NR-dye configurations. Dendritic cells were incubated with 100 pM of the NR-dye conjugates for 2 h and subsequently fixed and mounted for confocal imaging. A range of excitation wavelengths was used in order to scan for fluorescence across the spectrum. DTDCI-NR showed a fluorescence signal only when excited at 633 nm, while other samples did not show any intrinsic luminescence under the same experimental conditions (black images).

3.4 Universal SERRS Tags (USTs) for multimodal imaging

As outlined in the previous sections, gold nanorods have shown versatile optical capabilities for imaging under various techniques. The ability to consistently incorporate reporter dyes and form highly stable imaging tags is a great advantage of this system, when compared to more complex and less predictable approaches such as aggregation-based systems.[68,83] Additionally, conventional SERS-tag development approaches focus on detection at a single wavelength. Here, controlled coadsorption of multiple dyes onto single gold nanorods was performed, followed by polymer wrapping, creating highly stable nanoparticle conjugates that could be detected – to the single-nanoparticle level – across a wide range of excitation wavelengths.[42] The fact that the spectral profile, brightness and active optical window of individual particles could be tailored for specific applications makes the USTs valuable tools for intracellular imaging and compound delivery monitoring.

3.4.1 Development of USTs

This work was developed in collaboration with Dr. Alison McLintock as part of her PhD studies and published in 2014.[42] Briefly, NRs with longitudinal λ_{max} of 770 nm were produced using the scaled-up synthesis, followed by incorporation of a combination of dyes into the surfactant bilayer (section 2.1.2) and PSS-PDDAC coating. The dyes used here – DTDCI, DTTCI and IR-1048 – allowed for SERS signal to be obtained across a wide range of wavelengths (514-1064 nm), as well as permitting the use of the tags for imaging with other techniques. However, detailed analysis of SERS behaviour of the USTs would fall outside the scope of the current work. Figure 3.11 shows the SERS spectra obtained for USTs for the three wavelengths used for the single-dye combinations, indicating the ability of these tags to provide signal throughout the three wavelengths used. As shown in Chapter 1 (Figure 1.4), verification that strong SERRS signals could be obtained from single, non-aggregated USTs, was performed through a series of confocal Raman and scanning electron microscopy (SEM) measurements of surfaces where USTs were immobilised.[42]
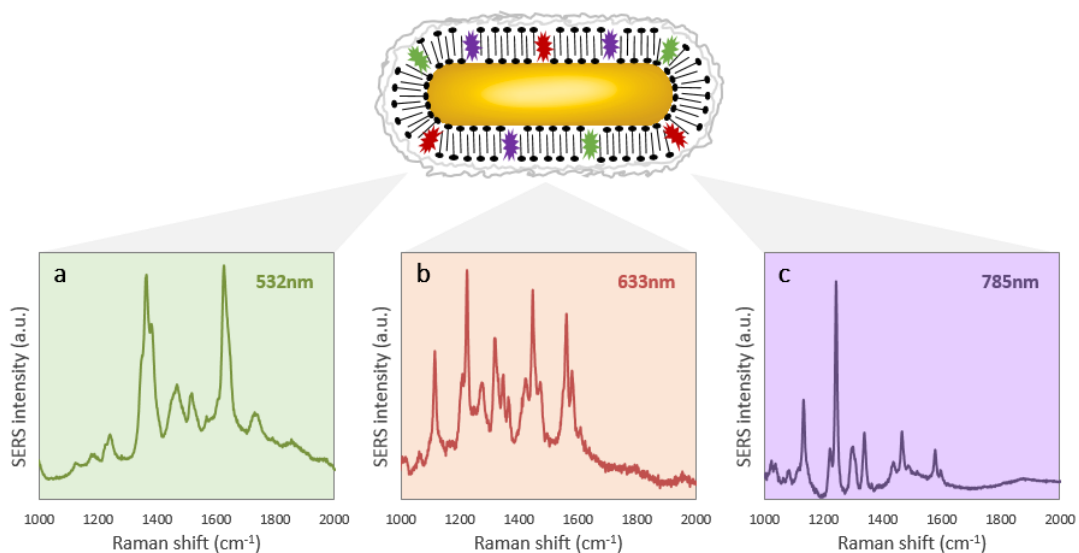
Figure 3.11 USTs were visible across a wide range of excitation wavelengths. The schematic shows the general design of the UST conjugates. Graphs show the bulk SERS spectra obtained for a suspension of USTs at (a) 532, (b) 633 and (c) 785 nm. Spectra have been background corrected and intensity normalised to the cyclohexane controls. Data shows that the USTs can be detected across all of these wavelengths with high specificity.

3.4.2 Toxicity and uptake assessment

Prior to the use of USTs for cell mapping, toxicity studies and assessment of uptake by dendritic cells were performed using flow cytometry and confocal microscopy. For this, cells were incubated with different concentrations of USTs and NRs without any incorporated dyes. Figure 3.12 shows data obtained for these tests, with flow cytometry data confirming that USTs were not inducing cell death at the concentrations used (Figure 3.12 b), even after 24 h incubation, when compared to the positive controls where camptothecin was used to induce apoptosis. Data also showed that the inherent DTDCI fluorescence was enough to make these nanoparticles visible using flow cytometry (Figure 3.12 a) and confocal fluorescence microscopy (Figure 3.12 c-d) at 633 nm excitation. Additionally, confocal imaging confirmed nanoparticle internalisation as opposed to adhesion to the cell membrane (Figure 3.12 d). Overall, the relatively low cytotoxicity and confirmed internalisation of USTs provided confidence that these nanoparticles were suitable for intracellular imaging applications, as shown in the next section.
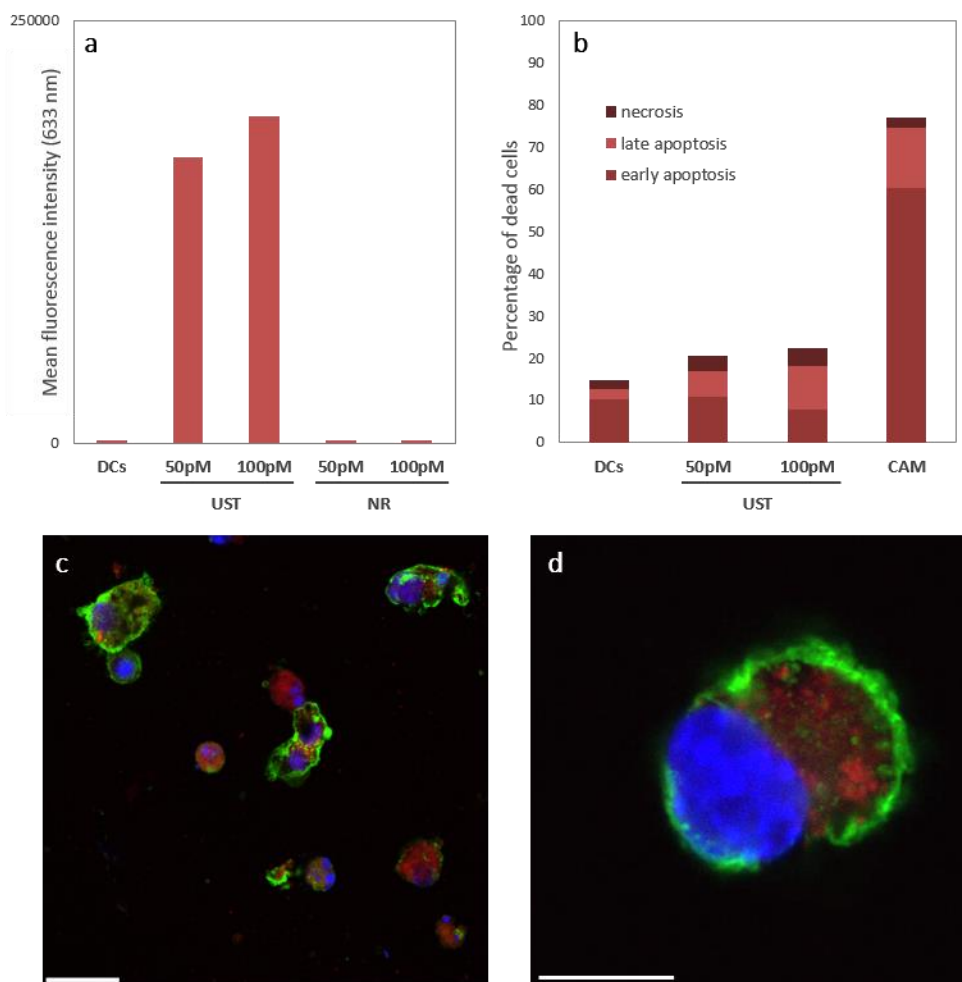
Figure 3.12 Cell uptake and cytotoxicity of USTs were evaluated. (a) Flow cytometry data showing the measured mean fluorescence intensity at 633 nm excitation of cells incubated with USTs or polymer wrapped NR controls with no reporter dyes for 2 h. (b) Toxicity of USTs to dendritic cells measured by flow cytometry of dendritic cells after 24 h incubation with USTs at 50 and 100 pM with unpulsed cells (DC) as a negative control and camptothecin (CAM) as positive control. Graph shows the percentage of cells undergoing early apoptosis (Annexin-V+/PI-), late apoptosis (Annexin-V+/PI+) and necrosis (Annexin-V-/PI+). (c-d) Composite confocal fluorescence images of fixed dendritic cells exposed to 10 pM USTs for 24h. Cholera-toxin-B staining is used to identify the cell membrane (green), DAPI for the nucleus (blue) and nanorod fluorescence is shown in red (from DTDCI). Image shown in (d) confirms nanoparticle internalisation. Scale bars (d) 20 μm, (c) 10 μm.

3.4.3   Multimodal imaging of intracellular USTs

The use of USTs as multimodal imaging contrast agents has a number of potential applications for intracellular imaging. For instance, changes in single-particle SERS could be used to monitor compound delivery to specific areas of the cell, while fluorescence or dark-field could track nanorod positions simultaneously. Additionally, it is important to investigate

how gold nanorods behave under different techniques, as changes in the density of particles in specific areas of the cell can lead to changes in SERS intensity, fluorescence quenching and polarisation. Here, having verified that the developed USTs were biocompatible and that dendritic cells would effectively internalise them, these particles' ability for imaging was then evaluated by obtaining intracellular maps using different techniques. To achieve this, dendritic cells were exposed to USTs for 4 hours, after which they were fixed and prepared for imaging as appropriate (section 2.3.6). Each of the analysed cells was mapped using confocal Raman at 532, 633 and 785 nm, dark-field and confocal fluorescence microscopy (Figure 3.13), to allow for potential co-localisation of signals from different maps. Control cells that were not exposed to nanoparticles showed no fluorescence and no characteristic Raman peaks associated with intracellular molecules at the relatively low laser powers and integration times used. Interestingly, the SERRS maps in Figure 3.13 display localised areas of varying signal intensity associated with different UST densities. Relative differences between maps at each excitation wavelength were due to a number of factors, including laser spot size, relative position and depth of the focal plane within the cell, as observed by acquiring repeat fluorescence and Raman maps at different focal depths for a number of cells. In any case, simple visual comparison between the dark-field, fluorescence and SERRS images obtained showed a number of correlative features and indicated the absence of particles within the cell nucleus (shown in blue in the confocal fluorescence images, from DAPI staining), consistently with previous reports of non-targeted gold nanoparticle uptake mechanisms.[204] It is also interesting to note that the areas of the brightest fluorescence intensity did not always correlate with the brightest SERS signal. It has also been observed that occasional dark areas seen in bright-field images, indicating a high density of nanoparticles, generally correlate with higher SERS intensities and low or no detectable fluorescence signal, suggesting that at certain NR densities the interaction between neighbouring particles leads to fluorescence quenching.

Overall, the USTs were successfully detected within dendritic cells using dark-field, fluorescence and a range of SERRS excitation wavelengths. This, together with these particles' strong signals detected at single-nanoparticle level[42] (data shown in Figure 1.4 for these particles), can lead to applications in high-resolution intracellular tracking of single nanorods. Additionally, the design of these nanoparticles has enough versatility that it can be translated to different dyes and surface coatings for specific applications. As an example,

the following section presents a different multi-dye combination which was also briefly investigated.
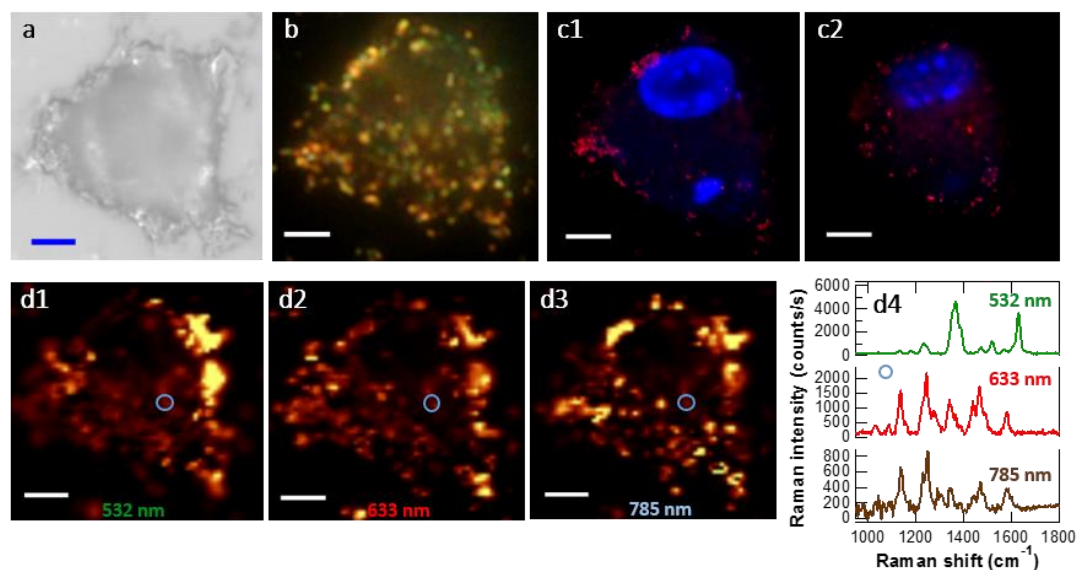
Figure 3.13 Multimodal optical imaging of a dendritic cell after incubation with USTs. Dendritic cells were incubated with 100 pM USTs for 4 h and subsequently fixed. (a) Brightfield image, (b) transmission dark-field image and (c) confocal fluorescence images of the lower (c1) and upper (c2) regions of a vertical image stack (DAPI in blue, 405 nm; USTs in red, 633 nm excitation) of the cell. The same cell was repeatedly mapped using a Raman confocal microscope at three different excitation wavelengths (d1-532 nm, d2-633 nm, d3-785 nm), with (d4) showing representative SERRS spectra (background corrected) from within the circled region in each of the Raman maps. All SERRS data were obtained using a 0.5 s integration time and at 0.4 μm steps. The Raman maps were created from max/min intensity analysis in peak regions at 1360 cm^{-1} for 532 nm (laser power 0.54 mW) and at 1245 cm^{-1} for both 633 and 785 nm (0.66 and 0.73 mW respectively). The brightest intensities in each map correspond to signals >18000-42000max (532 nm), >5000-8900max (633 nm), >2500-6000max (785 nm) counts/s. All scale bars = 5 μm. A version of this figure has been published in ACS Nano.[42]

3.4.4 A new UST design

While the USTs described in previous sections showed that detection at a wide range of wavelengths could be achieved within the same particle, specifically by incorporating the IR-1048 dye for infrared analysis as well as the visible dyes, their behaviour at 785 nm was not optimised as there was no dye overlapping strongly with that (widely used) excitation wavelength. Thus, a second multi-dye combination was tested in order to assess the possibility of using different dye combinations and optimise the behaviour of these complexes at 785 nm. For this, a premixed combination of NIR-797, MGITC and DCI (dyes also used in section 3.3 for the single-dye tests) was added to gold nanorods with a longitudinal λ_{max} of 712 nm, followed by PSS-PDDAC wrapping. These multi-dye conjugates are here

termed UST2, for simplicity of presentation. Bulk spectra (Figure 3.14) showed good behaviour of these conjugates when excited at 532, 633 and 785 nm and in comparison to measurements with NRs conjugated to each of the single dyes used, for the same batch of NR and under the same coating conditions. Interestingly, the multi-dye combination presented a notably higher SERS intensity for the same specific peak when compared to the NIR797-conjugated NR (Figure 3.14 a3), a phenomenon which would require further investigation.
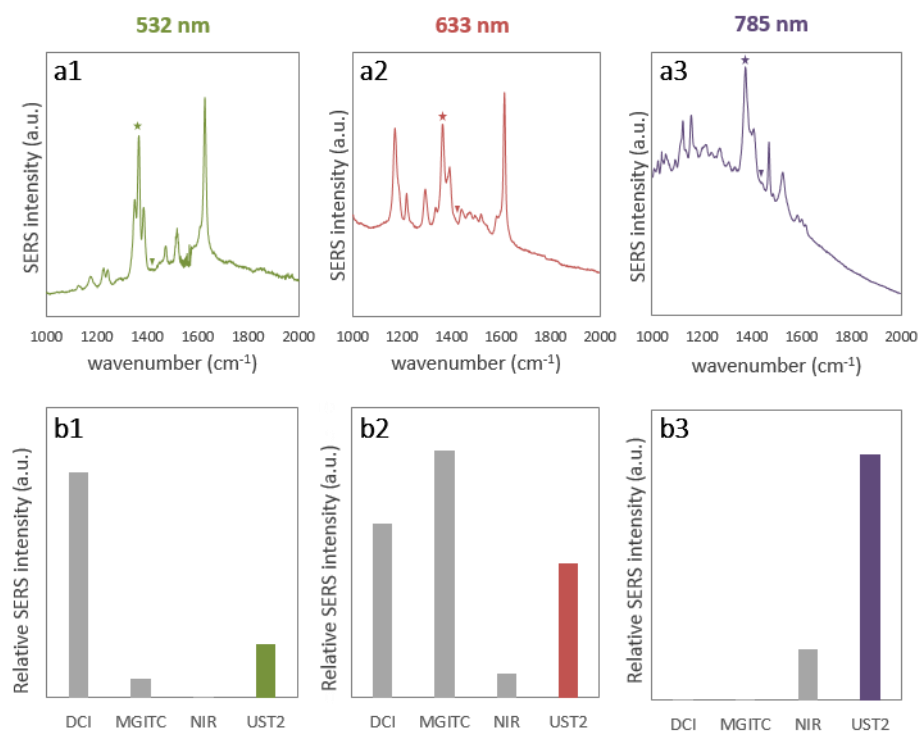
Figure 3.14 SERS spectra of a new multi-dye combination were obtained and compared to the individual dyes. (a) Bulk spectra for the UST2 multi-dye conjugates were obtained at (a1) 532, (a2) 633 and (a3) 785 nm excitation. (b) Comparison of obtained SERS intensities for NR with each of the single dyes (from Figure 3.9) and the UST2. Peak intensities were obtained by min/max analysis of specific peaks (max marked with ★, min marked with ▼) and normalised to the corresponding cyclohexane control peak at ~1270 cm^{-1}.

Confocal SERS maps of a low density monolayer of UST2 on a glass surface were also attempted as proof-of-concept for this new dye combination. However, it was verified that despite the good performance of these conjugates at 532 (Figure 3.15 a) and 633 nm (Figure 3.15 b) excitation, no maps could be obtained for 785 nm excitation. Specifically, while signal was obtained in some areas when setting up the mapping regions, it became undetectable within seconds of beam exposure even at lower (~0.5mW) laser power, indicating that the

dye was not stable enough to endure that procedure. In any case, raw spectra obtained at 532 and 633 nm (Figure 3.15 a2-b2) showed that specific UST2 peaks could be detected both from high density areas and very low density areas, suggesting single nanorod imaging was possible with these particles. Overall, this is an area that will require further research, in order to determine the most appropriate dye combination to overlap the three wavelengths considered that can be successfully used for intracellular mapping, potentially with single-particle resolution.
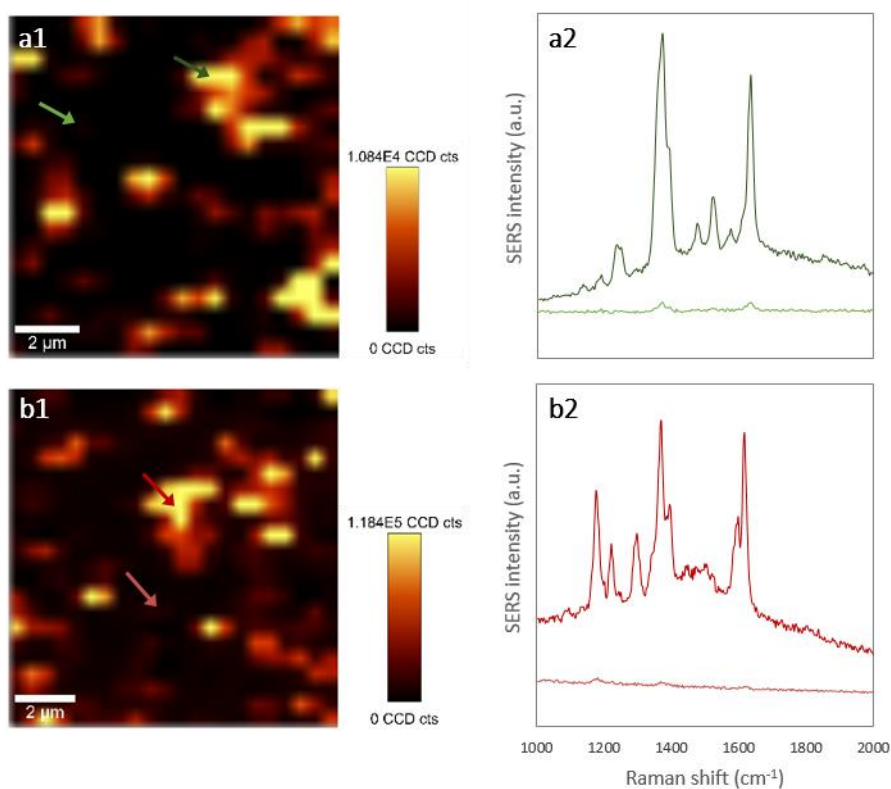
Figure 3.15 Multi-dye conjugates were mapped using confocal Raman. A low density monolayer of UST2 samples was mapped using a Raman confocal microscope at (a) 532 and (b) 633 nm excitation (~0.7 mW laser power, 1 s integration time) with 0.5 µm steps. No data was obtained for 785 nm due to dye instability. (a2,b2) show representative raw spectra obtained at 532 and 633 nm, respectively. The arrows indicate the location of the spectra for single (light colour) and clustered (dark colour) gold nanorods for each of the wavelengths.

3.5 Conclusions

This chapter described the development of highly specific formulations of gold nanorods for cellular imaging using different techniques. By changing the Raman reporter dye combinations, it was shown in section 3.3 that nanorods can be successfully tailored to target any common excitation wavelength, or multiple wavelengths simultaneously. Additionally, dye combinations can be chosen to make the nanorods visible or not during fluorescence imaging, which can be useful for applications involving different fluorescent probes, namely when using bioconjugated molecules on the surface of the nanorods. This versatility will enable single-nanoparticle tracking and shows the potential of these particles for vaccine or drug delivery monitoring at the molecular level.[64,205] Here, optimisation of gold nanorods with incorporated DTDCI and PSS-PDDAC-PSS polymer wrapping was achieved for application within the microfluidic platform described in Chapter 4, aiming to achieve real-time assessment of cell-nanoparticle interactions (Chapter 5) and of nanoparticle-mediated antigen delivery (Chapter 6). Additionally, the application of a multi-dye nanorod system for multimodal intracellular imaging was shown in section 3.4, with promising results in terms of colocalisation using different techniques and investigation of different multi-dye combinations. Together, these results indicate the high versatility of gold nanorods for biomedical applications.

Chapter 4

Development of a Microfluidic Device for High-Throughput Single-Cell Analysis

The emergence of lab-on-a-chip technologies for single-cell analysis has shown its promise for providing insight into cell function through analysis of population heterogeneity, dynamic morphological and functional studies and intracellular imaging.[31,206] The main aim of this work was to develop a microfluidic device where cells could be immobilised individually into low shear stress microtraps and kept in a controlled environment while being analysed in real-time using a range of microscopies and spectroscopies. This chapter presents the development of this device, discussing design considerations and prototyping issues as well as preliminary cell trapping experiments and controlled reagent delivery tests.

4.1 Microfluidic device development

Microfluidic devices were fabricated using standard soft lithography procedures[153] (section 2.4.1). The microfluidic design was based on previously described hydrodynamic cell trapping configurations.[29,30] Generally, each device comprised a trapping chamber containing an array of over 1,500 traps, with two or three inlets and one outlet. A schematic representation of the design used in this work is shown in Figure 4.1. Each trap had an inner width of 20 μm and three openings that facilitated cell trapping and allowed the fluid to flow through it without displacing the cell, thus exerting low shear stresses over the cell membrane.[30]
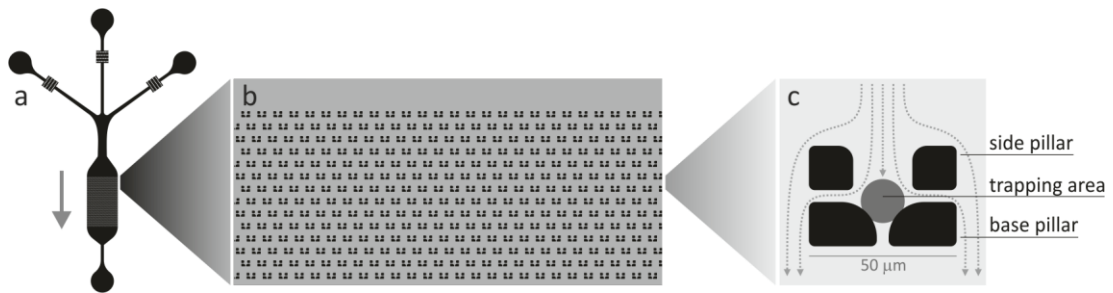
Figure 4.1 A microfluidic device was designed for single-cell trapping and perfusion. Schematic in (a) shows a device with three inlets, one outlet and one trapping chamber. The arrow shows the direction of the flow. Close-up area in (b) shows the full width of the trapping array (2 mm wide, drawn to scale) with asymmetrically-distributed trap rows. Further close-up in (c) shows a single trap and the general mechanism of hydrodynamic cell trapping, where a cell suspension is loaded into the trapping chamber and individual cells are captured within the microtrap structures. The grey sphere represents a 15 μm-diameter cell and the gaps between pillars measure 4 μm. Trap structures are drawn to scale.

4.1.1   Wafer fabrication

Fabrication of patterned silicon wafers was done by photolithography as described in Chapter 2. Optimisation of each step of the procedure was performed to achieve:

a) Good adhesion of the photoresist to the silicon surface, via constant monitoring of the temperatures used for soft baking and post-exposure baking, to allow for repeated and consistent device prototyping using the same patterned wafer.

b) Good feature resolution, by optimisation of exposure time and exposed resist development steps, achieving feature sizes in the order of 3-5 μm, such as the gaps between the trap pillars as shown in Figure 4.1. This was important especially for the gaps within the traps, which should allow for fluid to flow whilst being small enough to prevent cells from flowing through.

c) A chamber depth of approximately 25 μm, by optimisation of resist spin frequency when deposited onto the wafer surface, to enable cell flow and facilitate single-cell trapping while trying to minimise the occurrence of multiple layers of cells within one trap.

Assessment of wafer fabrication quality was done by Environmental Scanning Electron Microscopy of a PDMS cast of each wafer (Figure 4.2), while the measurement of structure height was done by profilometry of the cured SU-8 structures on the silicon wafer. As an example, structure height for one specific wafer measured at 10 different locations using a profilometer was 26.2 ± 1.5 μm.
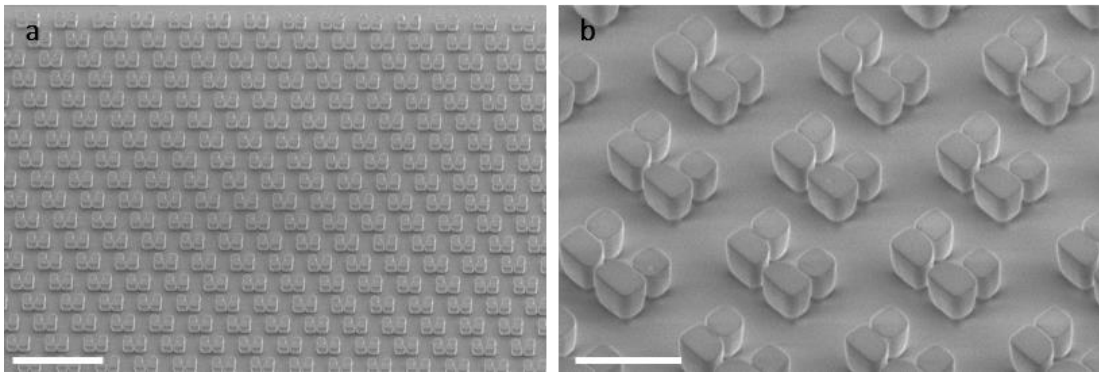
Figure 4.2 Scanning Electron Microscopy was used to assess fabrication quality. SEM images of a PDMS cast of an SU-8 wafer fabricated as described. Pictures are representative of all devices produced following the optimisation steps described in this section. Scale bars are (a) 200 μm and (b) 50 μm.

4.2   Design considerations

A number of different device designs were tested, varying the number and shape of trapping chambers, the number of inlets and the size and shape of the microtraps, in order to achieve good trapping efficiency and the best conditions for cell culture on-chip. This section briefly outlines some of the aspects considered for the various design iterations and their improvement towards a final, optimised design.

4.2.1   Parallel versus single trapping chambers

Initially, a device design developed by Dr. Michele Zagnoni was first tested for bead and cell trapping. This was a three-inlet device with four parallel trapping chambers (Figure 4.3 a) and a channel network that could eventually produce a gradient of concentrations, leading to each individual chamber to receive a separate concentration of, for example, nanorod conjugates. However, considering the early stages of nanorod development and nanorod delivery into the microfluidic chamber, as well as the challenges related to achieving uniform trapping of single-cells (points explored later in this chapter), it was considered that a single-chamber device would provide a better tool for optimising the nanoparticle-based assay. Thus, a simplified device was designed with two inlets and a single, wider trapping chamber (Figure 4.3 b). Following further experiments, a final design was produced and used for all the integrated system testing presented in Chapters 5 and 6 (Figure 4.3 c). This design recovered the three inlets, with the middle inlet being consistently used for cell loading into the device and the two side inlets for nanoparticle gradient generation, as well as dye, washing buffer or fixative perfusion. This provided the required flexibility while avoiding

reuse of the cell inlet, to prevent uncontrolled release of cells into the array at later stages in the experiment. Additionally, cell trapping was found to be more efficient, with more uniform coverage of the array being obtained when using the middle inlet in the three-inlet design for injecting the cell suspension (experimental data for this observation will be shown as an example for cell coverage analysis in section 4.3.5).
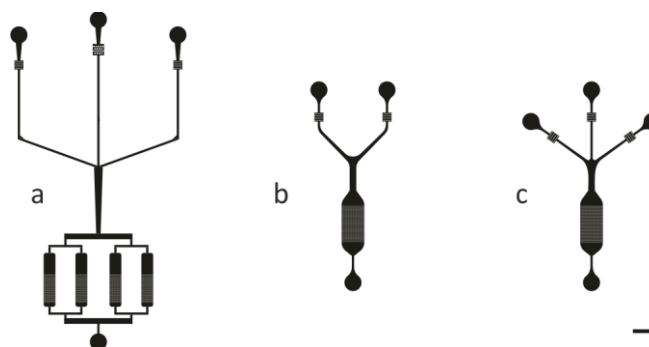
Figure 4.3 Different trapping chamber designs were tested. Drawing shows the initial design used for this work (a) and two of the most important evolutions of that initial design (b-c), with (c) being the one that was used for all experiments in Chapters 5 and 6. Designs are represented to scale at 150% of true size. Scale bar is 2 mm.

4.2.2   Trap shape and features

Trap shape improvements were also investigated. Figure 4.4 shows some of the designs tested experimentally during the course of this work. Importantly, all of the traps used had three openings, allowing for the fluid to flow through (Figure 4.1 c), keeping the cell in place while minimising shear stress on the cell surface.[30,207,208]

Figure 4.4 A range of trap designs was assessed. (a-e) Trap designs tested within this project. Trap design (b) was the most commonly used following the initial optimisation stage. Drawings are to scale relative to each other. Scale bar is 20 µm.

The initial trap design tested, shown in Figure 4.4 (a), was found to be susceptible to accumulate numerous cells within each trap, due to the length of the side pillars. To minimise this, the length of the side pillars was reduced in subsequent designs as much as the fabrication capabilities allowed. The traps shown in Figure 4.4 (b-c) had comparable performance in terms of cell trapping, but when compared to (b), trap (c) was found to be slightly more fragile in terms of the breakage of the top pillars when peeling off the PDMS.

In turn, trap (d) tended to accumulate larger numbers of cells per trap due to having a slightly larger inner volume, and that design was found to be a challenge to be made smaller. Additionally, the trap design shown in Figure 4.4 (e) was extremely fragile from the fabrication point of view, which following PDMS moulding quite often resulted in the smaller pillars being broken for most of the traps, for the fabrication conditions used. This had a negative effect on the ability of these traps to contain cells for long periods of time, which led to that design being abandoned at an early stage. Thus, trap (b) was the design used for the nanoparticle delivery experiments that will be described in later chapters. It is worth noting that the initial devices with designs (b-e) were fabricated under the same conditions, on the same wafer. This may mean that the robustness of fabrication of certain structures could vary due to their position in the wafer, especially in relation to UV exposure, or to sub-optimal fabrication conditions for certain feature shapes. Nonetheless, this section is not aiming to describe comprehensive testing of the different designs, rather an empirical evaluation of which design showed more reliable outcomes for the fabrication and experimental conditions used in this work.

4.2.3 Trap alignment

One important factor for maximising coverage of the trapping array with cells was the alignment of consecutive trap rows. Initially, traps in each row were designed to be exactly in the middle of two traps in the previous row, and thus were symmetrically distributed across the array. This was found to give poor cell coverage as many of the cells loaded into the chamber would simply flow between the structures without getting trapped, leading to approximately 35% of the traps being empty (Figure 4.5 a). Conversely, it has been shown that asymmetric distribution of traps in such hydrodynamic configurations can be beneficial for cell trapping efficiency.[29,207] Thus, an asymmetric configuration was tested (Figure 4.5 b), together with an adjustment of the distance between consecutive traps. This combination of factors led to a reduction in the occurrence of empty traps to approximately 2%, and that was the design adopted for the integrated system testing shown in Chapters 5 and 6.
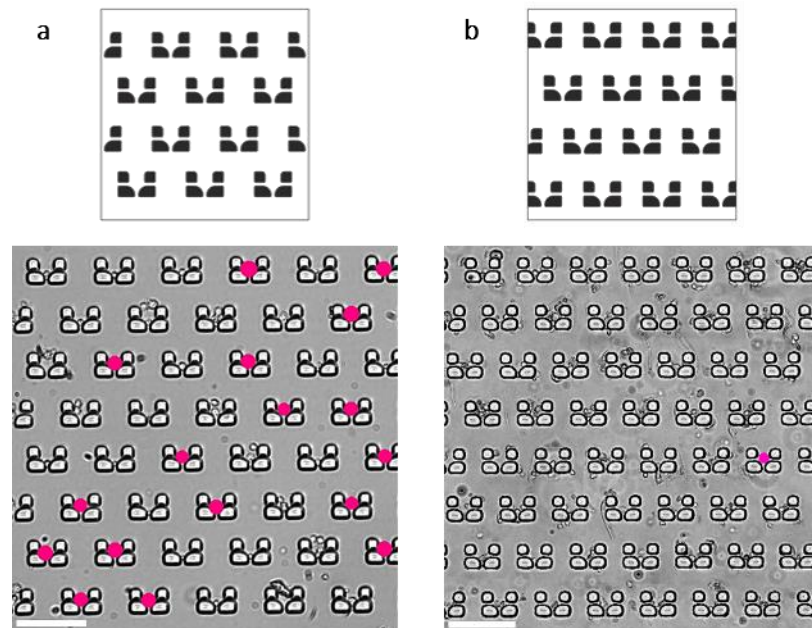
Figure 4.5 Different trap alignment configurations were tested. (a) Symmetrically distributed microtraps and (b) asymmetrical distribution of the same traps, also with different spacing between traps. Microscope images show examples of both array designs containing trapped cells, with empty traps marked with magenta circles. Scale bars are 100 µm.

4.2.4   Cell survival: shear stress

As mentioned in Chapter 1, control of the shear stress to which cells are exposed within microfluidic environments is crucial to the success of these devices for live-cell studies. Specifically, it is important that cells are exposed to physiological levels of shear stress (~0.1-10 dyn/cm^2), while excessive shear stress can be harmful to the cells.[156,159] Thus, when performing hydrodynamic cell trapping, it is important that not only during the cell loading procedure[201] – withdrawal into tubing, pumping into device, flowing through narrow channels – but also after trapping, cells are not exposed to magnitudes of shear stress higher than those found in physiological conditions. With this in mind, the trapping designs used were such that the regions within the traps constituted low shear-stress pockets, due to the openings around the trap area and to the majority of the flow being deviated outside of the traps.[29,30] Specifically, the shear stress around one of the trapping designs used was characterised by Dr. Michele Zagnoni through a numerical simulation, demonstrating that the average flow in regions outside of the traps was an order of magnitude greater than the flow rate inside the traps (800-2400 µm/s outside versus 50-150 µm/s within traps), depending on the flow condition.[30] Therefore, for the most commonly used perfusion flow rate of 0.5 µl/min, cells within the traps were exposed to shear stresses between 0.05-

0.15 dyn/cm^2, which are at the level of interstitial flow shear stresses, and cells outside traps to approximately 0.6 dyn/cm^2, also within physiological levels.

4.2.5 Cell survival: nutrient/gas exchange

Considering that the devices were designed for on-chip incubation of trapped primary cells for long periods of time (up to 24 h), it was important to ensure that the hydrodynamic conditions would maintain a biocompatible environment within the traps. The use of poly(dimethylsiloxane) (PDMS) for device fabrication is favourable for biological lab-on-a-chip applications, as besides its relative simplicity of fabrication and flexibility of design it is also optically transparent and permeable to gases.[153,209] Importantly, PDMS has also been shown to be biocompatible, allowing for long-term cell culture with no harmful effect on the cells.[32,157,161] Here, being a closed device (no open wells for gas exchange), the permeability of PDMS was relied on for gas exchange, with initial on-chip cell incubation experiments showing that cells were viable for long periods of time (1-2 days), indicating that this was a suitable approach. Considering nutrient exchange, however, it is known that different trap designs can facilitate the refreshment of medium within the traps, while others can block it, creating microenvironments within each trap that are not favourable to cell survival due to lack of nutrients and accumulation of cellular waste products.[208] This process depends on a balance between convective and diffusive processes, which is affected by the device geometry and flow conditions and can be assessed using the Péclet number, Pe (section 1.5.2, equation [2]). Here, taking the movement of bovine serum albumin (diffusivity $D \sim 9 \times 10^{-11} \ m^2/s$ at 37°C)[210] as a representation of nutrient circulation within the trapping chamber and based on the differences in velocity inside and outside of the traps (previous section), Péclet numbers of 0.03 and 0.44 were obtained, respectively, for inside and outside of the traps. This indicates that diffusion was the dominant mass transfer process in both areas ($Pe \ll 1$), with convection becoming more important outside of the traps (Pe closer to 1). The trap designs used had gap features that allowed for the liquid to flow through, facilitating nutrient exchange. Additionally, it was verified (using fluorescence microscopy) that both fluorescein and nanoparticle suspensions, despite their differences in size and consequently in diffusion coefficient (see section 4.4.2), were promptly reaching the inside of the traps, indicating that under the same flow conditions, cells would be under continual flow of cell culture medium. Naturally the delivery of medium would be harder to assess directly as it is not fluorescent. In any case, these observations, together with long-term

monitoring of cells cultured in the microfluidics chamber at 37°C and 5% CO_2 under continuous medium perfusion as well as preliminary on-chip viability testing (Chapter 5), provided the confidence that the design chosen was creating favourable conditions for cells to be maintained alive within the microtraps for real-time monitoring.

4.3 Cell trapping in the microfluidic device

Following all the design considerations from the previous section, a device was produced for cell trapping and real-time monitoring. This device was first tested with polystyrene beads for setup optimisation, followed by initial cell trapping tests and monitoring of cell activity as a measure of biocompatibility of the procedure for the cells and to establish the best cell trapping parameters. This section describes some of these optimisation aspects, necessary to achieve a robust platform that could be used for monitoring nanoparticle-cell interactions at the single-cell level, as will be described in Chapters 5 and 6.

4.3.1 Preliminary bead trapping tests

Initially, 20 μm-diameter polystyrene beads were used as a preliminary evaluation of cell trapping. It was observed that the addition of 1% Tween-80 to the bead solution in water was necessary to prevent the polystyrene beads from aggregating and adhering to the inner wall of the PTFE tubing. Beads were then successfully trapped in the described microfluidic designs (Figure 4.6), providing confidence that devices would be suitable for dendritic cell trapping, considering cell size dispersion (approximately from 5 to 20 μm in diameter). However, lack of uniformity of channel depth across those initial devices (wafers fabricated before this project started, with chamber depths varying between 17 and 22 μm) presented issues for the bead experiments as these, being not deformable, could not always flow easily through the channels.
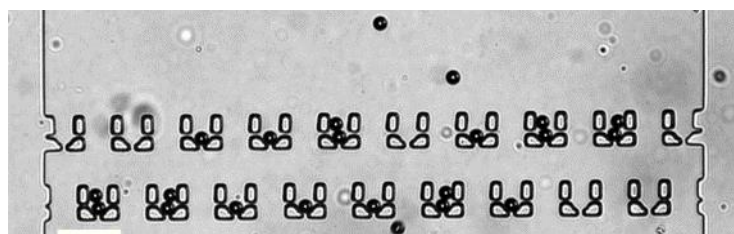
Figure 4.6 Polystyrene beads were successfully trapped within the microfluidic array. Bright-field image showing 20 μm-diameter beads flowing into the trapping chamber and getting trapped into 30 μm-wide microtraps. Scale bar is 100 μm.

4.3.2 Cell type

Primary dendritic cells were used for all cell trapping and monitoring tests. Using a population of primary cells (that are heterogeneous in morphology and size) better represents the *in vivo* state and allows for a more reliable assessment of cell function when compared to work done with cell lines. Specifically for dendritic cells, there is no real cell line that effectively represents their *in vivo* behaviour.[192] However, the inherent heterogeneity of these cell samples brought additional challenges to capturing and maintaining cells in traps, due to differences in morphology, size and activation status within the cell population (Figure 4.7). In any case, the devices and protocols developed generally resulted in the successful trapping of hundreds of dendritic cells at the single-cell level. The present section will analyse the various aspects of cell trapping that were considered for this work.
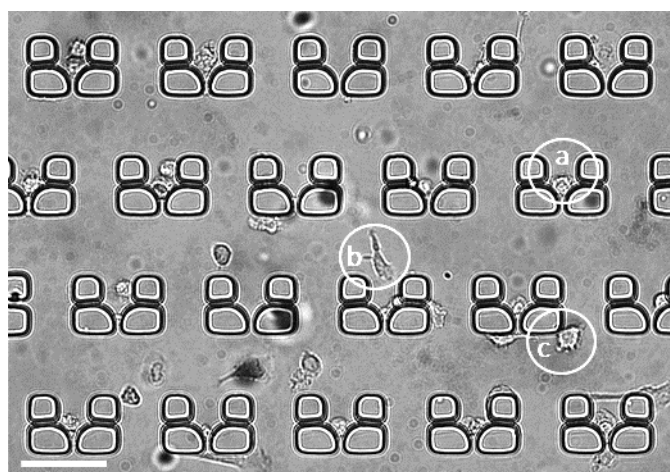
Figure 4.7 Trapping of primary dendritic cells showed the heterogeneity of the cell samples. Image shows an area of the trapping array following cell trapping, where it can be observed that while some cells are within the traps (a), a few cells adhere to the bottom glass surface, even under constant medium perfusion (b), and other cells adhere to the outside of the traps or display branched projections (dendrites) stretching out of the traps (c). Circles (a-c) show cells representative of the mentioned conditions, demonstrating the heterogeneity of the cell samples. Scale bar is 50 μm.

4.3.3 Effect of cell loading conditions

The conditions of cell withdrawal from a centrifuge tube into the PTFE tubing prior to loading into the device were found to have an effect in trapping efficiency and on-chip cell viability. Thus, in order to optimise the loading procedure, an experimental evaluation of the different conditions was performed. Generally, it was found that there were four important factors to consider:

a) Withdrawal flow rate: for flow rates under 1 µl/min, it was found that the cell density in the inlet tubing would be low, even at high cell concentrations in the source tube. A much improved cell withdrawal was achieved by using 2.5 µl/min for the first 5 µl (as measured by the syringe pump) and 5 µl/min for the remaining 25 µl.

b) Cell suspension concentration: it was observed that for concentrations around 10^7 cells/ml, traps were often overfilled and clogging was likely to occur within the trapping chamber or cell inlet channel. Conversely, concentrations ranging from 1-5x10^6 cells/ml provided good cell coverage, depending on the other points on this list.

c) Cell suspension status: prior to cell withdrawal, the centrifuge tube containing sedimented cells was either i) flicked to resuspend, ii) left untouched, with cells withdrawn directly from the sedimented pellet or iii) gently resuspended with a pipette prior to cell withdrawal. It was found that gentle resuspension was the most effective approach, considering cell coverage and cell viability.

d) Cell harvesting conditions: for the initial experiments, cells were harvested into a centrifuge tube at least one hour prior to loading into the microfluidic chamber and transported between different buildings during this time. Due to an improvement in laboratory facilities, in later experiments (Chapter 6) cells were harvested from the cell culture plates immediately before loading into the device and this proved to have a positive influence in array coverage and cell viability.

4.3.4   Effect of flow rate

During cell loading into the device, cells retained a round shape and, from 15 minutes after trapping, cells became progressively more active, indicating their viable condition within the traps. Subsequently, trapped cells would present different behaviours when exposed to different flow rates. Below a constant flow of 0.5 µl/min, cells that migrated outside the traps could easily move around the array by adhering to the bottom glass substrate. At a flow rate of 1 µl/min, cells outside the traps were often washed away towards the outlet, depending on their degree of adherence to the trap pillars (cells outside traps often adhered strongly to the trap pillars, in which cases they were not washed away), whilst cells in the traps remained stable. Conversely, at high flow rates ≥2 µl/min some cells were also washed away from inside the traps. With this in mind, the flow rates used for this work were generally 1.5 µl/min for the cell trapping phase and 0.5 µl/min for nanorod delivery and culture medium

perfusion. The effect of flow rate on the uptake of nanorods by cells will be discussed in Chapter 5.

4.3.5   Cell coverage analysis

Analysis of cell coverage provided an overview of whether the cell concentration was appropriate, as well as being a graphical assessment tool for the ability of the different designs tested to effectively capture and maintain cells for up to 24 hours under medium perfusion. Figure 4.8 shows two examples of cell coverage analysis performed in devices of different designs (previously shown in Figure 4.3 b-c) under different experimental conditions, simply to illustrate this analysis tool. Specifically, the figure refers to the comparison of a two-inlet (Figure 4.8 a) with a three-inlet device (Figure 4.8 b), showing that the former was more susceptible to irregular coverage of the trapping array, as mentioned in section 4.2.1. In the illustrated case, the irregularities were due to the occurrence of negative pressure on the unused side inlet while loading cells, which caused the cells to deviate to one side of the array rather than being uniformly distributed across the traps.
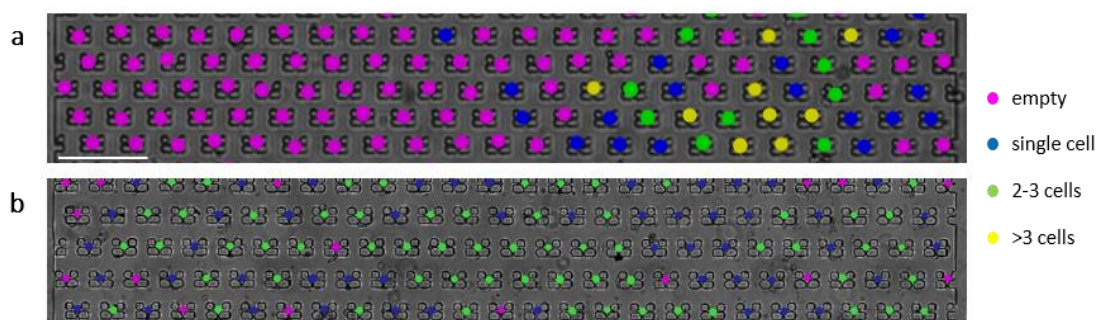
Figure 4.8 Cell coverage analysis provided information on the cell trapping ability of different designs. Microscope image of cells trapped within (a) a two-inlet device, where cells were injected from the left inlet, and (b) a three-inlet device, where cells were injected from the middle inlet. In (a) cells deviated towards the right inlet channel prior to flowing into the trapping chamber, leading to uneven cell coverage, while cell injection from the middle in (b) seemed to be more resistant to these fluctuations leading to more uniform cell coverage.

Finally, following the design optimisation and cell trapping tests described in this and the previous section, the optimised trapping device and experimental conditions would typically lead to 68% of the total trap sites (n=1,512) containing single-cells, 15% containing 2 or 3 cells and 17% remaining empty or containing cell debris. Additionally, single-cells could be tracked even in traps containing two or three cells, using time-lapse imaging, proving the capabilities of the system to monitor over 1200 single-cells within just one trapping chamber.

4.3.6 Viability dye testing

Having successfully trapped cells within the chamber, it was important to verify that the device could be used to assess cell function using fluorescence microscopy. Specifically, the use of cell death indicator dyes was of interest for on-chip nanomaterial toxicity assessment, as will be shown in Chapter 5. Thus, in order to simultaneously evaluate the performance of the microfluidics for delivering viability dyes and the sensitivity of the imaging setup to capture their fluorescence under the experimental conditions used, cell death was induced off-chip and dead cells subsequently loaded into the chamber and stained with commonly used viability dyes.
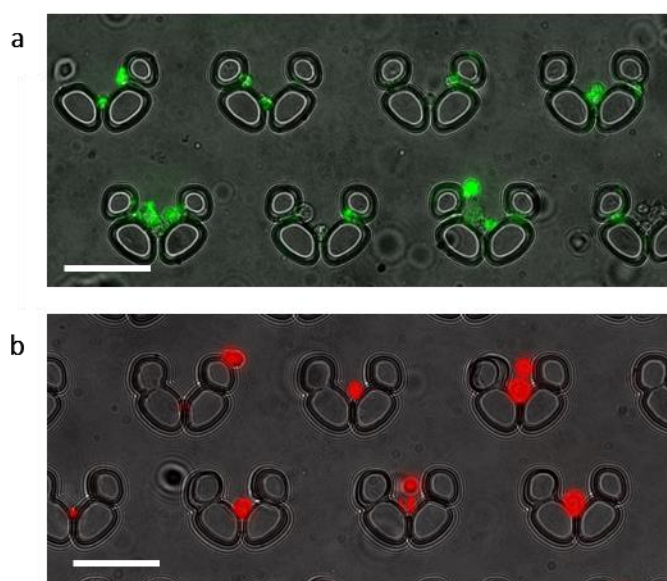
Figure 4.9 Viability staining was performed on-chip. (a) Composite (bright-field/fluorescence) image of trapped cells that were exposed to camptothecin overnight before trapping and Annexin-V FITC staining, showing bright fluorescence in many cells. (b) Composite (bright-field/fluorescence) image of trapped cells that were left in unfavourable conditions (room temperature, high concentration, centrifuge tube) for a few hours before Propidium Iodide staining, showing very bright fluorescence in all the cells. Experiments shown used an earlier trap design as these were performed during the development phase of the device, and trap design was not relevant to the results shown.

Initially, cells were treated with camptothecin for 18 h to induce apoptosis before loading into the device. Following cell trapping, a solution of Annexin-V FITC was delivered onto the trapping array and fluorescence images obtained with 450-490 nm excitation. Images (Figure 4.9 a) showed that apoptotic cells were brightly fluorescent for Annexin-V, indicating extensive apoptosis, while a control parallel device with untreated cells showed very low

Annexin-V fluorescence. To further assess the capacity of the device for fluorescence imaging of cells, two different dyes were tested: Propidium Iodide and Sytox Blue, both of which indicate damage to the cell membrane (associated with necrosis and the later stages of apoptosis) by crossing the damaged membrane and binding to intracellular DNA. Propidium Iodide (excitation 540-560 nm) was first tested, showing high fluorescence in cells that had been left to settle in a centrifuge tube out of the incubator for a few hours before loading into the device (Figure 4.9 b).

Importantly, it was observed that Propidium Iodide fluorescence would overlap with the nanorod-DTDCI conjugate fluorescence (excitation 608-648 nm) under the imaging conditions used, and thus, for NR viability assessment (Chapter 5), Sytox Blue (excitation 424-453 nm) was used instead. This dye behaves similarly to Propidium Iodide, forming highly fluorescent conjugates with DNA molecules, but with fluorescence excitation/emission in a region of the spectrum that would not interfere with NR fluorescence. Together, these observations indicated that the setup was able to clearly detect the differences between live and dead cells using a variety of staining procedures and also that the device was amenable to fluorescence imaging across a range of excitation/emission wavelengths.

4.4   Gradient generation in the microfluidic chamber

The generation of concentration gradients of compounds and nanoparticles across the microfluidic chamber was possible due to the low Reynolds number of microfluidic flows. In these conditions, pumping different solutions from the inlets into a single channel leads the fluids to flow side-by-side, mixing only via interfacial diffusion of solute species across the direction of the flow.[18,150,155] This property could be exploited to create concentration gradients of coated nanorods, allowing for the effect of such gradients to be assessed at the single-cell level. The current section describes the various aspects related to nanorod conjugate delivery and gradient generation within the developed microfluidic device.

4.4.1   Laminar flow and diffusion considerations

As seen in chapter 1, the Reynolds number is a dimensionless parameter which provides an indication of the characteristics of the flow (laminar/turbulent) for a given flow condition. Here, equation [1] (section 1.5.1) was used to calculate the Reynolds number, with:

- $\mu = 0.001$ Pa.s and $\rho = 1000$ kg/m^3 (for water);

- A volumetric flow of 0.5 µl/min, as that was the most commonly used flow rate for medium perfusion and parallel fluid dispensing , or $Q = 0.0083$ mm³/s;
- A cross-sectional area of the chamber $A = 5\text{x}10^{-8}$ m², for a chamber of 25 µm x 2 mm, corresponding to the most used device (Figure 4.3 c);
- A characteristic dimension (L) for chamber dimensions as above, $L = 0.049$ µm.

These parameters led to a Reynolds number of $Re = 0.0081$ for the trapping chamber at the flow rates used, which indicates that flow under these conditions will always be laminar. Thus, it was reasonable to assume that nanoparticle gradient formation will depend mostly on the diffusion of nanoparticles perpendicularly to the direction of flow. Consequently, it was important to look at the Péclet number (Pe) for these flow conditions, to assess the relative importance of convection and diffusion in the mixing processes. For this, equation [2] was used, as presented in chapter 1 (section 1.5.2). The diffusion constant for fluorescein at 25°C was obtained from the literature[211] as $D_{fluorescein} = 4.25 \text{ x } 10^{-10} \; m^2/s$. For the trapping chamber used ($L = 0.049$ µm as above) and at the most commonly used volumetric flow rate of 0.5 µl/min, this gave a Péclet number $Pe = 0.019$ (in water at 25°C). For nanoparticles, diffusivity was estimated from the Stokes-Einstein equation:

$$D = \frac{k_B T}{6\pi\mu r} \tag{3}$$

where k_B is the Boltzmann constant, T is the temperature, μ is the dynamic viscosity of the liquid (water, as above) and r is the radius of the particle. For simplicity, a spherical approximation was used here, as done for the numerical simulation (section 4.4.2). Thus, for 45 nm spheres at 25°C and flow conditions as above, the calculated diffusivity of nanoparticles was $D_{NP} = 9.7 \text{ x } 10^{-12} \; m^2/s$. This way, for flow conditions as above, the Péclet number obtained for nanoparticles was $Pe = 0.839$ (in water at 25°C). These values indicate that, under laminar flow conditions, where mixing can only occur by interfacial diffusion, this process can be relied on for the creation of concentration gradients. However, for nanoparticles, which are much larger than fluorescein molecules, diffusion is slower, and the Péclet number obtained suggests that the gradient region will be narrower than that of fluorescein for the same chamber dimensions and flow conditions. While some variation in the exact values of diffusivity and Pe will occur for other temperatures and for particles diffusing in culture medium, these values are provided here to illustrate these phenomena, and the difference in behaviour between nanoparticles and fluorescein will be maintained. Overall, these considerations will be relevant for the following sections, which explore the

theoretical and experimental generation of gradients of the two species within the microfluidic device.

4.4.2 Numerical simulation

In order to estimate the flow rates at the inlets of the device that would produce a suitable spatial gradient of nanorod concentrations across the microfluidic trapping array, 3D numerical simulations were performed in collaboration with Dr. Michele Zagnoni. COMSOL 3.5 was used to solve the Navier-Stokes equations to model pressure driven fluid transport together with Fick's law to model diffusive transport. Figure 4.10 shows the initial simulation with no trap structures. This allowed for a comparison between the behaviour that could be expected for small molecules, such as fluorescein (Figure 4.10 a), and gold nanoparticles (Figure 4.10 b), when simulated under the same flow conditions (condition shown in the figure is 1 μl/min from each inlet). As previously mentioned, computational modelling was performed using nanospheres of 45 nm diameter, rather than rod-shaped particles. As could be observed from the figures, the finite element model solution of the microfluidic system estimated a steeper gradient for nanoparticles than that formed for fluorescein for the same flow rate, due to their larger size and hence lower diffusion coefficient. This is consistent with the analysis of diffusion from the previous section, where the Péclet number indicated that diffusion of nanoparticles perpendicularly to the direction of the flow, for the flow conditions and device geometry used, would be much slower than for fluorescein under the same conditions.
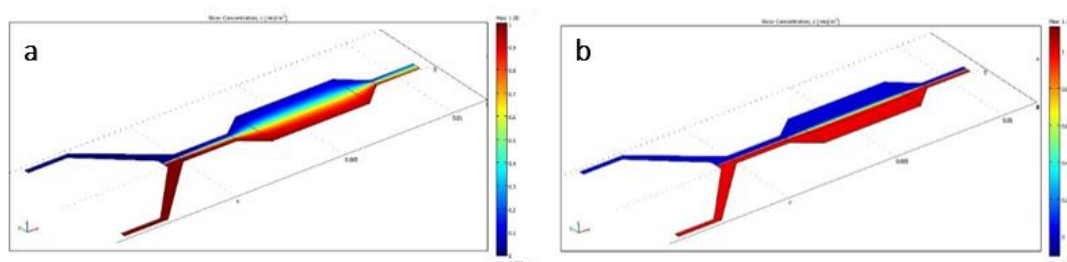
Figure 4.10 Gradient generation within the trapping chamber was estimated using numerical simulations. Images show the result of the simulation for (a) fluorescein and (b) gold nanospheres of 45 nm diameter. Both simulations shown here considered a flow rate of 1 μl/min from the two inlets. The colours correspond to a scale of concentrations, with blue being zero and red being the maximum concentration within the chamber.

Subsequently, the 3D numerical model was improved to include the microtraps, and the fluorescence intensity profile from the experimental data was compared with that obtained

from the numerical solution, demonstrating a close match to the sigmoidal signal obtained from the calibration experiments (Figure 4.11).
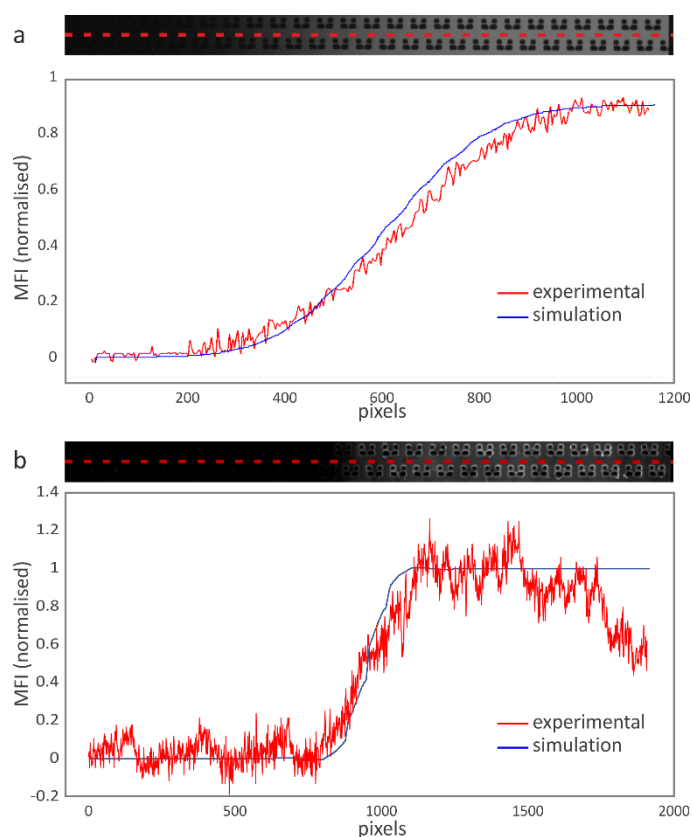
Figure 4.11 Data obtained for gradients on the microfluidic device was comparable to the numerical model. (a) Experimental image showing signal from a fluorescein concentration gradient (increasing from left to right from 0 to 100 µM) generated using the two lateral inlets of the device (one injecting a fluorescein solution at 0.5 µl/min and the other injecting water at 0.5 µl/min). The graph shows the comparison between the normalised fluorescence intensity profiles obtained from the finite element model solution (blue) and the experiment (red) in steady state condition across the full width of the array (red dashed line), showing the accuracy of the numerical model. (b) Experimental image showing fluorescence of a nanorod concentration gradient generated using the two lateral inlets of the device (one injecting a NR solution in culture medium at 0.5 µl/min and the other injecting culture medium at 0.5 µl/min). The graph shows the comparison between the normalised fluorescence intensity profiles obtained from the finite element model solution (blue) and the experiment (red) in steady state condition across the full width of the array (red dashed line), indicating that the numerical model was also suitable for predicting NR gradient formation.

Variation of the NR concentration gradient profile along the flow direction in the trapping chamber was also assessed to evaluate possible changes of the profile due to lateral molecular diffusion. According to the numerical simulation and to experimental results (obtained as per section 2.5.2), the variation of the NR distribution (i.e. gradient profile)

between the first and the last rows of traps was negligible, obtaining a variation of < 1% in the central region and ~3% at the sides of the chamber.

4.4.3 Fluorescein gradients

The necessary conditions for the delivery of a gradient into the trapping chamber were first tested by creating a fluorescein concentration gradient in water, using a device with no trapped cells and with fluorescence images being acquired in steady state condition. Different flow rates were evaluated and a few examples are shown in Figure 4.12.

| 0.01 µl/min | 0.1 µl/min | 0.5 µl/min |
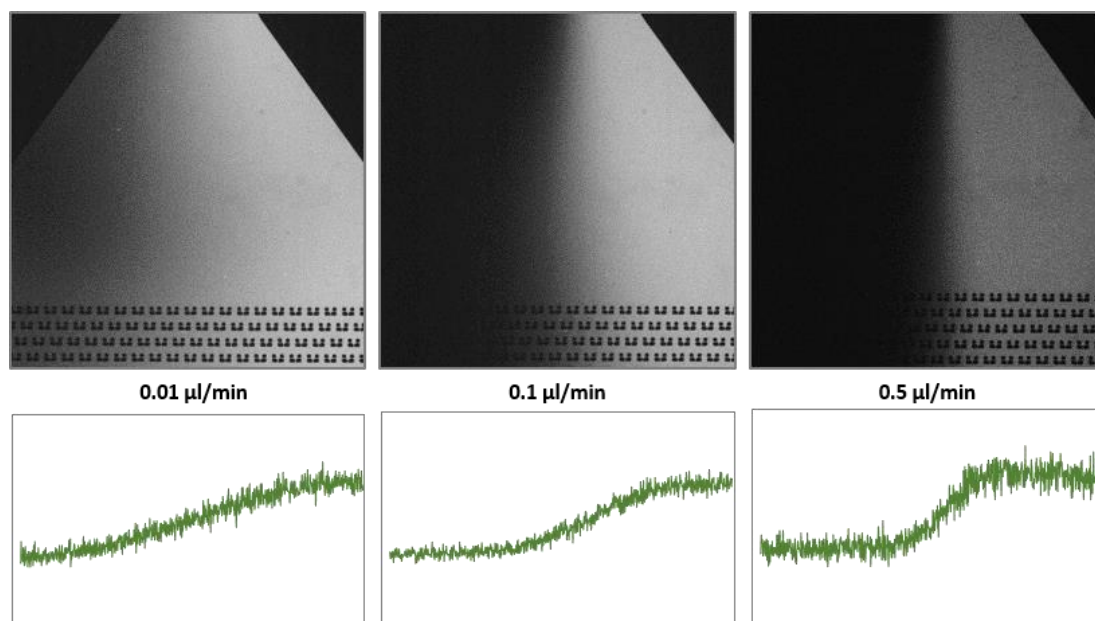
Figure 4.12 The microfluidic device was used to generate fluorescein concentration gradients. Images show fluorescence of the trapping array measured at 488 nm excitation following 5 minutes of constant flow conditions. The flow rate indicated was used in each case for water, on the left inlet, and 100 µM fluorescein, on the right inlet. Intensity profile data corresponds to the line profile obtained between the first and second rows of traps. From the three sets of conditions shown it can be observed that the fluorescein concentration gradient profile was strongly dependent on the flow rate.

When using flow rates below 0.5 µl/min with the current experimental setup, it was verified that the flow was delivered into the device in pulses, rather than continuously. This phenomenon, termed here "pulsatile flow", occurred due to the pumping mechanism in the syringe pumps used, which have a stepper motor that actuates the pumping head in quantised steps. Hence, at such flow rates, when delivering two parallel streams of liquid into the chamber as was done for the fluorescein gradient, it was observed that the interface between the two liquid streams presented an undulating pattern, rather than a straight line. An example of this phenomenon is shown in Figure 4.13, where consecutive fluorescence

microscopy images obtained during fluorescein gradient generation clearly show the pulsatile nature of the flow, revealed by the varying shape of the water/fluorescein interface.
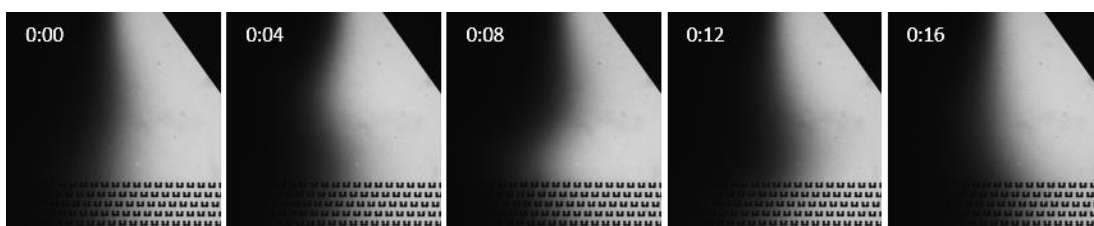
Figure 4.13 Pulsatile flow was observed at low flow rates within the microfluidic chamber. Figure shows a set of fluorescence images obtained consecutively over 16 seconds (time stamp shown in each image) when flowing water through the left-side inlet and a solution of fluorescein through the right-side inlet into the trapping chamber at 0.1 µl/min. Images show that rather than presenting a straight line dividing the two liquid streams, that line is showing an undulating pattern, due to the pulsatile nature of the syringe pumps used.

The pulsatile flow would affect the delivery of nanorods, especially in the middle region of the trap array. Thus, in most instances of gradient generation in these devices, 0.5 µl/min was used to deliver liquids in parallel into the chamber, in order to minimise this effect. This resulted in a compromise between the gradient slope that was possible to achieve and the steady state nature of the gradient, which could be improved either by changing the type of pumps used or the chamber design (as discussed in Chapter 7), or a combination of both. For the purpose of the current work and the proof-of-concept data presented in Chapters 5 and 6, however, these conditions were considered appropriate.

4.4.4   Nanorod gradient

In order to achieve optimal conditions for nanoparticle dispensing into the array of trapped cells, tests were performed with different nanorod coatings and dispensing procedures. The flow of positive and negatively charged nanorods inside the microfluidic device was first tested. For this, NRs with PSS-PDDAC or PSS-PDDAC-PSS coatings in water were loaded into the trapping chamber through one side inlet, while flowing water through the other side inlet. This experiment showed that nanorods, most notably positively charged particles (PSS-PDDAC-coated), adhered strongly to the glass surface of the chamber, as can be observed in Figure 4.14 (a). Additionally, some degree of adsorption to PDMS was also observed. To reduce this unwanted effect, prior to nanoparticle injection, the nanorods were resuspended in serum-containing medium (as opposed to saline buffer) and the microchannels were flushed through with the same solution during cell trapping. This allowed for serum proteins

to passively coat both the device and the nanorod surface, resulting in reduced non-specific adsorption of NRs both to PDMS and the glass surface. However, in the case of PSS-PDDAC-coated particles, as shown in Figure 4.14 (b) and consistently with data shown in section 3.2.3, NRs tended to aggregate and were thus deemed unsuitable for use within the trapping chamber. On the other hand, NRs with PSS-PDDAC-PSS coating showed reduced non-specific adsorption with no detectable aggregation when resuspended in serum-containing medium, and successful gradient generation with these particles was detected using fluorescence microscopy (Figure 4.14 c). This configuration was thus considered to be the most suitable for delivery into the trapping array.
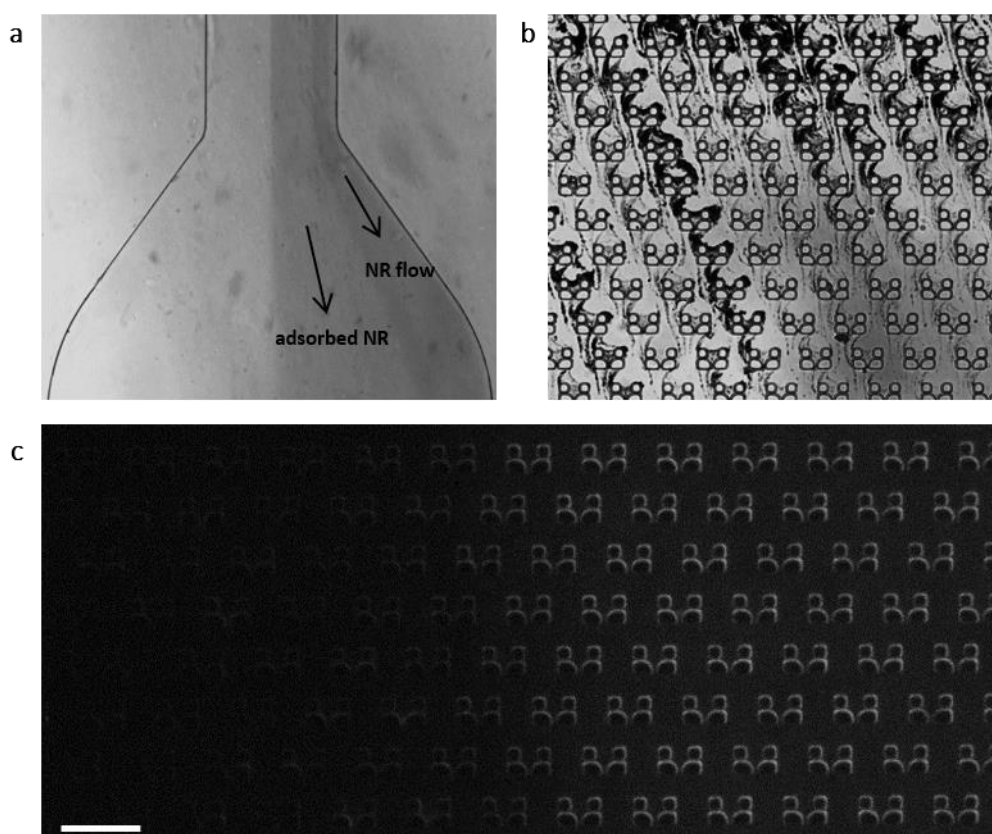
Figure 4.14 Nanorod dispensing into the microfluidic chamber required optimisation. (a) Image of the entrance of the trapping chamber showing a region where PSS-PDDAC-coated NRs have adsorbed to the surface when flowing side-by-side with water, demonstrated by the darker flow of nanorods in a narrower area upon changing of the relative flow rates of the inlets. Additionally, the area covered with rods was not cleared even after 30 minutes of washing the device with water. (b) Image showing notable aggregation of PSS-PDDAC-coated NRs following resuspension in serum-containing culture medium, consistently with data shown in Chapter 3. (c) NR fluorescence (DTDCI) during gradient generation (0.5 µl/min on each side inlet) with PSS-PDDAC-PSS-coated NRs in cRPMI flowing in through the right side inlet. Despite some degree of non-specific adsorption to the sides of the PDMS structures, gradient generation was successful and this was deemed the most suitable coating for use within the microfluidic device.

It is important to note that some degree of non-specific adsorption of nanorods was still observed around the vertical walls of the traps (surfaces perpendicular to the flow direction), as can be seen from the fluorescent outline of the trap structures in Figure 4.14 (c). However, in these cases, negligible signal was measured on the glass and PDMS top/bottom layers. Minimising background noise due to non-specific adsorption of nanorods to the microchannel walls will be fundamental to increase the resolution of detection, therefore this area will require further investigation for improving the performance of this specific microfluidic device/nanoparticle combination. In any case, the optimisation of the nanorod gradient generation procedure provided confidence that the experimental conditions used would permit successful delivery of a range of nanorod concentrations to trapped cells, a feature which will be explored in Chapters 5 and 6.

4.5   Conclusions

This chapter has presented the various optimisation steps involved in the development of a microfluidic platform for trapping, culturing and imaging primary dendritic cells as well as delivering controlled gradients of specific substances, such as nanorod conjugates, to the trapped cells. A number of design considerations were presented in section 4.2, which together with the optimisation of cell loading conditions (section 4.3.2) provided successful cell trapping for real-time single-cell monitoring. Additionally, the laminar flow properties of the microfluidic chamber were explored for controlled delivery of reagents (section 4.4), both experimentally and using computational methods, to achieve consistent nanoparticle delivery. The developed device configuration will be used for real-time monitoring of the interactions of the cells with nanoparticles, for cell uptake assessment using fluorescence and SERS and for viability testing, as presented in Chapter 5, and finally for monitoring of nanoparticle-mediated antigen delivery and processing, as presented in Chapter 6.

Chapter 5

An Integrated Platform for Real-Time, High-Throughput Assessment of Nanoparticle-Cell Interactions

This chapter describes the application of the microfluidic device optimised in Chapter 4 for real-time multimodal imaging of the controlled delivery of custom-developed gold nanorods (developed in Chapter 3) to cells and subsequent functional assessment. Results presented here demonstrate, for the first time, a novel multidisciplinary methodology for the dynamic assessment of the effects produced by different nanorod concentrations on primary cells at the single-cell level and in high-throughput manner using only one device.

5.1 Validation of the integrated platform

In order to achieve the proposed aims and demonstrate the use of the integrated microfluidic platform, it was first essential to assess (i) the suitability of the developed nanoparticles for cell imaging and (ii) the ability to obtain fluorescence and SERRS signals from nanoparticles inside cells trapped within the microfluidic devices. This section presents results obtained from these validation experiments.

5.1.1 Gold nanorods for cell imaging

The design and optical characterisation of the nanorod-dye conjugates used for the microfluidic system validation are described in Figure 5.1. Gold nanorods with a longitudinal plasmon resonance λ_{max} of 765 nm were prepared (section 2.1.1) and conjugated to DTDCI

followed by coating with three polyelectrolyte layers (PSS-PDDAC-PSS). This configuration was deemed the most suitable for nanorod visibility using both SERRS spectroscopy and fluorescence microscopy and for stability in serum-containing environments, as described in Chapter 3, and within the microfluidic chamber, as shown in Chapter 4. Figure 5.1 shows the UV-Visible, SERS and fluorescence behaviour of this batch of nanorods, which remained stable for >12 months. These gold nanorods were used to assess cell-nanoparticle interactions off-chip and on-chip and results are presented in the following sections. Throughout this chapter, as well as Chapter 6, "nanorods" or "NRs" will refer to gold nanorods with incorporated DTDCI and PSS-PDDAC-PSS coating, unless specifically stated otherwise.
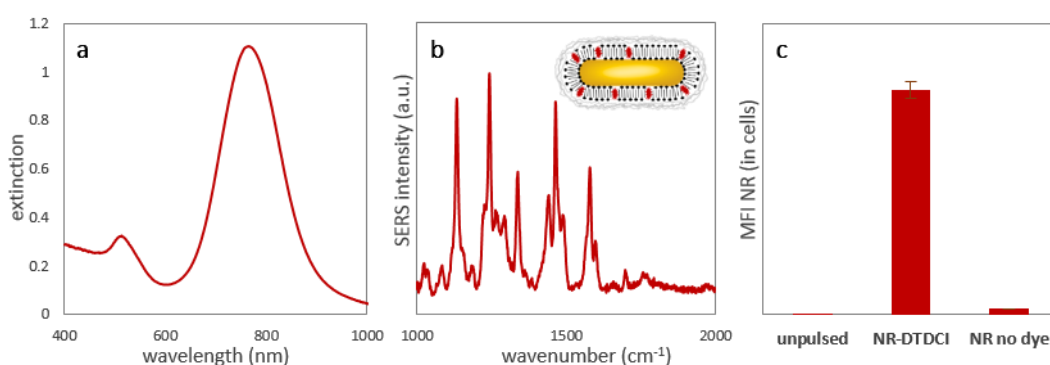
Figure 5.1 Gold nanorods were optimised for use within the microfluidic device. (a) UV-Visible spectrum of nanorods used in this chapter, with longitudinal λ_{max}=765 nm. (b) Representative SERRS spectrum (background corrected) of a colloidal solution of the polymer wrapped NR-DTDCI conjugates (633 nm excitation) with the schematic insert showing encapsulation of the reporter dye into the surrounding surfactant bilayer and 3-layer polyelectrolyte wrapping. (c) Intrinsic fluorescence of DTDCI-containing NRs following uptake by dendritic cells (633 nm excitation) as measured by flow cytometry and compared to unpulsed cells or cells incubated with non-dye containing NRs. Data is mean ± s.d. of triplicate samples.

5.1.2   Off-chip assessment of nanorod-cell interactions

In order to initially evaluate the interactions of nanorods with cells, off-chip testing was performed using standard techniques, which are presented in this section. Specifically, flow cytometry and confocal microscopy were used to study nanoparticle uptake, assessing concentration and time dependence of these interactions as well as checking whether the nanoparticles were reaching the inside of the cell rather than attaching to the cell membrane. Primary dendritic cells (section 2.2.2) were used for all the experiments, as these cells are privileged models for investigating the basic functions of the immune system,[36-38,192] an advantageous feature to the overall aims of the project, specifically nanovaccine delivery

testing, as will be further explored in Chapter 6. Additionally, dendritic cells are known to readily internalise pathogens and foreign materials,[36] which indicates that nanoparticle uptake and nanoparticle-mediated delivery of biomolecules can be achieved. This section presents representative results for these experiments as a baseline for the subsequent validation of the microfluidic platform for high-throughput screening of nanorod-cell interactions.

To assess uptake of nanorods by dendritic cells in static conditions (*i.e.* under zero flow), cells were first incubated in a 24-well plate with different concentrations of nanorods (0.01 pM – 100 pM). NR uptake was quantified after 2, 6 and 24 hours, using flow cytometry to determine the mean fluorescence intensity (Figure 5.2 a). As expected, flow cytometry data showed that nanorod uptake directly correlated with both the time of exposure and particle concentration used, demonstrating that the cells readily internalised DTDCI-containing nanorods. Subsequently, a more detailed assessment of time dependence was performed, in order to evaluate nanorod uptake in the early stages of exposure. For this, cells were incubated in a 24-well plate with 10 pM of the same NRs and uptake quantified every 15 minutes for a total of 90 minutes using flow cytometry (Figure 5.2 b).
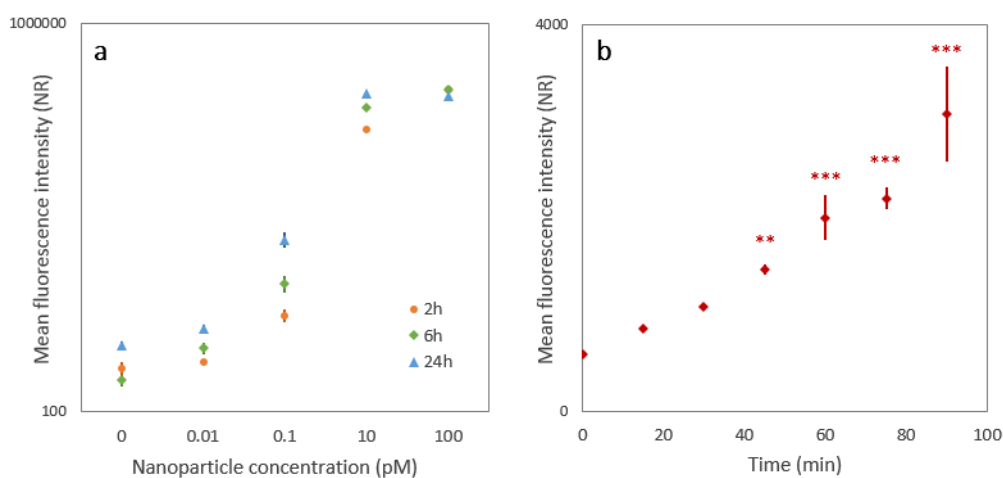
Figure 5.2 Dose and time dependence of nanorod uptake by dendritic cells was assessed using flow cytometry. (a) Cells were incubated in static condition with different nanoparticle concentrations and the fluorescence intensity at 633 nm excitation was obtained at different time points using a flow cytometer. The graph shows the average of duplicate samples for each condition (10,000 events each sample), with error bars representing standard deviation. (The plateau seen for 100 pM corresponds to the saturation of the detectors in the flow cytometer for that condition.) (b) Graph showing the MFI value for cell samples exposed to nanorods for increasing amounts of time measured using flow cytometry (10,000 events each sample). Data shown is mean ± s.d. of technical triplicates, with significant differences to the t0 sample determined by one-way analysis of variance with Tukey test (**p<0.01, ***p<0.001).

The flow cytometry data shown in Figure 5.2 (b) indicated that NR uptake was a rapid process, with an increase in fluorescence compared to the background (zero minutes) being detectable from as early as 15 minutes of exposure (not statistically significant) and a significant increase detectable from 45 minutes. It is interesting to note that the standard deviation increased notably with time as well, as the heterogeneity of the cell sample led to a greater variance in the fluorescence values due to differences in uptake. Subsequently, confocal fluorescence imaging of dendritic cells exposed to even lower concentrations of NRs (0.1 pM – Figure 5.3) provided confirmation that the nanorods were located within the cell as opposed to attached to the outer membrane, which will be important for delivery applications.
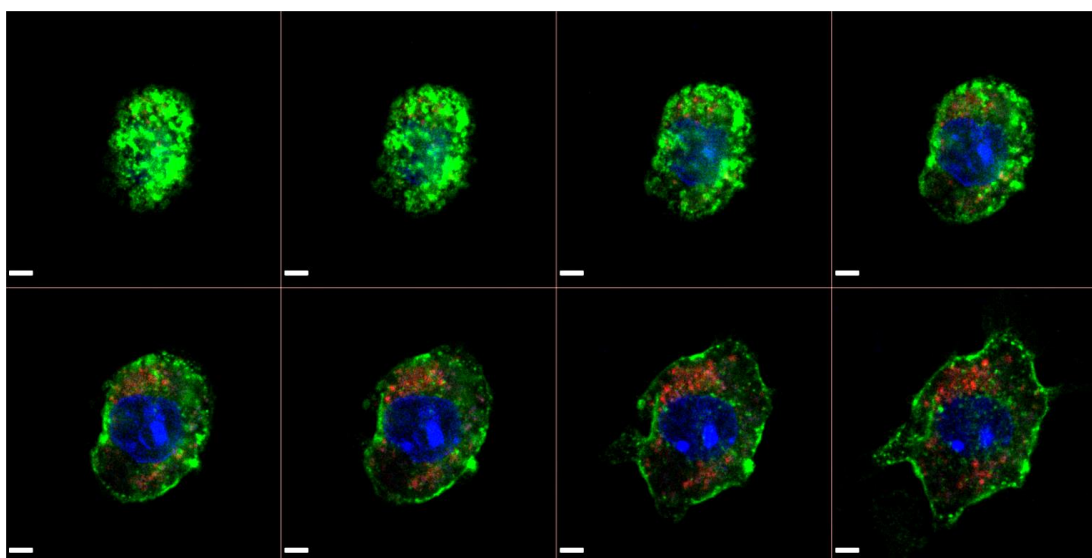
Figure 5.3 Nanorod internalisation was confirmed using confocal microscopy. Composite confocal fluorescence z-stack images (2 μm steps) of a fixed dendritic cell which has been exposed to 0.1 pM NRs conjugates for 2 h. Cholera-toxin-B staining is used to identify the cell membrane (green), DAPI for the nucleus (blue) and NR fluorescence (from DTDCI) is shown in red. Images shown confirm NR internalisation. Scale bar = 4 μm.

It was observed that in these experiments, performed in bulk cell-culture plates, nanorods sedimented to the bottom of the plate shortly after particle injection into the well, consistently with previous reports.[22,212] Thus, it is reasonable to assume that the degree of nanoparticle uptake by cells depended mostly on their level of activity or motility within the plate, with the most motile cells internalising nanomaterial at a greater rate than stationary or less motile cells. Additionally, bright-field time-lapse imaging showed (Figure 5.4) that

dendritic cells took up nanoparticles indefinitely as long as they were within their reach, which could have an impact on the overall dose received (section 5.1.3).
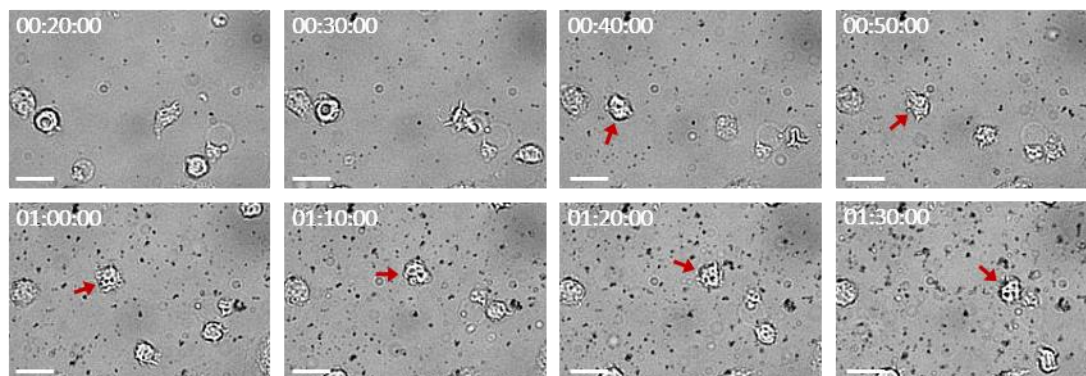
Figure 5.4 Dendritic cells move within the well to internalise sedimented nanorods. Dendritic cells were plated at 5×10^5 cells/ml into 50 μL cell culture dishes before adding 100 pM nanorods. Images were acquired at 30 s intervals for 2 h, with images shown shown representing 20 to 90 minutes after addition of NRs, as indicated in each panel. The red arrow indicates one example of a cell that was very actively taking up nanorods that had sedimented to the bottom surface of the well. Scale bar is 50 μm.

It is important to note that, in this case, the nanorods used had only a 2-layer coating (PSS-PDDAC) which was not very stable in cell culture medium (Chapter 3), as can be confirmed from the occurrence of aggregates in the image. In any case, the main point to be made here is that dynamic information on the interaction of cells with nanoparticles cannot be extracted from flow cytometry analysis such as that in Figure 5.2, while time-lapse imaging such as that shown in Figure 5.4 is not enough to get statistically relevant data. This reiterates the need for new tools that enable real-time analysis at the single-cell level with higher throughput.

5.1.3 Toxicity studies of nanorod formulations

Having observed, in the previous section, that dendritic cells internalised nanorods, it was important to evaluate their biocompatibility. Thus, dendritic cells were exposed to different concentrations of nanorods, as well as camptothecin (CAM), to induce apoptosis, and permeabilisation buffer (Perm), to induce necrosis. Samples were incubated for different periods of time and gold nanorod toxicity assessed using Annexin-V FITC and Propidium Iodide staining. Figure 5.5 shows a representative set of data obtained for a range of nanoparticle concentrations following 6 h (a) and 24 h (b) incubations. To improve clarity of presentation, cells were gated according to fluorescence intensity above background for Annexin-V only (early apoptosis), Propidium Iodide only (necrosis), or both dyes (late

apoptosis). Nanorods showed good biocompatibility in most conditions, when compared to the positive controls.
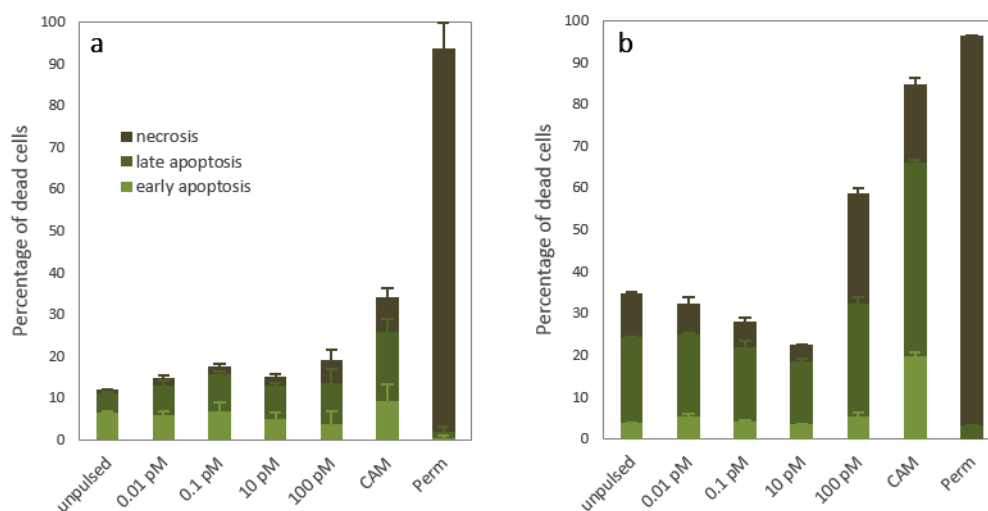
Figure 5.5 Gold nanorods showed good biocompatibility when incubated with dendritic cells off-chip. Flow cytometry data following (a) 6 h and (b) 24 h exposure of dendritic cells to discrete NR concentrations between 0.01-100 pM, as well as to camptothecin (CAM – apoptosis inducer) and permeabilisation buffer (Perm). "unpulsed" represents a negative control with no stimulation of the dendritic cells. Graph shows the percentage of cells undergoing early apoptosis (Annexin-V+/PI-), late apoptosis (Annexin-V+/PI+) and necrosis (Annexin-V-/PI+). Data shown is the average of duplicate samples ± standard error of the mean (s.e.m.).

From the data it could be noted that, whilst at the later time point (Figure 5.5 b) the highest concentration of nanorods tested (100 pM) did show some level of toxicity, cells exposed for a few hours or to lower doses showed high levels of viability relative to controls. However, it is important to note that nanorods were left in the cell solution for 24 h which, as discussed in the previous section, could lead to overaccumulation of nanorods within the cells. Overall, off-chip data indicated that not only were the nanorods quickly internalised by the dendritic cells, they were also detectable using fluorescence and were not cytotoxic.

5.1.4   Nanorod fluorescence within trapped cells

From the data shown so far in this chapter, it was observed that conventional techniques show limitations in simultaneously providing dynamic information and statistically relevant data at the single-cell level. Additionally, data obtained was from end-point measurements of separate cell wells, lacking the assessment of the same population of cells over different times and concentrations of nanoparticles. As shown in Chapter 4, one key feature of the developed microfluidic system was the ability to deliver a gradient of concentrations of

nanoparticles to the array of trapped cells, so that the effect of exposure to different concentrations could be assessed within the same device, on the same sample of cells and under the same environmental conditions. Successful NR gradient generation was previously shown in section 4.4.4. Here, as an initial validation experiment, it was important to assess whether cells on different sides of the array would show different levels of fluorescence following exposure to a gradient of NR concentrations. Thus, dendritic cells were trapped in the microfluidic device and a NR suspension was delivered onto the array to establish the dose gradient defined in section 4.4.4. Having demonstrated that internalisation of NRs was a rapid process (Figure 5.2), fluorescence images were acquired after 2 hours of exposure to nanoparticles and representative images are shown in Figure 5.6.
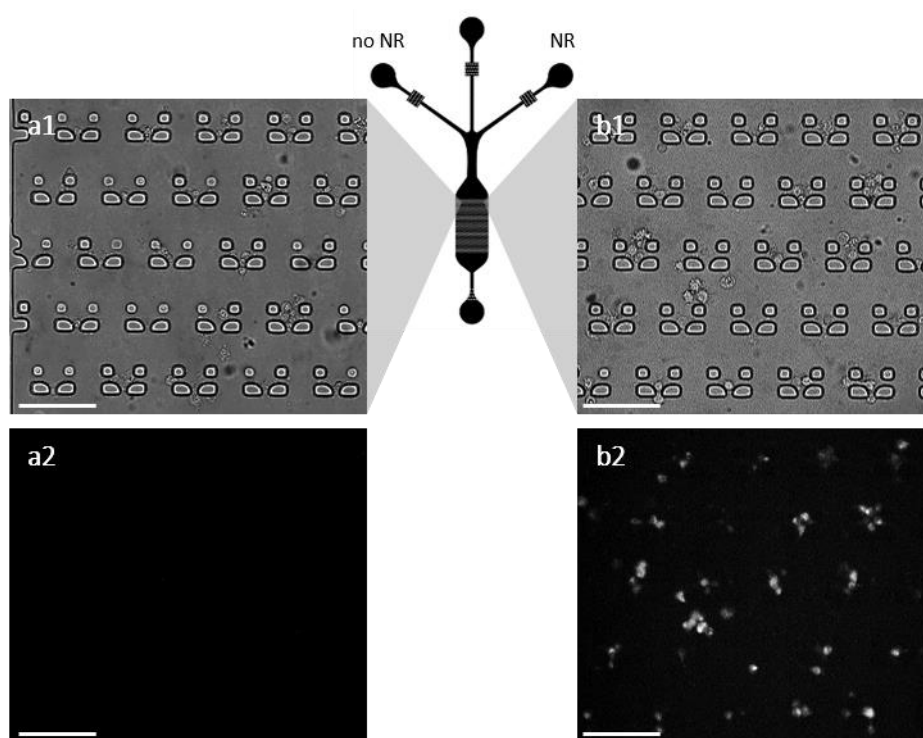
Figure 5.6 Cells in regions of low/high concentration of nanorods showed corresponding fluorescence after 2 h. Dendritic cells were loaded into the microfluidic array and subsequently exposed to a gradient of NR concentrations (0-500 pM) for 2 h. Images were obtained for the two extremities of the trapping array, where no NRs were delivered (a1-brightfield, a2-NR fluorescence) and where the highest concentration of NR was delivered (b1-brightfield, b2-NR fluorescence). NR fluorescence was measured using 100 ms exposure time. Scale bars are 100 μm.

As predicted, results show that cells on the side of the array where NR concentration was zero displayed no fluorescence in the NR channel (Figure 5.6 a), while cells on the opposite side of the array, where NR concentration was at its highest (~500 pM), showed visible

fluorescence within most cells (Figure 5.6 b). This indicated that, as expected, cells exposed to high concentrations of NRs became fluorescent, while cells exposed to no NRs did not, under the same conditions and within the same microfluidic chamber, and showed that these differences could be monitored in real-time.

5.1.5   Confocal fluorescence imaging

As part of the development of the cell imaging platform, it was important to evaluate the possibility to go from high-throughput single-cell analysis down to intracellular imaging within the same device. For this, cells that had been trapped and exposed to NRs within the microfluidic device as above were fixed, perfused with mounting medium (section 2.6.5) and confocal fluorescence microscopy was performed in order to obtain images of the delivered NRs at subcellular level. Confocal microscopy was used for increased resolution in the z-direction, reducing noise resulting from fluorescence coming from different areas of the cell. Results showed that NR fluorescence could be detected within the trapped cell in highly localised areas (Figure 5.7), indicating the potential of the microfluidic platform for higher resolution cellular imaging, such as to assess uptake pathways and nanoparticle-mediated drug delivery mechanisms.
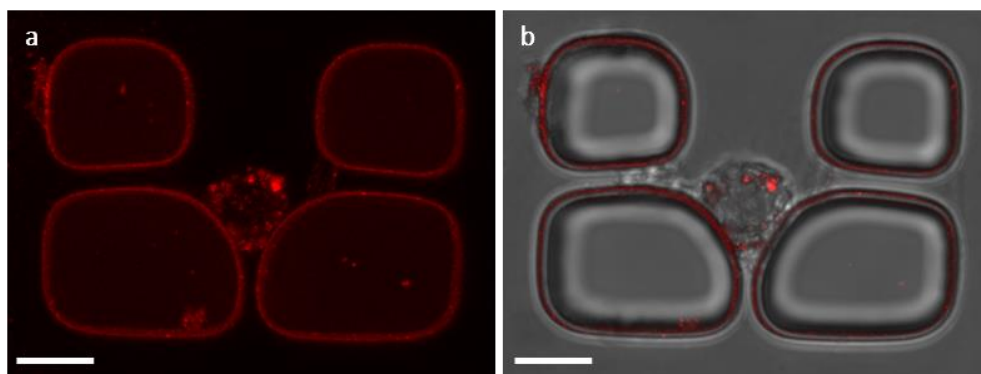
Figure 5.7 Intracellular nanoparticle signal identification was achieved using confocal fluorescence. Dendritic cells were loaded into microfluidic devices and exposed to NRs as above. Subsequently, the cell array was fixed and perfused with mounting medium for imaging by confocal microscopy. (a) Confocal fluorescence image of a trapped dendritic cell showing NR fluorescence at 633 nm excitation. (b) Composite confocal bright-field and fluorescence image of the same cell. Scale bars are 10 μm.

5.1.6   SERRS signal from trapped cells

As mentioned in Chapter 3, SERRS spectroscopy is a highly specific technique that can be used for real-time nanoparticle identification,[42] with potential for single-nanoparticle

intracellular tracking and biomolecule delivery monitoring at the molecular level.[64,133] Within the scope of the current work, this technique would be interesting for providing complementary data on nanorod location and, with its high specificity, to potentially provide information on surface modifications from intracellular particles, either resulting from changes in the protein corona or from the delivery of conjugated molecules. Here, an initial experiment was devised to assess the possibility of obtaining specific SERRS data from intracellular NRs in cells trapped within the microfluidic device. For this, cells were trapped, exposed to NRs for 2 hours and then fixed, as described in section 2.6.5. Subsequently, SERRS spectra were acquired from a trapped cell and from the PDMS surface of the same microfluidic device where there were no cells (Figure 5.8). Control spectra were obtained from the NR suspension (solution-based) and from PDMS only.
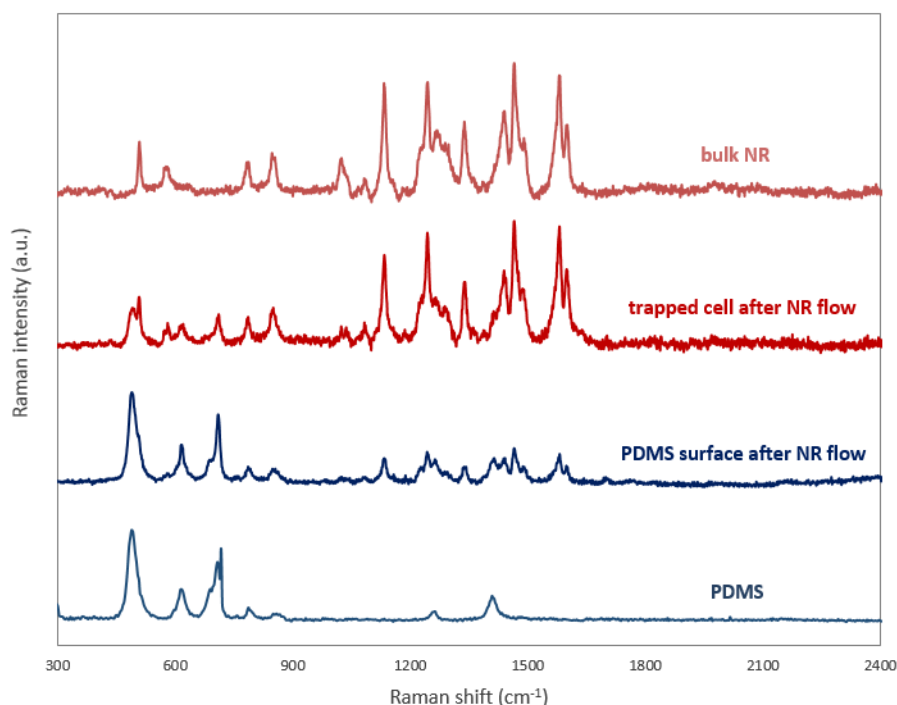
Figure 5.8 Specific intracellular nanoparticle signal identification was obtained using SERRS. Representative SERRS spectra obtained at 633 nm excitation (from top to bottom): bulk NR suspension, trapped cell after NR uptake, PDMS surface in the vicinity of the trapped cell and a representative Raman spectrum for PDMS only, acquired separately. The PDMS Raman spectrum intensity has been amplified for clarity. The traces show the relative location of specific peaks for NRs and PDMS as well as their relative intensity for each condition.

Results showed a background SERS signal from the PDMS surface of the microfluidic device following NR exposure, corresponding to the characteristic PDMS spectrum combined with some degree of non-specific adsorption of NRs. However, the spectral intensity associated

with intracellular nanorods was over four times brighter than that of the background, for the same device and under identical acquisition conditions (633 nm excitation, 10 s integration time). Additionally, data obtained indicated that SERRS maps could be generated at a spectral region (1560-1620 cm^{-1}) containing specific DTDCI peaks which would be clearly distinct from nearby PDMS Raman peaks at ~1261 and ~1410 cm^{-1}, allowing for specific NR localisation to be acquired with negligible interference of the PDMS background. Importantly, the optical brightness of the NR tags was such that, at the incident laser powers used, there was a negligible background Raman signal from the cell itself. Overall, data obtained suggested that SERRS could be used within the device to measure NR uptake by cells and that the signal could be mapped, to provide data on the intracellular localisation of NRs. The use of the microfluidic device was therefore shown to be compatible with a range of microscopies and spectroscopies, allowing for both high-throughput assessment of the array of trapped cells and higher resolution imaging of intracellular nanoparticles at the single-cell level.

5.2   Real-time assessment of nanoparticle-cell interactions

Suitable conditions for on-chip cell injection and culture were identified and the spectral properties of the functionalised gold nanorods were characterised separately in previous chapters. Following the validation experiments presented earlier in this chapter, this section presents the application of the developed microfluidic platform as a high-throughput tool for (i) the dynamic assessment of nanorod uptake, over a range of concentrations, and (ii) the consequent changes in cell function and viability over time, at the single-cell level.

5.2.1   Dynamic monitoring of nanorod uptake by trapped cells

Obtaining information on the dynamics of nanoparticle uptake and subsequent cellular processing is paramount when investigating cell responses, as the complexity of cell function is dictated by underlying dynamic processes[206] and uptake pathways can strongly influence functional outcomes.[88,91] It was previously shown in section 5.1.2 that nanorod uptake showed a strong time dependence (Figure 5.2 b). Here, nanorods were delivered to the microfluidic chamber with trapped cells while real-time assessment of nanorod delivery and subsequent uptake was performed using time-lapse fluorescence microscopy. Specifically, for these experiments, cells were loaded into the trapping chamber as before and a nanorod concentration gradient (from 0 pM to ~440 pM) was delivered across the width of the array for 120 minutes (section 2.6.5). This process was monitored via time-lapse fluorescence

113

microscopy (Figure 5.9 a) and the kinetics of nanorod uptake by cells was qualitatively assessed by tracking the fluorescence signal of single-cells over time, in a region of approximately constant nanoparticle concentration within the array (Figure 5.9 b).
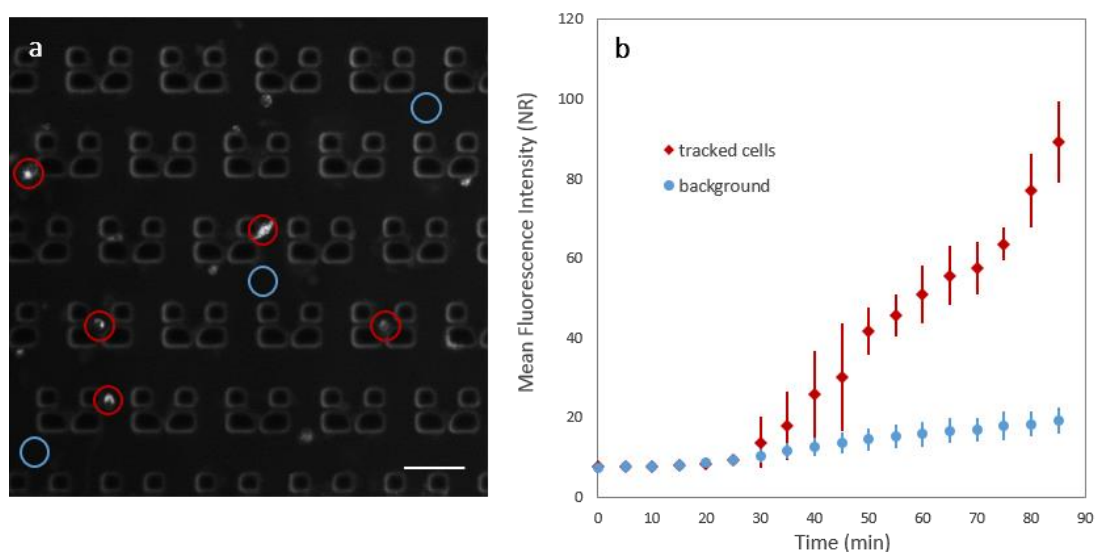
Figure 5.9 Nanorod uptake by cells in the microfluidic device was qualitatively estimated by monitoring the increase in fluorescence intensity over time. Dendritic cells were loaded into the array chamber and NRs delivered at 0.2 μl/min. Time-lapse fluorescence (excitation 633 nm; emission >650 nm) imaging was acquired at 1 frame/min for 90 minutes. (a) Image showing fluorescence of five tracked cells (red circles) and three tracked background areas (blue circles) during NR delivery. Scale bar = 50 μm. (b) Graph showing the temporal progression of the average mean fluorescence intensity (MFI) value of the three background regions and of the five cells tracked from (a), with t = 0 being the beginning of NR delivery. Error bars represent standard deviation.

It can be noted from Figure 5.9 (b) that there was an initial delay of the fluorescent signal (0-15 minutes), which corresponded to a lag time between activation of the flow of nanorods and their presence in the array due to the compliance of the system (syringe-PDMS). Subsequently, as expected, the fluorescence intensity of the tracked cells increased progressively over time. Whilst a clear increase in background signal, due to non-specific adsorption, was also detected (as discussed in Chapter 4), this was of significantly lower magnitude than fluorescence associated with nanorod uptake in single-cells. From this data, it could also be observed that whilst there was some degree of cell-to-cell variability, there was a clear time-dependent nanoparticle uptake by dendritic cells cultured on the device. This early uptake of nanorods by dendritic cells had also been assessed in static conditions (section 5.1.2) and the results were qualitatively compared to the microfluidic experiments. As expected, nanorod uptake directly correlated with the time of exposure for both on and

off-chip experiments, demonstrating that the cells readily internalised DTDCI-containing, polymer-wrapped nanorods. Confocal fluorescence imaging of the cells had also shown internalization of the nanorods (Figure 5.3). Overall, the data obtained with the microfluidic device has shown that this platform could be used for providing data on nanorod uptake in a similar way to conventional methods, while allowing for information to be obtained in real-time and at the single-cell level. This shows the ability of the setup used for longer-term dynamic studies of nanoparticle internalisation and processing.

5.2.2   Effect of flow rate in nanorod uptake

Given the differences in flow rate obtained inside and outside the microtraps with the design used (section 4.2.4), and from NR uptake fluorescence data such as that shown in Figure 5.9 (a), it was hypothesised that cells adhering to the outside of the traps and consequently exposed to the higher flow rates could take up nanoparticles more effectively than cells located within the traps, where flow rates were an order of magnitude lower. Thus, in order to evaluate this hypothesis, it was necessary to assess whether NR uptake would be influenced by the magnitude of the flow rate (and corresponding shear stress) that the cells were subject to, according to their location relative to the trapping structures. For this, the fluorescence intensity of single-cells located inside and outside traps in a region of approximately constant NR concentration was measured in five different experiments, to evaluate whether there were any significant differences between the values obtained.

Results (Figure 5.10) showed that NR uptake was comparable between cells inside and outside the traps in all experiments, with no significant differences being detected even with the flow velocity being one order of magnitude lower inside. Also, fluorescence intensity was found to be comparable across experiments, demonstrating the reproducibility of the NR delivery procedure, with slightly higher fluorescence being obtained only in an experiment where the NR flow rate was higher.
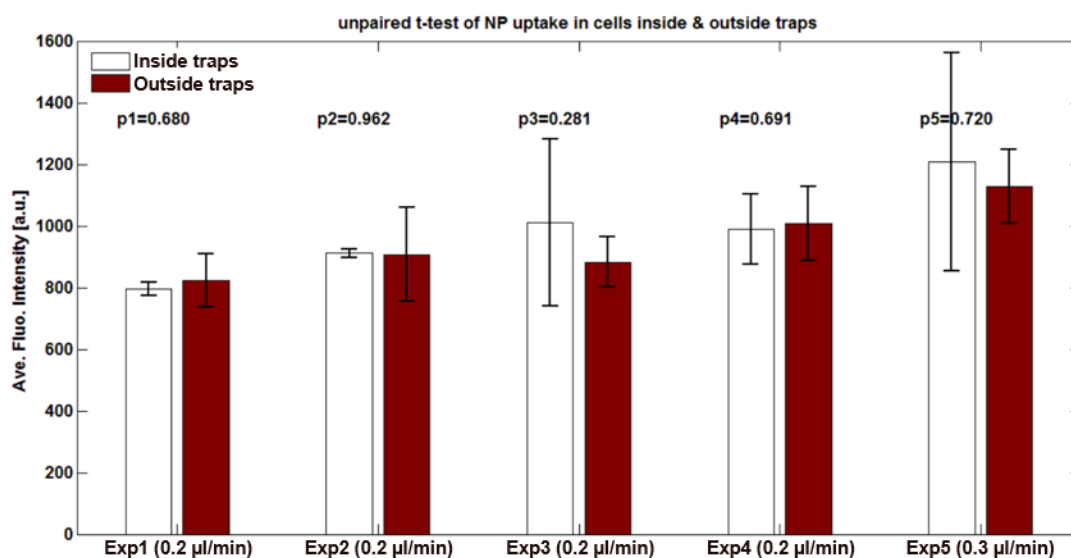
Figure 5.10 Cells inside and outside traps showed similar degrees of uptake, despite exposure to different flow velocities. The mean fluorescence intensity of cells due to NR uptake was compared for cells inside or outside the microfluidic traps during NR delivery on-chip (N between 4 and 9 for each condition), across five separate experiments (p-values shown are from unpaired t-tests between cells inside and outside traps).

5.2.3   High-throughput nanomaterial toxicity testing

As mentioned in Chapter 1, there are currently many limitations to the consistent screening of nanomaterials for biomedical applications. Specifically, there is a lack of high-throughput tools for nanotoxicity testing, and while lab-on-a-chip presents a number of opportunities for this purpose, these have to date not been successfully applied.[17,23,51] Having shown above that dead cell staining could be achieved on-chip (section 4.3.6) and that trapped cells could be monitored in real-time using fluorescence time-lapse imaging (section 5.2.1), the device was then used to investigate the cytotoxic effects of the nanorods to dendritic cells, in high-throughput. For this, experiments were carried out using cell death indicator dyes (FITC-conjugated Annexin-V for apoptosis and Sytox Blue for necrosis), and results from cells in the microfluidic device were compared to those obtained from flow cytometry where cells were exposed to different concentrations of nanoparticles in standard cell culture plates (section 5.1.3). Initially, as a positive control, a gradient of 10% to 0% isopropanol was applied across the trapped cells. After staining, this resulted in a corresponding gradient of fluorescence intensities for markers of both apoptosis and necrosis across the width of the array, confirming the applicability of the microfluidic device to detect cell viability (Figure 5.11).
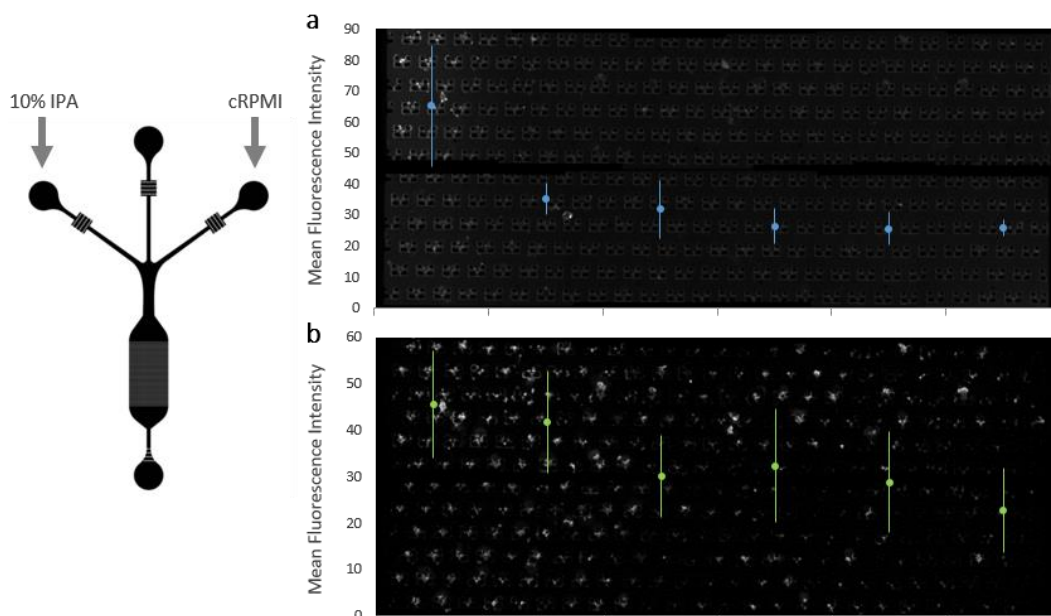
Figure 5.11 Cell death was induced and measured within the microfluidic device. Cells were exposed to a gradient of 10% IPA for 90 minutes and then stained with Sytox Blue and Annexin-V FITC. (a) Overlay of the average mean fluorescence intensity for each of 6 slices of the microfluidic array with the fluorescence picture of Sytox Blue staining from which these values were obtained. (b) Overlay of the average mean fluorescence intensity for each of 6 slices of the microfluidic array with the fluorescence picture of Annexin-V FITC staining from which these values were obtained.

Subsequently, to assess nanoparticle toxicity, trapped cells in two devices were simultaneously exposed to NR concentration gradients for 2 hours before labelling with Annexin-V FITC and Sytox Blue either immediately or following an overnight incubation (with continuous medium perfusion). Images of the same area of the array were obtained before NR delivery, immediately after NR delivery and after the overnight incubation. Following staining, cells were fixed, perfused with DAPI-containing mounting medium and imaged again. These images were then used to determine the mean fluorescence intensity of viability dye-staining in all DAPI-positive cells across the full width of the device (Figure 5.12 a-b). Parallel experiments analysed bulk populations of cells exposed to similar nanoparticle concentrations using flow cytometry (Figure 5.12 c-d). These results showed that the NR formulation used did not induce significant cell death at the concentrations analysed even after 24 h exposure, and validated the applicability of the developed microfluidic device for monitoring both nanoparticle uptake and cell viability and function. Typically, due to current setup limitations, only half of the device chamber could be continuously monitored, leading to approximately 400 single cells to be analysed per device. In any case, the data obtained

showed the high-throughput capabilities of the platform for assessment of nanoparticle-cell interactions.
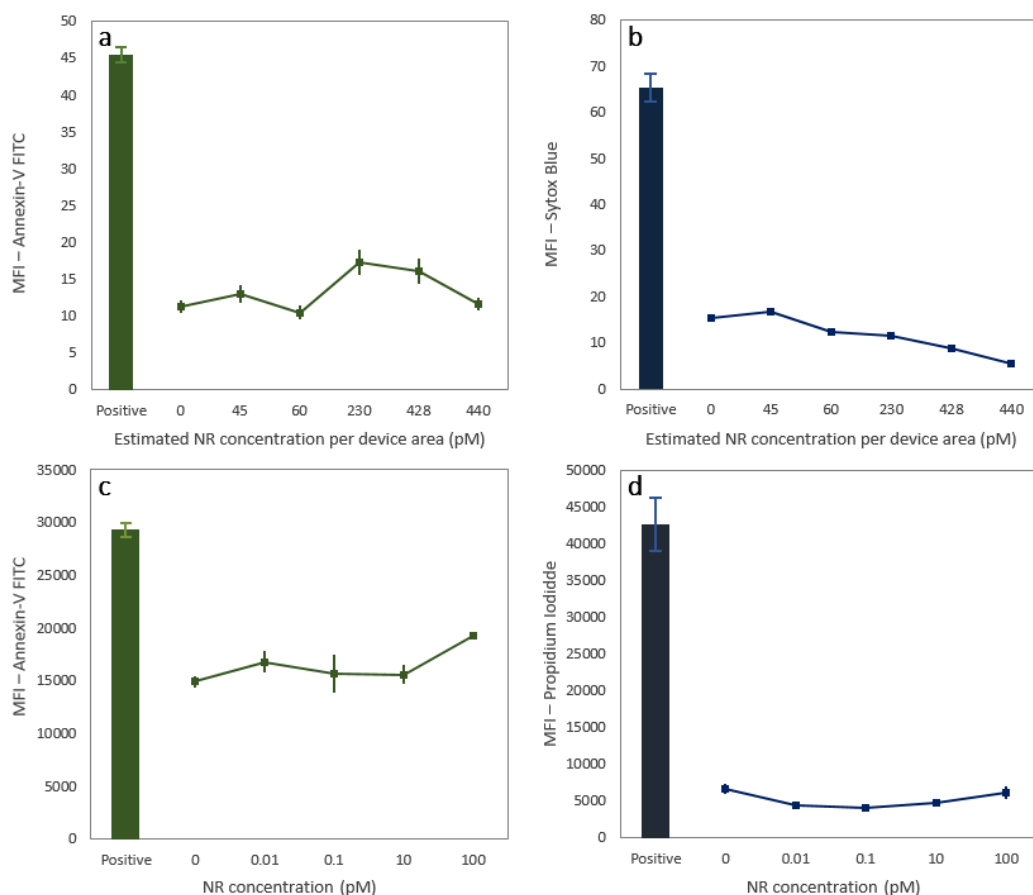
Figure 5.12 Nanoparticle toxicity analysis was performed in the microfluidic chamber. (a-b) Mean fluorescence intensity (MFI) of Annexin-V FITC (a) and Sytox Blue (b) as measured from fluorescence microscopy images of dendritic cells exposed to a gradient of nanoparticle doses and stained 24 h after 2 h of nanoparticle exposure within microfluidic devices. Data was obtained for six contiguous fields of view across the full width of the trapping array. Positive control samples were exposed to isopropanol to induce cell death (Figure 5.11). Each data point shows the mean ± s.e.m of between 56 and 99 cells per field of view, with the estimated NR concentration calculated from the average NR MFI in the same cells based on a maximum concentration of 440 pM. (c-d) MFI of Annexin-V FITC (c) and Propidium Iodide (d) from flow cytometry of cells exposed to the indicated nanoparticle concentrations, compared to the corresponding positive controls, as in Figure 5.5. Data points are mean ±s.e.m. of triplicate samples.

A further confirmation of the lack of toxic effects due to incubation with NRs was obtained by monitoring the trapped cells via time-lapse imaging before, during and immediately after nanoparticle exposure, as well as after overnight incubation of the cells in microfluidics using brightfield microscopy. Results revealed comparable cell activity in all cases, further supporting that cell function and viability was not compromised by NR uptake.

5.2.4 Multimodal imaging of nanoparticles in trapped cells

In previous sections it has been shown that, under the controlled laminar flow conditions provided by microfluidics, fluorescence microscopy could be used to assess NR uptake without requiring additional surface functionalisation with fluorescent probes. This highlights the potential of this system to integrate multimodal imaging capabilities. Additionally, it was also shown earlier in this chapter that SERRS signals could be successfully identified from NRs within trapped cells (Figure 5.8). In this section, the possibility of obtaining SERRS mapping data across the microfluidic array following delivery of a NR concentration gradient was investigated. As above, cells were trapped and the delivery and uptake of a range of concentrations of nanorods across the width of the trap array chamber was first confirmed using live-cell epifluorescence microscopy (Figure 5.13 a-b). Subsequently, cells were fixed and imaged using SERRS confocal mapping. In order for data from both imaging procedures to be compared, cells were mapped based on their individually-addressable position on the array (Figure 5.13 c-e). The SERRS maps obtained showed intracellular NR signal provided further means of spatially identifying non-specific adsorption of nanorods to the walls of the PDMS traps (Figure 5.13 d). Additionally, the magnitude of DTDCI-specific SERRS peaks (arrows in Figure 5.13 e) followed qualitatively the same increasing trend observed with fluorescence microscopy. This correlation between the fluorescence and SERRS measurements of nanoparticle uptake indicated that the developed platform is amenable to applying more than one imaging modality for the real-time monitoring of nanoparticle-cell interactions, along with particle intracellular distribution.
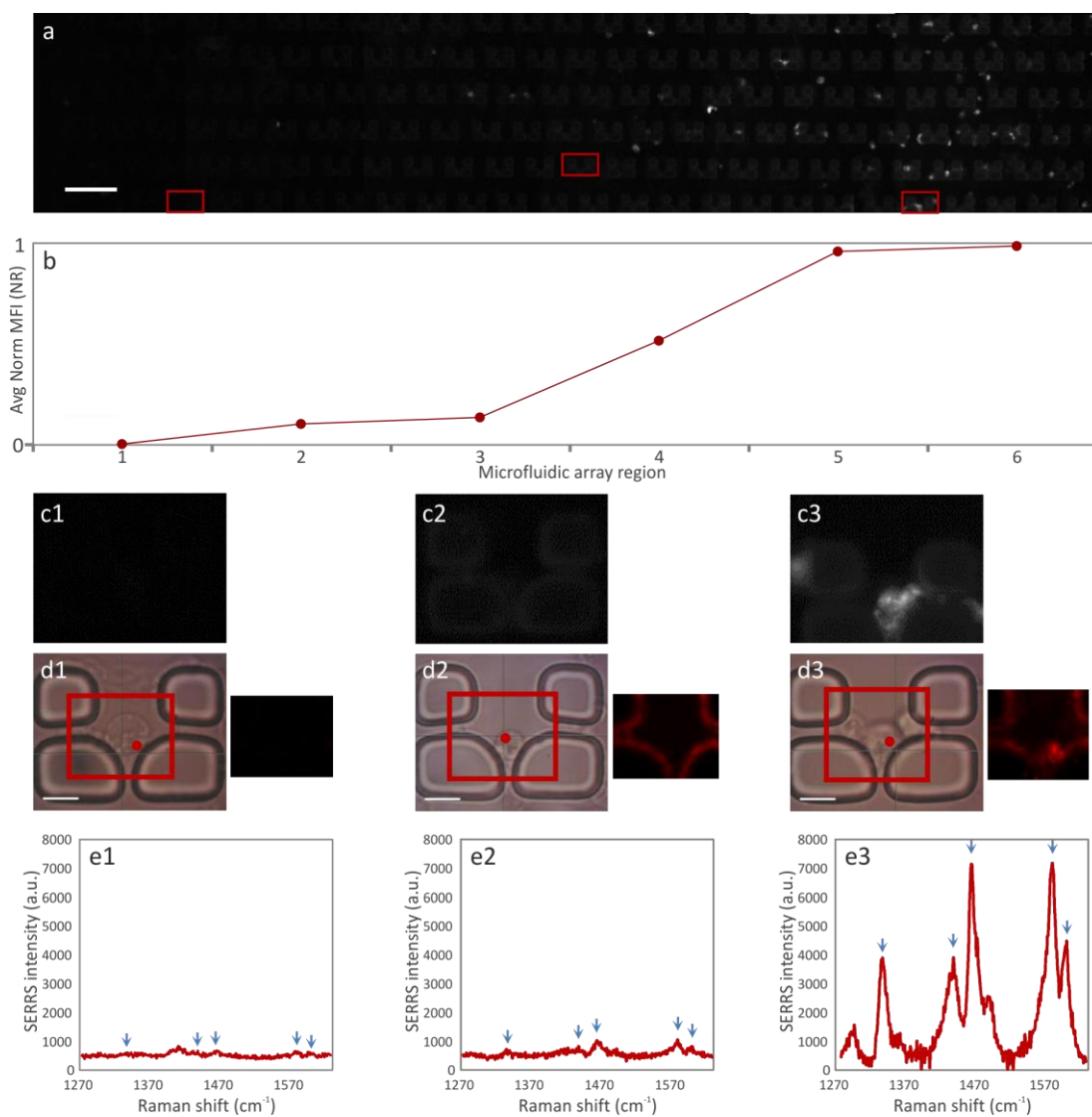
Figure 5.13 Multimodal imaging demonstrated nanoparticle uptake by cells trapped within a microfluidic device. (a) Composite (tiled) fluorescent image of the width of the array chamber. Scale bar = 100 μm. (b) Representative normalised values of the average MFI of nanoparticles inside cells after nanorod delivery (red points). This was obtained by defining six array regions (along x axis) across the width of the trap array and averaging the nanorod MFI from within all the cells in each region. Cells were identified via DAPI staining of the nucleus. (c1-3) Representative fluorescence images of single trapped cells (highlighted with a red square in (a)) in regions of low, medium and high nanoparticle concentration areas spanning the width of the microfluidic array, and (d1-3) corresponding bright-field images and graphic maps of DTDCI-specific SERRS signal intensity (measured in the 1560-1620 cm^{-1} region) of the same cells following fixation. Scale bar = 10 μm. (e1-3) SERRS spectra (background corrected) obtained as indicated by the red dot in the respective bright-field images, corresponding to the highest intensity signal from within each trapped cell. The arrows indicate the position of DTDCI-specific peaks.

5.3 Conclusions

Results presented in this chapter show the applicability of the developed microfluidic system for trapping and maintaining primary dendritic cells, followed by controlled delivery of concentration gradients of highly specific, biocompatible and stable nanorod probes and simultaneous multimodal imaging. Real-time assessment of nanoparticle uptake was achieved using time-lapse fluorescence microscopy (section 5.2.1), showing that the uptake followed a consistent trend, proportional to the time of exposure to nanoparticle flow without affecting cell motility and comparable with results obtained by flow cytometry for cells exposed to nanoparticles for the same period of time. Additionally, the ability to obtain dynamic information on different fluorescent readouts simultaneously, such as viability dyes, was demonstrated in section 5.2.3. These features allowed for the direct investigation at the single-cell level of the effects of different nanoparticle concentrations on hundreds of cells using just one microfluidic device. Importantly, in addition to delivering nanorods at different concentrations simultaneously, the microfluidic procedure ensured that nanoparticles were in contact with cells only for a defined amount of time. Subsequent SERRS mapping (section 5.2.4) provided consistency between the intracellular nanoparticle signal, the fluorescence signal and the distribution of nanoparticles across the width of the microfluidic array, providing proof-of-principle of successful multimodal imaging within the microfluidic system. So far, no reports have been found of microfluidic systems with these combined functionalities.[17,23,51]

Chapter 6

Dynamic Assessment of Nanoparticle-Mediated Antigen Delivery in a Microfluidic Platform

As mentioned in Chapter 1, as new nanomaterials emerge for a variety of immune-based applications there is a growing need for tools that enable the assessment of the dynamics involved in the intracellular processing of these materials.[37,38] Additionally, gold nanoparticles have been shown to be a useful tool as vaccine carriers due to their biocompatibility and potent adjuvant ability.[9,35] In this chapter, assessment of nanoparticle-mediated antigen delivery is presented as a proof-of-concept application of the microfluidic platform described in previous chapters. Specifically, the development and validation of ovalbumin-conjugated gold nanorods is shown, as well as real-time monitoring of their interactions with primary dendritic cells within the microfluidic device. Some of the work presented in this chapter has been published in Lab on a Chip.[165]

6.1 Nanorod bioconjugation considerations

Ovalbumin is widely used as a model antigen to characterise the immune system response.[198] Therefore, nanorods were conjugated to ovalbumin molecules in order to produce a nanovaccine model for use within the microfluidic platform. For this, gold nanorods with incorporated DTDCI and PSS-PDDAC-PSS coating were conjugated electrostatically to ovalbumin (OVA) or DQ™ ovalbumin (DQOVA) as described in section 2.1.6. The current section outlines the procedure used to estimate the number of molecules of ovalbumin per nanorod as an approximate measure of the dose of antigen delivered. Gold nanorods used in this chapter were measured from SEM images as before (Chapter 3) and had an average

size of 52.6 ± 4.4 x 13.1 ± 1.6 nm (N=44), giving an aspect ratio of approximately 4. The size of the ovalbumin molecule was taken from the literature[213] as 7.0×3.6×3.0 nm. Additionally, using a coating concentration of 10 µM OVA/DQOVA to ~0.2 nM nanorods (50,000 OVA molecules/NR in solution) ensured maximum coverage of the gold nanorod surface. Subsequently, calculations were made based on the following assumptions:

i.   Nanorods can be considered a two-dimensional rectangle-like shape, with ovalbumin molecules spreading across the length and width of the rod (Figure 6.1);

ii.   Ovalbumin molecules attach to the rod surface on their longest dimension (7 nm).
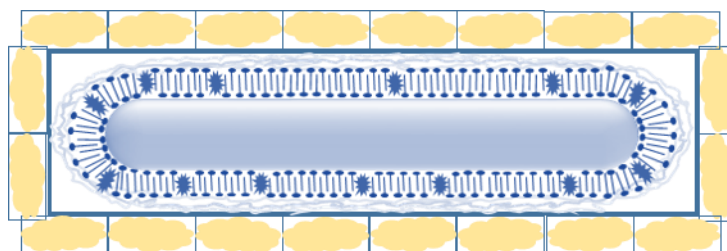
Figure 6.1 Ovalbumin molecules attach to gold nanorod surface. Schematic representation of a gold nanorod surrounded by ovalbumin molecules. Rectangle dimensions are proportional to the average nanorod and ovalbumin molecule dimensions. The number of OVA molecules on each dimension of the NR was, as a convention, rounded up to the next integer.

This led to an estimated amount of 20 ovalbumin molecules per nanorod. Limitations to this model include the lack of consideration of the variability in ovalbumin shape and position on the nanorod, the variability of nanorod size and the interactions between individual ovalbumin molecules and between ovalbumin and PSS, all of which can have an effect in the actual coverage of the nanorod surface. In any case, considering that detailed analysis of surface coverage was beyond the scope of this work, the model described provided an estimated magnitude for the amount of protein on the nanorods which could be used for comparison of results between samples exposed to solution-delivered and to nanorod-delivered antigen.

6.2 Off-chip evaluation of the developed nanovaccine model

As previously mentioned, this study focuses on the use of biologically-relevant primary dendritic cells,[192,199] which represent a key cell of the mammalian immune system. These cells readily internalise antigens and initiate adaptive immune responses through presentation of antigen to T cells, stimulating lymphocyte activation, proliferation and differentiation into effector T cells, which are capable of producing cytokines.[36] This makes them a privileged target for vaccine delivery studies.[38] Thus, in order to functionally validate the developed nanoparticle-antigen model, dendritic cells were stimulated with OVA-conjugated NRs and then left to interact with OVA-specific OT-II T cells[198] (section 2.6.1) to assess whether the antigen on the NR surface would be available for processing and presentation. Figure 6.2 shows microscopy images of the interaction between dendritic cells and T cells when exposed to (a) soluble OVA or (b) NR-OVA conjugates for 72 h. Uptake of NRs is clearly shown where dendritic cells were exposed to NR-OVA conjugates, as evidenced by the intracellular pigmentation in Figure 6.2 (b). In both conditions, a number of the OVA-specific T cells were proximal to dendritic cells, suggesting antigen recognition.
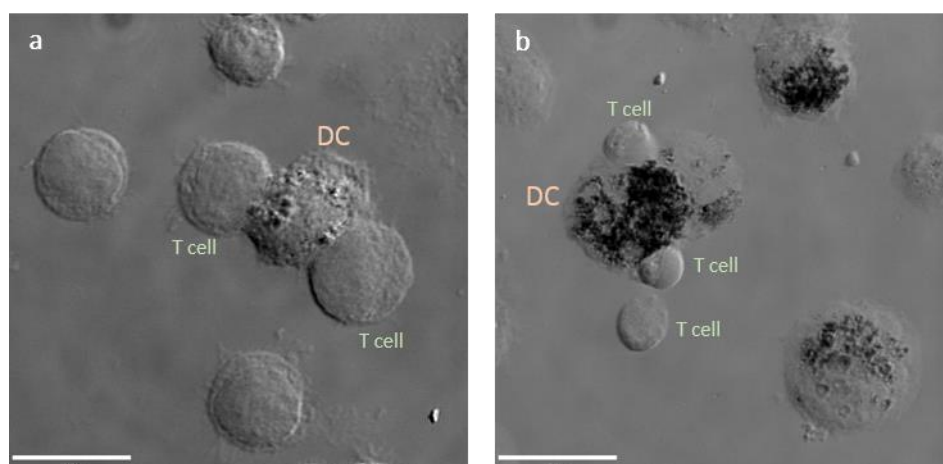
Figure 6.2 Stimulated dendritic cells interact with OVA-specific T cells. Differential interference contrast (DIC) microscopy images of fixed cell samples showing T cells interacting with dendritic cells (DC) following 72 h incubation with (a) 11 μM OVA and (b) 50 pM NR-OVA. Dendritic cells exposed to nanorod conjugates have taken up large amounts of nanoparticles, which show up as black areas within the cells. Images are representative of four separate experiments.

Subsequently, cell samples were analysed using flow cytometry to assess lymphocyte activation, proliferation and differentiation. T cell activation can be measured by assessing expression of the CD69 protein on the surface of CD4+ T cells, while recently-divided cells can be identified on the basis of Ki67 expression. Additionally, quantifying forward scatter,

which is a measure of cell size, can provide information on lymphocyte shape changes as part of their differentiation into effector T cells. Figure 6.3 shows the general gating strategy used to analyse CD4+ T cells, which was used to obtain the data presented in the following sections.
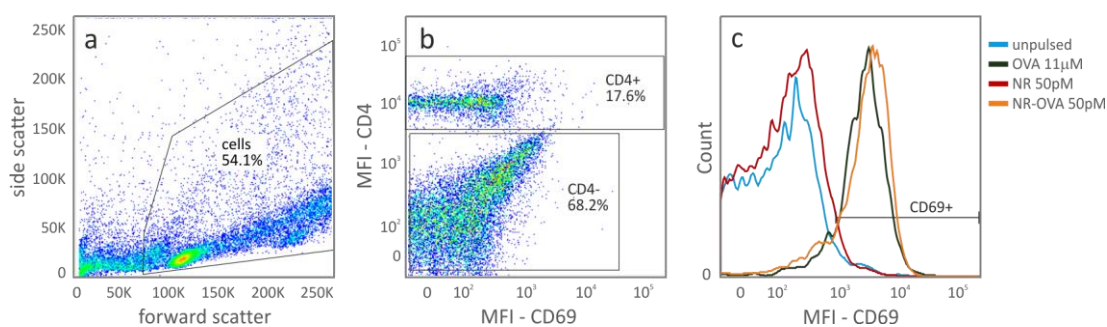
Figure 6.3 Flow cytometry analysis was used to assess T cell function following co-culture with dendritic cells exposed to NR-OVA. OVA-specific OT-II T cells were stimulated for 72 h with dendritic cells stimulated with different concentrations of soluble OVA, unconjugated NRs or OVA-conjugated NRs. Graphs (a-c) show the general gating procedure used for (a) cell objects, according to forward and side scatter measures, taking into account changes in shape due to lymphocyte activation, (b) CD4+ cells, according to the detected expression of CD4 by antibody staining (FITC) and (c) CD69+ cells, as a marker of lymphocyte activation.

6.2.1   NR conjugate optimisation

Initially, it was necessary to determine the most effective coating concentration for the production of NR-OVA conjugates, as well as the most effective NR-OVA conjugate dose given to the cells. To achieve this, NRs were incubated with different concentrations of OVA (0.1, 1 or 10 µM), washed and prepared for adding to cell samples as per section 2.1.6.2. Subsequently, dendritic cells were stimulated with different concentrations of each conjugate type and OVA-specific T cells, as described above. This way, T cell activation after 72 h could be assessed and used as a measure of the ability of the different NR-OVA conjugate formulations to successfully deliver antigen to dendritic cells. Figure 6.4 shows the data obtained with flow cytometry. From the data obtained, it could be observed that NR-OVA conjugates were most effective at inducing specific T cell activation when coated with 10 µM OVA, especially when delivered at higher (50 pM) concentrations, in which case the configuration had an effect comparable to that of 11 µM soluble OVA. Thus, throughout this work and unless otherwise stated, "NR-OVA" and "NR-DQOVA" refer to nanorods coated with 10 µM ovalbumin or DQ™ ovalbumin, respectively.
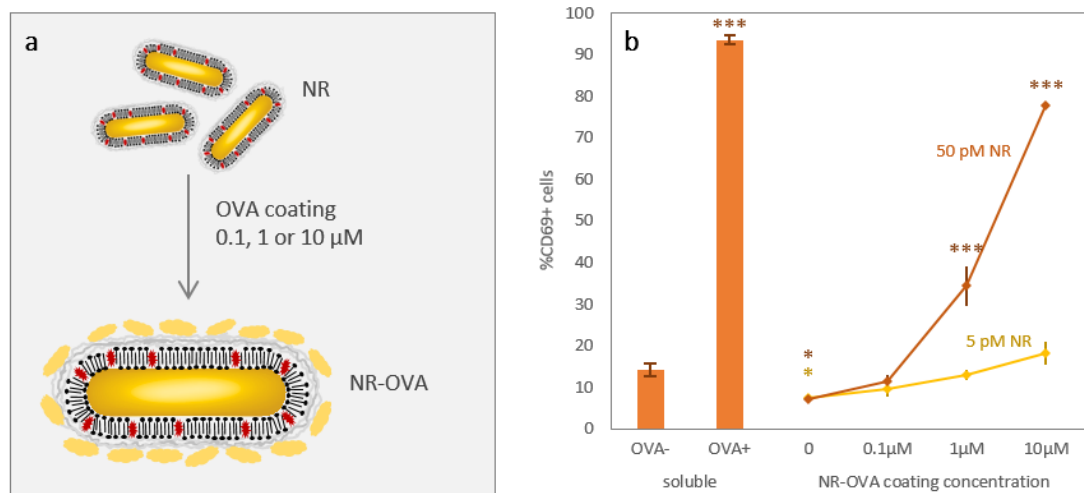
Figure 6.4 NR-OVA bioconjugation was optimised by testing different coating conditions. (a) Schematic illustrating the production of NR-OVA conjugates. (b) Graph showing flow cytometry data obtained for CD4+ T cells following exposure to dendritic cells and different NR-OVA conjugates, where CD69 expression was used as a marker of T cell activation. OVA- is the equivalent data for unstimulated cells and OVA+ for cells stimulated with 11 µM soluble OVA. A clear dose response relating to the amount of OVA used to coat the NRs could be observed for cells exposed to two different concentrations of NR-OVA conjugates. Overall, data indicates that the most effective condition tested was 50 pM of NRs coated with 10 µM OVA. Data shown is mean ± s.d. of triplicate samples, with significant differences to the unstimulated (OVA-) sample determined by one-way analysis of variance with Tukey test (*p<0.05, ***p<0.001).

6.2.2 Lymphocyte activation, differentiation and effector function

In order to further evaluate the ability of NR-OVA conjugates to deliver antigen to dendritic cells for presentation to lymphocytes, OVA-specific OT-II T cells were incubated for 72 h with dendritic cells previously stimulated with different concentrations of soluble OVA, unconjugated NRs or OVA-conjugated NR. Figure 6.5 shows an overview of the data obtained across four independent experiments. Data indicates that while CD4+ T cells in the samples exposed to NRs only or low concentrations of soluble OVA did not show activation, proliferation or blastogenesis when compared to the unstimulated sample, samples exposed to a high concentration of soluble OVA (11 µM) or to 50 pM NR-OVA conjugates consistently showed those effects across different experiments, despite the inherent variability associated with separate cell cultures and equipment readings. This indicated that incubation with 50 pM NR-OVA conjugates (an equivalent 0.8 nM OVA as per section 6.1) led to efficient processing of antigen by dendritic cells and subsequent presentation to T cells.
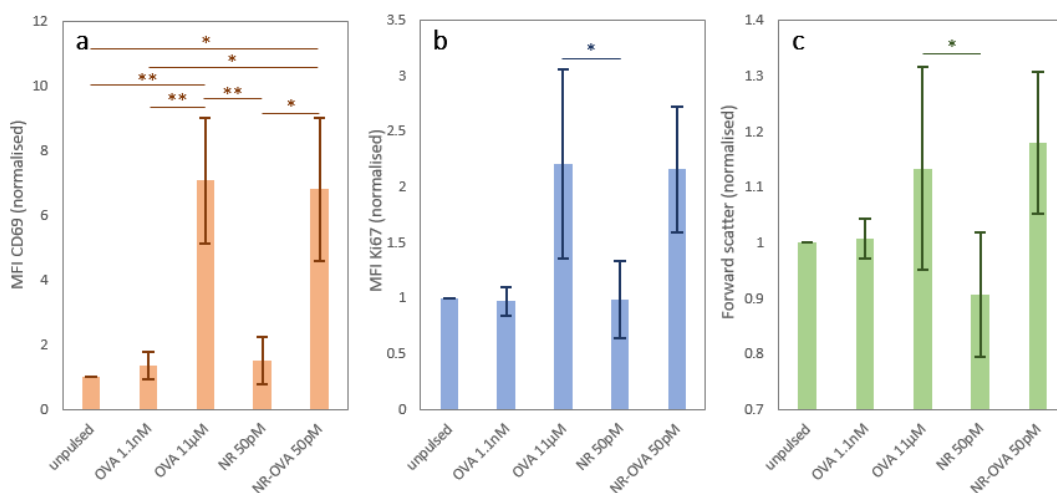
Figure 6.5 NR-OVA conjugates consistently induced an adaptive immune response. OVA-specific OT-II T cells were incubated with dendritic cells and different NR formulations or soluble OVA for 72 h. Graphs show flow cytometry data of CD4+ T cells, showing (a) CD69 MFI as a measure of lymphocyte activation, (b) Ki67 MFI as a measure of lymphocyte proliferation and (c) forward scatter data as a measure of blastogenesis. Data has been normalised to the unpulsed sample for each separate experiment, for presentation clarity, and results shown are mean ± s.e.m. of four independent experiments. Significant differences were determined on the original (not normalised) MFI values by two-way analysis of variance with Fisher means comparison (*$p<0.05$, **$p<0.01$). Overall, data indicates that despite the inherent variability from different cell cultures and equipment settings, the response verified for cells exposed to NR-OVA conjugates was comparable to that obtained with 11 µM soluble OVA.

An ELISA was also performed to assess interferon-γ and IL-5 production by the activated lymphocytes. These cytokines are only produced by T cells that have been efficiently activated by antigen-presentation.[36] Data obtained (Figure 6.6) showed that T cells were actively producing high levels of IFNγ and IL-5 after 72 h of co-culture.

Together, the results presented in Figure 6.6 and Figure 6.5 indicate that NR-OVA conjugates provide an efficient mechanism to deliver antigen to dendritic cells to subsequently initiate an adaptive immune response. Additionally, it is worth noting that the concentration of OVA delivered by NRs (~1 nM, as per section 6.1) was approximately four orders of magnitude lower than the soluble OVA concentration given as positive control (11 µM), but the response measured was comparable, whilst no T cell activation was elicited by equivalent concentrations (1.1 nM) of soluble OVA. This suggests that the NR formulation used may increase antigen uptake and/or processing or could have strong adjuvant activity in addition to being the antigen carrier, consistently with existing evidence that polymer-wrapped gold nanorods can act as powerful adjuvants,[9] which is a valuable feature for the development of efficient nanovaccines.[35,214,215]
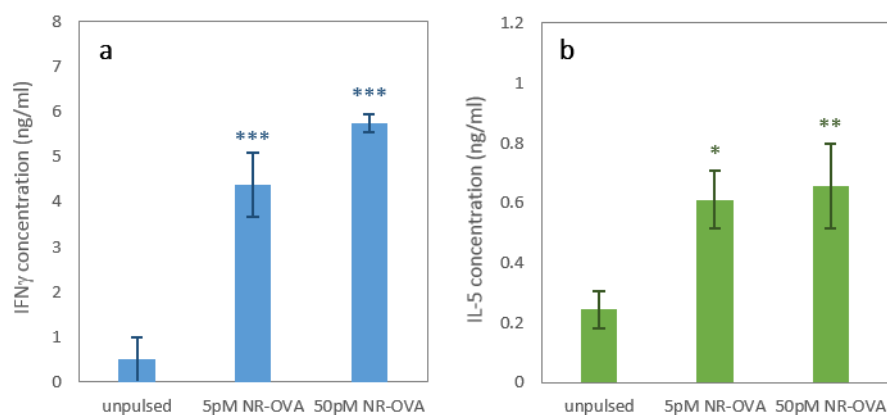
Figure 6.6 Effector function of T cells was confirmed by ELISA. Cytokine production by T cells exposed to dendritic cells and NR-OVA conjugates for 72 h was assessed using an enzyme-linked immunosorbent assay (ELISA). Data indicated that cells were actively producing significant levels of (a) IFNγ and (b) IL-5, indicating lymphocyte maturation following antigen recognition. Data shown is mean ± s.d. of triplicate samples, with significant differences of each condition to the unpulsed sample determined by one-way analysis of variance with Tukey test ($*p<0.05$, $**p<0.01$, $***p<0.001$).

6.2.3 Detection of antigen processing by Dendritic Cells

DQ Ovalbumin (DQOVA) is ovalbumin conjugated to a quenched fluorescence dye which becomes fluorescent when cleaved by intracellular proteases. It is widely used for monitoring the initial stages of antigen processing by dendritic cells.[197] NR-DQOVA conjugates were produced and tested off-chip with cells (section 2.6.2), in an initial attempt to quantify processing of NR-conjugated antigen under different experimental conditions prior to their use in the microfluidic device. Specifically, the timescales required for real-time monitoring of antigen processing by primary dendritic cells were investigated. Flow cytometry data obtained by end-point measurement of cell samples exposed to a range of concentrations of NR-DQOVA, unconjugated NRs or soluble DQOVA for different periods of time is shown in Figure 6.7.

Data obtained provided information on both the time- and dose-dependent nature of antigen uptake and processing, showing that DQOVA cleavage could be detected as early as 5 minutes after pulsing, for high concentrations of soluble protein. In the case of NR-DQOVA conjugates, it was verified that the nanoparticles were taken up at a comparable rate to that of unconjugated NR. For these samples, DQOVA processing was detectable from about 60 minutes of incubation. In addition, fluorescence of the NR-delivered DQOVA complexes was comparable to that obtained from the soluble DQOVA, even if the dose carried by NRs was

much lower – specifically, for 10 pM NR-DQOVA (approximately 0.2 nM DQOVA, estimated as per section 6.1), fluorescence intensities closely matched those obtained with 2.2 nM soluble DQOVA. This suggests that the gold nanorod carrier may facilitate antigen delivery to the cells, as discussed in the previous section.
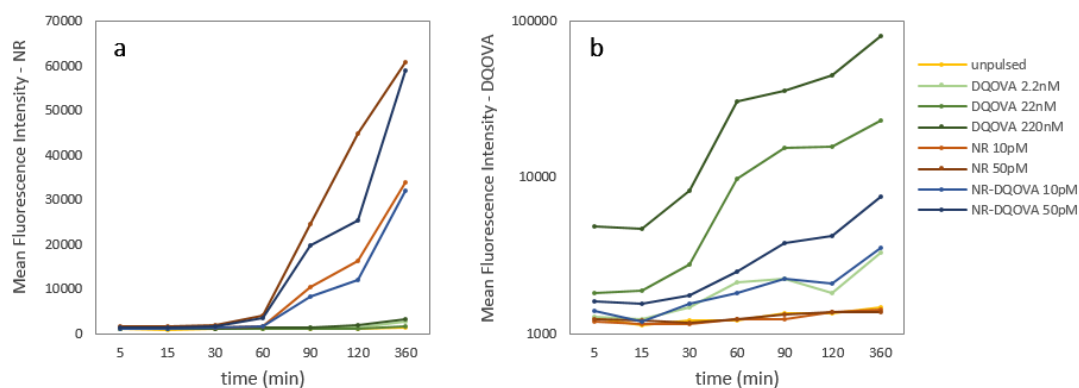
Figure 6.7 NR-conjugated antigen is efficiently processed by dendritic cells. Dendritic cells were exposed to soluble DQ-OVA, unconjugated NRs or NR-DQOVA conjugates at a range of concentrations. At various times, cells were harvested and analysed by flow cytometry to quantify (a) the uptake of NRs (NR fluorescence at 633 nm excitation) and (b) the processing of DQ-OVA (DQOVA fluorescence at 488 nm excitation).

The initial screening experiment shown in Figure 6.7 did not include any replicate samples as the main aim was to provide an overview of antigen processing behaviour in various conditions. Thus, a subsequent experiment was performed considering only a selected number of conditions and time points (specifically, representative concentrations of NR, NR-DQOVA and soluble DQOVA), for which triplicate samples were measured by flow cytometry as above. An overview of data obtained is shown in Figure 6.8, with NR uptake displaying comparable levels with and without DQOVA conjugation and demonstrating the detection of DQOVA in samples exposed to NR-DQOVA conjugates from the earliest time point. Overall, these experiments confirmed the ability of NR-DQOVA conjugates to deliver antigen to dendritic cells at a clearly detectable level for the concentrations used, providing a strong basis for their use for real-time monitoring of antigen processing within the microfluidic platform (section 6.4).
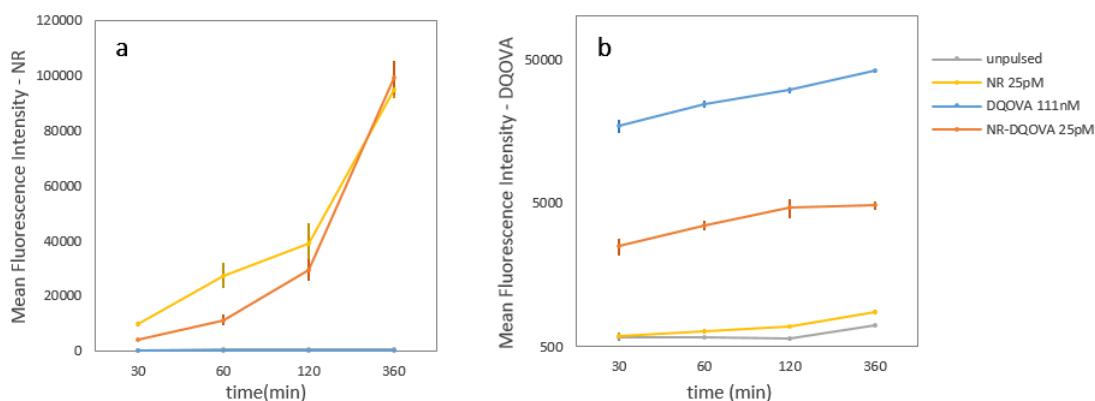
Figure 6.8 NR-mediated DQOVA processing was verified in a larger experiment. Dendritic cells were incubated with 25 pM NRs or NR-DQOVA, as well as with 111 nM soluble DQOVA, in triplicates, and harvested at 30, 60, 120 and 360 minutes. Data shows mean ± s.d. of triplicate samples.

Subsequently, in order to assess nanoparticle internalisation and colocalisation with antigen fluorescence, confocal microscopy was performed on cells that were exposed to the conditions presented in Figure 6.8 for 6 hours. Representative images obtained for each of the cell samples are shown in Figure 6.9. Images show bright fluorescence of the DQOVA complexes in both the soluble (b) and NR-delivered forms (d), as well as bright DTDCI fluorescence from NRs in (c) and (d).
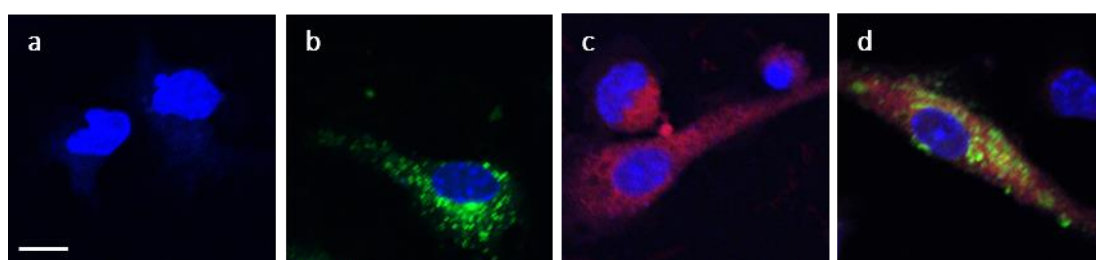
Figure 6.9 Dendritic cells take up and process NR-DQOVA conjugates. Confocal fluorescence imaging of fixed dendritic cells following a 6 hour incubation with (a) nothing added, (b) 5 µg/ml soluble DQOVA, (c) 25 pM NRs and (d) 25 pM NR-DQOVA. Blue represents DAPI staining of cell nuclei, red shows NR fluorescence (excitation 633 nm) and green shows DQOVA fluorescence (excitation 488 nm). Scale bar is 10 µm.

Interestingly, as seen in Figure 6.9 (d) and highlighted in Figure 6.10, DQOVA fluorescence showed a localisation distinct to the NR fluorescence signal, suggesting that the antigen could have detached from the nanorod surface. This is something that could benefit from further investigation with the microfluidic platform, as will be discussed in section 6.5.
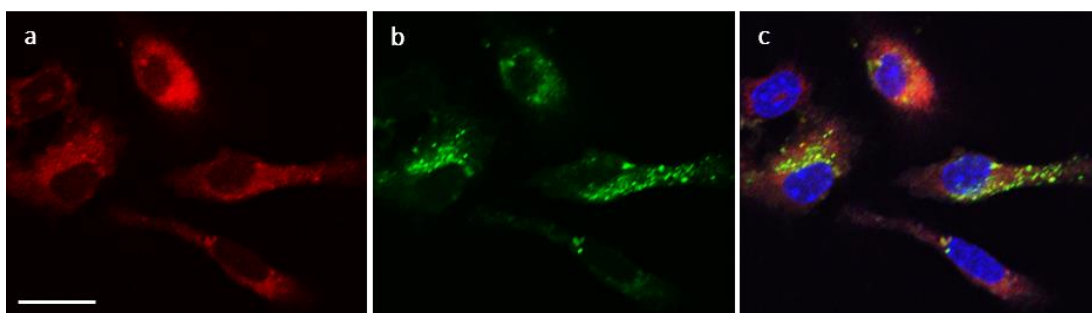
Figure 6.10 Nanorod and DQOVA fluorescence show differences in localisation. Confocal fluorescence imaging of fixed dendritic cells following a 6 hour incubation with 25 pM NR-DQOVA, where (a) shows NR fluorescence (b) shows DQOVA fluorescence and (c) shows an overlay of both channels, with DAPI staining the nuclei. Scale bar is 20 μm.

6.3 Microfluidics for real-time antigen processing by single-cells

The previous section showed the ability of conventional techniques such as flow cytometry and confocal microscopy to provide some information on nanoparticle conjugate uptake and antigen processing. However, as discussed in Chapter 5, these techniques are based on end-point measurements of separate samples, failing to provide information about the single-cell responses as well as the dynamics underlying those events. Thus, prior to NR experiments, the developed microfluidic platform was used to test delivery and uptake of known concentrations of soluble DQOVA. This section describes the preparation of this test and real-time antigen processing data obtained for hundreds of trapped cells.

6.3.1 Gradient optimisation using soluble AFBSA

Given that DQOVA fluorescence in solution is initially quenched, fluorescently-labelled bovine serum albumin (AFBSA) was initially used to optimise the delivery of a gradient of concentrations of soluble protein to the microfluidic trapping array. Importantly, the diffusion coefficients of the two proteins are very similar, with $D_{BSA} = 6.75 \times 10^{-11} \, m^2/s$ and $D_{OVA} = 6.38 \times 10^{-11} \, m^2/s$ at 25°C.[211] Thus, the gradient behaviour is expected to be comparable, with Péclet numbers (equation [2], section 1.5.2) obtained for 0.5 μl/min being 0.121 and 0.127 respectively for BSA and OVA.

This way, different flow settings could be tested for AFBSA and assessed using fluorescence microscopy prior to their application to soluble antigen delivery. Specifically, a number of different flow rates from the two side inlets was assessed in order to produce the best possible concentration gradient across the trapping chamber. Figure 6.11 shows the data

obtained for each of the settings used, indicating that all the conditions tested resulted in two side regions where an approximately constant concentration of protein was delivered (0 on the left, 100 nM on the right), with the middle area showing a transition region where a gradient was observed.
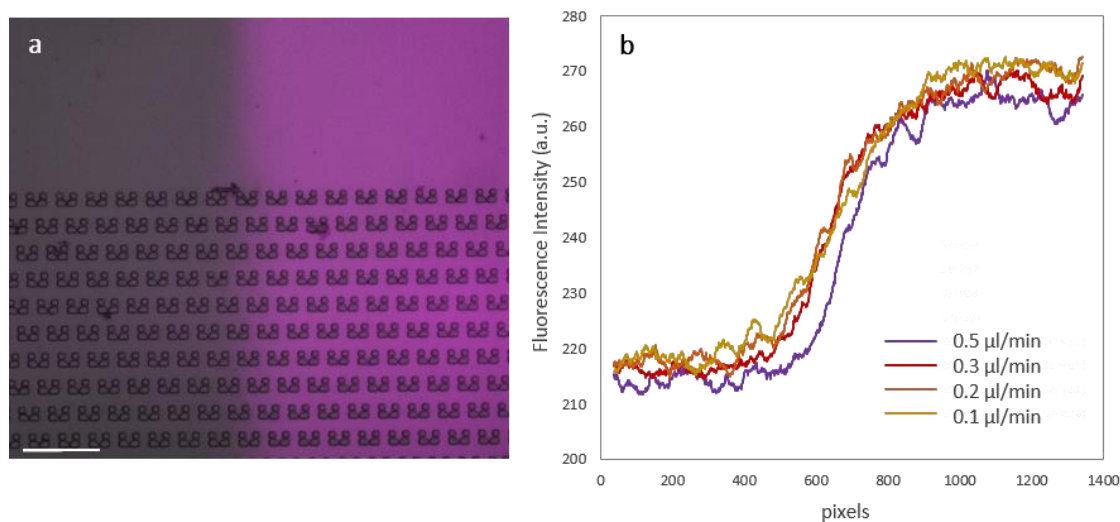
Figure 6.11 A gradient of AFBSA was visualised using fluorescence microscopy. (a) Composite image showing the central area of the trapping array with overlay of AFBSA fluorescence (magenta) when excited at 625 nm, for the 0.5 µl/min condition. (b) Fluorescence intensity profile across the trapping array when exposed to a gradient of AFBSA at different flow rates. Graph was obtained by performing a 30-step moving average of the line profile across the array width shown in (a).

Ideally, the concentration gradient profile would be less steep and extend further to the sides of the chamber, so that more intermediate concentrations would be delivered to the cells. However, this was not possible due to the microfluidic pumps available (see discussion in section 4.3). Data obtained revealed a very similar fluorescence profile for all the different flow rates used, only showing a slightly steeper gradient for 0.5 µl/min which resulted in a difference of just one less trap per row being exposed to that gradient. Importantly however, the lowest flow rates showed a pulsatile flow effect (section 4.4.3), which would be detrimental to the assessment of cell response as cells in the transition area would be exposed to varying concentrations. Additionally, it was observed that when the flow was too low (<0.5 µl/min) within the trapping array, cells were more likely to escape from the traps (section 4.3.4), something that would become a problem when doing long-term monitoring of individual cells. Thus, 0.5 µl/min was deemed to be the best flow rate considering the current setup and microfluidic design, and that was the value chosen for DQOVA delivery and monitoring as presented in the next section.

6.3.2 Delivery of a gradient of DQOVA to trapped cells

In order to assess the suitability of the microfluidic platform developed in Chapters 4 and 5 for monitoring antigen delivery to trapped cells, a gradient of soluble DQOVA concentrations was then delivered to an array of trapped dendritic cells (section 2.6.3), using the parameters defined in section 6.3.1. This experiment aimed to establish the appropriate acquisition timescales and fluorescence parameters (e.g. excitation intensity and duration) prior to the use of the microfluidic platform for assessing the delivery of antigen from the nanovaccine model developed.
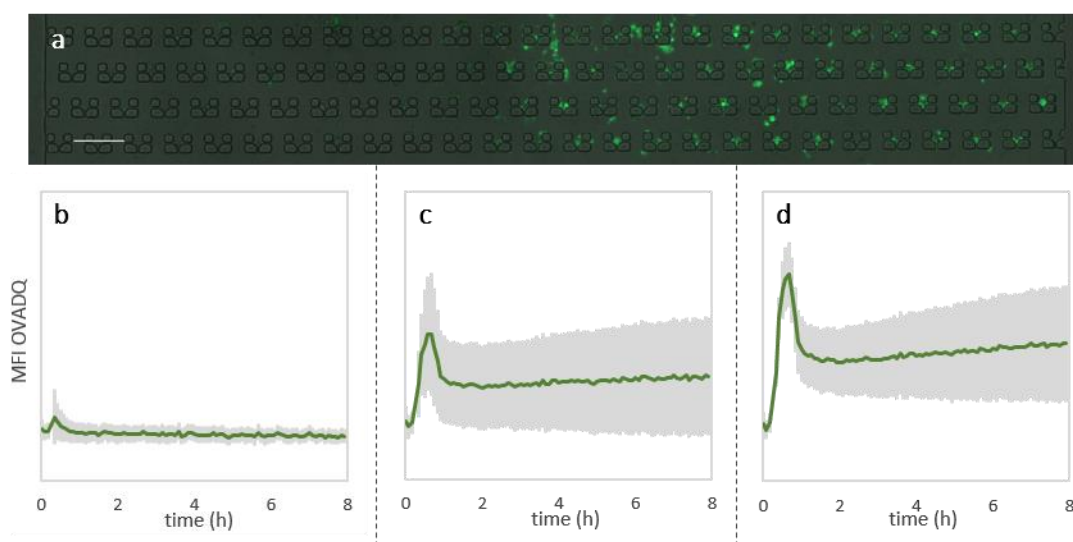
Figure 6.12 Antigen was delivered into the microfluidic device and intracellular processing detected at the single-cell level. (a) Composite image of the full width of the microfluidic array, showing DQOVA fluorescence in green (488 nm excitation). ROIs were drawn within individual cell-containing traps and data acquired every 5 minutes over 8 hours. For analysis purposes, three regions were defined according to different antigen concentrations: (b) null concentration (N=91), (c) intermediate concentration (N=123) and (d) high concentration (N=111) regions. Graphs show average DQOVA fluorescence intensity (background corrected) measured at 488 nm excitation ±s.e.m. for all the traps in each of these regions.

Time-lapse imaging across the array of dendritic cells allowed for the fluorescence intensity of the cells to be monitored over a period of eight hours, with intracellular fluorescence showing a dose-dependent response (Figure 6.12 a). Regions of interest (ROIs) were defined within all traps containing cells and divided into three areas with approximately the same number of traps, according to the concentration of antigen delivered – null, intermediate and high (approximately 222 nM) concentration of DQOVA in cRPMI (Figure 6.12 b-d). An early peak of DQOVA fluorescence intensity was evident, corresponding to the delivery of the fluorescently-labelled antigen solution, which happened only for a defined amount of time.

Subsequently, constant medium perfusion was maintained at the same flow rate for the duration of the experiment. The remaining fluorescence measured within the traps after the initial peak corresponded to intracellular processing of the antigen molecules, leading to a gradual increase in fluorescence over the course of the experiment, which was consistent with data obtained using flow cytometry (section 6.2.3). This way, real-time monitoring of antigen processing was achieved, as measured by DQOVA cleavage within the cells. The same procedure could then be adapted for use with the NR-DQOVA conjugates as described in the next sections.

6.4 Real-time assessment of nanoparticle-mediated antigen delivery

Having shown in this chapter that the DQOVA-coated NRs can be successfully delivered to cells off-chip and that dendritic cells can acquire fluorescent antigen on-chip, this section seeks to validate the microfluidic platform described in earlier chapters to investigate the interactions between NR-OVA conjugates and dendritic cells, using time-lapse microscopy to quantify nanoparticle uptake and intracellular antigen processing over long periods of time. Such an approach can provide crucial information regarding the dynamics of the interactions between nanovaccines and cells at both the population and single-cell levels.

6.4.1   Delivery of nanorod-antigen conjugates to trapped cells

Cell trapping was performed as previously described (Chapter 4) and cells allowed to settle into the trap array (Figure 6.13 a). Subsequently, time-lapse imaging was initiated and a suspension of 400 pM NR-DQOVA conjugates in medium delivered to one side of the array, with medium only being delivered to the opposite side in order to create a concentration gradient across the trapping chamber (Figure 6.13 b), as described in more detail in sections 2.5.2 and 4.3. Delivery of NRs to the cells was initiated approximately 30 minutes into the imaging period and continued for approximately two hours. Perfusion with medium alone was then maintained until the end of the experiment (Figure 6.13 c). Wide-field images of approximately 550 traps were obtained every five minutes over eight hours, with phase contrast used to identify the cells in the traps and nanorod uptake and antigen processing monitored using the red (625 nm excitation) and green (488 nm excitation) channels, corresponding to DTDCI fluorescence and DQOVA fluorescence following intracellular enzymatic cleavage, respectively. For analysis purposes, single-cells were identified as circular ROIs and MFI data was obtained for 525 individual cells as described in section

2.6.4.2. Figure 6.13 (a3-c3) shows the average fluorescence intensity profile for single-cells over five rows across the entire width of the array. As expected, during nanoparticle delivery there was a clear increase in nanoparticle fluorescence in cells exposed to a high concentration of NRs (right-hand side of the images in Figure 6.13), which was followed by a subsequent increase in green fluorescence as the dendritic cells processed the delivered antigen. Conversely, cells receiving no NRs showed no detectable fluorescence signal. Both measurements showed a clear dependence of dose with position across the array. Additionally, substantial variability was observed for cells in the same trap positions (i.e., exposed to the same concentration of NR-DQOVA conjugates), a fact which is analysed in more detail in the next sections.
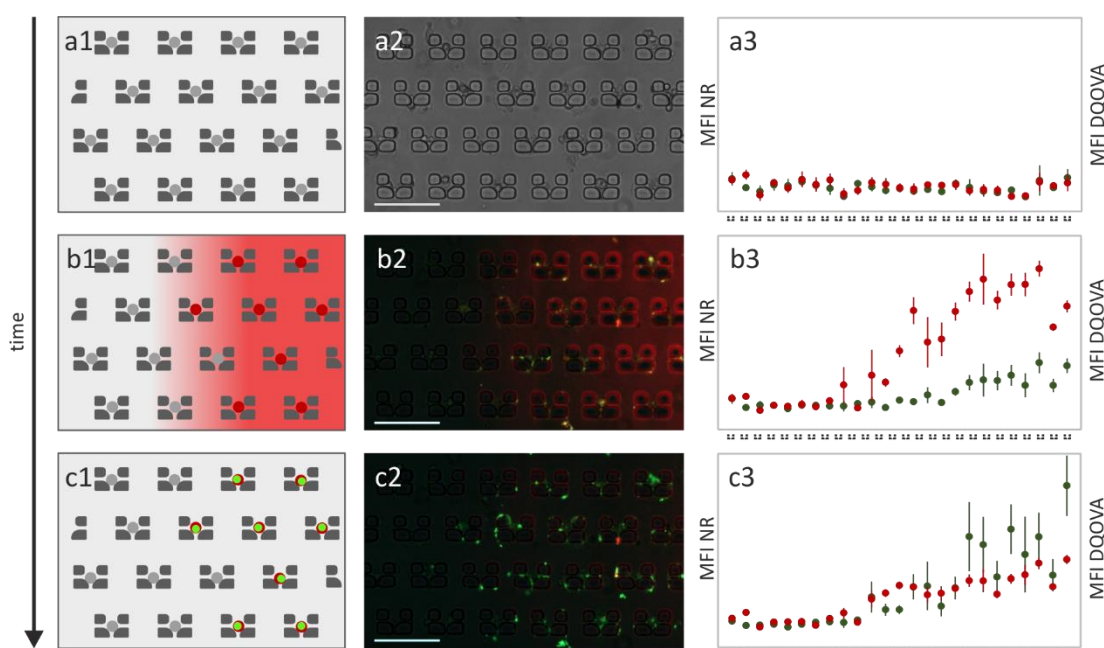
Figure 6.13 NR-DQOVA conjugates were delivered in gradient form to an array of trapped cells, with NR uptake and antigen processing monitored in real-time. (a1-c1) Schematic representation of the key temporal aspects of the microfluidic protocol: cell trapping, NR conjugate delivery and antigen processing, respectively, from top to bottom. Cells are represented in grey: they become red when in contact with NRs and turn green after antigen processing. (a2-c2) Phase contrast and composite images of the trapping array (Scale bar = 100 μm) corresponding to the time points of the schematics in a1-c1. (a3-c3) Fluorescence intensity profile showing responses to NR uptake and antigen processing across the width of the array chamber for the time points corresponding to the schematics in b1-d1. Each data point represents the mean fluorescence intensity (MFI) (background corrected) of single-cell ROIs located in the same vertical region of the chamber over five rows ± s.e.m., with red representing NR fluorescence measured at 625 nm excitation and green representing DQOVA fluorescence measured at 488 nm excitation. Results are representative of four separate experiments. A version of this figure has been published in Lab on a Chip.[165]

6.4.2 Analysis of time-dependence of cell response

Fluorescence data obtained from single-cell ROIs allowed for the response of hundreds of single cells to be monitored for the duration of the experiment. To further analyse the time-dependent nature of antigen uptake and processing at the single-cell level, the array was divided into three areas containing approximately the same number of traps and based on the concentration of nanoparticle conjugates delivered – i.e. null, intermediate (transition area) and high (approximately 400 pM) concentration. Figure 6.14 shows the high throughput capabilities of the developed platform, providing information on the average response of N>150 single-cells in each of these areas. Data shows a clear peak in red fluorescence corresponding to NR delivery into the array and uptake by the cells (b1-c1), followed by a gradual increase in green fluorescence corresponding to antigen processing as measured by DQOVA cleavage (b2-c2).

Results shown in Figure 6.14 for NR fluorescence differ to those obtained using flow cytometry (Figure 6.7), specifically because in the latter case the NR conjugates were not removed from the cell environment, leading to a steady increase in NR fluorescence over the whole experiment. Within the microfluidic device, NRs were controllably delivered and perfused away after a defined period of time, resulting in the peak seen in Figure 6.14 (b1-c1). These clear differences in delivery method and cell environment led to differences in NR uptake, as discussed in section 5.2.1. On the other hand, NR-delivered DQOVA fluorescence data obtained within the device was consistent with data obtained both in flow cytometry (Figure 6.7) and with soluble DQOVA within the device (Figure 6.12), showing a steady gradual increase in fluorescence following exposure to antigen. Overall, results demonstrate the capacity of the developed microfluidic platform for monitoring the time- and dose-dependent uptake and processing of antigen-coated nanoparticles in real-time across a population of trapped cells.
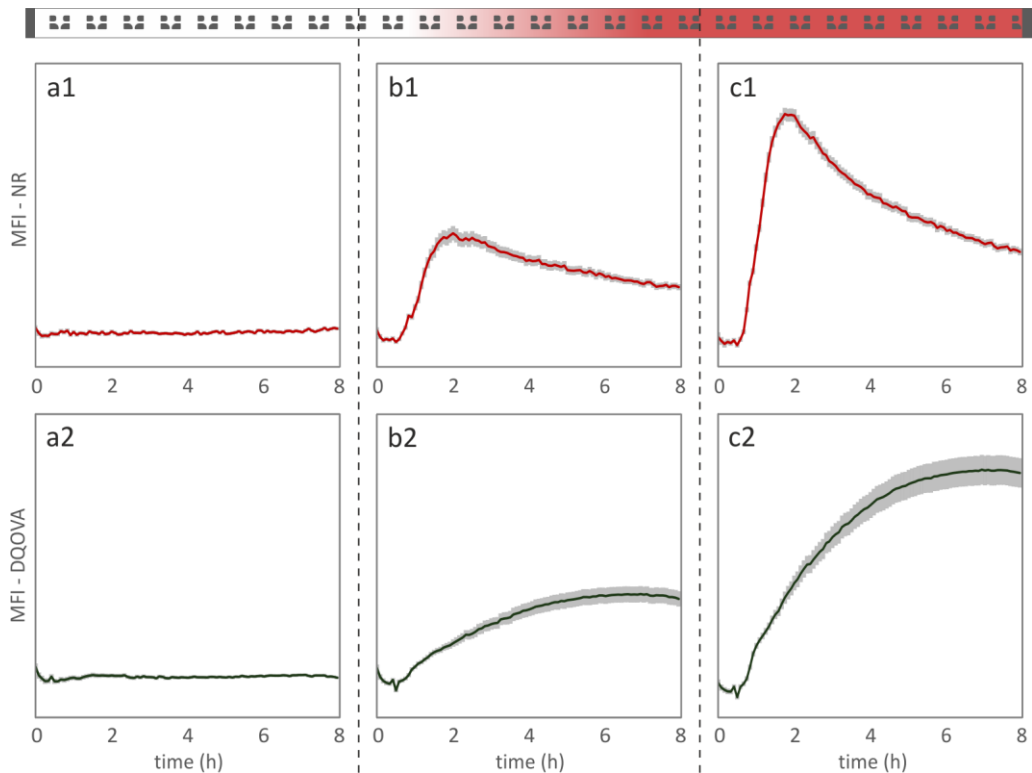
Figure 6.14 Single-cell analysis of NR uptake and DQOVA processing provided information about the population response over time. Cells were trapped in the microfluidic array and exposed to a range of concentrations of NR-DQOVA conjugates. Circular ROIs were defined around individual cells for data acquired every 5 minutes over 8 hours. For analysis purposes, three regions across the array were defined according to different NR concentrations: (a) null concentration (N=151), (b) intermediate concentration (N=203) and (c) high concentration (N=171) regions, as per the illustrated NR concentration gradient profile (top). Graphs show averaged single-cell responses for each region. (a1-c1) Average NR fluorescence intensity (background corrected) measured at 625 nm excitation ± s.e.m. (a2-c2) Average DQOVA fluorescence intensity (background corrected) measured at 488 nm excitation ± s.e.m. Results are representative of four separate experiments. A version of this figure has been published in Lab on a Chip.[165]

6.5 Assessment of cell response at the single-cell level

To better assess the variation between single cells exposed to different doses of NR-DQOVA conjugates, the response of individual cells in different positions across the array was investigated. Figure 6.15 shows the response for one trapped cell in each of the array areas as defined above. Comparison of NR uptake and DQOVA processing as measured by the fluorescence intensities for these cells over time shows that there are clear differences in dose delivered and consequent cellular response depending on position on the array at the single-cell level. The use of an imaging approach with this microfluidic platform allows for specific aspects of intracellular fluorescence localisation to be assessed, which has the potential to provide dynamic data about the intracellular processing pathways involved in antigen delivery from the surface of nanoparticles. In previous sections, confocal fluorescence imaging of fixed cells that were exposed to NR-DQOVA conjugates (Figure 6.10) indicated that the nanoparticles were in a different location from the antigen after the incubation period, which underlines the importance of such an approach for this application.
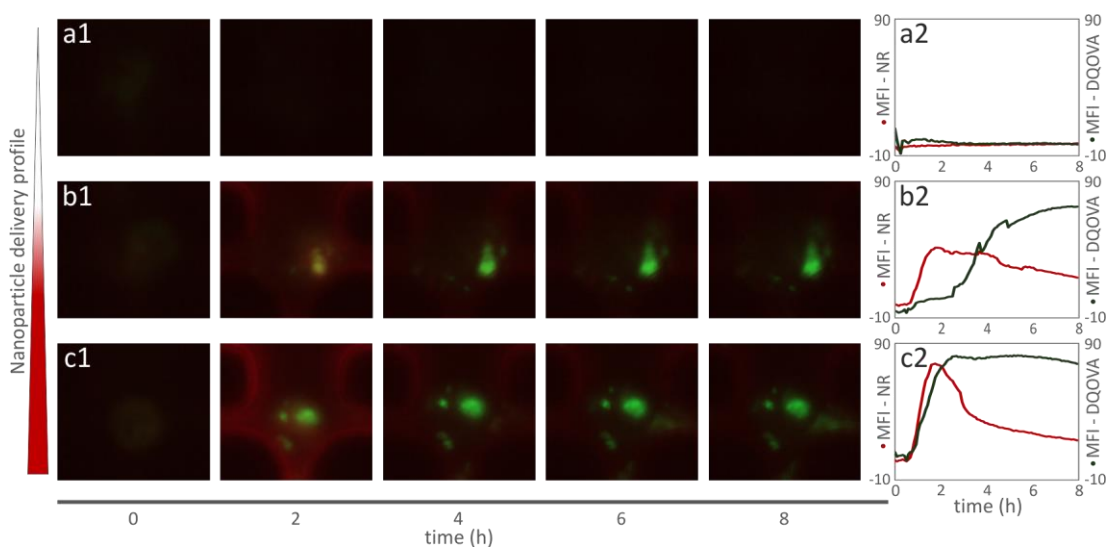
Figure 6.15 Single-cell response was distinct for different areas of the microfluidic array. Comparison of single-cell responses to NR-conjugate delivery across the array in (a) null, (b) intermediate and (c) high NR concentration regions of the microfluidic array. Examples of single-cell ROIs were selected from each area and their fluorescence intensity profiles plotted to show response patterns. (a1-c1) Composite fluorescence images of the cells within the traps for different time points over 8 hours and (a2-c2) MFI plots for the same ROIs over 8 hours where red shows NR fluorescence measured at 633 nm excitation and green shows DQOVA fluorescence measured at 488 nm excitation. A version of this figure has been published in Lab on a Chip.[165]

138

6.5.1   Cell response heterogeneity

The heterogeneity of cellular responses in primary dendritic cells can be due to a number of causes, including different degrees of cell activation leading to changes in phagocytosis and pinocytosis of antigenic material.[36,49,216] The ability to track single cells throughout the duration of antigen uptake and processing would allow researchers to further characterise the multitude of parameters that might affect these steps, essential for determining functional immunity. To explore this, heat maps showing the intensity of DQOVA fluorescence of single cells throughout the imaging period were produced. These data provide a useful means to compare the intensity and speed of antigen processing across a population of cells analysed within one device (Figure 6.16 a-c). This is further emphasised in Figure 6.16 (d), where single-cell traces for DQOVA fluorescence of cells in the same trap position (i.e. exposed to the same concentration of NR-DQOVA conjugates) are compared.
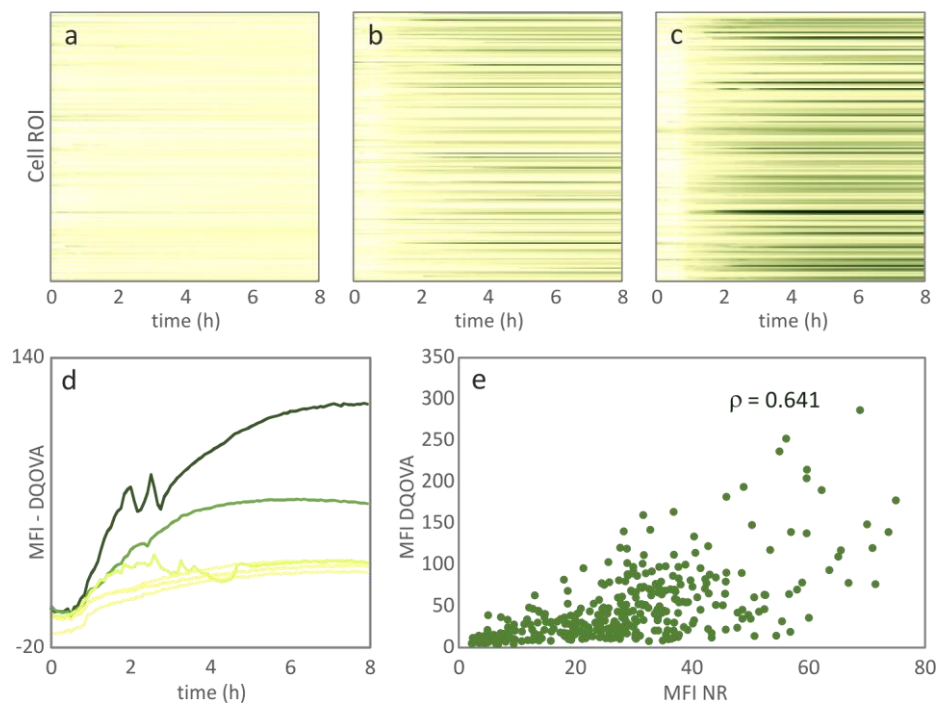
Figure 6.16 Cells exposed to similar doses of NR conjugates reveal heterogeneity in antigen processing response. (a-c) Heat maps showing processing of DQOVA within individual cell ROIs in the (a) null concentration (N=151), (b) intermediate concentration (N=203) and (c) high concentration (N=171) regions as defined in Figure 6.14. White corresponds to a null response and dark green is the maximum MFI value across the whole array, with the midpoint (yellow) at the 50th percentile. (d) Examples of MFI profiles for DQOVA from six cells in different trap sites within the high NR concentration region, indicating heterogeneous cell response to antigen-coated NR. (e) Dot plot of DQOVA MFI range (max-min) for NR+/DQOVA+ gated single-cell ROIs versus NR MFI range (max-min). A Pearson's correlation coefficient of 0.641 was obtained for this data. A version of this figure has been published in Lab on a Chip.[165]

To further investigate the relationship between the level of nanoparticle uptake and the degree of antigen processing detected, cell ROIs were gated as NR+/DQOVA+ based on their fluorescence intensities above background level for both channels, to identify cells that both took up nanoparticles and processed antigen. This double-positive population represented 0.6% of cells in the null dose region, 43.3% of cells in the intermediate dose region and 84.3% of cells in the high dose region. Figure 6.16 (e) shows the intensity of antigen processing by gated single-cells with different levels of NR uptake. It was observed that higher concentrations of nanorods within the cells correlated with higher levels of DQOVA processing, suggesting that the heterogeneity of cellular response was more related to differences in uptake than to differences in processing of NR conjugates. Overall, data obtained shows clear heterogeneity in the measured responses between cells exposed to similar concentrations of NR conjugates and underlines the importance of acquiring single-cell information to better understand cellular behaviour, as opposed to averaged population responses, which will often mask this variability and potentially lead to erroneous observations.[33,109,216]

6.5.2   Time to response

The dynamics of vaccine uptake, processing and presentation can have a key role in determining the magnitude and type of immune response induced and new approaches to understand these factors are important in vaccine design. Using the data presented above, the lag time between the peak of NR uptake and the peak of antigen processing could be calculated for all the NR+/DQOVA+ gated cells across the array. This was defined as the difference between the time of half-maximum NR MFI and the time of half-maximum DQOVA MFI (Figure 6.17 a). Results obtained (Figure 6.17 b) indicated that despite being exposed to different concentrations and acquiring different amounts of NR conjugates, the time delay between NR uptake and antigen processing followed a Gaussian distribution, with the standard deviation of the fitted curve (continuous line in Figure 6.17 b) being representative of response heterogeneity.
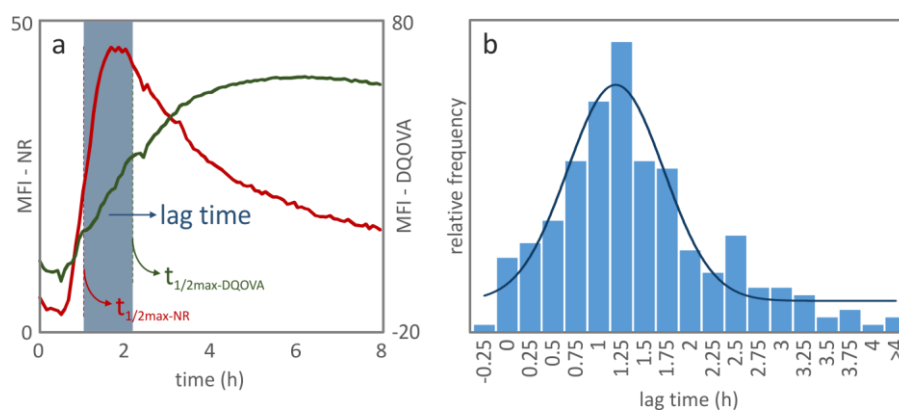
Figure 6.17 Time from uptake of NRs to antigen processing was not dependent on dose. The time delay between nanoparticle uptake and antigen processing for each individual cell ROI ("lag time") was calculated as the time difference between NR half-maximum MFI and DQOVA half-maximum MFI. (a) MFI traces for NR and DQOVA for one single-cell ROI, showing the time parameters chosen to calculate lag time (blue bar), as a representation of the procedure used to calculate the lag times for all the single cell ROIs. (b) Histogram showing the lag time response for all the NR+DQOVA+ gated single-cell ROIs with superimposed damped least-squares Gaussian fit (σ=0.526). A version of this figure has been published in Lab on a Chip.[165]

This data indicates that, under normal conditions, dendritic cells will take approximately the same time to process antigen regardless of the NR-OVA dose they receive. This further emphasises that the focus for nanovaccine screening needs to be in optimising the dose delivered to cells, to which the developed microfluidic platform can be a powerful tool. Overall, this data represents a novel, dynamic measure of the interaction of nanoparticles with cells, which can be used for assessing and comparing the efficiency of compound delivery by different types and formulations of nanoparticle carriers.

6.6 Conclusions

In this chapter, the microfluidic device and nanoparticles presented in previous chapters were combined and applied to monitoring the delivery of antigen from nanoparticle conjugates to hundreds of dendritic cells. Firstly, nanorod-ovalbumin conjugates were produced and tested off-chip, proving their ability to deliver antigen to dendritic cells and elicit an adaptive immune response in CD4+ T cells (section 6.2). Bioconjugation of nanorods to fluorescently-labelled DQ™ Ovalbumin was also tested and assessed off-chip, with results showing that these NR-DQOVA conjugates could be used for live monitoring of antigen processing by dendritic cells (section 6.2.3). Importantly, this data indicated that NR could facilitate uptake of antigen when compared to the soluble form, while the T cell activation

data strongly suggested that NR were having a significant effect in enhancing the immune response, potentially through a separate biological mechanism.[217] Subsequently, monitoring of the delivery and processing of soluble antigen was performed within the microfluidic device (section 6.3), after which NR-DQOVA conjugates were delivered to trapped cells (section 6.4). The microfluidic platform developed allowed for nanoparticle uptake and antigen processing information to be obtained from the cell population with a throughput comparable to that of flow cytometry, but allowing for dynamic assessment of the same sample through time, with single-cell resolution. Importantly, this approach provided simultaneous imaging and quantification of cellular responses, while being substantially more time and resource efficient than conventional techniques. For instance, all the microfluidics data presented in this chapter required approximately 45,000 cells for each experiment (section 6.4), in comparison with 14 million cells used to run the off-chip equivalent in static wells (section 6.2.3). This is especially relevant when dealing with rare or patient-derived cell samples and further highlights the capabilities of the system as a pre-screening tool for nanomaterials for clinical applications.

Chapter 7

Discussion and Conclusions

The goal of the work presented in this thesis was the integration of single-cell microfluidics with nanoparticle chemistry and imaging techniques into a tool for high-throughput, real-time investigation of cellular interactions with nanomaterials. This final chapter will discuss the main results and the potential future developments for various aspects of this work.

7.1   Research achievements and future work

The analysis of the literature shown in chapter 1 revealed the great potential of nanomaterials for biomedical applications such as the probing of intracellular events and drug or vaccine delivery.[1-3] Although a wide range of such nanomaterials have been proposed, there is an unmet need for high-throughput screening tools that provide a better understanding of the interaction of those nanomaterials with cells. Key aspects like nanomaterial toxicity, efficiency of drug or vaccine delivery, or the long-term functional effects on the cells should be assessed in a standardised manner.[4,17,23] This would not only provide important biological data about how cells process nanomaterials and interact with them, depending on composition, shape, size, surface chemistry or functionalisation, but also important preclinical data on the suitability of those materials for use on patients.[1,104] However, despite the promise of new technologies, such as lab-on-a-chip, for this purpose, there is currently no robust, high-throughput platform for screening the dynamics of the interactions of nanomaterials with cells.[17,23,51] Thus, the work described in this thesis has endeavoured to produce and validate a microfluidic device and protocols that could fill this technical gap. The device was shown to be capable of parallel single-cell analysis within an

array chamber containing low shear stress microtraps, allowing for real-time measurements to be obtained both at the population and individual cell levels. With this, cell trapping was successfully achieved, as well as on-chip cell incubation, allowing for real-time imaging of hundreds of live single-cells over several hours. In parallel, versatile and stable gold nanorod formulations were produced to achieve specific optical properties and successful delivery to live cells within the microfluidic device, with nanorod uptake monitored using fluorescence microscopy. Functional readouts such as viability markers could also be obtained from the trapped cells. As proof-of-concept, a nanovaccine model was formulated and nanoparticle-mediated antigen delivery and processing was monitored in real-time using the developed platform. These results will be discussed here in more detail, with a focus on future work.

7.1.1   Gold nanorods as molecule carriers

The development and optimisation of gold nanorods was described in chapter 3, towards a nanorod formulation that was not only possible to image within cells but was also stable in biological media. The main reasons for using gold nanorods were: i) their material properties and anisotropy, which confer great optical versatility and remarkable specificity for imaging,[42,43,69] and ii) their previously demonstrated ability in a range of biomedical applications, from intracellular imaging to drug delivery and photothermal therapy.[4,9,42] Initially, nanorods were synthesised using the seed-mediated growth method[67,68] and their aspect ratio was tuned for preferentially absorbing at given wavelengths. Subsequent incorporation of a range of reporter dyes into the nanorod surfactant bilayer resulted in specific imaging capabilities for different wavelengths or multi-wavelengths simultaneously, with or without incorporated fluorescence. This demonstrated the high versatility of the nanorods as imaging systems that can be tailored for specific applications. Also, fine tuning of the nanorod LSPR to each specific dye's resonance wavelength will lead to optimised SERRS signal enhancement. Importantly, for biological applications, the absorbance of nanorods should be tailored to the NIR region of the spectrum, as that is considered the "water window" where light used for *in vivo* imaging or nanorod-based therapy will have the least effect on the surrounding tissue.[112]

The developed nanorods were coated with a series of electrostatically self-assembled polyelectrolyte layers (predominantly, PSS-PDDAC or PSS-PDDAC-PSS), in order to become more biocompatible and stable. This coating could be further investigated to achieve a finer control of the nanorod interaction with cells. Firstly, the use of different polymers

(introducing different functional groups) could be assessed, as well as varying the layer thicknesses through variation of polymer concentration and/or salt concentration during coating. Additionally, one report[136] has demonstrated that addition of BSA to the third polyelectrolyte layer on gold nanorods, in a combined PSS-BSA coating, results in stable nanoparticles with improved drug loading efficiency and cell affinity, as well as being more resistant to oscillations in surface charge as a result of the formation of a protein corona. This would be a straightforward approach to implement and test in the current nanoparticle system, as the simple addition of BSA to the PSS wrapping solution would imply no changes in protocol, equipment or time used to produce the particles. Another possible route for improving nanorod coating features would be the use of biomimetic coatings such as polydopamine. It has been reported that biomimetic coatings can enhance nanoparticle uptake and nanovaccine adjuvanticity.[138-140] Gold nanorod coating with polydopamine was briefly tested during the course of this project, but more data would have to be gathered in terms of coating performance in cellular imaging and biomolecule delivery applications. Nevertheless, one example from the literature[218] reports that gold nanorods with polydopamine coating are not only stable in serum-containing culture medium but also represent a versatile platform for further coating with biomolecules. This indicates that polydopamine wrapping of nanorods could represent another avenue for taking the aims of this project forward.

When exposed to serum-containing medium, nanoparticles become coated with a layer of serum proteins, called protein corona. As described in chapter 1, the composition and properties of this protein layer depend very much on the initial properties of the nanoparticles.[99,100] In chapter 3, results from stability testing in serum-containing culture medium showed that nanorods with a PSS-PDDAC-PSS coating (negatively charged outer surface) endured the serum protein coating without aggregating, while PSS-PDDAC coated (positively charged) did not. In any case, further studies would have to be undertaken in order to further investigate this protein layer formation for different formulations of nanorods, especially when functionalised, as it has been suggested that some effects of particle functionalisation can be masked by the protein corona.[102] Specifically, exposing nanorod formulations to serum proteins under varying conditions (e.g. medium composition, temperature, duration) and performing protein quantification assays (see below), as well as assessing their interactions with cells, could provide a better understanding of this phenomenon. Such a comprehensive investigation would enhance control over the

interactions of nanorods with cells for clinical applications, and the microfluidic platform developed during this project would be the ideal tool for this assessment.

In terms of bioconjugation of gold nanorods to proteins, testing performed with BSA (chapter 3) and OVA (chapter 6) indicated the successful attachment of protein molecules to the polymer-coated gold nanorods. It is speculated that this attachment is due to the simple electrostatic interaction between the polyelectrolyte and the proteins. Additionally, chapter 6 presented a theoretical estimate of the number of molecules per nanorod, which was used for helping to interpret the data when compared to soluble protein. One important next development would be to quantify the real amount of protein on the surface of gold nanorods coated in these conditions, as well as to assess the repeatability of the coating procedure in terms of coverage and stability of the particles. For this, a specific protein quantification protocol would have to be established, considering the physical and chemical characteristics of the nanoparticles. Previous studies have reported the use of sodium dodecyl sulfate polyacrylamide gel electrophoresis (SDS-PAGE) for this purpose, alone or in combination with mass spectrometry, to assess nanoparticle functionalisation with peptides,[139] adsorption of serum proteins[73] or incorporation of BSA into a polyelectrolyte layer.[136] Another method that would be interesting to develop for this would be a fluid-based single-nanoparticle imaging tool, based on previous work by Wark et al,[219] to which a concept was developed during the course of this project. Specifically, a simple microfluidic channel created with two glass coverslips and adhesive tape walls was developed for nanoparticle imaging. The idea was that nanorods could be electrostatically coated onto the device surface and imaged in real-time, using dark-field and fluorescence microscopy, as stimuli were pumped into the channel. For instance, NR-DQOVA could be immobilised onto PDDAC-coated chambers and exposed to a solution of trypsin (a protease which would cleave the DQOVA substrates) while imaging. This simple experiment has the potential to obtain single-nanorod fluorescence, dark-field and SERS in real-time, before and after DQOVA cleavage. This should in turn provide information on the amount of protein on the nanorods and on the heterogeneity of coating between different individual particles. This data was not obtained during the course of this project due to time constraints – but would definitely be one of the subsequent steps for nanorod optimisation.

Another interesting feature of gold nanorod-mediated delivery that could be explored would be the triggered release of the carried molecules. This would ensure that the carried antigen (or drug) was not released before reaching the intracellular environment, minimising the

possibility of side-effects. Given that most of the uptake pathways through which dendritic cells take up nanomaterial involve processing within acidic vesicles, the existence of a pH sensitive polymer layer on the nanorods could trigger polymer detachment and subsequent antigen release from the surface. Importantly, the fact that DQOVA cleavage from the surface of nanorods was detected, with these vesicles being where proteases are most active, indicates that the nanorods used in this project may have been processed in this way. Thus, the use of pH-sensitive or degradable polyelectrolytes could be of interest, as an approach to pH-triggered drug release. Some groups have reported the use of pH-degradable polymer microcapsules for triggered drug delivery, either on their own[220] or containing functionalised gold nanoparticles inside.[221] Going back to polydopamine as a potential coating, its ability as a pH-triggered delivery agent has also been shown in the literature.[222] Specifically, mesoporous silica nanoparticles with embedded doxorubicin and polydopamine coating demonstrated gradual drug delivery at specific pH values.[222] This indicates that, if using that coating for the gold nanorods developed in this project, the same pH sensitivity could be tested for controlled antigen delivery.

7.1.2   Gold nanorods as cellular imaging tools

Multimodal imaging can provide important information on the biological fate of gold nanorods within cells, for example when used for the delivery of biomolecules. Results shown in chapter 3 demonstrated that the flexibility in gold nanorod aspect ratio and surface chemistry, including incorporation of multiple dyes, can result in very specific probes for intracellular imaging. Images obtained with fluorescence, dark-field and SERS on fixed cells with USTs confirmed the multimodal imaging potential of these particles. For the future, it would be interesting to return to these multi-dye combinations, in order to achieve a stable formulation that can be imaged using a range of wavelengths with high specificity and down to the single-nanoparticle level. Additionally, it would be important to perform this imaging on live cells, to obtain insight into the intracellular pathways involved in nanoparticle processing. Previous reports have shown that gold nanorods can be tracked intracellularly within live cells, with high resolution, using techniques such as two-photon luminescence or liquid STEM.[119,123,124] Here, to explore the potential of the developed multimodal imaging tags, it would be necessary to use an integrated imaging setup where at least SERS and confocal fluorescence could be obtained simultaneously on live cells, something that was not possible with the setup used in this work. This would be a natural future development that

combined with the microfluidic device would lead to high-throughput multimodal imaging of live single-cells. In chapter 6, it was shown that the intracellular localisation of the fluorescence signals from nanorods and fluorescently-labelled antigen molecules was not the same, suggesting that the antigen could have been removed from the surface of the particles. Using such high resolution imaging within the microfluidic device, the dynamics of intracellular processing of the nanovaccine model could be further investigated, potentially down to single-nanoparticle tracking[116,121] and antigen delivery monitoring at the molecular level.[130-133] This could provide a better understanding of the underlying biochemical events.

Due to their highly specific and strong signal, the developed gold nanorods have the potential to be monitored non-invasively *in vivo*. Reports found in the literature have demonstrated some of this ability for gold nanoparticles, mostly using SERS and fluorescence.[130,131,133,135,136] Following from the current project, it could be relevant to image the developed nanovaccine model *in vivo* using mouse models. This, if successful, would provide real-time information on nanorod trafficking, antigen delivery to dendritic cells, dendritic cell migration, and the fate of the nanorods following antigen delivery. Such techniques would be decisive in obtaining a deeper understanding of nanoparticle-mediated antigen delivery and, using different antigens and/or targeting molecules, could provide new insight into the immune system response.

7.1.3   Microfluidic platform: single-cell trapping and gradient formation

Chapter 4 described the various design iterations that led to a final microfluidic device design for cell trapping and nanoparticle gradient formation. Importantly, this development process consisted in a number of compromises between different conditions, towards the best possible combination of parameters that would make the overall aims of the project achievable within reasonable time and resource frames. This section will outline the aspects of the device which would deserve further optimisation and the possible routes for those improvements.

Results showed that primary dendritic cells could be successfully loaded into the microfluidic chamber, captured into the microtrap array and incubated on-chip, indicating that the device was amenable for real-time imaging of live cells over long periods. As mentioned in chapter 4, these experiments also demonstrated the heterogeneity of these primary cell samples, with great variability in size, shape and morphology of the dendritic cells leading to heterogeneous trapping. Chapter 4 described a number of parameters that were tested to

achieve the best possible cell trapping, from the trap design to the cell loading conditions, cell suspension concentration and perfusion flow rates. Further improvements in the cell trapping and long-term culture performance of the device could be achieved, for example, by micro-patterning of the trap areas[158] (e.g. 3D patterning of polymerisable matrices[24] or 2D patterning of adhesive molecules such as collagen[223] or poly-L-lysine[224]). These features would, however, increase the complexity of the fabrication process, and their incorporation would thus have to be weighed in terms of real benefit compared to simple hydrodynamic trapping. Additionally, the effect of these coatings on cellular response should also be assessed.

The use of PDMS devices, very common in biological applications of microfluidics due to their ease of fabrication, optical transparency, biocompatibility and gas permeability, should also be critically evaluated for this application.[153,209] Specifically, it has been reported[225] that PDMS can leach uncured oligomers into the cell culture environment and also absorb proteins and other small hydrophilic molecules from the medium. These features, together with the device surface properties, may affect cell function and viability, and their effect should thus be assessed within the current device to avoid misinterpretation of results.[209,225] Another possibility would be to adapt the developed design for fabrication in harder polymers, such as polystyrene, which is the traditional substrate for off-chip cell culture.[226]

The laminar flow conditions existent in microfluidic chambers can be used to achieve fine control of fluid mixing, for example, for the formation of concentration gradients. This is a useful feature, for example, to obtain data from trapped cells exposed to a range of well-defined concentrations of drugs or nanomaterials in a single chamber.[155] Gradient generation within the device was tested for fluorescein and fluorescent gold nanorods and compared with computational models to estimate the best flow rates to use. However, the syringe pumps used in the current experimental setup led to the occurrence of pulsatile flow at flow rates below ~0.5 µl/min, which was a limitation for gradient optimisation, especially for gold nanorods as these have a lower diffusion coefficient (Chapter 4). Consequently, a stable concentration gradient was formed using the device design and experimental setup developed here, but the nanorod concentration gradient occurred only across a narrow region at the centre of the array, with the sides displaying nearly constant fluorescence intensities corresponding to no nanorods on one side and the maximum concentration on the other. Therefore, further optimisation would be required in order to obtain the delivery of a gradual range of nanorod concentrations to the cells across the width of the device

chamber. One possible alteration would be to increase the width of the trapping chamber, which would allow for a less steep gradient of concentrations to be delivered across the array of trapped cells. In that case, the occurrence of pulsatile flow would have to be eliminated by using better performing syringe pumps. Investigation of different designs, namely the device with smaller parallel chambers shown in Figure 4.2 (a), would potentially lead to finer control of the concentrations delivered to the cells in each chamber. Additionally, the use of a channel network for gradient generation[18,155] could result in a more discrete set of stimuli that would provide high-throughput data on the interactions of cells with a range of well-defined doses of nanoparticles. However, the presence of these channel networks could affect the efficiency of cell loading into the device, a key aspect that would also have to be considered in future designs.

Another aspect to be considered would be the occurrence of non-specific adsorption of nanorods to the PDMS channel walls. During this work, it was observed that simple coating of the device surfaces with serum proteins prior to nanoparticle delivery successfully reduced this incidence. Similar procedures could be investigated for further optimisation, namely via adjustments in different factors such as surface functionalisation of the nanoparticles and/or of the channel walls.[227]

When performing experiments with the microfluidic system, it was observed that there was a possibility of occurrence of air bubbles within the fluidic setup. These could not only block the tubing and affect dispensing flow rates, but could also get trapped in the array chamber, affecting cell viability and nanoparticle delivery profiles. In the current work this was minimised by extreme care in withdrawing and dispensing liquids, plugging in connectors and managing flow rates. However, a simple practical improvement to further minimise these blockages would be the introduction of a bubble-trapping feature[228] into the device design, leading to more robust testing of the developed platform.

7.1.4   Real-time and multimodal imaging of cell-nanorod interactions

In chapter 5, the aim was to demonstrate the successful integration of the microfluidic device designed in chapter 4 with the gold nanorod formulation developed in chapter 3 to achieve on-chip real-time imaging of cell-nanoparticle interactions. Importantly, this work used biologically-relevant primary cells in all experiments, which presents numerous advantages over previous work using cell lines, especially when translating results towards *in vivo* development.[192] Initially, nanorods were tested off-chip with cells, in order to obtain

information on nanorod uptake, intracellular location and biocompatibility using conventional techniques. Results obtained provided information on the timings of nanoparticle uptake, with nanorod fluorescence being detected significantly by flow cytometry from 45 minutes of exposure, and provided a baseline for comparing results obtained on-chip. Confocal fluorescence imaging of dendritic cells exposed to nanorods confirmed nanoparticle internalisation and indicated discrete, highly concentrated areas of nanorods within the cell. This is consistent with the generally accepted mechanisms for nanomaterial uptake by cells, which involve the formation of endocytic vesicles in most cases.[87,90] Additionally, toxicity testing indicated good biocompatibility of the particles up to 24 h exposure. These results indicated that the nanoparticles would be suitable for on-chip testing with live cells.

As previously mentioned, in static cell culture conditions nanoparticles tend to sediment to the bottom of the plate soon after inoculation of the cultures, leading to heterogeneous distribution of particles to cells.[22] Additionally, under those conditions, motile dendritic cells scan the surface and take up nanorods for as long as they are available, which has a potential effect on the actual nanoparticle dose the cells receive, especially during longer incubation times. This "vacuuming" effect has been explored by other groups[212] to assess cell-nanoparticle interactions, in a different setup where the effect of different nanoparticle formulations on cell migration characteristics was tested. However, for the present study, it was crucial to consider physiological conditions for nanomaterial delivery, which were achieved under the laminar flow environment within the microfluidic platform. Another advantage of the microfluidic chamber for delivery of nanoparticles was the control of the exposure time – for on-chip viability studies, for example, cells were pulsed with nanorods for 2 hours only before assessing viability either immediately following exposure or after 24 hours. This way, the occurrence of long-term effects from the same degree of exposure to nanorods could be assessed, rather than the effect of cumulative uptake over 24 hours. For clinical applications, this is expected to be the most plausible scenario, where the organism is exposed to a certain dose of nanoparticle-based drugs or vaccines for a short period of time, due to the natural clearance of nanoparticles that is expected to occur *in vivo*.[104-107]

Following the off-chip testing of nanorods with primary dendritic cells, chapter 5 presented results demonstrating this integration. Firstly, nanoparticle delivery to trapped cells in gradient form was tested and assessed using fluorescence microscopy of the live cells. Subsequently, different techniques such as confocal fluorescence and Raman spectroscopy

were used to obtain signal from intracellular nanorods in trapped cells, confirming the suitability of the device and procedures developed for that purpose. Building upon this, nanorod uptake by trapped cells could then be assessed in real-time using fluorescence microscopy, with results showing that the fluorescence intensity of cells within the device increased with exposure time and consistently with flow cytometry results for short-term exposure. These results, together with on-chip cytotoxicity data, demonstrated the ability of the developed platform to obtain real-time information on the interaction of nanoparticles with cells, a crucial feature for testing nanomaterials.[17,23] Here, it would be important to further investigate the effect of the nanoparticles on cells, through functional testing beyond simple cell death measures, such as assessing effects on mitochondrial membrane potential or intracellular oxidative stress. The developed microfluidic platform would be a useful tool to obtain this data in high-throughput, with single-cell resolution.

In order to explore the possibility of performing multimodal imaging assessment of the interactions of nanoparticles with cells, SERRS maps were obtained from trapped cells which were fixed following on-chip nanorod exposure. As mentioned in chapter 1, proof-of-concept works from the literature have shown SERS-based nanoparticle detection in similar microfluidic single-cell arrays.[185] However, that study failed to investigate the dynamic interactions between cells and nanoparticles, as the cells were exposed to nanoparticles prior to being loaded into the device. In the current work, as shown in chapter 5, SERRS maps of cells trapped in different positions of the array showed consistency between the fluorescence signal and the SERRS signal obtained from intracellular nanoparticles. This, together with the future goal of using an integrated imaging setup for combined SERS/SERRS mapping and fluorescence imaging in real-time, will open way for unprecedented[17,23] information on the effect of nanomaterial on cells at the population and single-cell levels.

A more complex three-dimensional cell culture model could also be used within this microfluidic device. One group[229] has recently reported a similar approach for hepatocyte aggregates with scaffolding (e.g. hydrogel) which were formed into bead-like structures and trapped into a similar microtrap array. This provided the high-throughput, perfusion versatility and individual trap imaging ability of the trapping device with the added features of three-dimensional models, which could be used for applications such as cancer drug screening.

7.1.5   Real-time monitoring of nanovaccine delivery in the microfluidic device

As a demonstration of the functionality of the developed system, a nanovaccine model was prepared, based on the developed gold nanorods, so that real-time assessment of nanoparticle-mediated antigen delivery could be obtained on-chip. This work was presented in chapter 6 and has been published in Lab on a Chip.[165] Firstly, nanorods were conjugated to OVA molecules bound to a fluorophore which becomes fluorescent only when cleaved by proteases, as an indicator of antigen processing. These particles were tested off-chip and results demonstrated that this fluorophore could be visualised in cells that were previously exposed to the nanovaccines. Additionally, the same nanovaccines could induce antigen presentation to OVA-specific T cells with subsequent T cell activation, proliferation and effector function having been successfully detected. This indicated the functionality of the model nanovaccine and also suggested that these particles may have strong adjuvant activity when it comes to antigen-specific lymphocyte activation. It is important to note that the specific mechanism through which adjuvants enhance the immune response is still a controversial topic.[217] In any case, data shown in Chapter 6 not only indicated that NR could facilitate antigen uptake (section 6.2.3) but also that NR-mediated delivery of antigen could have a very significant effect in increasing lymphocyte response (section 6.2.1). This is consistent with previous reports of gold nanorod adjuvanticity[9] which, together with their optical capabilities, underlines the potential of gold nanorods for efficient (and tracked) vaccine delivery applications.

Subsequent delivery of a nanovaccine concentration gradient into the microfluidic trapping array with primary dendritic cells allowed for real-time monitoring of both nanorod uptake and OVA processing using fluorescence microscopy. Importantly, the experimental setup used for obtaining the data in chapter 6 allowed for wide-field time-lapse images to be acquired over several hours, something which was not possible with the setup used for data shown in previous chapters, where both the image acquisition and stitching were done manually. This enabled the collection of data from hundreds of single-cells simultaneously at short intervals, providing a truly dynamic picture of their interaction with the nanovaccines. Additionally, results obtained represented a throughput that can be comparable with that of standard flow cytometry, but from very small sample volumes and at the single-cell level. Specifically, the number of cells required for one microfluidic experiment, providing the full range of data presented in section 6.3, was approximately 300 times less (section 6.6) than

to run the equivalent experiment in static culture wells. This feature is particularly important for applications involving rare cell samples or patient-derived cells.

The developed method represents a cost-saving and time-effective screening tool, when compared to standard flow cytometry techniques. For the current work, following the first silicon master fabrication, PDMS device prototyping (which could be done repeatedly using the same wafer) took one day and yielded up to 12 devices. Each device (or two devices in parallel) could then be used for one experiment which involved preparing the fluid handling setup and setting up the microscope, as well as cell harvesting prior to loading into the device, in a total of approximately two hours. After this, the experiment could be run seamlessly, from cell trapping, to nanoparticle dispensing and time-lapse imaging. Thus, taking the nanovaccine experiments as an example, one experiment would typically take 24 h to run, with very little user intervention besides the initial setup, and providing a comprehensive set of data on hundreds of cells over several hours. To replicate this data using a flow cytometer would not even be feasible due to the time taken to prepare and read samples being longer than the time intervals of the images taken here.

The data obtained from time-lapse imaging of the array of trapped cells provided information on the distribution of nanoparticles across the chamber and consequent levels of uptake by cells located in different regions of the array, at the population and single-cell levels. Further analysis provided insight into the heterogeneity of the cellular response, with cells exposed to the same concentration of nanoparticles displaying very different uptake and antigen processing responses. As mentioned in chapter 1, the heterogeneity of cell function is generally overlooked when using conventional methods that focus on the average response of the cell population.[31] However, it has been demonstrated that looking at the range of individual cell responses can provide important information on the effect of nanomaterials on cells.[109] The proof-of-concept experiments described in chapter 6 demonstrated the ability of the developed system to provide information on this heterogeneity of cell behaviour, while also providing high-throughput information on the overall cell response. In the future, to support these results, the homogeneity of chamber dimensions and consequently of fluidic conditions throughout the whole cell array should be verified. For example, monodisperse beads of known dimensions could be injected into the array to evaluate chamber depth consistency. These experiments would rule out the possibility of cellular heterogeneity being due to variations in, for example, shear stress or nanoparticle delivery conditions. Following this confirmation that the observed heterogeneity of response

is due to cellular heterogeneity only, the developed tool can be used to further drive the development of better nanovaccines. For example, on-chip cell pairing experiments could be designed to evaluate the communication between dendritic cells and T cells following nanovaccine exposure, using a variety of readouts, concomitantly with other on-chip cell pairing experiments.[49]

As a future development, it would also be relevant to address real-world problems by using the platform to develop novel vaccine models for specific diseases. For example, investigation of the effect of pathogens such as *Leishmania* on the behaviour of dendritic cells and subsequent investigation of potential nanovaccines could lead to improvements in prevention and treatment of associated disease states. Specifically, the importance of adjuvants in effective *Leishmania* immunisation[214] and the fact that gold nanorods have demonstrated strong adjuvant ability[9] could mean that this is a potential application for gold nanorod-based vaccines.

7.2 Conclusion

This thesis has described the development and proof-of-concept of a microfluidic platform and associated procedures towards an integrated platform for real-time assessment of nanoparticle-cell interactions. Specifically, the following capabilities were demonstrated for this system:

- High-throughput measurement of the average response of a cell population;
- Single-cell function and viability assessment;
- Live single-cell tracking and monitoring over long periods of time (up to 24 h);
- Controlled multi-step reagent delivery under laminar flow conditions, which are of physiological relevance;
- Controlled time delivery of reagents and clean monitoring of cells after exposure;
- Real-time delivery of a range of nanoparticle concentrations to cells;
- Dynamic, real-time assessment of cell-nanoparticle interactions;
- Ability to assess nanoparticle uptake using multimodal imaging techniques;
- Potential for single-nanoparticle intracellular tracking and live biomolecule delivery monitoring.

Overall, this very interdisciplinary project has brought together technical strengths from different areas into one integrated platform, providing great improvements over existing monitoring procedures for investigating nanoparticle-cell interactions. Proof-of-concept was achieved with a nanovaccine model, tested in real-time on hundreds of primary dendritic cells. Importantly, the developed system also has the potential for high-resolution intracellular tracking of nanoparticles and adaptability to different cell and nanomaterial types, making it a versatile tool for the initial screening of nanomaterials for biomedical applications.

References

1.   L. K. Bogart, G. Pourroy, C. J. Murphy, V. Puntes, T. Pellegrino, D. Rosenblum, D. Peer, R. Lévy. Nanoparticles for Imaging, Sensing, and Therapeutic Intervention. *Acs Nano* 8, 3107-3122 (2014).

2.   E. C. Dreaden, A. M. Alkilany, X. Huang, C. J. Murphy, M. A. El-Sayed. The golden age: gold nanoparticles for biomedicine. *Chemical Society Reviews* 41, 2740-2779 (2012).

3.   L. Zhao, A. Seth, N. Wibowo, C.-X. Zhao, N. Mitter, C. Yu, A. P. J. Middelberg. Nanoparticle vaccines. *Vaccine* 32, 327-337 (2014).

4.   A. M. Alkilany, L. B. Thompson, S. P. Boulos, P. N. Sisco, C. J. Murphy. Gold nanorods: Their potential for photothermal therapeutics and drug delivery, tempered by the complexity of their biological interactions. *Advanced Drug Delivery Reviews* 64, 190-199 (2012).

5.   B. D. Chithrani, A. A. Ghazani, W. C. W. Chan. Determining the Size and Shape Dependence of Gold Nanoparticle Uptake into Mammalian Cells. *Nano Letters* 6, 662-668 (2006).

6.   H. Herd, N. Daum, A. T. Jones, H. Huwer, H. Ghandehari, C.-M. Lehr. Nanoparticle Geometry and Surface Orientation Influence Mode of Cellular Uptake. *Acs Nano* 7, 1961-1973 (2013).

7.   A. M. Alkilany, P. K. Nagaria, C. R. Hexel, T. J. Shaw, C. J. Murphy, M. D. Wyatt. Cellular Uptake and Cytotoxicity of Gold Nanorods: Molecular Origin of Cytotoxicity and Surface Effects. *Small* 5, 701-708 (2009).

8.   K. L. Cheung, H. Chen, Q. Chen, J. Wang, H. P. Ho, C. K. Wong, S. K. Kong. CTAB-coated gold nanorods elicit allergic response through degranulation and cell death in human basophils. *Nanoscale* 4, 4447-4449 (2012).

9.   L. Xu, Y. Liu, Z. Chen, W. Li, Y. Liu, L. Wang, Y. Liu, X. Wu, Y. Ji, Y. Zhao et al. Surface-Engineered Gold Nanorods: Promising DNA Vaccine Adjuvant for HIV-1 Treatment. *Nano Letters* 12, 2003-2012 (2012).

10.   S. T. Kim, K. Saha, C. Kim, V. M. Rotello. The Role of Surface Functionality in Determining Nanoparticle Cytotoxicity. *Accounts of Chemical Research* (2013).

11.   J. Wan, J.-H. Wang, T. Liu, Z. Xie, X.-F. Yu, W. Li. Surface chemistry but not aspect ratio mediates the biological toxicity of gold nanorods in vitro and in vivo. *Scientific Reports* 5, 11398 (2015).

12. D. Hühn, K. Kantner, C. Geidel, S. Brandholt, I. De Cock, S. J. H. Soenen, P. Rivera_Gil, J.-M. Montenegro, K. Braeckmans, K. Müllen et al. Polymer-Coated Nanoparticles Interacting with Proteins and Cells: Focusing on the Sign of the Net Charge. *Acs Nano* 7, 3253-3263 (2013).

13. T. A. Larson, P. P. Joshi, K. Sokolov. Preventing Protein Adsorption and Macrophage Uptake of Gold Nanoparticles via a Hydrophobic Shield. *Acs Nano* 6, 9182-9190 (2012).

14. M. Mahmoudi, M. A. Shokrgozar, S. Behzadi. Slight temperature changes affect protein affinity and cellular uptake/toxicity of nanoparticles. *Nanoscale* 5, 3240-3244 (2013).

15. P. P. Pillai, S. Huda, B. Kowalczyk, B. A. Grzybowski. Controlled pH Stability and Adjustable Cellular Uptake of Mixed-Charge Nanoparticles. *Journal of the American Chemical Society* 135, 6392-6395 (2013).

16. A. M. Alkilany, C. J. Murphy. Toxicity and cellular uptake of gold nanoparticles: what we have learned so far? *Journal of Nanoparticle Research* 12, 2313-2333 (2010).

17. P. Shah, A. Kaushik, X. Zhu, C. Zhang, C.-Z. Li. Chip based single cell analysis for nanotoxicity assessment. *Analyst* 139, 2088-2098 (2014).

18. S. K. W. Dertinger, D. T. Chiu, N. L. Jeon, G. M. Whitesides. Generation of Gradients Having Complex Shapes Using Microfluidic Networks. *Analytical Chemistry* 73, 1240-1246 (2001).

19. G. M. Whitesides. The origins and the future of microfluidics. *Nature* 442, 368-373 (2006).

20. P. M. Valencia, E. M. Pridgen, M. Rhee, R. Langer, O. C. Farokhzad, R. Karnik. Microfluidic Platform for Combinatorial Synthesis and Optimization of Targeted Nanoparticles for Cancer Therapy. *ACS Nano* 7, 10671-10680 (2013).

21. J. Thiele, M. Windbergs, A. R. Abate, M. Trebbin, H. C. Shum, S. Forster, D. A. Weitz. Early development drug formulation on a chip: Fabrication of nanoparticles using a microfluidic spray dryer. *Lab on a Chip* 11, 2362-2368 (2011).

22. S. K. Mahto, T. H. Yoon, S. W. Rhee. A new perspective on in vitro assessment method for evaluating quantum dot toxicity by using microfluidics technology. *Biomicrofluidics* 4, 034111 (2010).

23. V. Giridharan, Y. Yun, P. Hajdu, L. Conforti, B. Collins, Y. Jang, J. Sankar. Microfluidic Platforms for Evaluation of Nanobiomaterials: A Review. *Journal of Nanomaterials* 2012, 789841 (2012).

24. Y. Qiao, J. An, L. Ma. Single cell array based assay for in vitro genotoxicity study of nanomaterials. *Analytical Chemistry* 85, 4107-4112 (2013).

25. D. Huh, Y. S. Torisawa, G. A. Hamilton, H. J. Kim, D. E. Ingber. Microengineered physiological biomimicry: Organs-on-Chips. *Lab on a Chip* 12, 2156-2164 (2012).

26. A. Albanese, A. K. Lam, E. A. Sykes, J. V. Rocheleau, W. C. W. Chan. Tumour-on-a-chip provides an optical window into nanoparticle tissue transport. *Nature Communications* 4, 2718 (2013).

27. B. Kwak, A. Ozcelikkale, C. S. Shin, K. Park, B. Han. Simulation of complex transport of nanoparticles around a tumor using tumor-microenvironment-on-chip. *Journal of Controlled Release* 194, 157-167 (2014).

28. M. B. Esch, G. J. Mahler, T. Stokor, M. L. Shuler. Body-on-a-chip simulation with gastrointestinal tract and liver tissues suggests that ingested nanoparticles have the potential to cause liver injury. *Lab on a Chip* 14, 3081-3092 (2014).

29. D. Di Carlo, L. Y. Wu, L. P. Lee. Dynamic single cell culture array. *Lab on a Chip* 6, 1445-1449 (2006).

30. D. Wlodkowic, S. Faley, M. Zagnoni, J. P. Wikswo, J. M. Cooper. Microfluidic Single-Cell Array Cytometry for the Analysis of Tumor Apoptosis. *Analytical Chemistry* 81, 5517-5523 (2009).

31. H. Yin, D. Marshall. Microfluidics for single cell analysis. *Current Opinion in Biotechnology* 23, 110-119 (2012).

32. J. El-Ali, P. K. Sorger, K. F. Jensen. Cells on chips. *Nature* 442, 403-411 (2006).

33. M. A. Walling, J. R. E. Shepard. Cellular heterogeneity and live cell arrays. *Chemical Society Reviews* 40, 4049-4076 (2011).

34. J. J. Moon, B. Huang, D. J. Irvine. Engineering Nano- and Microparticles to Tune Immunity. *Advanced Materials* 24, 3724-3746 (2012).

35. M. Zaman, M. F. Good, I. Toth. Nanovaccines and their mode of action. *Methods* 60, 226-231 (2013).

36. K. Murphy, P. Travers, M. Walport, C. Janeway. *Janeway's immunobiology*. 8th edition, Garland Science (2012).

37. L. E. Paulis, S. Mandal, M. Kreutz, C. G. Figdor. Dendritic cell-based nanovaccines for cancer immunotherapy. *Current Opinion in Immunology* 25, 389-395 (2013).

38. S. T. Reddy, M. A. Swartz, J. A. Hubbell. Targeting dendritic cells with biomaterials: developing the next generation of vaccines. *Trends in Immunology* 27, 573-579 (2006).

39. L. J. Cruz, P. J. Tacken, J. M. Pots, R. Torensma, S. I. Buschow, C. G. Figdor. Comparison of antibodies and carbohydrates to target vaccines to human dendritic cells via DC-SIGN. *Biomaterials* 33, 4229-4239 (2012).

40. M. Kreutz, P. J. Tacken, C. G. Figdor. Targeting dendritic cells—why bother? *Blood* 121, 2836-2844 (2013).

41. P. J. Tacken, I. S. Zeelenberg, L. J. Cruz, M. A. van Hout-Kuijer, G. van de Glind, R. G. Fokkink, A. J. A. Lambeck, C. G. Figdor. Targeted delivery of Toll-like receptor ligands to human and mouse dendritic cells strongly enhances adjuvanticity. *Blood* 118, 6836-6844 (2011).

42. A. McLintock, C. A. Cunha-Matos, M. Zagnoni, O. R. Millington, A. W. Wark. Universal Surface-Enhanced Raman Tags: Individual Nanorods for Measurements from the Visible to the Infrared (514–1064 nm). *Acs Nano* 8, 8600-8609 (2014).

43. C. J. Murphy, T. K. San, A. M. Gole, C. J. Orendorff, J. X. Gao, L. Gou, S. E. Hunyadi, T. Li. Anisotropic metal nanoparticles: Synthesis, assembly, and optical applications. *Journal of Physical Chemistry B* 109, 13857-13870 (2005).

44. M. Junkin, S. Tay. Microfluidic single-cell analysis for systems immunology. *Lab on a Chip* 14, 1246-1260 (2014).

45. S. Mahmood, S. Nandagopal, I. Sow, F. Lin, S. K. P. Kung. Microfluidic-based, live-cell analysis allows assessment of NK-cell migration in response to crosstalk with dendritic cells. *European Journal of Immunology* 44, 2737-2748 (2014).

46. N. Gopalakrishnan, R. Hannam, G. P. Casoni, D. Barriet, J. M. Ribe, M. Haug, O. Halaas. Infection and immunity on a chip: a compartmentalised microfluidic platform to monitor immune cell behaviour in real time. *Lab on a Chip* 15, 1481-1487 (2015).

47. S. Faley, K. Seale, J. Hughey, D. K. Schaffer, S. VanCompernolle, B. McKinney, F. Baudenbacher, D. Unutmaz, J. P. Wikswo. Microfluidic platform for real-time signaling analysis of multiple single T cells in parallel. *Lab on a Chip* 8, 1700-1712 (2008).

48. I. Zaretsky, M. Polonsky, E. Shifrut, S. Reich-Zeliger, Y. E. Antebi, G. Aidelberg, N. Waysbort, N. Friedman. Monitoring the dynamics of primary T cell activation and differentiation using long term live cell imaging in microwell arrays. *Lab on a Chip* 12, 5007-5015 (2012).

49. B. Dura, S. K. Dougan, M. Barisa, M. M. Hoehl, C. T. Lo, H. L. Ploegh, J. Voldman. Profiling lymphocyte interactions at the single-cell level by microfluidic cell pairing. *Nature Communications* 6, 5940 (2015).

50. J. L. Garcia-Cordero, C. Nembrini, A. Stano, J. A. Hubbell, S. Maerkl. A high-throughput nanoimmunoassay chip applied to large-scale vaccine adjuvant screening. *Integrative Biology* 5, 650-658 (2013).

51. P. M. Valencia, O. C. Farokhzad, R. Karnik, R. Langer. Microfluidic technologies for accelerating the clinical translation of nanoparticles. *Nature Nanotechnology* 7, 623-629 (2012).

52. J. Wu, Q. Chen, W. Liu, J.-M. Lin. A simple and versatile microfluidic cell density gradient generator for quantum dot cytotoxicity assay. *Lab on a Chip* 13, 1948-1954 (2013).

53. F. Sambale, F. Stahl, D. Bahnemann, T. Scheper. In vitro toxicological nanoparticle studies under flow exposure. *Journal of Nanoparticle Research* 17, 1-12, 298 (2015).

54. J. Banchereau, F. Briere, C. Caux, J. Davoust, S. Lebecque, Y.-J. Liu, B. Pulendran, K. Palucka. Immunobiology of Dendritic Cells. *Annual Review of Immunology* 18, 767-811 (2000).

55. J. A. Hubbell, S. N. Thomas, M. A. Swartz. Materials engineering for immunomodulation. *Nature* 462, 449-460 (2009).

56. S. T. Reddy, A. J. van der Vlies, E. Simeoni, V. Angeli, G. J. Randolph, C. P. O'Neil, L. K. Lee, M. A. Swartz, J. A. Hubbell. Exploiting lymphatic transport and complement activation in nanoparticle vaccines. *Nature Biotechnology* 25, 1159-1164 (2007).

57. C. Kilkenny, W. J. Browne, I. C. Cuthill, M. Emerson, D. G. Altman. Improving Bioscience Research Reporting: The ARRIVE Guidelines for Reporting Animal Research. *PLoS Biology* 8, e1000412 (2010).

58. Q. Ramadan, M. A. M. Gijs. In vitro micro-physiological models for translational immunology. *Lab on a Chip* 15, 614-636 (2015).

59. S. Baratchi, K. Khoshmanesh, C. Sacristán, D. Depoil, D. Wlodkowic, P. McIntyre, A. Mitchell. Immunology on chip: Promises and opportunities. *Biotechnology Advances* 32, 333-346 (2014).

60. C. J. Murphy, A. M. Gole, S. E. Hunyadi, J. W. Stone, P. N. Sisco, A. Alkilany, B. E. Kinard, P. Hankins. Chemical sensing and imaging with metallic nanorods. *Chemical Communications*, 544-557 (2008).

61. N. D. Burrows, W. Lin, J. G. Hinman, J. M. Dennison, A. M. Vartanian, N. S. Abadeer, E. M. Grzincic, L. M. Jacob, J. Li, C. J. Murphy. Surface Chemistry of Gold Nanorods. *Langmuir* 32, 9905-9921 (2016).

62. K. L. Kelly, E. Coronado, L. L. Zhao, G. C. Schatz. The optical properties of metal nanoparticles: The influence of size, shape, and dielectric environment. *Journal of Physical Chemistry B* 107, 668-677 (2003).

63. H. Chen, X. Kou, Z. Yang, W. Ni, J. Wang. Shape- and Size-Dependent Refractive Index Sensitivity of Gold Nanoparticles. *Langmuir* 24, 5233-5237 (2008).

64. P. Zijlstra, P. M. R. Paulo, M. Orrit. Optical detection of single non-absorbing molecules using the surface plasmon resonance of a gold nanorod. *Nature Nanotechnology* 7, 379-382 (2012).

65. I. A. Larmour, D. Graham. Surface enhanced optical spectroscopies for bioanalysis. *The Analyst* 136, 3831-3853 (2011).

66. T. K. Sau, C. J. Murphy. Seeded high yield synthesis of short Au nanorods in aqueous solution. *Langmuir* 20, 6414-6420 (2004).

67. B. Nikoobakht, M. A. El-Sayed. Preparation and growth mechanism of gold nanorods (NRs) using seed-mediated growth method. *Chemistry of Materials* 15, 1957-1962 (2003).

68. A. McLintock, N. Hunt, A. W. Wark. Controlled side-by-side assembly of gold nanorods and dye molecules into polymer-wrapped SERRS-active clusters. *Chemical Communications* 47, 3757-3759 (2011).

69. A. McLintock, H. J. Lee, A. W. Wark. Stabilized gold nanorod-dye conjugates with controlled resonance coupling create bright surface-enhanced resonance Raman nanotags. *Physical Chemistry Chemical Physics* 15, 18835-18843 (2013).

70. A. M. Alkilany, R. L. Frey, J. L. Ferry, C. J. Murphy. Gold Nanorods as Nanoadmicelles: 1-Naphthol Partitioning into a Nanorod-Bound Surfactant Bilayer. *Langmuir* 24, 10235-10239 (2008).

71. A. Gole, C. J. Murphy. Polyelectrolyte-coated gold nanorods: Synthesis, characterization and immobilization. *Chemistry of Materials* 17, 1325-1330 (2005).

72. H. Ding, K.-T. Yong, I. Roy, H. E. Pudavar, W. C. Law, E. J. Bergey, P. N. Prasad. Gold nanorods coated with multilayer polyelectrolyte as contrast agents for multimodal imaging. *Journal of Physical Chemistry C* 111, 12552-12557 (2007).

73. P. N. Sisco, C. G. Wilson, D. Chernak, J. C. Clark, E. M. Grzincic, K. Ako-Asare, E. C. Goldsmith, C. J. Murphy. Adsorption of Cellular Proteins to Polyelectrolyte-Functionalized Gold Nanorods: A Mechanism for Nanoparticle Regulation of Cell Phenotype? *PLoS One* 9, e86670 (2014).

74. E. Smith, G. Dent. *Modern Raman Spectroscopy - A Practical Approach*. John Wiley & Sons, Ltd (2005).

75. C. L. Haynes, A. D. McFarland, R. P. Van Duyne. Surface-enhanced Raman spectroscopy. *Analytical Chemistry* 77, 338A-346A (2005).

76. K. Kneipp, H. Kneipp, I. Itzkan, R. R. Dasari, M. S. Feld. Surface-enhanced Raman scattering and biophysics. *Journal of Physics: Condensed Matter* 14, R597–R624 (2002).

77. P. L. Stiles, J. A. Dieringer, N. C. Shah, R. P. Van Duyne. Surface-Enhanced Raman Spectroscopy. *Annual Review of Analytical Chemistry* 1, 601-626 (2008).

78. G. McNay, D. Eustace, W. E. Smith, K. Faulds, D. Graham. Surface-Enhanced Raman Scattering (SERS) and Surface-Enhanced Resonance Raman Scattering (SERRS): A Review of Applications. *Applied Spectroscopy* 65, 825-837 (2011).

79. Y. Wang, B. Yan, L. Chen. SERS Tags: Novel Optical Nanoprobes for Bioanalysis. *Chemical Reviews* 113, 1391-1428 (2012).

80. Y. Wang, S. Schlucker. Rational design and synthesis of SERS labels. *Analyst* 138, 2224-2238 (2013).

81. J. Kneipp, H. Kneipp, A. Rajadurai, R. W. Redmond, K. Kneipp. Optical probing and imaging of live cells using SERS labels. *Journal of Raman Spectroscopy* 40, 1-5 (2009).

82. K. Willets. Surface-enhanced Raman scattering (SERS) for probing internal cellular structure and dynamics. *Analytical and Bioanalytical Chemistry* 394, 85-94 (2009).

83. K. L. Wustholz, A.-I. Henry, J. M. McMahon, R. G. Freeman, N. Valley, M. E. Piotti, M. J. Natan, G. C. Schatz, R. P. V. Duyne. Structure–Activity Relationships in Gold Nanoparticle Dimers and Trimers for Surface-Enhanced Raman Spectroscopy. *Journal of the American Chemical Society* 132, 10903-10910 (2010).

84.   L. Xu, H. Kuang, C. Xu, W. Ma, L. Wang, N. A. Kotov. Regiospecific Plasmonic Assemblies for in Situ Raman Spectroscopy in Live Cells. *Journal of the American Chemical Society* 134, 1699-1709 (2012).

85.   A. Albanese, W. C. W. Chan. Effect of Gold Nanoparticle Aggregation on Cell Uptake and Toxicity. *Acs Nano* 5, 5478-5489 (2011).

86.   P. Rivera-Gil, D. Jimenez De Aberasturi, V. Wulf, B. Pelaz, P. Del Pino, Y. Zhao, J. M. De La Fuente, I. Ruiz De Larramendi, T. Rojo, X.-J. Liang et al. The Challenge To Relate the Physicochemical Properties of Colloidal Nanoparticles to Their Cytotoxicity. *Accounts of Chemical Research* 46, 743-749 (2012).

87.   L. Y. T. Chou, K. Ming, W. C. W. Chan. Strategies for the intracellular delivery of nanoparticles. *Chemical Society Reviews* 40, 233-245 (2011).

88.   F. M. Mickler, L. Möckl, N. Ruthardt, M. Ogris, E. Wagner, C. Bräuchle. Tuning Nanoparticle Uptake: Live-Cell Imaging Reveals Two Distinct Endocytosis Mechanisms Mediated by Natural and Artificial EGFR Targeting Ligand. *Nano Letters* 12, 3417-3423 (2012).

89.   V. Marchesano, Y. Hernandez, W. Salvenmoser, A. Ambrosone, A. Tino, B. Hobmayer, J. M. De La Fuente, C. Tortiglione. Imaging Inwards and Outwards Trafficking of Gold Nanoparticles in Whole Animals. *Acs Nano* 7, 2431-2442 (2013).

90.   F. Zhao, Y. Zhao, Y. Liu, X. Chang, C. Chen, Y. Zhao. Cellular Uptake, Intracellular Trafficking, and Cytotoxicity of Nanomaterials. *Small* 7, 1322-1337 (2011).

91.   A. Huefner, D. Septiadi, B. D. Wilts, Patel, II, W. L. Kuan, A. Fragniere, R. A. Barker, S. Mahajan. Gold nanoparticles explore cells: Cellular uptake and their use as intracellular probes. *Methods* 68, 354-363 (2014).

92.   C. Huang, P. J. Butler, S. Tong, H. S. Muddana, G. Bao, S. Zhang. Substrate Stiffness Regulates Cellular Uptake of Nanoparticles. *Nano Letters* 13, 1611-1615 (2013).

93.   Y. Qiu, Y. Liu, L. Wang, L. Xu, R. Bai, Y. Ji, X. Wu, Y. Zhao, Y. Li, C. Chen. Surface chemistry and aspect ratio mediated cellular uptake of Au nanorods. *Biomaterials* 31, 7606-7619 (2010).

94.   B. D. Chithrani, W. C. W. Chan. Elucidating the Mechanism of Cellular Uptake and Removal of Protein-Coated Gold Nanoparticles of Different Sizes and Shapes. *Nano Letters* 7, 1542-1550 (2007).

95. D. Bartczak, O. L. Muskens, S. Nitti, T. Sanchez-Elsner, T. M. Millar, A. G. Kanaras. Interactions of Human Endothelial Cells with Gold Nanoparticles of Different Morphologies. *Small* 8, 122-130 (2012).

96. T. S. Hauck, A. A. Ghazani, W. C. W. Chan. Assessing the Effect of Surface Chemistry on Gold Nanorod Uptake, Toxicity, and Gene Expression in Mammalian Cells. *Small* 4, 153-159 (2008).

97. C. Kinnear, H. Dietsch, M. J. D. Clift, C. Endes, B. Rothen-Rutishauser, A. Petri-Fink. Gold Nanorods: Controlling Their Surface Chemistry and Complete Detoxification by a Two-Step Place Exchange. *Angewandte Chemie* 52, 1934-1938 (2013).

98. T. B. Huff, M. N. Hansen, Y. Zhao, J.-X. Cheng, A. Wei. Controlling the Cellular Uptake of Gold Nanorods. *Langmuir* 23, 1596-1599 (2007).

99. M. Lundqvist, J. Stigler, G. Elia, I. Lynch, T. Cedervall, K. A. Dawson. Nanoparticle size and surface properties determine the protein corona with possible implications for biological impacts. *Proceedings of the National Academy of Sciences* 105, 14265-14270 (2008).

100. S. Tenzer, D. Docter, J. Kuharev, A. Musyanovych, V. Fetz, R. Hecht, F. Schlenk, D. Fischer, K. Kiouptsi, C. Reinhardt et al. Rapid formation of plasma protein corona critically affects nanoparticle pathophysiology. *Nature Nanotechnology* 8, 772-781 (2013).

101. C. D. Walkey, J. B. Olsen, H. Guo, A. Emili, W. C. W. Chan. Nanoparticle Size and Surface Chemistry Determine Serum Protein Adsorption and Macrophage Uptake. *Journal of the American Chemical Society* 134, 2139-2147 (2011).

102. A. Salvati, A. S. Pitek, M. P. Monopoli, K. Prapainop, F. B. Bombelli, D. R. Hristov, P. M. Kelly, C. Aberg, E. Mahon, K. A. Dawson. Transferrin-functionalized nanoparticles lose their targeting capabilities when a biomolecule corona adsorbs on the surface. *Nature Nanotechnology* 8, 137-143 (2013).

103. J. C. Y. Kah, J. Chen, A. Zubieta, K. Hamad-Schifferli. Exploiting the Protein Corona around Gold Nanorods for Loading and Triggered Release. *Acs Nano* 6, 6730-6740 (2012).

104. A. D. Ostrowski, T. Martin, J. Conti, I. Hurt, B. H. Harthorn. Nanotoxicology: characterizing the scientific literature, 2000–2007. *Journal of Nanoparticle Research* 11, 251-257 (2008).

105. N. Lewinski, V. Colvin, R. Drezek. Cytotoxicity of Nanoparticles. *Small* 4, 26-49 (2008).

106. B. Fadeel, A. E. Garcia-Bennett. Better safe than sorry: Understanding the toxicological properties of inorganic nanoparticles manufactured for biomedical applications. *Advanced Drug Delivery Reviews* 62, 362-374 (2010).

107. B. Pelaz, G. Charron, C. Pfeiffer, Y. L. Zhao, J. M. de la Fuente, X. J. Liang, W. J. Parak, P. del Pino. Interfacing Engineered Nanoparticles with Biological Systems: Anticipating Adverse NanoBio Interactions. *Small* 9, 1573-1584 (2013).

108. S. J. Soenen, B. Manshian, J. M. Montenegro, F. Amin, B. Meermann, T. Thiron, M. Cornelissen, F. Vanhaecke, S. Doak, W. J. Parak et al. Cytotoxic Effects of Gold Nanoparticles: A Multiparametric Study. *Acs Nano* 6, 5767-5783 (2012).

109. B. B. Manshian, S. Munck, P. Agostinis, U. Himmelreich, S. J. Soenen. High content analysis at single cell level identifies different cellular responses dependent on nanomaterial concentrations. *Scientific Reports* 5, 13890 (2015).

110. C. Rosman, S. Pierrat, A. Henkel, M. Tarantola, D. Schneider, E. Sunnick, A. Janshoff, C. Sönnichsen. A New Approach to Assess Gold Nanoparticle Uptake by Mammalian Cells: Combining Optical Dark-Field and Transmission Electron Microscopy. *Small* 8, 3683-3690 (2012).

111. B. Pelaz, S. Jaber, D. J. de Aberasturi, V. Wulf, T. Aida, J. M. de la Fuente, J. Feldmann, H. E. Gaub, L. Josephson, C. R. Kagan et al. The State of Nanoparticle-Based Nanoscience and Biotechnology: Progress, Promises, and Challenges. *Acs Nano* 6, 8468-8483 (2012).

112. D. Pissuwan, T. Niidome. Polyelectrolyte-coated gold nanorods and their biomedical applications. *Nanoscale* 7, 59-65 (2015).

113. I. Mannelli, M. P. Marco. Recent advances in analytical and bioanalysis applications of noble metal nanorods. *Analytical and Bioanalytical Chemistry* 398, 2451-2469 (2010).

114. J. W. Kang, P. T. C. So, R. R. Dasari, D.-K. Lim. High Resolution Live Cell Raman Imaging Using Subcellular Organelle-Targeting SERS-Sensitive Gold Nanoparticles with Highly Narrow Intra-Nanogap. *Nano Letters* 15, 1766-1772 (2015).

115. C. Smith. Microscopy: Two microscopes are better than one. *Nature* 492, 293-297 (2012).

116. J. Ando, K. Fujita, N. I. Smith, S. Kawata. Dynamic SERS imaging of cellular transport pathways with endocytosed gold nanoparticles. *Nano Letters* 11, 5344-5348 (2011).

117. K.-C. Huang, K. Bando, J. Ando, N. I. Smith, K. Fujita, S. Kawata. 3D SERS (surface enhanced Raman scattering) imaging of intracellular pathways. *Methods* 68, 348-353 (2014).

118. T. Sannomiya, J. Voros. Single plasmonic nanoparticles for biosensing. *Trends in Biotechnology* 29, 343-351 (2011).

119. T. Wang, D. Halaney, D. Ho, M. D. Feldman, T. E. Milner. Two-photon luminescence properties of gold nanorods. *Biomedical Optics Express* 4, 584-595 (2013).

120. H. Wang, T. B. Huff, D. A. Zweifel, W. He, P. S. Low, A. Wei, J.-X. Cheng. In vitro and in vivo two-photon luminescence imaging of single gold nanorods. *Proceedings of the National Academy of Sciences* 102, 15752-15756 (2005).

121. B. van den Broek, B. Ashcroft, T. H. Oosterkamp, J. van Noort. Parallel Nanometric 3D Tracking of Intracellular Gold Nanorods Using Multifocal Two-Photon Microscopy. *Nano Letters* 13, 980-986 (2013).

122. D.-S. Wang, F.-Y. Hsu, C.-W. Lin. Surface plasmon effects on two photon luminescence of gold nanorods. *Optics Express* 17, 11350-11359 (2009).

123. D. B. Peckys, N. de Jonge. Visualizing gold nanoparticle uptake in live cells with liquid scanning transmission electron microscopy. *Nano Letters* 11, 1733-1738 (2011).

124. E. S. Pohlmann, K. Patel, S. Guo, M. J. Dukes, Z. Sheng, D. F. Kelly. Real-Time Visualization of Nanoparticles Interacting with Glioblastoma Stem Cells. *Nano Letters* 15, 2329-2335 (2015).

125. A. Astolfo, F. Arfelli, E. Schultke, S. James, L. Mancini, R.-H. Menk. A detailed study of gold-nanoparticle loaded cells using X-ray based techniques for cell-tracking applications with single-cell sensitivity. *Nanoscale* 5, 3337-3345 (2013).

126. J. Qian, L. Jiang, F. Cai, D. Wang, S. He. Fluorescence-surface enhanced Raman scattering co-functionalized gold nanorods as near-infrared probes for purely optical in vivo imaging. *Biomaterials* 32, 1601-1610 (2011).

127. J. V. Jokerst, A. J. Cole, D. Van de Sompel, S. S. Gambhir. Gold Nanorods for Ovarian Cancer Detection with Photoacoustic Imaging and Resection Guidance via Raman Imaging in Living Mice. *Acs Nano* 6, 10366-10377 (2012).

128. P. Ghosh, G. Han, M. De, C. K. Kim, V. M. Rotello. Gold nanoparticles in delivery applications. *Advanced Drug Delivery Reviews* 60, 1307-1315 (2008).

129. Y. Yan, G. K. Such, A. P. R. Johnston, J. P. Best, F. Caruso. Engineering Particles for Therapeutic Delivery: Prospects and Challenges. *Acs Nano* 6, 3663-3669 (2012).

130. S. Zong, Z. Wang, H. Chen, J. Yang, Y. Cui. Surface Enhanced Raman Scattering Traceable and Glutathione Responsive Nanocarrier for the Intracellular Drug Delivery. *Analytical Chemistry* 85, 2223-2230 (2013).

131. K. Ock, W. I. Jeon, E. O. Ganbold, M. Kim, J. Park, J. H. Seo, K. Cho, S. W. Joo, S. Y. Lee. Real-Time Monitoring of Glutathione-Triggered Thiopurine Anticancer Drug Release in Live Cells Investigated by Surface-Enhanced Raman Scattering. *Analytical Chemistry* 84, 2172-2178 (2012).

132. K. S. Ock, E. O. Ganbold, J. Park, K. Cho, S. W. Joo, S. Y. Lee. Label-free Raman spectroscopy for accessing intracellular anticancer drug release on gold nanoparticles. *Analyst* 137, 2852-2859 (2012).

133. B. Kang, M. M. Afifi, L. A. Austin, M. A. El-Sayed. Exploiting the Nanoparticle Plasmon Effect: Observing Drug Delivery Dynamics in Single Cells via Raman/Fluorescence Imaging Spectroscopy. *Acs Nano* 7, 7420-7427 (2013).

134. N. X. Zhao, J. You, Z. H. Zeng, C. Li, Y. L. Zu. An Ultra pH-Sensitive and Aptamer-Equipped Nanoscale Drug-Delivery System for Selective Killing of Tumor Cells. *Small* 9, 3477-3484 (2013).

135. J.-H. Park, G. von Maltzahn, L. L. Ong, A. Centrone, T. A. Hatton, E. Ruoslahti, S. N. Bhatia, M. J. Sailor. Cooperative Nanoparticles for Tumor Detection and Photothermally Triggered Drug Delivery. *Advanced Materials* 22, 880-885 (2010).

136. H. Chen, X. Chi, B. Li, M. Zhang, Y. Ma, S. Achilefu, Y. Gu. Drug loaded multilayered gold nanorods for combined photothermal and chemotherapy. *Biomaterials Science* 2, 996-1006 (2014).

137. A. N. Ilinskaya, M. A. Dobrovolskaia. Understanding the immunogenicity and antigenicity of nanomaterials: Past, present and future. *Toxicology and Applied Pharmacology* 299, 70-77 (2016).

138. K. M. Harkness, B. N. Turner, A. C. Agrawal, Y. Zhang, J. A. McLean, D. E. Cliffel. Biomimetic monolayer-protected gold nanoparticles for immunorecognition. *Nanoscale* 4, 3843-3851 (2012).

139. N. M. Molino, A. K. L. Anderson, E. L. Nelson, S.-W. Wang. Biomimetic Protein Nanoparticles Facilitate Enhanced Dendritic Cell Activation and Cross-Presentation. *Acs Nano* 7, 9743-9752 (2013).

140. D. P. Patterson, A. Rynda-Apple, A. L. Harmsen, A. G. Harmsen, T. Douglas. Biomimetic Antigenic Nanoparticles Elicit Controlled Protective Immune Response to Influenza. *Acs Nano* 7, 3036-3044 (2013).

141. D. F. Moyano, M. Goldsmith, D. J. Solfiell, D. Landesman-Milo, O. R. Miranda, D. Peer, V. M. Rotello. Nanoparticle Hydrophobicity Dictates Immune Response. *Journal of the American Chemical Society* 134, 3965-3967 (2012).

142. V. Manolova, A. Flace, M. Bauer, K. Schwarz, P. Saudan, M. F. Bachmann. Nanoparticles target distinct dendritic cell populations according to their size. *European Journal of Immunology* 38, 1404-1413 (2008).

143. A. Stano, C. Nembrini, M. A. Swartz, J. A. Hubbell, E. Simeoni. Nanoparticle size influences the magnitude and quality of mucosal immune responses after intranasal immunization. *Vaccine* 30, 7541-7546 (2012).

144. A. Y. Lin, J. Lunsford, A. S. Bear, J. K. Young, P. Eckels, L. Luo, A. E. Foster, R. A. Drezek. High-density sub-100-nm peptide-gold nanoparticle complexes improve vaccine presentation by dendritic cells in vitro. *Nanoscale Research Letters* 8, 72 (2013).

145. C. Y. Tsai, S. L. Lu, C. W. Hu, C. S. Yeh, G. B. Lee, H. Y. Lei. Size-Dependent Attenuation of TLR9 Signaling by Gold Nanoparticles in Macrophages. *The Journal of Immunology* 188, 68-76 (2012).

146. Y. S. Chen, Y. C. Hung, W. H. Lin, G. S. Huang. Assessment of gold nanoparticles as a size-dependent vaccine carrier for enhancing the antibody response against synthetic foot-and-mouth disease virus peptide. *Nanotechnology* 21, 195101 (2010).

147. D. Mahony, A. S. Cavallaro, F. Stahr, T. J. Mahony, S. Z. Qiao, N. Mitter. Mesoporous Silica Nanoparticles Act as a Self-Adjuvant for Ovalbumin Model Antigen in Mice. *Small* 9, 3138-3146 (2013).

148. I.-H. Lee, H.-K. Kwon, S. An, D. Kim, S. Kim, M. K. Yu, J.-H. Lee, T.-S. Lee, S.-H. Im, S. Jon. Imageable antigen-presenting gold nanoparticle vaccines for effective cancer immunotherapy in vivo. *Angewandte Chemie* 51, 8800-8805 (2012).

149. H. Bruus. *Theoretical Microfluidics*. 1 1, Oxford University Press (2008).

150. T. M. Squires, S. R. Quake. Microfluidics: Fluid physics at the nanoliter scale. *Reviews of Modern Physics* 77, 977-1026 (2005).

151. P. Yager, T. Edwards, E. Fu, K. Helton, K. Nelson, M. R. Tam, B. H. Weigl. Microfluidic diagnostic technologies for global public health. *Nature* 442, 412-418 (2006).

152. R. N. Zare, S. Kim. Microfluidic Platforms for Single-Cell Analysis. *Annual Review of Biomedical Engineering* 12, 187-201 (2010).

153. S. K. Sia, G. M. Whitesides. Microfluidic devices fabricated in poly(dimethylsiloxane) for biological studies. *Electrophoresis* 24, 3563-3576 (2003).

154. A. Schmid, H. Kortmann, P. S. Dittrich, L. M. Blank. Chemical and biological single cell analysis. *Current Opinion in Biotechnology* 21, 12-20 (2010).

155. J. T. S. Fernandes, S. Tenreiro, A. Gameiro, V. Chu, T. F. Outeiro, J. P. Conde. Modulation of alpha-synuclein toxicity in yeast using a novel microfluidic-based gradient generator. *Lab on a Chip* 14, 3949-3957 (2014).

156. L. G. Griffith, M. A. Swartz. Capturing complex 3D tissue physiology in vitro. *Nature Reviews Molecular Cell Biology* 7, 211-224 (2006).

157. D. Wlodkowic, S. Faley, J. Skommer, D. McGuinness, J. M. Cooper. Biological implications of polymeric microdevices for live cell assays. *Analytical Chemistry* 81, 9828-9833 (2009).

158. L. Kim, Y.-C. Toh, J. Voldman, H. Yu. A practical guide to microfluidic perfusion culture of adherent mammalian cells. *Lab on a Chip* 7, 681-694 (2007).

159. L. Kim, M. D. Vahey, H.-Y. Lee, J. Voldman. Microfluidic arrays for logarithmically perfused embryonic stem cell culture. *Lab on a Chip* 6, 394-406 (2006).

160. K. M. Kim, Y. J. Choi, J.-H. Hwang, A. R. Kim, H. J. Cho, E. S. Hwang, J. Y. Park, S.-H. Lee, J.-H. Hong. Shear Stress Induced by an Interstitial Level of Slow Flow Increases the Osteogenic Differentiation of Mesenchymal Stem Cells through TAZ Activation. *PLoS One* 9, e92427 (2014).

161. P. J. Hung, P. J. Lee, P. Sabounchi, R. Lin, L. P. Lee. Continuous perfusion microfluidic cell culture array for high-throughput cell-based assays. *Biotechnology and Bioengineering* 89, 1-8 (2005).

162. D. Huh, B. D. Matthews, A. Mammoto, M. Montoya-Zavala, H. Y. Hsin, D. E. Ingber. Reconstituting Organ-Level Lung Functions on a Chip. *Science* 328, 1662-1668 (2010).

163. H. J. Kim, D. Huh, G. Hamilton, D. E. Ingber. Human gut-on-a-chip inhabited by microbial flora that experiences intestinal peristalsis-like motions and flow. *Lab on a Chip* 12, 2165-2174 (2012).

164. S. N. Bhatia, D. E. Ingber. Microfluidic organs-on-chips. *Nature Biotechnology* 32, 760-772 (2014).

165.	C. A. Cunha-Matos, O. R. Millington, A. W. Wark, M. Zagnoni. Real-time assessment of nanoparticle-mediated antigen delivery and cell response. *Lab on a Chip* 16, 3374-3381 (2016).

166.	J. R. Rettig, A. Folch. Large-Scale Single-Cell Trapping And Imaging Using Microwell Arrays. *Analytical Chemistry* 77, 5628-5634 (2005).

167.	Y. Liu, B. Kirkland, J. Shirley, Z. Wang, P. Zhang, J. Stembridge, W. Wong, S.-i. Takebayashi, D. M. Gilbert, S. Lenhert et al. Development of a single-cell array for large-scale DNA fluorescence in situ hybridization. *Lab on a Chip* 13, 1316-1324 (2013).

168.	J. M. Collins, R. T. S. Lam, Z. Yang, B. Semsarieh, A. B. Smetana, S. Nettikadan. Targeted delivery to single cells in precisely controlled microenvironments. *Lab on a Chip* 12, 2643-2648 (2012).

169.	A. C. Rowat, J. C. Bird, J. J. Agresti, O. J. Rando, D. A. Weitz. Tracking lineages of single cells in lines using a microfluidic device. *Proceedings of the National Academy of Sciences* 106, 18149-18154 (2009).

170.	E. Brouzes, M. Medkova, N. Savenelli, D. Marran, M. Twardowski, J. B. Hutchison, J. M. Rothberg, D. R. Link, N. Perrimon, M. L. Samuels. Droplet microfluidic technology for single-cell high-throughput screening. *Proceedings of the National Academy of Sciences* 106, 14195-14200 (2009).

171.	R. J. Kimmerling, G. Lee Szeto, J. W. Li, A. S. Genshaft, S. W. Kazer, K. R. Payer, J. de Riba Borrajo, P. C. Blainey, D. J. Irvine, A. K. Shalek et al. A microfluidic platform enabling single-cell RNA-seq of multigenerational lineages. *Nature Communications* 7, 10220 (2016).

172.	K. Chung, C. A. Rivet, M. L. Kemp, H. Lu. Imaging single-cell signaling dynamics with a deterministic high-density single-cell trap array. *Analytical Chemistry* 83, 7044-7052 (2011).

173.	J.-P. Frimat, M. Becker, Y.-Y. Chiang, U. Marggraf, D. Janasek, J. G. Hengstler, J. Franzke, J. West. A microfluidic array with cellular valving for single cell co-culture. *Lab on a Chip* 11, 231-237 (2011).

174.	S. A. Kobel, O. Burri, A. Griffa, M. Girotra, A. Seitz, M. P. Lutolf. Automated analysis of single stem cells in microfluidic traps. *Lab on a Chip* 12, 2843-2849 (2012).

175.	R. D. Sochol, M. E. Dueck, S. Li, L. P. Lee, L. Lin. Hydrodynamic resettability for a microfluidic particulate-based arraying system. *Lab on a Chip* 12, 5051-5056 (2012).

176. D. Di Carlo, N. Aghdam, L. P. Lee. Single-cell enzyme concentrations, kinetics, and inhibition analysis using high-density hydrodynamic cell isolation arrays. *Analytical Chemistry* 78, 4925-4930 (2006).

177. A. H. Jeorrett, S. L. Neale, D. Massoubre, E. Gu, R. K. Henderson, O. Millington, K. Mathieson, M. D. Dawson. Optoelectronic tweezers system for single cell manipulation and fluorescence imaging of live immune cells. *Optics Express* 22, 1372-1380 (2014).

178. Y. Lin, R. l. Trouillon, G. Safina, A. G. Ewing. Chemical Analysis of Single Cells. *Analytical Chemistry* 83, 4369-4392 (2011).

179. F. T. G. van den Brink, E. Gool, J.-P. Frimat, J. Bomer, A. van den Berg, S. Le Gac. Parallel single-cell analysis microfluidic platform. *Electrophoresis* 32, 3094-3100 (2011).

180. H. Kortmann, F. Kurth, L. M. Blank, P. S. Dittrich, A. Schmid. Towards real time analysis of protein secretion from single cells. *Lab on a Chip* 9, 3047-3049 (2009).

181. M. Wu, T. D. Perroud, N. Srivastava, C. S. Branda, K. L. Sale, B. D. Carson, K. D. Patel, S. S. Branda, A. K. Singh. Microfluidically-unified cell culture, sample preparation, imaging and flow cytometry for measurement of cell signaling pathways with single cell resolution. *Lab on a Chip* 12, 2823-2831 (2012).

182. S. L. Faley, M. Copland, D. Wlodkowic, W. Kolch, K. T. Seale, J. P. Wikswo, J. M. Cooper. Microfluidic single cell arrays to interrogate signalling dynamics of individual, patient-derived hematopoietic stem cells. *Lab on a Chip* 9, 2659-2664 (2009).

183. A. Prokop, Z. Prokop, D. Schaffer, E. Kozlov, J. Wikswo, D. Cliffel, F. Baudenbacher. NanoLiterBioReactor: Long-Term Mammalian Cell Culture at Nanofabricated Scale. *Biomedical Microdevices* 6, 325-339 (2004).

184. S. Faley, M. Copland, J. Reboud, J. M. Cooper. Intracellular protein trafficking kinetics in chronic myeloid leukemia stem cells using a microfluidic platform. *Integrative Biology* 4, 368-373 (2012).

185. C. D. Syme, N. M. S. Sirimuthu, S. L. Faley, J. M. Cooper. SERS mapping of nanoparticle labels in single cells using a microfluidic chip. *Chemical Communications* 46, 7921-7923 (2010).

186. P. Neuzil, S. Giselbrecht, K. Lange, T. J. Huang, A. Manz. Revisiting lab-on-a-chip technology for drug discovery. *Nature Reviews Drug Discovery* 11, 620-632 (2012).

187. L. Businaro, A. De Ninno, G. Schiavoni, V. Lucarini, G. Ciasca, A. Gerardino, F. Belardelli, L. Gabriele, F. Mattei. Cross talk between cancer and immune cells: exploring complex dynamics in a microfluidic environment. *Lab on a Chip* 13, 229-239 (2013).

188. L. M. McLaughlin, H. Xu, S. E. Carden, S. Fisher, M. Reyes, S. C. Heilshorn, D. M. Monack. A microfluidic-based genetic screen to identify microbial virulence factors that inhibit dendritic cell migration. *Integrative Biology* 6, 438-449 (2014).

189. B. Mitra, R. Jindal, S. Lee, D. X. Dong, L. Li, N. Sharma, T. Maguire, R. Schloss, M. L. Yarmush. Microdevice integrating innate and adaptive immune responses associated with antigen presentation by dendritic cells. *RSC Advances* 3, 16002-16010 (2013).

190. B. G. Ricart, M. T. Yang, C. A. Hunter, C. S. Chen, D. A. Hammer. Measuring traction forces of motile dendritic cells on micropost arrays. *Biophysical Journal* 101, 2620-2628 (2011).

191. N. Li Jeon, H. Baskaran, S. K. W. Dertinger, G. M. Whitesides, L. Van De Water, M. Toner. Neutrophil chemotaxis in linear and complex gradients of interleukin-8 formed in a microfabricated device. *Nature Biotechnology* 20, 826-830 (2002).

192. S. F. G. van Helden, F. N. van Leeuwen, C. G. Figdor. Human and murine model cell lines for dendritic cell biology evaluated. *Immunology Letters* 117, 191-197 (2008).

193. E. P. Kartalov, J. F. Zhong, A. Scherer, S. R. Quake, C. R. Taylor, W. F. Anderson. High-throughput multi-antigen microfluidic fluorescence immunoassays. *Biotechniques* 40, 85-90 (2006).

194. O. C. Farokhzad, A. Khademhosseini, S. Jon, A. Hermmann, J. Cheng, C. Chin, A. Kiselyuk, B. Teply, G. Eng, R. Langer. Microfluidic System for Studying the Interaction of Nanoparticles and Microparticles with Cells. *Analytical Chemistry* 77, 5453-5459 (2005).

195. D. L. Priwitaningrum, J.-B. G. Blondé, A. Sridhar, J. van Baarlen, W. E. Hennink, G. Storm, S. Le Gac, J. Prakash. Tumor stroma-containing 3D spheroid arrays: A tool to study nanoparticle penetration. *Journal of Controlled Release* 244B, 257-268 (2016).

196. C. J. Orendorff, C. J. Murphy. Quantitation of metal content in the silver-assisted growth of gold nanorods. *Journal of Physical Chemistry B* 110, 3990-3994 (2006).

197. I. Johnson. *The Molecular Probes Handbook: A Guide to Fluorescent Probes and Labeling Technologies*. 11th edition, Life Technologies Corporation (2010).

198. M. J. Barnden, J. Allison, W. R. Heath, F. R. Carbone. Defective TCR expression in transgenic mice constructed using cDNA-based [agr]- and [bgr]-chain genes under the control of heterologous regulatory elements. *Immunology & Cell Biology* 76, 34-40 (1998).

199. M. B. Lutz, N. Kukutsch, A. L. J. Ogilvie, S. Rößner, F. Koch, N. Romani, G. Schuler. An advanced culture method for generating large quantities of highly pure dendritic cells from mouse bone marrow. *Journal of Immunological Methods* 223, 77-92 (1999).

200. J. W. Park, B. Vahidi, A. M. Taylor, S. W. Rhee, N. L. Jeon. Microfluidic culture platform for neuroscience research. *Nature Protocols* 1, 2128-2136 (2006).

201. K. T. Seale, S. L. Faley, J. Chamberlain, J. P. Wikswo. Macro to nano: a simple method for transporting cultured cells from milliliter scale to nanoliter scale. *Experimental Biology and Medicine* 235, 777-783 (2010).

202. N. M. S. Sirimuthu, C. D. Syme, J. M. Cooper. Investigation of the stability of labelled nanoparticles for SE(R)RS measurements in cells. *Chemical Communications* 47, 4099-4101 (2011).

203. W. Ni, H. Chen, J. Su, Z. Sun, J. Wang, H. Wu. Effects of Dyes, Gold Nanocrystals, pH, and Metal Ions on Plasmonic and Molecular Resonance Coupling. *Journal of the American Chemical Society* 132, 4806-4814 (2010).

204. M. K. Gregas, J. P. Scaffidi, B. Lauly, T. Vo-Dinh. Surface-Enhanced Raman Scattering Detection and Tracking of Nanoprobes: Enhanced Uptake and Nuclear Targeting in Single Cells. *Applied Spectroscopy* 64, 858-866 (2010).

205. E. Ringe, B. Sharma, A.-I. Henry, L. D. Marks, R. P. Van Duyne. Single nanoparticle plasmonics. *Physical Chemistry Chemical Physics* 15, 4110-4129 (2013).

206. D. G. Spiller, C. D. Wood, D. A. Rand, M. R. H. White. Measurement of single-cell dynamics. *Nature* 465, 736-745 (2010).

207. M.-C. Kim, Z. Wang, R. H. W. Lam, T. Thorsen. Building a better cell trap: Applying Lagrangian modeling to the design of microfluidic devices for cell biology. *Journal of Applied Physics* 103, 044701 (2008).

208. M. Khoury, A. Bransky, N. Korin, L. Konak, G. Enikolopov, I. Tzchori, S. Levenberg. A microfluidic traps system supporting prolonged culture of human embryonic stem cells aggregates. *Biomedical Microdevices* 12, 1001-1008 (2010).

209. S. Halldorsson, E. Lucumi, R. Gómez-Sjöberg, R. M. T. Fleming. Advantages and challenges of microfluidic cell culture in polydimethylsiloxane devices. *Biosensors and Bioelectronics* 63, 218-231 (2015).

210. L. Medda, M. Monduzzi, A. Salis. The molecular motion of bovine serum albumin under physiological conditions is ion specific. *Chemical Communications* 51, 6663-6666 (2015).

211. C. T. Culbertson, S. C. Jacobson, J. M. Ramsey. Diffusion coefficient measurements in microfluidic devices. *Talanta* 56, 365-373 (2002).

212. J. A. Yang, H. T. Phan, S. Vaidya, C. J. Murphy. Nanovacuums: Nanoparticle Uptake and Differential Cellular Migration on a Carpet of Nanoparticles. *Nano Letters* 13, 2295-2302 (2013).

213. H. P. Erickson. Size and Shape of Protein Molecules at the Nanometer Level Determined by Sedimentation, Gel Filtration, and Electron Microscopy. *Biological Procedures Online* 11, 32-51 (2009).

214. A. Badiee, V. Heravi Shargh, A. Khamesipour, M. R. Jaafari. Micro/nanoparticle adjuvants for antileishmanial vaccines: Present and future trends. *Vaccine* 31, 735-749 (2013).

215. M. A. Dobrovolskaia, S. E. McNeil. Immunological properties of engineered nanomaterials. *Nature Nanotechnology* 2, 469-478 (2007).

216. A. E. Christakou, M. Ohlin, B. Vanherberghen, M. A. Khorshidi, N. Kadri, T. Frisk, M. Wiklund, B. Onfelt. Live cell imaging in a micro-array of acoustic traps facilitates quantification of natural killer cell heterogeneity. *Integrative Biology* 5, 712-719 (2013).

217. S. Awate, L. A. Babiuk, G. Mutwiri. Mechanisms of Action of Adjuvants. *Frontiers in Immunology* 4, 114 (2013).

218. K. C. L. Black, J. Yi, J. G. Rivera, D. C. Zelasko-Leon, P. B. Messersmith. Polydopamine-enabled surface functionalization of gold nanorods for cancer cell-targeted imaging and photothermal therapy. *Nanomedicine* 8, 17-28 (2012).

219. A. W. Wark, R. J. Stokes, S. B. Darby, W. E. Smith, D. Graham. Dynamic Imaging Analysis of SERS-Active Nanoparticle Clusters in Suspension. *Journal of Physical Chemistry C* 114, 18115-18120 (2010).

220. A. Abbaspourrad, S. S. Datta, D. A. Weitz. Controlling Release From pH-Responsive Microcapsules. *Langmuir* 29, 12697-12702 (2013).

221. M. T. Popescu, C. Tsitsilianis. Controlled Delivery of Functionalized Gold Nanoparticles by pH-Sensitive Polymersomes. *Acs Macro Letters* 2, 222-225 (2013).

222. Q. S. Zheng, T. R. Lin, H. Y. Wu, L. Q. Guo, P. R. Ye, Y. L. Hao, Q. Q. Guo, J. Z. Jiang, F. F. Fu, G. N. Chen. Mussel-inspired polydopamine coated mesoporous silica nanoparticles as pH-sensitive nanocarriers for controlled release. *International Journal of Pharmaceutics* 463, 22-26 (2014).

223. Z. Guan, S. Jia, Z. Zhu, M. Zhang, C. J. Yang. Facile and Rapid Generation of Large-scale Micro-collagen-gel Array for Long-term Single Cell 3D Culture and Cell Proliferation Heterogeneity Analysis. *Analytical Chemistry* 86, 2789-2797 (2014).

224. S. K. W. Dertinger, X. Jiang, Z. Li, V. N. Murthy, G. M. Whitesides. Gradients of substrate-bound laminin orient axonal specification of neurons. *Proceedings of the National Academy of Sciences* 99, 12542-12547 (2002).

225. K. J. Regehr, M. Domenech, J. T. Koepsel, K. C. Carver, S. J. Ellison-Zelski, W. L. Murphy, L. A. Schuler, E. T. Alarid, D. J. Beebe. Biological implications of polydimethylsiloxane-based microfluidic cell culture. *Lab on a Chip* 9, 2132-2139 (2009).

226. E. W. K. Young, D. J. Beebe. Fundamentals of microfluidic cell culture in controlled microenvironments. *Chemical Society Reviews* 39, 1036-1048 (2010).

227. H. Bi, S. Meng, Y. Li, K. Guo, Y. Chen, J. Kong, P. Yang, W. Zhong, B. Liu. Deposition of PEG onto PMMA microchannel surface to minimize nonspecific adsorption. *Lab on a Chip* 6, 769-775 (2006).

228. W. Zheng, Z. Wang, W. Zhang, X. Jiang. A simple PDMS-based microfluidic channel design that removes bubbles for long-term on-chip culture of mammalian cells. *Lab on a Chip* 10, 2906-2910 (2010).

229. A. Schepers, C. Li, A. Chhabra, B. T. Seney, S. Bhatia. Engineering a perfusable 3D human liver platform from iPS cells. *Lab on a Chip* 16, 2644-2653 (2016).